

NASA/CP—2002-211831



17th Space Photovoltaic Research and Technology Conference

October 2002

The NASA STI Program Office . . . in Profile

Since its founding, NASA has been dedicated to the advancement of aeronautics and space science. The NASA Scientific and Technical Information (STI) Program Office plays a key part in helping NASA maintain this important role.

The NASA STI Program Office is operated by Langley Research Center, the Lead Center for NASA's scientific and technical information. The NASA STI Program Office provides access to the NASA STI Database, the largest collection of aeronautical and space science STI in the world. The Program Office is also NASA's institutional mechanism for disseminating the results of its research and development activities. These results are published by NASA in the NASA STI Report Series, which includes the following report types:

- **TECHNICAL PUBLICATION.** Reports of completed research or a major significant phase of research that present the results of NASA programs and include extensive data or theoretical analysis. Includes compilations of significant scientific and technical data and information deemed to be of continuing reference value. NASA's counterpart of peer-reviewed formal professional papers but has less stringent limitations on manuscript length and extent of graphic presentations.
- **TECHNICAL MEMORANDUM.** Scientific and technical findings that are preliminary or of specialized interest, e.g., quick release reports, working papers, and bibliographies that contain minimal annotation. Does not contain extensive analysis.
- **CONTRACTOR REPORT.** Scientific and technical findings by NASA-sponsored contractors and grantees.

- **CONFERENCE PUBLICATION.** Collected papers from scientific and technical conferences, symposia, seminars, or other meetings sponsored or cosponsored by NASA.
- **SPECIAL PUBLICATION.** Scientific, technical, or historical information from NASA programs, projects, and missions, often concerned with subjects having substantial public interest.
- **TECHNICAL TRANSLATION.** English-language translations of foreign scientific and technical material pertinent to NASA's mission.

Specialized services that complement the STI Program Office's diverse offerings include creating custom thesauri, building customized databases, organizing and publishing research results . . . even providing videos.

For more information about the NASA STI Program Office, see the following:

- Access the NASA STI Program Home Page at <http://www.sti.nasa.gov>
- E-mail your question via the Internet to help@sti.nasa.gov
- Fax your question to the NASA Access Help Desk at 301-621-0134
- Telephone the NASA Access Help Desk at 301-621-0390
- Write to:
NASA Access Help Desk
NASA Center for Aerospace Information
7121 Standard Drive
Hanover, MD 21076

NASA/CP—2002-211831



17th Space Photovoltaic Research and Technology Conference

Proceedings of a conference
held at Ohio Aerospace Institute
and sponsored by NASA Glenn Research Center
Brook Park, Ohio, September 11–13, 2001

National Aeronautics and
Space Administration

Glenn Research Center

October 2002

Trade names or manufacturers' names are used in this report for identification only. This usage does not constitute an official endorsement, either expressed or implied, by the National Aeronautics and Space Administration.

Available from

NASA Center for Aerospace Information
7121 Standard Drive
Hanover, MD 21076

National Technical Information Service
5285 Port Royal Road
Springfield, VA 22100

Available electronically at <http://gltrs.grc.nasa.gov>

Foreword

The 17th Space Photovoltaic Research and Technology (SPRAT XVII) Conference was held September 11–13, 2001, at the Ohio Aerospace Institute (OAI) in Cleveland, Ohio. The SPRAT conference, hosted by the Photovoltaic and Space Environments Branch of the NASA Glenn Research Center, brought together representatives of the space photovoltaic community from around the world to share the latest advances in space solar technology.

While the tragic events of the morning of September 11, 2001, affected the conference attendance and format, we felt that it would have been an even greater loss to cancel the meeting after all the preparation by the organizers and attendees. In light of the closing of both NASA Glenn and OAI on September 11, 2001, the decision was made to cancel the conference workshops, normally a highlight of the meeting, in order to have all of the conference papers presented.

This year's conference continued to build on many of the trends shown in SPRAT XVI; the use of new high-efficiency cells for commercial use and the development of novel array concepts such as Boeing's Solar Tile concept. In addition, new information was presented on space environmental interactions with solar arrays.

At the 14th SPRAT conference, the Irving Weinberg Award was established in memory of Dr. Irving Weinberg, a leading contributor to the field of space photovoltaic research and development for most of his professional career. Past recipients have been Prof. Chandra Goradia, Dr. Masafumi Yamaguchi, and Dr. Dennis Flood. I had the honor of presenting this year's award to Henry Curtis, who has been a contributor to the space photovoltaic community for many years.

In conclusion, I would like to thank all of the conference organizers, session chairs, attendees, and presenters for making the 17th SPRAT conference a success under the most trying circumstances.

Eric B. Clark, Chairman

Table of Contents

HIGH EFFICIENCY TRIPLE JUNCTION MANUFACTURING AND DEVELOPMENT AT EMCORE PHOTOVOLTAICS Daniel J. Aiken, Navid S. Fatemi, Chris S. Murray, Paul R. Sharps, Frank Spadafora, and Mark A. Stan, Emcore Photovoltaics	1
PROGRESS IN THE DEVELOPMENT OF METAMORPHIC MULTI-JUNCTION III–V SPACE-SOLAR CELLS AT ESSENTIAL RESEARCH INCORPORATED Samar Sinharoy, Martin O. Patton, Thomas M. Valko, Sr., and Victor G. Weizer, Essential Research Incorporated	8
THE STRETCHED LENS ARRAY (SLA): AN ULTRA-LIGHT PHOTOVOLTAIC CONCENTRATOR Mark J. O'Neill, ENTECH, Inc.; Michael F. Piszczor, NASA Glenn Research Center; Michael I. Eskenazi, AEC–ABLE; A.J. McDanal, ENTECH, Inc.; Patrick J. George, NASA Glenn Research Center; Matthew M. Botke, AEC–ABLE; Henry W. Brandhorst, Space Power Institute, Auburn University; David L. Edwards, NASA Marshall Space Flight Center; and Paul A. Jaster, 3M	14
34% EFFICIENT InGaP/GaAs/GaSb CELL-INTERCONNECTED-CIRCUITS FOR LINE-FOCUS CONCENTRATOR ARRAYS L.M. Fraas, W.E. Daniels, H.X. Huang, L.E. Minkin, and J.E. Avery, JX Crystals Inc.; C. Chu and P. Iles, Tecstar, Inc.; M.J. O'Neill and A.J. McDanal, ENTECH, Inc.; and Mike Piszczor, NASA Glenn Research Center	24
CARRIER RECOMBINATION AND ESCAPE IN P-I-N MULTIQUANTUM WELL SPACE SOLAR CELLS A. Alemu, C. Monier, L. Williams, and A. Freundlich, University of Houston	32
PROCEDURES AT NREL FOR EVALUATING MULTI-JUNCTION ONE SUN AND CONCENTRATOR CELLS Tom Moriarty, Keith Emery, and Don Dunlavy, National Renewable Energy Laboratory	38
UPDATE ON THE DISPLACEMENT DAMAGE DOSE MODEL FOR PROTON DAMAGE IN GALLIUM ARSENIDE SOLAR CELLS S.R. Messenger and E.A. Burke, SFA, Inc.; and G.P. Summers and R.J. Walters, Naval Research Laboratory	45
BOEING'S HIGH VOLTAGE SOLAR TILE TEST RESULTS Brian J. Reed and David E. Harden; Boeing Phantom Works; and Dale C. Ferguson and David B. Snyder, NASA Glenn Research Center	49
PROTON AND ELECTRON RADIATION DATA AND ANALYSIS OF GaInP ₂ /GaAs/Ge SOLAR CELLS P.R. Sharps, D.J. Aiken, M.A. Stan, C.H. Thang, and Navid Fatemi, Emcore Photovoltaics	55

COMPARISON OF THE ELECTRICAL PERFORMANCE OF VARIOUS AMORPHOUS SILICON THIN FILM SOLAR CELLS PRODUCED FOR THE POWERSPHERE CONCEPT Edward J. Simburger, Jasen Ross, James Matsumoto, Jean Baer, and Nathan Presser, The Aerospace Corporation; and Frank R. Jeffery, Iowa Thin Film Technologies, Inc.	65
THIN-FILM SOLAR ARRAY EARTH ORBIT MISSION APPLICABILITY ASSESSMENT David J. Hoffman, Thomas W. Kerslake, and Aloysius F. Hepp, NASA Glenn Research Center; and Ryne P. Raffaele, Rochester Institute of Technology	74
ATMOSPHERIC PRESSURE SPRAY CHEMICAL VAPOR DEPOSITED CuInS ₂ THIN FILMS FOR PHOTOVOLTAIC APPLICATIONS J.D. Harris, Cleveland State University; R.P. Raffaele, Rochester Institute of Technology; K.K. Banger, M.A. Smith, and D.A. Scheiman, Ohio Aerospace Institute; and A.F. Hepp, NASA Glenn Research Center	84
CIGS ₂ THIN-FILM SOLAR CELLS ON FLEXIBLE FOILS FOR SPACE POWER Neelkanth G. Dhere, Shantinath R. Ghongadi, Mandar B. Pandit, and Anant H. Jahagirdar, Florida Solar Energy Center; and David Scheiman, Ohio Aerospace Institute.....	91
OVERVIEW OF PHOTOVOLTAIC CALIBRATION AND MEASUREMENT STANDARDS AT GRC Cosmo Baraona, David Snyder, David Brinker, Sheila Bailey, and Henry Curtis, NASA Glenn Research Center; and David Scheiman and Phillip Jenkins, Ohio Aerospace Institute.....	101
RADIATION HARDNESS TESTS OF FLEXIBLE, THIN-FILM PHOTOVOLTAICS FOR SPACE APPLICATIONS Pawel Tlomak and Kitt C. Reinhardt, Air Force Research Laboratory, Kirtland Air Force Base; Robert J. Walters, U.S. Naval Research Laboratory; and Scott R. Messenger, SFA, Inc.	105
A REVIEW OF SINGLE SOURCE PRECURSORS FOR THE DEPOSITION OF TERNARY CHALCOPYRITE MATERIALS K.K. Banger, Ohio Aerospace Institute; J. Cowen, J. Harris, R. McClarnon, D.G. Hehemann, and S.A. Duraj, Cleveland State University; D. Scheiman, QSS Inc.; and A.F. Hepp, NASA Glenn Research Center	115
SOLAR FLIGHT ON MARS AND VENUS Geoffrey A. Landis, NASA Glenn Research Center; Christopher LaMarre, University of Illinois; and Anthony Colozza, Analex Corporation.....	126
MEASURED AND SIMULATED DARK J-V CHARACTERISTICS OF a-Si:H SINGLE JUNCTION p-i-n SOLAR CELLS IRRADIATED WITH 40 keV ELECTRONS Kenneth Lord and James R. Woodyard, Wayne State University	128
REPORT ON PROJECT TO CHARACTERIZE MULTI-JUNCTION SOLAR CELLS IN THE STRATOSPHERE USING LOW-COST BALLOON AND COMMUNICATION TECHNOLOGIES Ali Mirza, David Sant, and James R. Woodyard, Wayne State University; Richard R. Johnston, Lawrence Technological University; and William J. Brown, High Altitude Research Corporation.....	137

ADVANCE POWER TECHNOLOGY DEMONSTRATION ON STARSHINE 3 Phillip Jenkins and David Scheiman, Ohio Aerospace Institute; David Wilt, NASA Glenn Research Center; Ryne Raffaele, Rochester Institute of Technology; Robert Button, NASA Glenn Research Center; Mark Smith, Ohio Aerospace Institute; and Thomas Kerslake and Thomas Miller, NASA Glenn Research Center.....	145
SOLAR ARRAY ARCING FAILURE MODE AND HIGH VOLTAGE ARRAY TESTING Dale C. Ferguson, NASA Glenn Research Center	151
CHARGING OF THE INTERNATIONAL SPACE STATION DUE TO ITS HIGH VOLTAGE SOLAR ARRAYS Dale C. Ferguson, NASA Glenn Research Center	154
SINGLE JUNCTION InGaP/GaAs SOLAR CELLS GROWN ON Si SUBSTRATES USING SiGe BUFFER LAYERS S.A. Ringel, J.A. Carlin, C.L. Andre, M.K. Hudait, M. Gonzalez, The Ohio State University; D.M. Wilt, E.B. Clark, P. Jenkins, and D. Scheiman, NASA Glenn Research Center; A. Allerman, Sandia National Laboratory; and E.A. Fitzgerald and C.W. Leitz, Massachusetts Institute of Technology	160
QUANTUM DOT SOLAR CELLS Ryne P. Raffaele, Rochester Institute of Technology; Stephanie L. Castro, Ohio Aerospace Institute; and Aloysius F. Hepp and Sheila G. Bailey, NASA Glenn Research Center.....	178
MISSION APPLICABILITY ASSESSMENT OF INTEGRATED POWER COMPONENTS AND SYSTEMS R.P. Raffaele, Rochester Institute of Technology; A.F. Hepp, G.A. Landis, and D.J. Hoffman, NASA Glenn Research Center	187
A SUMMARY OF THE 2000–2001 NASA GLENN LEAR JET AM0 SOLAR CELL CALIBRATION PROGRAM David Scheiman, Ohio Aerospace Institute; David Brinker, David Snyder, and Cosmo Baraona, NASA Glenn Research Center; Phillip Jenkins, Ohio Aerospace Institute; William J. Rieke and Kurt S. Blankenship, NASA Glenn Research Center; and Ellen M. Tom, Federal Aviation Administration	195
SPACE AND TERRESTRIAL PHOTOVOLTAICS—SYNERGY AND DIVERSITY Sheila Bailey, NASA Glenn Research Center; Ryne Raffaele, Rochester Institute of Technology; and Keith Emery, National Renewable Energy Lab	202
Weinberg Award.....	211
2001 Group Photograph	213

HIGH EFFICIENCY TRIPLE JUNCTION MANUFACTURING AND DEVELOPMENT AT EMCORE PHOTOVOLTAICS

Daniel J. Aiken, Navid S. Fatemi, Chris S. Murray, Paul R. Sharps,
Frank Spadafora, and Mark A. Stan

Emcore Photovoltaics,
10420 Research Rd. SE
Albuquerque, NM 87123

ABSTRACT

This paper describes recent progress in the development of extremely radiation hard, high efficiency triple junction InGaP/GaAs/Ge space solar cells at Emcore Photovoltaics. To address the increasing demand for space satellite power, Emcore Photovoltaics has an on going development program to increase the triple junction 1 sun AM0 BOL efficiency while maintaining the exceptional radiation hardness. This program is partially funded by the Air Force under its Broad Agency Announcement program. Efforts to date have resulted in a 27.5 cm^2 triple junction cell with a 1 sun AM0 BOL efficiency of 27.9% for solar cells designed for maximum EOL performance. This is a 2% absolute efficiency gain over the current production average. Development efforts have included the use of an InGaAs middle cell lattice-matched to Ge and better matched to the AM0 spectrum, as well as an improved MOCVD growth process resulting in a significant boost in the Ge subcell performance.

INTRODUCTION

Emcore Photovoltaics is presently shipping 27.5 cm^2 triple junction InGaP/GaAs/Ge solar cells with an average 1 sun AM0 beginning-of-life (BOL) efficiency of 25.6% (solar constant = 136.7 mW/cm^2). An efficiency distribution of over 55,000 production triple junction solar cells is shown in Figure 1. These cells have very high power remaining factors of 0.90 and 0.87 at 1MeV electron fluences of $5\text{e}14$ and $1\text{e}15/\text{cm}^2$, respectively. To address the increasing demand for high efficiency multi-junction solar cells, Emcore Photovoltaics initiated a development program in the third quarter of 2000 to increase the triple junction efficiency at beginning of life, while also maintaining the exceptional radiation hardness. Early efforts included an establishment of the theoretical and semi-empirical efficiency limits for the present InGaP/GaAs/Ge system. A comparison of our present production solar cell device results versus the theoretical/empirical limits has identified several key areas for improvement within this bandgap system. Development work has focused on addressing these areas for improvement within the InGaP/GaAs/Ge system, while also investigating other bandgap combinations such as adding indium to the GaAs middle cell to lower the bandgap, and adding aluminum to the top InGaP cell to increase the bandgap.

DEVICE MODELING

Establishing the practical and theoretical upper limits on solar cell performance is useful for identifying which subcells in the multi-junction stack have the most to gain from a development project, and what performance and design aspects within those subcell technologies should receive the most focus. Such a model also indicates when a given technology has plateaued, suggesting either a re-evaluation of the assumptions made in the model, or a technology shift to change those assumptions such that higher efficiency can be achieved.

Limiting efficiency modeling has been conducted for each of the three subcells in our production InGaP/GaAs/Ge solar cell. Assumptions made in the model include finite thickness absorption using thicknesses typical of our production devices, no reflection loss and unity collection efficiency. The Wehrli AM0 spectrum was used with a solar constant of 136.7 mW/cm^2 and a lower spectral cutoff of 350 nm. Two different reverse saturation current models were used to gauge both a theoretical upper limit and a more practical limit on Voc. Both a radiative recombination limit as established by Henry [1], as well as an empirical limit as given by Green [2] were used. Ideal diodes were assumed.

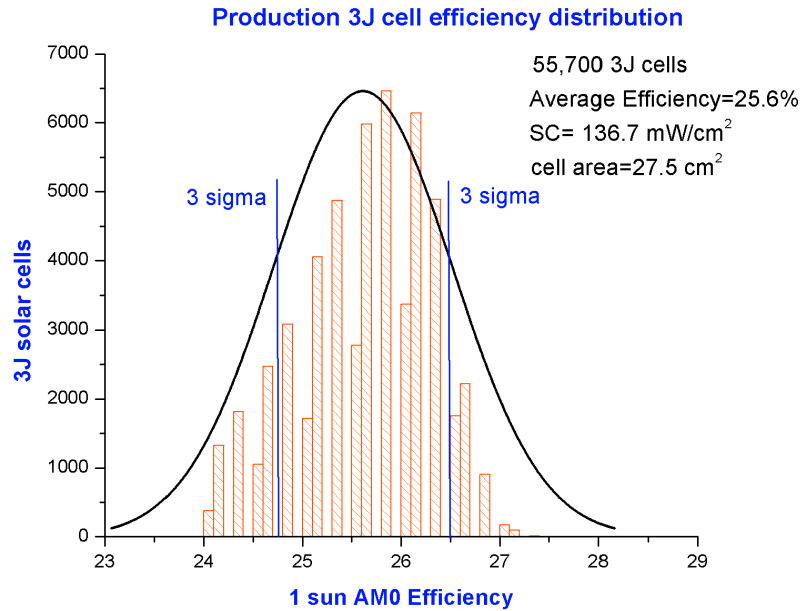


Figure 1 Efficiency distribution for over 55,000 production triple junction solar cells with a device area of 27.5 cm² and using a solar constant of 136.7 mW/cm².

The results of this modeling are shown in Figure 2. Each subcell shows four different parameter limits corresponding to photocurrent, radiatively limited Voc, practically limited Voc, and fill factor determined from the practical Voc limit. The shaded portion of each bar represents the fraction of the limiting parameter values that Emcore's production devices have achieved. The percent of the limiting values achieved as indicated in Figure 2 are also tabulated in Table 1.

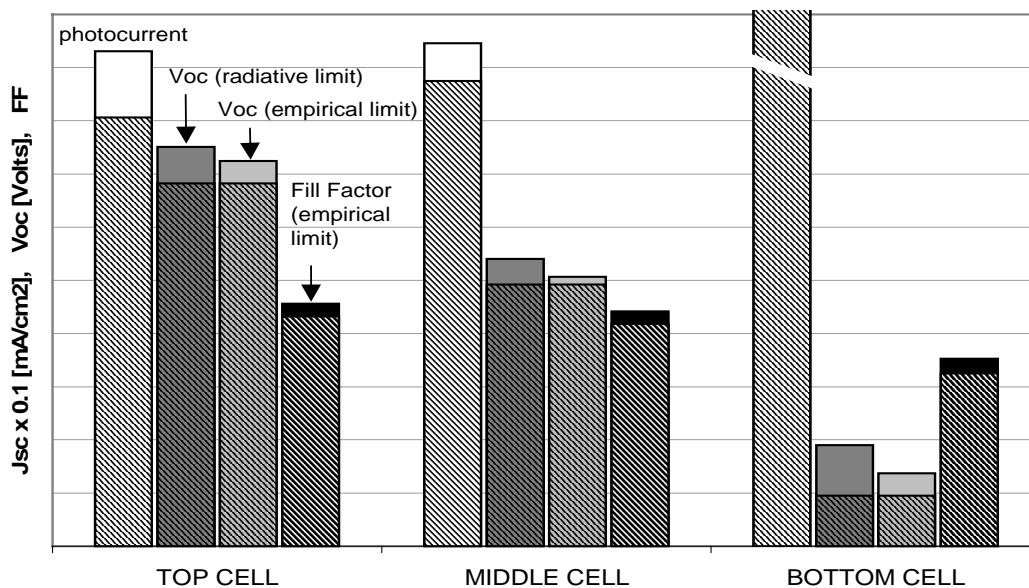


Figure 2 Results of a limiting efficiency model, showing the limiting Jsc, Voc and FF for each subcell in a multi-junction. Shaded regions indicate the fraction of those limits achieved in production.

Achieved photocurrent percentages greater than about 90% indicate very high internal collection efficiency, with the remaining 10% resulting mainly from grid obscuration and reflection loss. This modeling therefore suggests very good collection efficiency from the GaAs subcell, and also that the top subcell current collection could be improved. The Ge subcell photocurrent is well below the limiting value but is not a critical path for improvement in our present multi-junction configuration due to the excess current already generated by this subcell. However, such a low photocurrent percentage is indicative of a lack of control of recombination within the Ge subcell, which suggests that an increase in the Ge Voc may be possible. Additionally, addressing the relatively low “blue” response in the quantum efficiency of the Ge subcell will become important in future 3 or 4 junction solar cells where the Ge subcell is more closely current matched with the other subcells.

Table 1 Percentages of the limiting output parameters achieved in production, as shown graphically in Figure 2.

	percent of limit achieved			
	photocurrent	radiatively limited Voc	practically limited Voc	fill factor
Top InGaP subcell	87	91	94	95
Middle GaAs subcell	92	91	97	95
Bottom Ge subcell	58	51	70	88

The practical Voc limit is an empirical number determined by assigning favorable yet practical values to the recombination and transport parameters used in analytical expressions for the reverse saturation current. This Voc limit can be considered a soft limit, while the radiatively limited Voc can be considered a hard limit. Achieving Voc values slightly greater than the practical limit is difficult but is not considered unrealizable. The GaAs subcell Voc is very close to the practical limit, suggesting that further device improvements should be directed elsewhere. A modest gain in the top subcell Voc appears possible, while the model indicates large gains in the germanium bottom subcell Voc are possible. Development efforts within the InGaP/GaAs/Ge bandgap system have been concentrated in these areas.

A parallel approach for improving the efficiency of the present InGaP/GaAs/Ge triple junction solar cell is to move away from the InGaP/GaAs/Ge bandgap system. Figure 3 shows a theoretical iso-efficiency contour for a triple junction solar cell as a function of the top and middle subcell bandgaps and assuming a germanium bottom subcell. Similar modeling has been presented by Takamoto et al. [3] and Kurtz et al. [4]. This theoretical iso-efficiency contour does not consider lattice matching constraints. A consideration of lattice matching constraints suggests that not all bandgap combinations are realistically possible. However, superimposed on the plot are lines corresponding to certain top and middle cell material compositions which are lattice matched to each other. These lines were generated using $\text{In}(x)\text{Ga}(1-x)\text{As}$ or $\text{GaAs}(1-x)\text{Sb}(x)$ for the middle cell with $0 < x < 0.08$, and $\text{In}(1-x-y)\text{Ga}(x)\text{Al}(y)\text{P}$ for the top cell with $0 < y < 0.08$. Bandgap data and bowing coefficients are from Adachi [5] and Madelung [6]. Vegard's law was assumed in cases where coefficients were not available.

Walking left along a solid line changes the middle cell composition from GaAs to $\text{In}(x)\text{Ga}(1-x)\text{As}$. Walking left along a broken line changes the middle cell composition from GaAs to $\text{GaAs}(1-x)\text{Sb}(x)$. Each of the five sets of lines corresponds to a different top cell $\text{In}(1-x-y)\text{Ga}(x)\text{Al}(y)\text{P}$ composition in $y=0.02$ steps. Using this plot, a triple junction device can be designed with top and middle cells lattice matched to each other (although not necessarily lattice matched to the substrate) and the expected efficiency gain resulting from that new bandgap system can be determined.

It is clear from Figure 3 that changing either the top cell composition from ternary InGaP to a quaternary, or changing the middle cell from GaAs to a ternary compound, results in only modest gains in efficiency. Changing either the top or middle cell bandgaps results in movement that is significantly parallel to the iso-efficiency contours. The most effective way to increase the efficiency is to move perpendicular to the iso-efficiency contours by both lowering the middle cell bandgap and raising the top cell bandgap. This results in significant efficiency gains with only a modest change in both the top and middle cell bandgaps. This approach therefore also minimizes the lattice mismatch of the epitaxial layers with respect to the substrate. This approach is currently being pursued at Emcore.

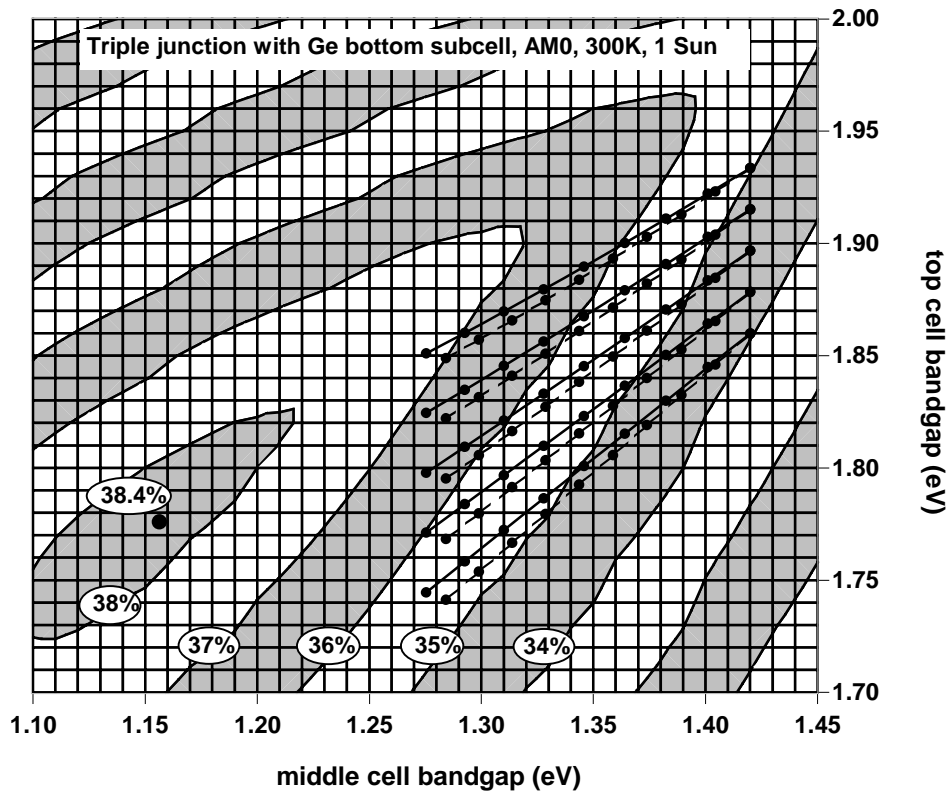


Figure 3 Iso-efficiency contour for a triple junction solar cell as a function of the top and middle subcell bandgaps and assuming a germanium bottom subcell. Superimposed on the plot are efficiency contours for lattice matched top and middle cells using an $\text{In}(x)\text{Ga}(1-x)\text{As}$ (solid line) or $\text{GaAs}(1-x)\text{Sb}(x)$ (broken line) middle cell with an $\text{In}(1-x-y)\text{Ga}(x)\text{Al}(y)\text{P}$ top cell.

DEVICE RESULTS

The modeling presented here suggests that a significant performance increase is available from the germanium subcell. Extensive development work has therefore been devoted to understanding the factors limiting the performance of this subcell. Modeling suggests that both the open circuit voltage and short circuit current of the germanium subcell is emitter limited. Current production cells yield integrated currents of approximately 24 mA/cm^2 as shown in Figure 4, which is well below the theoretical limit. This suggests that the V_{oc} of this subcell may be increased significantly with an improved germanium emitter formation process. An altered MOCVD growth recipe has resulted in a 40% increase in the integrated current for the germanium subcell as shown in Figure 4. The quantum efficiency of the improved germanium junction is limited only by reflection loss. More importantly, the modified growth recipe has improved the germanium junction V_{oc} by as much as 36%. This increase in integrated current and open circuit voltage can be attributed to better control of recombination in the emitter.

Figure 5 shows the increased single junction germanium illuminated current-voltage characteristics resulting from the improved growth recipe. The flat response in the IV curve corresponding to the new growth recipe is an artifact of the measurement. Software used to control the measurement process is presently configured to limit the current at 800 mA. The benefits in multi-junction device performance resulting from the enhanced germanium subcell performance are evident from Figure 5. The increased V_{oc} and increased J_{sc} of the improved germanium junction result in both an improved V_{oc} and FF in the triple junction device.

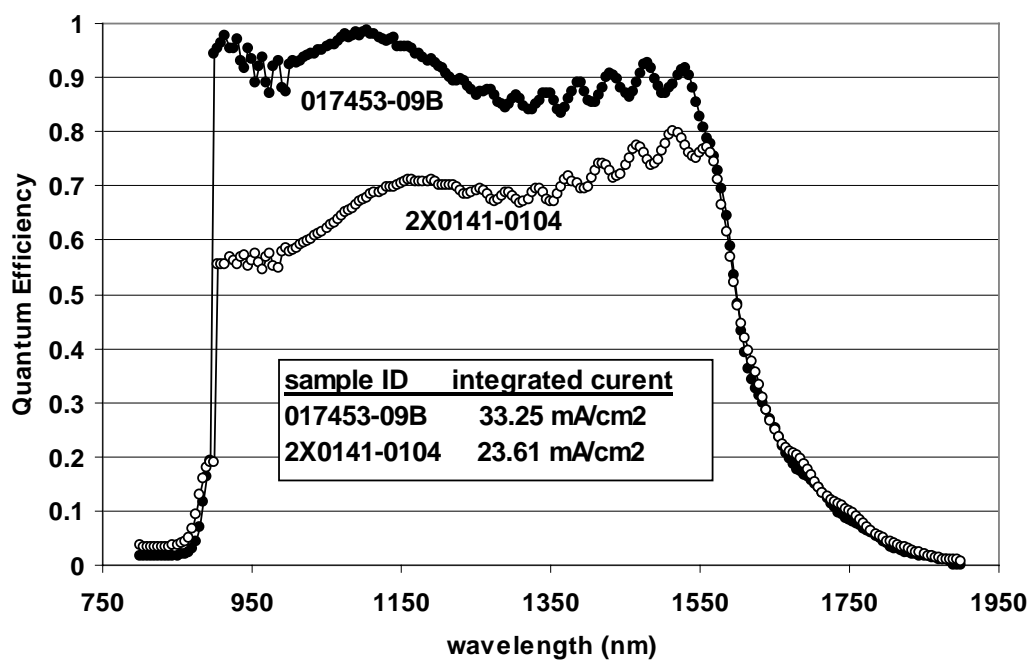


Figure 4 Germanium subcell quantum efficiency using the current production process as compared to an improved germanium emitter formation process.

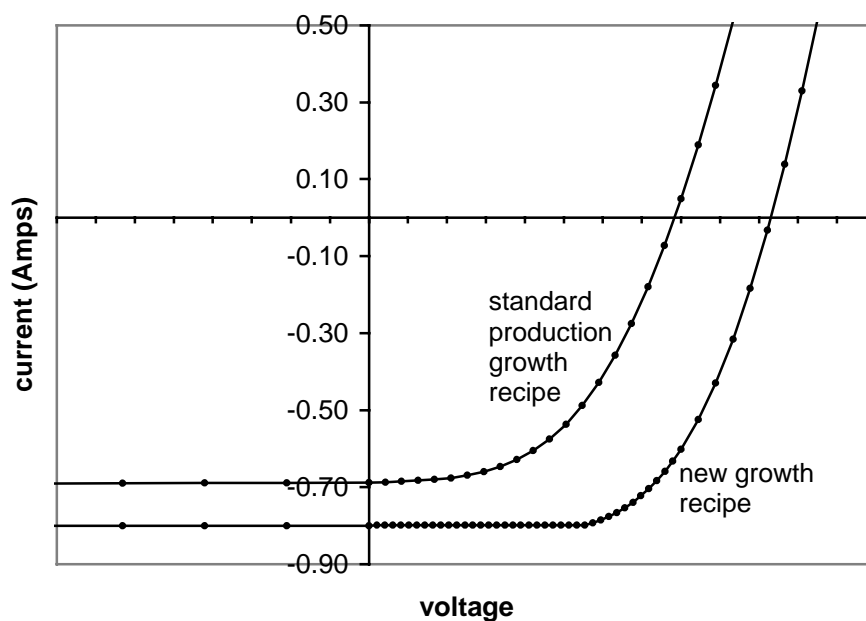


Figure 5 Full size, single junction germanium I-V curves showing the improvement in device performance resulting from changes in the MOCVD growth recipe.

Modeling presented in Figure 3 suggests that decreasing the middle cell bandgap and increasing the top cell bandgap result in a higher limiting efficiency. Efforts to date in this regard have involved shifting the middle cell bandgap to the red by adding ~2% indium to the GaAs subcell. This increases the limiting efficiency of the device and also results in closer lattice match of the germanium substrate and middle cell epitaxial layers. Figure 6 shows the internal quantum efficiency of the top and middle cells for triple junctions with and without 2% indium added to the middle cell. The quantum efficiency response edge for the middle cell suggests an approximately 10 nm red shift in the bandgap. The composition of the top cell has remained constant. The QE response of Figure 6 suggests no degradation in the top cell collection efficiency. Table 2 compares lot average electrical data for triple junctions with GaAs and $x=0.02$ In(x)Ga(1-x)As middle cells. The Voc of the InGaAs containing device has dropped by an average of 12 mV. This is consistent with the apparent 10 mV shift in the middle cell bandgap. The short circuit current of the InGaAs containing device is slightly higher due to normal variation in the anti-reflection coating performance from lot to lot. These two lots had identical top cell active region thicknesses. In this case the extra photocurrent contributed by adding indium to the middle cell results in an increased current mismatch between the top and middle subcells. Thickening the top subcell active region to account for this effect and maintain the same current mismatch factor is expected to boost the efficiency of In(0.02)Ga(0.98)As-based triple junction devices by 0.1% absolute over current GaAs-based production solar cells.

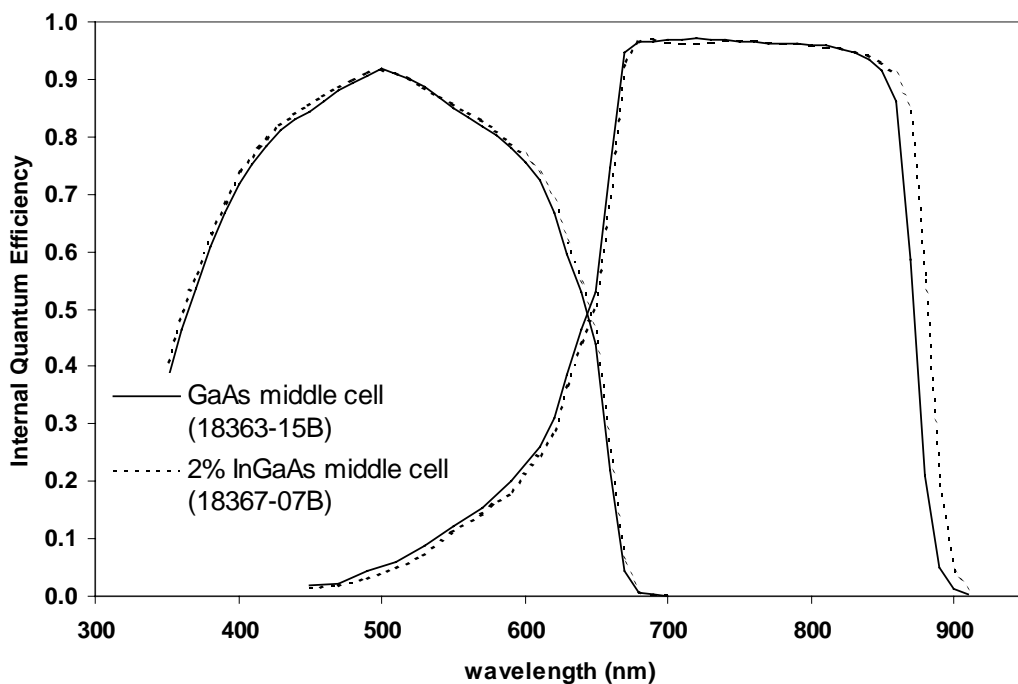


Figure 6 Internal quantum efficiency of the top and middle subcells in a triple junction using both GaAs and $x=0.02$ In(x)Ga(1-x)As middle cells.

Table 2 Lot average data comparing development triple junctions using either GaAs or 2% InGaAs middle cells.

Lot ID	Middle cell composition	Voc (mV)	Jsc (mA/cm ²)	FF (%)	Efficiency (%)
18363	GaAs	2633	16.6	85.8	27.45
18367	InGaAs, 2% In	2621	16.8	85.5	27.50

Incorporation of several triple junction technology improvements including those discussed here have resulted in a lot efficiency improvement of 2% absolute over the long term average of production solar cells. Shown in Figure 7 is the illuminated current-voltage characteristic of a full sized triple junction with an efficiency of 27.9%. The median lot efficiency was 27.6%. These development solar cells are designed for optimum end-of-life performance assuming a 1MeV electron fluence of $1 \times 10^{15} / \text{cm}^2$.

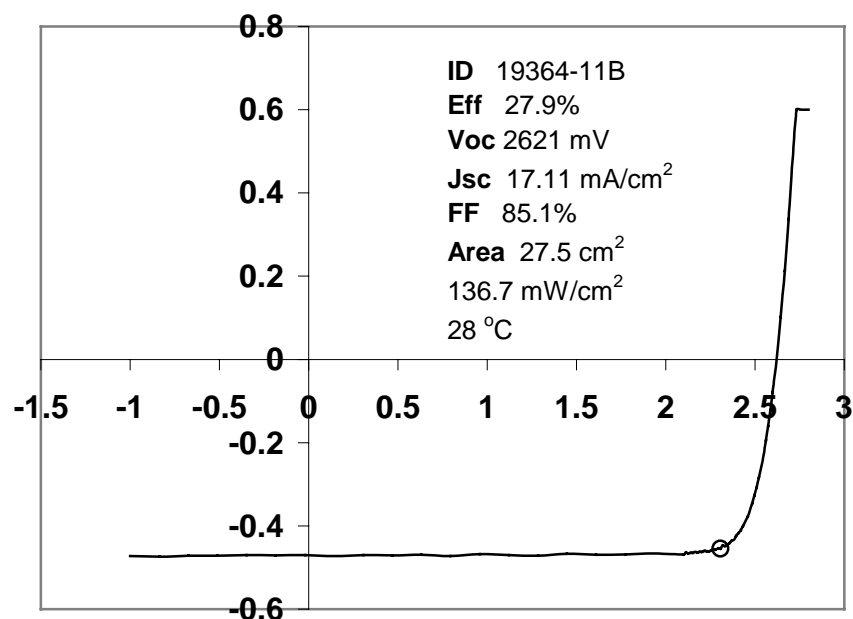


Figure 7 Current-voltage curve for full sized (27.5 cm^2) triple junction solar cell designed for maximum end-of-life performance.

CONCLUSIONS

Emcore Photovoltaics is presently shipping 27.5 cm^2 triple junction InGaP/GaAs/Ge solar cells with an average 1 sun AM0 beginning-of-life (BOL) efficiency of 25.6% (solar constant = 136.7 mW/cm^2). These cells have very high power remaining factors of 0.90 and 0.87 at 1MeV electron fluences of 5×10^{14} and $1 \times 10^{15} / \text{cm}^2$, respectively. Further development has focused on increasing the efficiency of production devices while maintaining the exceptional radiation hardness. Improvements have involved both increasing the efficiency of the present InGaP/GaAs/Ge triple junction as well as incorporating indium into the middle cell for improved match to the AM0 spectrum. Results include a 2% absolute improvement in triple junction efficiency over present production devices. A beginning-of-life efficiency of 27.9% has been measured on a full sized cell designed for maximum end-of-life, with a median lot efficiency of 27.6%.

REFERENCES

- [1] C. H. Henry, J. Applied Physics, **51**, (1980), p. 4494.
- [2] M.A. Green, Solar Cells, Prentice Hall, Englewood Cliffs, N.J., p. 88
- [3] T. Takamoto, E. Ikeda, H. Kurita, M. Yamaguchi, 14th European Photovoltaic Energy Conference, (1997), p. 970.
- [4] S.R. Kurtz, P. Faine, J.M. Olson, J. Applied Physics, **68**, (1990), p. 1890.
- [5] S. Adachi, Physical Properties of III-V Semiconductor Compounds, Wiley, N.Y., (1992).
- [6] O. Madelung, Semiconductors – Basic Data, Springer-Verlag, Berlin, (1996).

PROGRESS IN THE DEVELOPMENT OF METAMORPHIC MULTI-JUNCTION III-V SPACE-SOLAR CELLS AT ESSENTIAL RESEARCH INCORPORATED¹

Samar Sinharoy, Martin O. Patton, Thomas M. Valko, Sr., and Victor G. Weizer

Essential Research Incorporated, Cleveland, OH 44142

Abstract

Theoretical calculations have shown that highest efficiency III-V multi-junction solar cells require alloy structures that cannot be grown on a lattice-matched substrate. Ever since the first demonstration [1] of high efficiency metamorphic single junction 1.1 eV and 1.2 eV InGaAs solar cells by Essential Research Incorporated (ERI), interest has grown in the development of multi-junction cells of this type using graded buffer layer technology. ERI is currently developing a dual-junction 1.6 eV InGaP/1.1 eV InGaAs tandem cell (projected practical air-mass zero (AM0), one-sun efficiency of 28%, and 100-sun efficiency of 37.5%) under a Ballistic Missile Defense Command (BMDO) SBIR Phase II program. A second ongoing research effort at ERI involves the development of a 2.1 eV AlGaInP/1.6 eV InGaAsP/1.2 eV InGaAs triple-junction concentrator tandem cell (projected practical AM0 efficiency of 36.5% under 100 suns) under a SBIR Phase II program funded by the Air Force. We are in the process of optimizing the dual-junction cell performance. In case of the triple-junction cell, we have developed the bottom and the middle cell, and are in the process of developing the layer structures needed for the top cell. A progress report is presented in this paper.

Introduction

Multi-junction tandem space solar cells currently in production consist of an InGaP top cell and a GaAs bottom cell for the dual-junction cell, and an InGaP top cell, GaAs middle cell, and Ge bottom cell in case of the triple-junction cell. The top two cells are lattice-matched, whereas GaAs and Ge are nearly lattice-matched to each other. Typical AM0, one-sun efficiencies of these production cells are 23% for the dual-junction cell, and 25 – 26% for the triple-junction cell. Further optimization of these lattice-matched cells is not expected to yield significant improvement in the efficiency values. Theoretical calculations [2] for the dual-junction configuration have shown that significant enhancement in the upper limit efficiency can be achieved only if the constraint of lattice-matched growth is relaxed. The approach taken by ERI towards the realization of very high efficiency space solar cells is to develop a proprietary, step-graded buffer layer scheme that allows the growth of very low defect density, lattice-mismatched InGaAs on GaAs and InP substrates. The validity of this approach was demonstrated for the first time when ERI researchers announced [1] the fabrication of high efficiency, metamorphic, single-junction 1.1 eV and 1.2 eV InGaAs solar cells on GaAs substrates using their buffer layer scheme. Following that first success, ERI [3 – 5] and other laboratories [6, 7] have demonstrated other metamorphic single-junction cells, as well as multi-junction tandem cells using variations of this buffer layer scheme.

ERI is currently developing a dual-junction 1.62 eV InGaP/1.1 eV InGaAs concentrator tandem cell (projected practical AM0, 100-sun efficiency of 37.5%) under a Ballistic Missile Defense Command (BMDO) SBIR Phase II program. A second ongoing research effort at ERI involves the development of a 2.1 eV AlGaInP/1.6 eV InGaAsP/1.2 eV InGaAs triple-junction concentrator tandem cell (projected practical AM0 efficiency of 36.5%

¹ Work supported by BMDO SBIR Phase II contract NAS3-99174, and Air Force SBIR Phase II contract F29601-99-C-0135 sponsored by the AFRL Space Vehicles Directorate (AFRL/VS). The POC for the AFRL/VS effort is Dr. Donna Senft and can be contacted at (505)846-9340.

under 100 suns) under a SBIR Phase II program funded by the Air Force. In both cases, the tandem cells are lattice-matched to each other, as shown in Figure 1. The bottom InGaAs cell structure is lattice-mismatched to the GaAs substrate, and is grown using a proprietary, graded buffer layer that confines most of the misfit and threading dislocations to the substrate-buffer interface [3], resulting in very low defect density active cell regions. Results of modeling calculations of theoretical and practical AM0, one-sun efficiencies of the two tandem cells under development are shown in Table 1. Modeled experimental efficiencies of these cells are significantly higher than currently available commercial dual- and triple-junction cells. Progress in the development of the two tandem cells is described in the following sections.

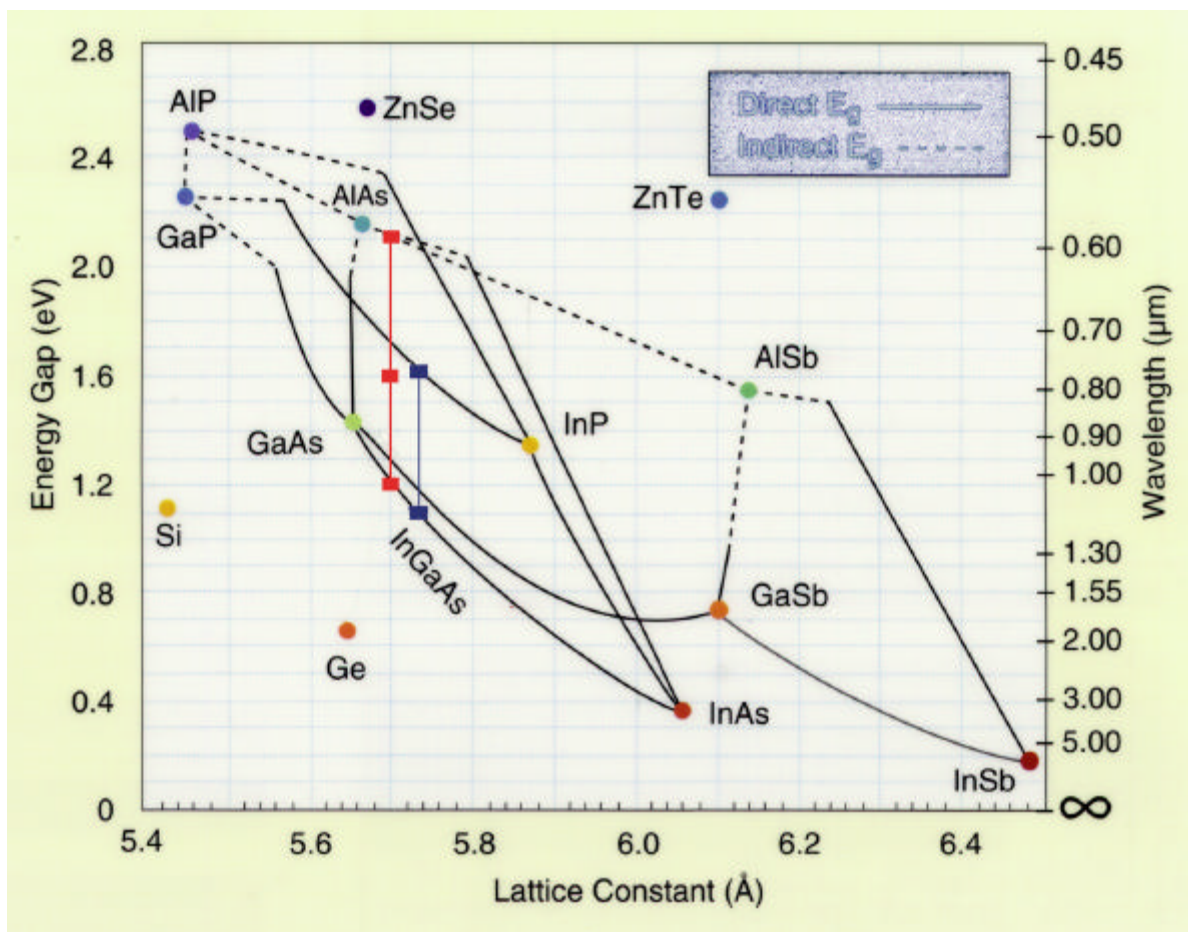


Figure 1.— Common semiconductor bandgap vs. lattice constant chart showing the designs of the metamorphic dual-junction InGaP/InGaAs and triple-junction AlGaInP/InGaAsP/InGaAs cells under development at ERI. The component cells are connected by a vertical line in each case in the Figure.

Table I—Modeled efficiencies of the proposed dual- and triple-junction cells.

Cell Structure	Cell Bandgap (eV)			Expected AM0, One-Sun Efficiency (%)	
	Top	Middle	Bottom	Theoretical	Practical
InGaP/InGaAs	1.62	None	1.1	32.5	28
InGaAlP/InGaAsP/InGaAs	2.1	1.6	1.2	37.9	31.5

Device Fabrication

All epitaxial layer structures for the cells were grown at NASA Glenn Research Center (GRC) using low pressure metal organic vapor phase epitaxy (LP-MOVPE) in a horizontal reactor, as described in previous publications.[3,5] The layer structures were characterized at GRC using X-ray, Hall effect measurement, and electrochemical capacitance-voltage (ECV) profiling. Transmission electron microscopy (TEM) and secondary ion mass spectroscopy (SIMS) analysis were performed by external commercial laboratories. The cells were processed at ERI facilities using standard photolithographic techniques. AM0 conversion efficiencies were measured at 25 °C using a single source, Spectrolab X25 solar simulator at GRC. Spectral response measurements were performed at GRC to determine the external quantum efficiency (EQE) of the cells. Figure 2 shows the current design of our dual-junction and triple-junction cells. In the case of the triple-junction cell, we have started by fabricating and evaluating stand-alone InGaAs and InGaAsP cells prior to combining them in a tandem cell using an appropriate tunnel junction. The results shown here will be for these two stand-alone cells. We are currently evaluating the AlGaInP top cell layer structure, and no cells have been fabricated with that material yet.

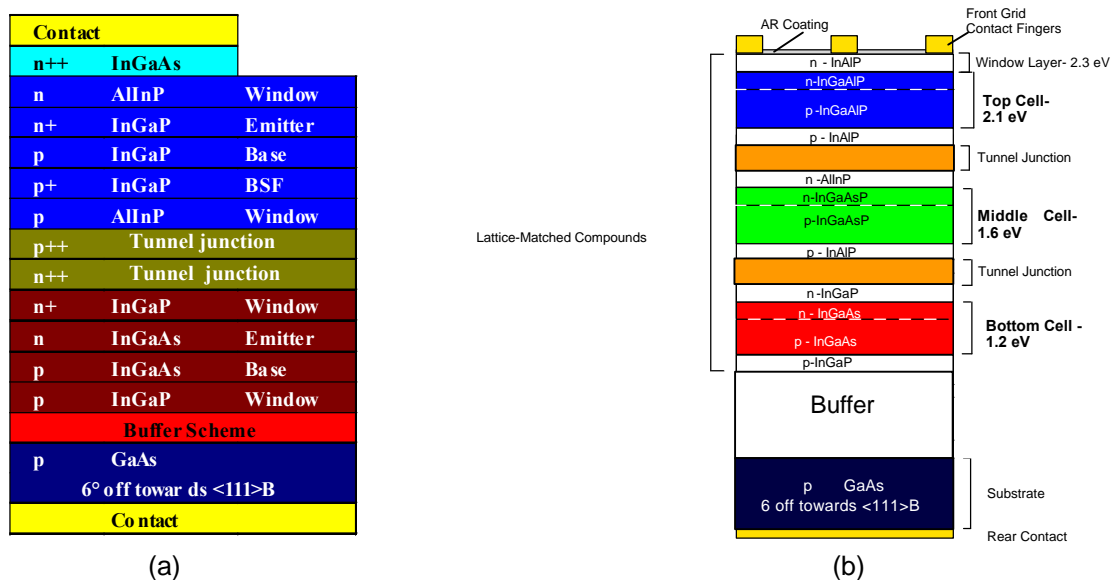


Figure 2.—Dual-junction (a) and triple-junction (b) cell structures.

Results and Discussion

It should be noted prior to discussion of the results that none of the cells discussed in this paper has been coated with anti-reflection (AR) coating. Shown in Figure 3 is the light current-voltage characteristic of a 1.62 eV/1.1 eV n/p dual-junction cell. The cell is characterized by open circuit voltage (V_{oc}) = 1864 mV, short circuit current (J_{sc}) = 15.605 mA, fill factor (FF) of 83.4%, and an AM0, one-sun efficiency of 17.76%. With an appropriate AR coating, this efficiency should increase to 24.8%. This is a significant improvement over our previously reported [5] result of 19%, and can be attributed to switching the tunnel junction material from 1.1 eV InGaAs to a wider bandgap material, as well as thinning of the top cell. The external quantum efficiency (EQE) of the subcells of the dual-junction cell was measured using appropriate filters, and the results are shown in Figure 4. Analysis of the I-V and EQE data and comparison with computer modeled data shows that the performance of the dual-junction cell is being controlled by the bottom cell, in spite of the top cell thinning so far to achieve current matching conditions. Further optimization experiments are currently underway, and we expect to achieve the predicted practical efficiency of 28% in the near future.

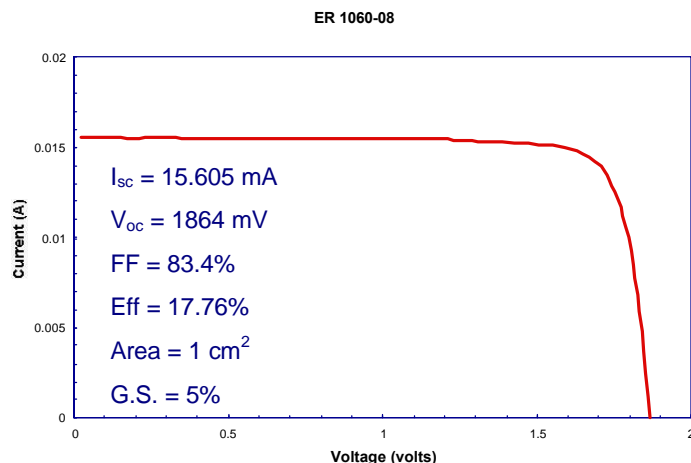


Figure 3.—I-V characteristic of dual-junction cell. Expected AM0, one-sun efficiency with appropriate AR coating = 24.8%

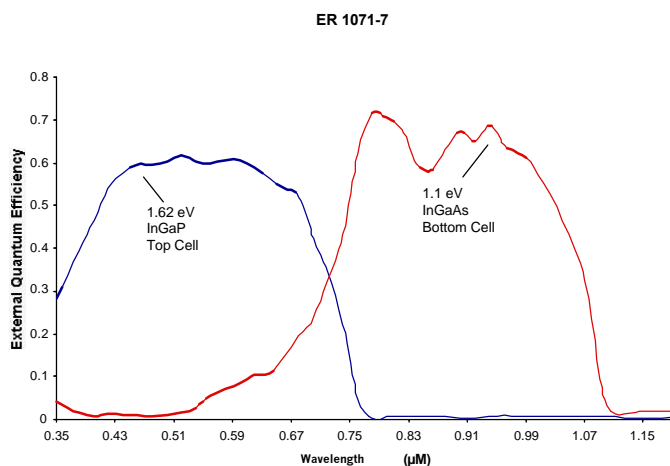


Figure 4.—External quantum efficiency of dual-junction cell.

In case of the triple-junction cell shown in Figure 2(b), we have started by fabricating and testing the component individual cells first, prior to putting them in tandem configuration. The 1.2 eV InGaAs bottom cell, and the 1.6 eV InGaAsP middle cell structures were grown on GaAs substrates using an appropriate buffer layer structure. In case of the 1.6 eV cell, the structure was similar to that shown in fig. 2(b), except that we used 1.7 eV InGaP instead of wider bandgap AlInP as the window layers for initial testing purposes. Both cells were capped with a thin InGaAs layer.

Current-voltage and external quantum efficiency characteristics of the 1.2 eV InGaAs cell are shown in Figure 5. The measured efficiency under AM0, one-sun condition was 11.73% without AR coating. With an appropriate AR coating, this efficiency should increase to 16.4%. The high efficiency value compares well with similar cells fabricated by ERI in the past. However, as can be seen from the EQE data of Figure 5, it should be possible to improve the efficiency even further by increasing the absorption in the blue region through improvements in the window material.

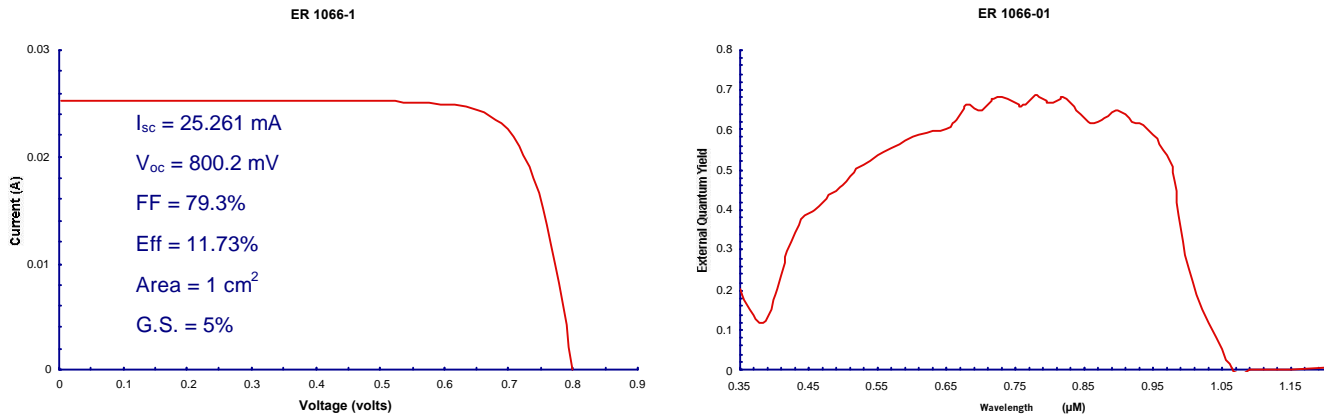


Figure 5.—I-V and EQE characteristics of 1.2 eV InGaAs cell. AM0, one-sun efficiency of this cell with appropriate AR coating is expected to be 16.4%.

Current-voltage and external quantum efficiency characteristics of the 1.6 eV InGaAsP cell are shown in Figure 6. The measured efficiency under AM0, one-sun condition was 8.99% without AR coating. With an appropriate AR coating, the efficiency should increase to 12.4%. Since this is the very first metamorphic 1.6 eV InGaAsP cell, there is no prior cell to compare it with. However, the drop off in the blue response in the EQE data indicates that significant loss in blue light conversion occurred due to absorption in the InGaP window. Replacing the InGaP window with 2.3 eV AlInP window should correct this problem and increase efficiency further.

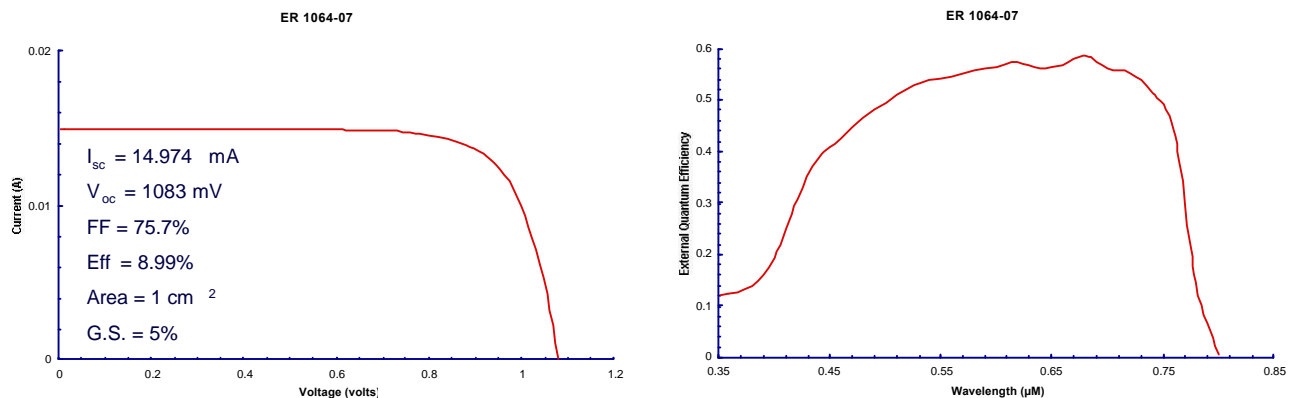


Figure 6.—I-V and EQE characteristics of 1.6 eV InGaAsP cell. AM0, one-sun efficiency of this cell is expected to increase to 12.4% with an appropriate AR coating.

The next step in the development of the triple-junction cell is the fabrication and testing of a 2.1 eV AlGaInP top cell, as well as combining the 1.2 eV InGaAs bottom cell and the 1.6 eV InGaAsP middle cell into a dual-junction tandem cell for evaluation. We have grown epitaxial AlGaInP layers on GaAs using our graded buffer layer. Triple-axis X-ray reciprocal lattice map analysis coupled with photoluminescence measurements indicate that the material is of high crystalline quality, and has the expected lattice constant and bandgap. We are in the process of performing p- and n-doping calibration experiments of this material prior to growing a cell structure. The tunnel junction between the bottom and the middle cell will be similar to that used in the dual-junction cell. The tunnel junction between the middle and the top cell will have to be a wider bandgap material. One of the candidate materials is AlGaInP. We plan to evaluate degenerate n- and p-doping characteristics of this material in the near future prior to fabricating a triple-junction cell.

Summary

In summary, we have demonstrated ~25% AM0, one-sun efficiency in a 1.6 eV/1.1 eV InGaP/InGaAs metamorphic dual-junction tandem cell on a GaAs substrate using a proprietary step-graded buffer layer. External quantum efficiency measurements showed that the dual-junction cell performance was bottom cell current limited. We expect to achieve the predicted practical efficiency of 28% in the very near future through further optimization of the cell structure. Our approach to the development of a triple-junction metamorphic 2.1 eV AlGaInP/1.6 eV InGaAsP/1.2 eV InGaAs cell on GaAs has been to fabricate and evaluate the individual cells on GaAs first, prior to combining them in the tandem configuration. So far, we have demonstrated the InGaAs bottom cell and InGaAsP middle cell with AM0, one-sun efficiencies of 16.4% and 12.4% respectively. The efficiency of the InGaAsP cell is expected to improve substantially once the window material is changed from 1.7 eV InGaP to 2.3 eV InAlP in this cell. Development of the AlInGaP top cell and the tunnel junction structures are in progress.

References

- [1] Richard W. Hoffman, Jr., Navid S. Fatemi, Mark A. Stan, Philip Jenkins, Victor G. Weizer, David A. Scheiman, and David J. Brinker, "High Efficiency InGaAs-on-GaAs Devices for Monolithic Multi-junction Solar Cell Applications", Proc. 2nd World Conf. Photovoltaic Solar Energy Conversion, pp3604-3608, Vienna, Austria, 6 – 10 July, 1998.
- [2] J. C. C. Fan, B-Y. Tsaur, and B. J. Palm, "Optimal Design of High Efficiency Tandem Cells", Proc. 16th IEEE Photovoltaic Specialists Conf., p692 (1982).
- [3] R. W. Hoffman, Jr., N. S. Fatemi, M. A. Stan, P. Jenkins, V. G. Weizer, D. A. Scheiman, and D. J. Brinker, "High Efficiency Monolithic Multi-junction Solar Cells using Lattice-Mismatched Growth", Materials Research Society Symp. Proc. 551, 51 (1999).
- [4] Mark A. Stan, Victor G. Weizer, AnnaMaria Pal, Linda M. Garverick, Osman Khan, Samar Sinharoy, Richard W. Hoffman, Philip P. Jenkins, David A. Scheiman, and Navid S. Fatemi, "High Efficiency Multi-junction Space Solar Development Utilizing Lattice Grading", 16th Space Photovoltaic Research and Technology Conf. (SPRAT), pp122 – 128, Cleveland, OH, Aug. 31 to Sept. 2, 1999.
- [5] Samar Sinharoy, Mark A. Smith, Victor G. Weizer, AnnaMaria Pal, Osman Khan, David A. Scheiman, and Philip P. Jenkins, "1.62 eV/1.1 eV InGaP/InGaAs Dual-junction Solar Cell Development on Lattice-mismatched GaAs", Proc. 28th IEEE Photovoltaic Specialists Conf. (PVSC), pp1285 – 1288, Anchorage, AK, 15 – 22 Sept. 2000.
- [6] Frank Dimroth, Peter Lanyi, Mathias Meusel, Ute Schubert, and Andreas W. Bett, "New Lattice-mismatched GaInP/GaInAs Tandem Solar Cell Concepts for High Efficiency Space and Terrestrial Concentrator Solar Cells", Proc. 16th European Photovoltaic Solar energy Conf. Glasgow, UK 1 – 5 May, 2000.
- [7] R. R. King, M. Haddad, T. Isshiki, P. Colter, J. Ermer, H. Yoon, D. E. Joslin, and N. H. karam, "Metamorphic GaInP/GaInAs/Ge Solar Cells", Proc. 28th IEEE PVSC, pp982 – 985, Anchorage, AK, 15 – 22 Sept. 2000.

THE STRETCHED LENS ARRAY (SLA): AN ULTRA-LIGHT PHOTOVOLTAIC CONCENTRATOR ¹

Mark J. O'Neill
ENTECH, Inc.
Keller, Texas 76248 USA

Michael F. Piszczor
NASA Glenn
Cleveland, Ohio 44135 USA

Michael I. Eskenazi
AEC-ABLE
Goleta, CA 93117 USA

A. J. McDanal
ENTECH, Inc.
Keller, Texas 76248 USA

Patrick J. George
NASA Glenn
Cleveland, Ohio 44135 USA

Matthew M. Botke
AEC-ABLE
Goleta, CA 93117 USA

Henry W. Brandhorst
Space Power Institute
Auburn Univ., AL 36849 USA

David L. Edwards
NASA Marshall
Huntsville, Alabama 35812 USA

Paul A. Jaster
3M
St. Paul, MN 55144 USA

ABSTRACT

A high-performance, ultralight, photovoltaic concentrator array is being developed for space power. The stretched lens array (SLA) uses stretched-membrane, silicone Fresnel lenses to concentrate sunlight onto triple-junction photovoltaic cells. The cells are mounted to a composite radiator structure. The entire solar array wing, including lenses, photovoltaic cell flex circuits, composite panels, hinges, yoke, wiring harness, and deployment mechanisms, has a mass density of 1.6 kg/sq.m. NASA Glenn has measured 27.4% net SLA panel (Fig. 1) efficiency, or 375 W/sq.m. power density, at room temperature. At GEO operating cell temperature (80C), this power density will be 300 W/sq.m., resulting in more than 180 W/kg specific power at the full wing level. SLA is a direct ultralight descendent of the successful SCARLET array on NASA's Deep Space 1 spacecraft. This paper describes the evolution from SCARLET to SLA, summarizes the SLA's key features, and provides performance and mass data for this new concentrator array.

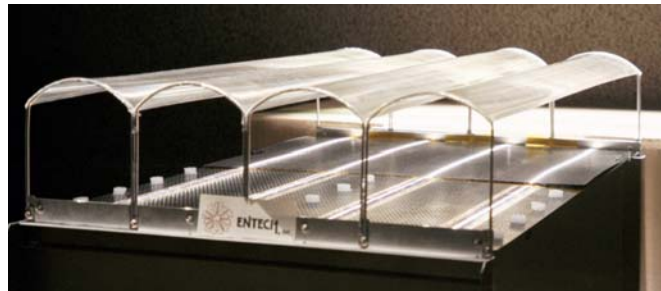


Fig. 1 – Stretched Lens Array (SLA) Prototype Panel

INTRODUCTION AND BACKGROUND

Since 1986, ENTECH and NASA have been developing and refining space photovoltaic arrays using refractive concentrator technology [1]. Unlike reflective concentrators, these refractive Fresnel lens concentrators can be configured to minimize the effects of shape errors, enabling straightforward manufacture, assembly, and operation on orbit. By using a unique arch shape, these Fresnel lenses provide more than 100X larger slope error tolerance than either reflective concentrators or conventional flat Fresnel lens concentrators [2].

1. This work has been conducted under several NASA-sponsored programs, including the Space Solar Power program, the Advanced Cross-Enterprise Technology Development program, and the New Millennium Space Technology 6 program.

In the early 1990's, the first refractive concentrator array was developed and flown on the PASP+ mission, which included a number of small advanced arrays [3]. The refractive concentrator array used ENTECH mini-dome lenses over Boeing mechanically stacked multi-junction (MJ) cells (GaAs over GaSb). The mini-dome lenses were made by ENTECH from space-qualified silicone (DC 93-500), and coated by Boeing to provide protection against space ultraviolet (UV) radiation and atomic oxygen (AO). This array performed extremely well throughout the year-long mission in a high-radiation elliptical orbit, validating both the high performance and radiation hardness of the refractive concentrator approach [3]. In addition, in high-voltage space plasma interaction experiments, the refractive concentrator array was able to withstand cell voltage excursions to 500 V relative to the plasma with minimal environmental interaction [3].

In the middle 1990's, ENTECH, NASA, and 3M developed a new line-focus Fresnel lens concentrator, which is easier to make and more cost-effective than the mini-dome lens concentrator. Using a continuous roll-to-roll process, 3M can now rapidly mass-produce the line-focus silicone lens material in any desired quantity.

In 1994, AEC-ABLE joined the refractive concentrator team and led the development of the SCARLET® (Solar Concentrator Array using Refractive Linear Element Technology) solar array [4]. SCARLET uses a small (8.5 cm wide aperture) silicone Fresnel lens to focus sunlight at about 8X concentration onto radiatively cooled multi-junction cells. Launched in October 1998, a 2.5 kW SCARLET array powers both the spacecraft and the ion engine on the NASA/JPL Deep Space 1 spacecraft, shown in Fig. 2. SCARLET achieved over 200 W/sq.m. areal power and over 45 W/kg specific power. With SCARLET working flawlessly, Deep Space 1 is currently about 150 million miles from earth, on its way to a comet rendezvous on September 22, 2001 [5].

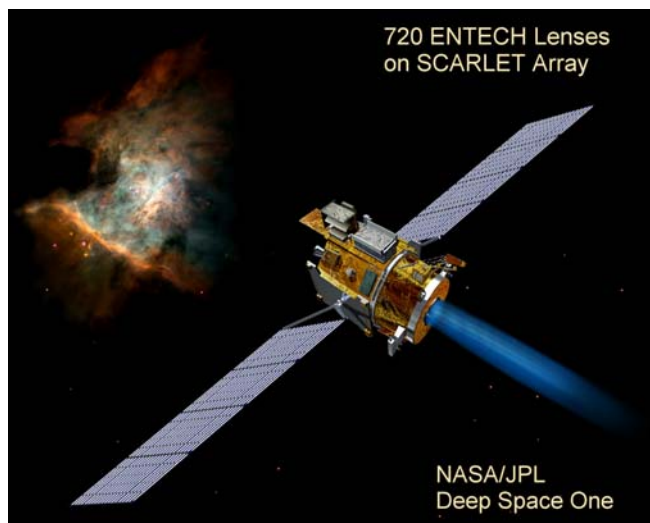


Fig. 2 - Deep Space 1 Probe Launched October 1998

Over the past three years, the team, now including Auburn's Space Power Institute, has developed a new space concentrator array technology, called the stretched lens array (SLA). SLA provides even higher performance than SCARLET at dramatically reduced mass and cost [6 and 7]. Both SCARLET and SLA use the same unique, patented, arched lens optical concentrator (Fig. 3), which provides outstanding optical performance and unparalleled tolerance of real world aberrations and errors [2]. The primary difference between the SCARLET lens and the SLA lens relates to their means of support: SCARLET used an arched glass superstrate to support the silicone lens, while SLA uses simple lengthwise tensioning of the silicone lens itself for support.

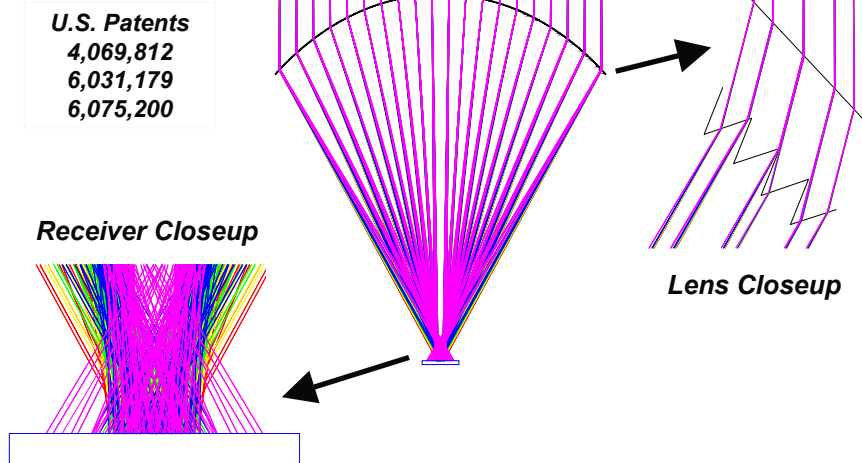


Fig. 3 - Unique Fresnel Lens Used in Both SCARLET and SLA Arrays

In 1999-2000, under NASA's Space Solar Power program, the SLA team designed, developed, fabricated, and tested a fully functional prototype SLA panel (Fig. 1). This panel achieved unprecedented performance, characterized by a net solar-to-electrical conversion efficiency of 27.4% under simulated space sunlight at room temperature [7]. Furthermore, the same SLA technology provided unprecedented performance under outdoor terrestrial sunlight, characterized by 25-29% net conversion efficiency at operating temperature [8].

In 2001-2002, under NASA's Advanced Cross-Enterprise Technology Development program, the SLA team is developing an optimized, near-term, robust, SLA solar array wing. This SLA wing builds upon the 15 year heritage of refractive concentrators for space power, including the successful flight heritage of the PASP+ and SCARLET arrays referenced above. The SLA team is also working on a NASA/JPL New Millennium Program Space Technology 6 study which could lead to a near-term flight test for SLA.

EVOLUTION FROM THE SCARLET ARRAY TO THE STRETCHED LENS ARRAY (SLA)

The patented SLA [6 and 9] is an ultralight descendent of SCARLET as shown by comparing Figs. 4 and 5, and as discussed in the following paragraphs. Both SCARLET and SLA use the same small, arch-shaped, line-focus Fresnel lenses (8.5 cm aperture width) to focus sunlight onto high-efficiency multi-junction solar cells (1.0 cm active width). This concentration ratio (8.5X) provides ± 2 degree sun-pointing tolerance about the critical axis, and can be adjusted for specific mission requirements. 3M makes the continuous web of thin lensfilm material (about 150 microns thick) from space-qualified DC93-500 silicone.

Fig. 4 shows a SCARLET panel during assembly at ABLE. To support and UV-protect the 200-micron-thick silicone lens material, each lens was laminated to a 75-micron-thick, thermally shaped, ceria-doped glass arch. The laminated lenses were then inserted into a protective frame, made from composite material. The lens-populated lens frame is the upper deck in Fig. 4. The photovoltaic receivers were attached to a high thermal conductivity composite honeycomb panel, which is the lower deck in Fig. 4. For launch, the lens frames were stowed against the honeycomb panels, which were folded together in the same fashion as for a planar solar array. Once on orbit, the SCARLET panels unfolded to form a wing, and the lens frames deployed to their proper position [5].

Fig. 5 shows a prototype SLA panel. The thin silicone lens material is now supported as a stretched membrane between end arches, so both the glass arches and the lens frame have been eliminated. The composite radiator is now a thin composite sheet, which is more than adequate for excellent thermal performance. Like the silicone lens, the radiator sheet is now supported as a stretched membrane between edge elements, so the honeycomb panel has been eliminated. Without any sacrifice in optical, thermal, or electrical functionality, the SLA panel in Fig. 5 is approximately four times lighter (per square meter of lens aperture) than the SCARLET panel in Fig. 4. Indeed, the SLA performance is



Fig. 4 - Deep Space 1 *SCARLET* Panel Assembly

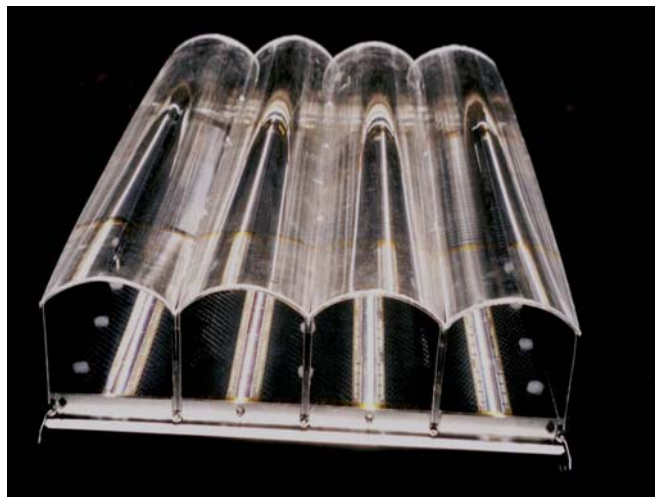


Fig. 5 – Stretched Lens Array (SLA) Prototype Panel

significantly higher than SCARLET because the optical losses caused by the glass arches and the lens frame have been eliminated. A UV-rejection coating is used on the outer surface of the lens.

Fig. 5 shows the SLA prototype panel under terrestrial sunlight illumination. Note the focal lines on each of the four photovoltaic receivers, which utilize conventional copper-clad polyimide flex circuit construction. Performance measurements for this SLA prototype panel are discussed below.

PROTOTYPE SLA PANEL PERFORMANCE TESTING

Under the NASA Space Solar Power program, the prototype SLA panel shown in Figs. 1 and 5 was designed, developed, fabricated, and tested by the refractive concentrator team. Both Spectrolab and TECSTAR developed monolithic triple junction (GaInP/GaAs/Ge) concentrator cells for the prototype panel. These cells were equipped with ENTECH prism covers to eliminate the normal gridline shadowing loss. Cells were assembled into photovoltaic receivers using polyimide flex circuits, which were attached to the graphite sheet radiator with space-qualified silicone pressure sensitive adhesive (PSA).

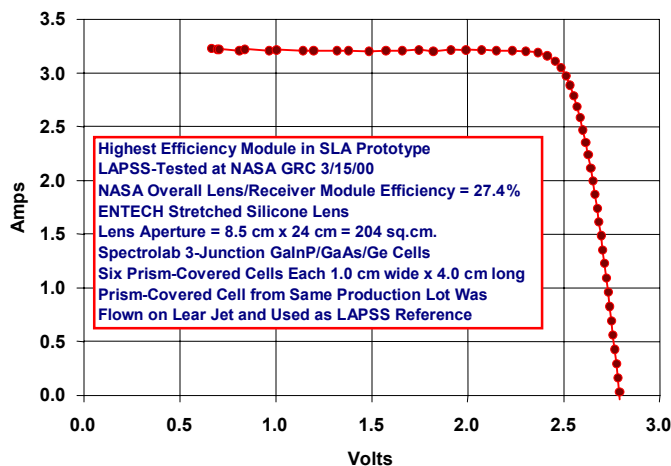


Fig. 6 – NASA-Measured 27.4% Module Efficiency (AM0)

The prototype SLA panel was first tested under terrestrial sunlight by ENTECH, then tested in a large area pulsed solar simulator (LAPSS) by ABLE, and finally LAPSS-tested by NASA Glenn. To ensure accuracy, NASA Glenn flew cells from the same production run on the NASA Lear Jet to determine their AM0 short-circuit currents, and then used one of these cells to set the intensity of the LAPSS lamp to maintain 1 AM0 sun irradiance at the lens aperture. Fig. 6 shows the measured IV curve for the best of the four lens/receiver modules in the prototype panel. These results were measured at room temperature (about 20C), and correspond to 27.4% net module efficiency and 375 W/sq.m. output power density, based on the module aperture area (8.5 cm lens aperture width x 24.0 cm photovoltaic receiver active length = 204 sq.cm.).

OTHER SLA TESTING

A number of other important tests have been performed for the key elements of the stretched lens array (SLA), as summarized in the following paragraphs.

Stretched Lens Optical Efficiency

Numerous stretched membrane lenses have been tested under outdoor terrestrial sunlight by ENTECH, to determine the net optical efficiency. Since the top cell (GaInP) limits the current of the triple-junction stack, the short-circuit current output of a reference GaInP cell is used to determine the lens efficiency. Under a variety of test conditions, the optical efficiency of the stretched silicone lens has typically been measured at 92-93%. Knowing this lens efficiency value, the corresponding cell efficiency for the prototype panel discussed in the previous paragraph is seen to be 30% (27.4% module/92% lens). This cell efficiency value is in very close agreement with Spectrolab's in-house cell efficiency measurement.

Stretched Lens Thermal Cycling

To verify the thermal durability of the new stretched membrane lens, multiple samples were exposed to GEO thermal cycling by ABLE, and all passed the equivalent of more than 20 years in GEO (over 1,830 thermal cycles from -180C to +90C).

Lens Material Space Ultraviolet Exposure Testing

Like the silicone mini-dome lenses on the PASP+ mission, the SLA lenses will be equipped with a thin-film ultraviolet rejection (UVR) coating to protect the silicone. To verify the durability of the coated lens material, NASA Marshall has completed 7,000 equivalent sun hours (ESH) of near ultraviolet (NUV) exposure testing on both coated and uncoated lens material samples made by ENTECH [10 and 11]. Figs. 7 and 8 show the NASA Marshall spectral transmittance measurements for coated and uncoated samples, respectively. Interestingly, the NUV-exposed uncoated lens material still has a 93% transmittance, for the current-limiting top cell (GaInP) response spectrum, after 7,000 ESH of NUV. The coated material has degraded to 89% transmittance for the top cell response spectrum after 7,000 ESH of NUV. NASA Marshall is currently running combined vacuum ultraviolet (VUV) and NUV testing of lens material samples. Initial results of these tests indicate that a UVR coating may be needed to block damaging wavelengths in the VUV range below 200 nm, instead of all wavelengths below 300 nm as previously anticipated.

Proton and Electron Testing of Stretched Lens Sample

A stretched lens sample (Fig. 9) was recently fabricated by ENTECH and exposed to proton and electron radiation by NASA Marshall. First, the lens optical efficiency was measured outdoors by ENTECH, using a single-junction GaInP



Fig. 9 – Stretched Lens Sample for Proton and Electron Exposure Testing

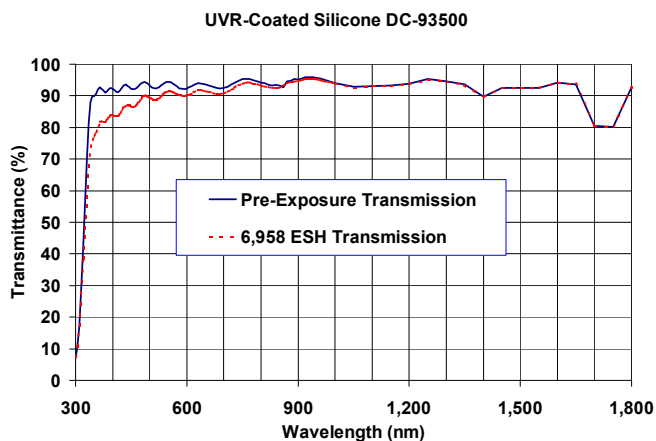


Fig. 7 – NASA Marshall NUV Exposure Test Results for UVR-Coated DC93-500 Lens Material Sample

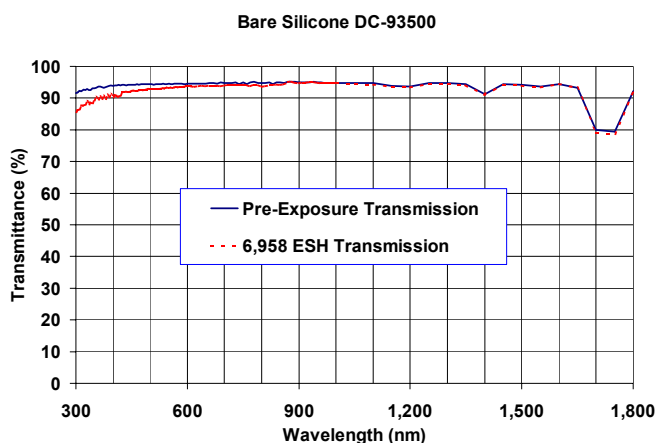


Fig. 8 – NASA Marshall NUV Exposure Test Results for Uncoated DC93-500 Lens Material Sample

reference cell at 9.3X geometric concentration. The cell was provided by the National Renewable Energy Laboratory (NREL). Next, NASA Marshall exposed the sample to protons equivalent to 15 years on GEO, based on a detailed dose-depth profile analysis resulting in this test exposure combination:

- ◆ 4.3×10^{12} protons/sq.cm. at 700 keV
- ◆ 9.0×10^{11} protons/sq.cm. at 525 keV
- ◆ 5.7×10^{13} protons/sq.cm. at 225 keV

Then the lens optical efficiency was re-measured outdoors by ENTECH with no measurable degradation. Next, NASA Marshall exposed the sample to electrons:

- ◆ 1×10^{15} electrons/sq.cm. at 1 MeV

The lens optical efficiency was once again re-measured outdoors by ENTECH with no measurable degradation (optical efficiency still 90-92%).

Micrometeoroid Impact Testing of Lenses and Photovoltaic Receivers at High Voltage in Plasma

Auburn University's Space Power Institute has conducted numerous simulated micrometeoroid impact tests (at 10-12 km/sec) of both lens and photovoltaic receiver samples in a plasma chamber. These tests included:

- ◆ Stretched Lenses Alone
- ◆ Receivers Alone
- ◆ Combined Lenses over Receivers
- ◆ Front and Back Impact
- ◆ Cells Biased at -400 V and -1,000 V Relative to Plasma During Tests

The lens impact tests showed clean penetrations with no peripheral damage such as tearing (Fig. 10).



Fig. 10 – Stretched Lens Sample Showing Micrometeoroid Puncture

ENTECH mounted the single-cell photovoltaic receivers to composite radiator sheet, and fully encapsulated the receivers to enable high-voltage operation. Two of the receivers were tested multiple times (Fig. 11). Auburn first tested these receiver samples in a simulated LEO plasma, with the cells biased to more than 400 volts (negative) relative to the plasma. Micrometeoroids were then shot at the samples, causing minor damage to the cover glass over each cell, but no electrical discharge or current leakage problems were observed. After this successful test, the receiver samples were re-tested, with the cells biased to more than 1,000 volts (negative) relative to the plasma. Micrometeoroids were then shot again at the samples, and the only discharge which occurred was a transient event due to a puncture of the polyimide tape over the lead wire located inside the white circle in Fig. 11. This event was self-healing, with no lasting leakage current to the plasma. Despite many impacts over the photovoltaic receivers, as evidenced by the many pockmarks in the photo in Fig. 11, the receivers had no discharge events during or after these tests.

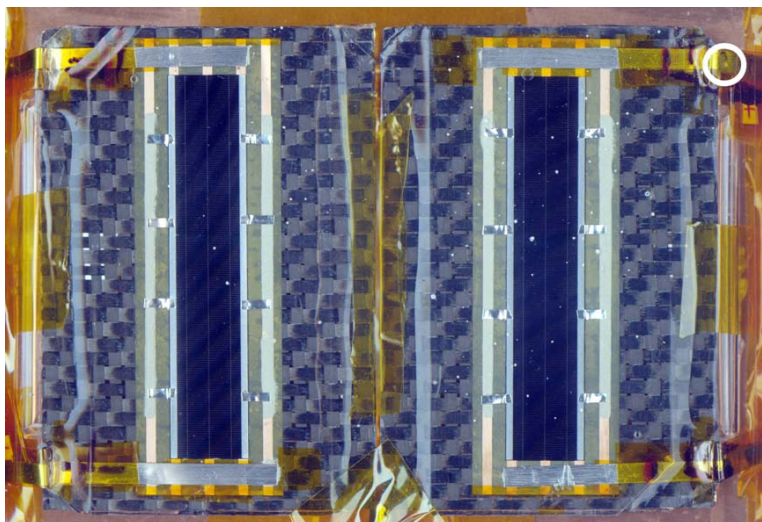


Fig. 11 – Photovoltaic Receiver Samples After Micrometeoroid Impact

A final set of tests was conducted with the lens stretched in front of the receivers to simulate the flight-like configuration. The receivers were once again held at 1,000 V (negative) relative to the plasma. Micrometeoroids were first shot at the front (lens side) of the units, and the lens proved to be an excellent natural micrometeoroid shield for the receivers, preventing any direct impact on the receivers. Micrometeoroids were then shot from the back (radiator side) of the units. No discharge problems of any kind occurred during or after these combined lens/receiver tests.

This high-voltage capability, with very little mass penalty, is one of the key advantages of the SLA approach over conventional planar arrays. The small cells can be super-insulated without adding much mass to the array, due to the small size of the solar cells. For high-power arrays (e.g., 20 kW and larger), this high-voltage capability provides significant savings in wiring mass and cost compared to conventional lower-voltage planar arrays. The added encapsulation can also be designed to provide excellent radiation tolerance for high-radiation missions.

SLA RIGID PANEL WING APPROACH

In 1999-2000, the SLA team thoroughly investigated a flexible blanket platform for the stretched lens array (SLA) [7]. While this blanket approach has an advantage in stowage volume over more conventional rigid panel platforms, it lacks the maturity and flight heritage of the rigid panel wing. This year, under the new NASA Advanced Cross-Enterprise Technology Development program, the SLA team is developing a new ultralight rigid panel wing as the platform of choice for SLA. Figs. 12-14 show the basic rigid panel SLA wing approach in schematic form. The flexible lenses fold down flat against the rigid panels for compact stowing during launch (Fig. 12). On orbit, as the panels unfold, spring driven end arches deploy and tension the individual stretched lenses across the panel's length (Fig. 13). The wing continues to deploy until the panels are all co-planar in their final locked wing position (Fig. 14).

This unfolding rigid panel solar array approach has been widely used for many years for NASA, DOD, and commercial spacecraft. One unique feature in the new SLA rigid panel array relates to the panels themselves, which use only a single face sheet and no honeycomb, except as a support frame around each panel. The use of very lightweight "picture-frame" panels is enabled by the very low mass of the supported cells and lenses, and by snubbing during launch to the inboard and outboard panels which are reinforced honeycomb panels. The thin composite face sheet forms the photovoltaic receiver mounting surface and the waste heat radiator, and is stretched in drum-like fashion over the peripheral honeycomb picture-frame structure. The individual pop-up lenses use the same basic deployment and support approach that has been used successfully on numerous SLA prototypes (Fig. 15).



Fig. 12 – Stowed Rigid Panel SLA Wing

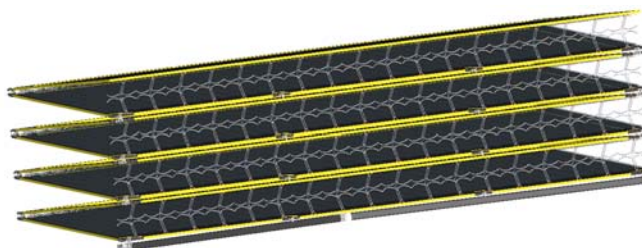


Fig. 13 – Lenses Deploying on Rigid Panel SLA Wing

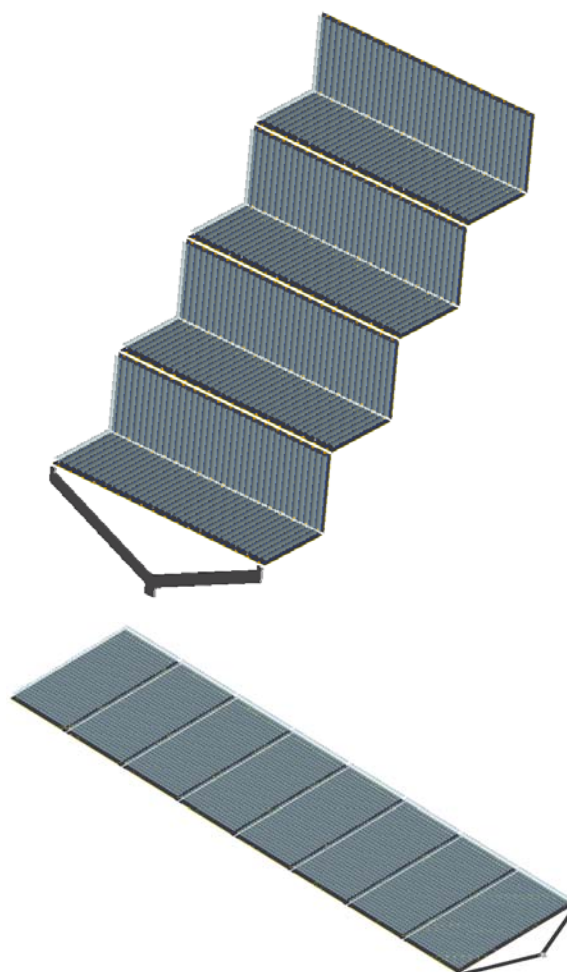


Fig. 14 – Panels Deploying on Rigid Panel SLA Wing

PROTOTYPE FOUR-PANEL SLA WING

Recently, the SLA team has fabricated a prototype four-panel SLA wing to demonstrate the mechanical functionality of the rigid-panel SLA wing approach (Fig. 16). Two of the four panels have been equipped with pop-up lenses, as shown in the photo of Fig. 16. Each panel is about 0.5 m long by 1.0 m wide, with 12 side-by-side pop-up lenses, each 0.5 m long. Flight-like hinges and other mechanical hardware are also incorporated into the prototype SLA wing. The prototype wing has already validated the expected robustness and mechanical functionality of the rigid-panel SLA approach.

Next fiscal year, all four prototype panels will be equipped with lenses, and one of the panels will be equipped with several "live" photovoltaic receivers. This final SLA wing will be the key deliverable under the NASA Advanced Cross-Enterprise Technology Development program.

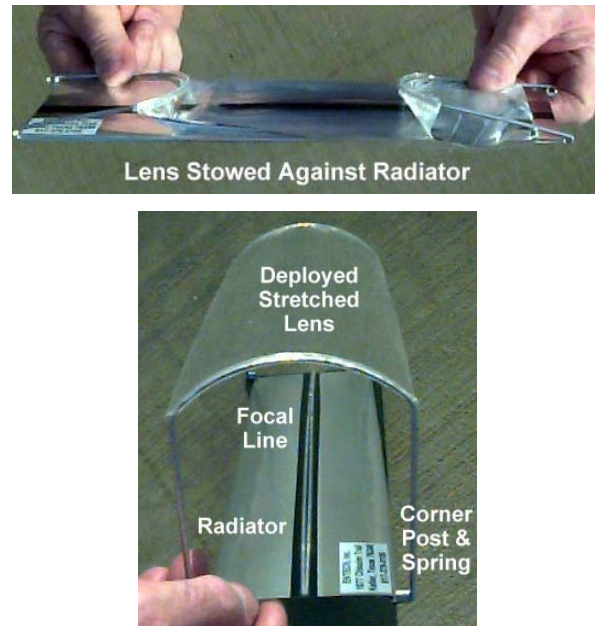


Fig. 15 – Prototype SLA Model with Pop-Up Lens



Fig. 16 – Prototype SLA Wing with Pop-Up Lenses

SLA WING-LEVEL MASS AND PERFORMANCE

A detailed mass and performance analysis has been done for the rigid panel SLA wing point design shown in Fig.17. This wing has a total mass of 39 kg and provides a total lens aperture area of 24 sq.m. At beginning of life (BOL), this wing provides over 7 kW of output power and over 180 W/kg of specific power. These values are based on the use of existing cells with a demonstrated efficiency of 30% at 8 suns and 28C. With improved 32%-efficient cells, wing-level BOL specific power should exceed 190 W/kg in 2002.

Key features of the rigid-panel SLA wing are summarized in Table 1. In addition to excellent performance, mass, and stiffness characteristics, the rigid panel SLA wing approach also enables the outermost panel to be populated with planar cells for pre-deployment power generation (e.g., during LEO to GEO orbit transfer), if a specific mission needs this capability. Furthermore, many mission planners and spacecraft program managers prefer the low-risk, rigid panel deployment approach over flexible blanket approaches.



Fig. 18 – Outdoor Test of World-Record-Performance SLA Mini-Module

Fig. 18 is currently the performance world record holder at 27% net efficiency at operating temperature, confirmed by NREL in outdoor testing. Recently, ENTECH has measured over 27% net efficiency for similar mini-concentrator modules using cells from three different suppliers: Spectrolab, EMCORE, and JX Crystals (using

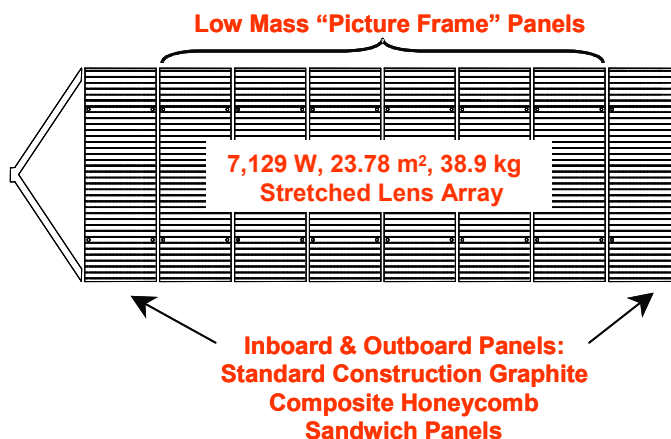


Fig. 17 – Point Design Parameters for SLA Wing

Feature	Value or Characteristic
Point Design Basis	7,129 Watts (BOL)
SLA Implementation	Pop-up lenses
Base Platform Design Maturity	Most components flight proven on DS1
Specific Power	183 W/kg
Stowed Volume	0.11 m³/kW
Stowed Stiffness	40 Hz
Deployed Stiffness	0.1 Hz
Stowed Power	Easily implemented on outer panel
Ease of Adding Planar Panel	Easily implemented on outer panel
Flatness & Warping	Well understood flat stable platform
Deployment Testing	Can use existing off-loaders
Power Testing	Pop-up lenses allow each panel to be tested as a complete assembly before wing integration
Commercial Appeal	Easier to integrate on commercial spacecraft. Readily accepted configuration.
Self Shadowing	No self shadowing

Table 1 – Key Features of the Rigid Panel SLA Wing

SYNERGY WITH TERRESTRIAL PHOTOVOLTAIC CONCENTRATORS

Many aspects of the SLA technology are directly applicable to future terrestrial photovoltaic systems, including the color-mixing lens optical concentrator and the multi-junction cells operating under multi-sun concentration. Indeed, ENTECH is working with NREL on the development of a 27% efficient terrestrial concentrator system using color-mixing lenses and multi-junction cells. The feasibility of this combination has already been demonstrated in mini-module tests at both ENTECH and NREL. The SLA mini-concentrator shown in

TECSTAR top cells). High-concentration (400X) terrestrial concentrator modules are now under development by ENTECH.

SLA ADVANTAGES OVER OTHER SPACE ARRAYS

The Stretched Lens Array (SLA) offers outstanding wing-level performance:

- Operational Power Density: $> 300 \text{ W/sq.m.}$
- Specific Power: $> 180 \text{ W/kg}$
- Compact Stowage for Launch: $> 9 \text{ kW/cu.m.}$
- High-Voltage Operation: $> 400 \text{ V.}$

SLA is inherently lower in cost than planar high-efficiency arrays:

- 80% Savings in Most Expensive Cost Element, the Solar Cells
- Silicone Lensfilm Is Mass-Produced by Continuous Process by 3M.

Panel structure and wing deployment are conventional and simple.

SLA appears to be durable for the space environment:

- Protons, Electrons, UV, Thermal Cycling, Micrometeoroids.

SLA is the ultralight descendent of the SCARLET array on Deep Space 1, and builds on that successful flight heritage.

CONCLUSIONS

A new lightweight rigid-panel concentrator array is under development for future space power applications. SLA provides a substantial cost advantage over planar arrays by using only one-eighth as much expensive solar cell material for the same power output. In addition, the thin silicone lensfilm and the thin composite sheet radiator provide a substantial mass/area advantage over conventional planar cell assemblies. The new rigid-panel SLA wing employs a conventional, conservative, well-proven approach to array deployment and support on orbit, while offering outstanding performance, high-voltage capability, and radiation tolerance.

REFERENCES

1. M.F. Piszczor and M.J. O'Neill, "Development of a Dome Fresnel Lens/GaAs Photovoltaic Concentrator for Space Applications," 19th IEEE-PVSC, 1987.
2. M.J. O'Neill, "Silicon Low-Concentration, Line-Focus, Terrestrial Modules," Chapter 10 in **Solar Cells and Their Applications**, John Wiley & Sons, 1995.
3. H. Curtis and D. Marvin, "Final Results from the PASP Plus Flight Experiment," 25th IEEE-PVSC, 1996.
4. P.A. Jones et al., "The SCARLET Light Concentrating Solar Array," 25th IEEE-PVSC, 1996.
5. D.M. Murphy, "The SCARLET Solar Array: Technology Validation and Flight Results," Deep Space 1 Technology Validation Symposium, Pasadena, 2000.
6. M.J. O'Neill, "Stretched Fresnel Lens Solar Concentrator for Space Power," U.S. Patent 6,075,200, 2000.
7. M.J. O'Neill et al., "The Stretched Lens Ultralight Concentrator Array," 28th IEEE-PVSC, 2000.
8. M.J. O'Neill et al., "Development Of Terrestrial Concentrator Modules Incorporating High-Efficiency Multi-Junction Cells," 28th IEEE-PVSC, 2000.
9. M.J. O'Neill, "Color-Mixing Lens for Solar Concentrator System and Methods of Manufacture and Operation Thereof," U.S. Patent 6,031,179, 2000.
10. D.L. Edwards et al., "Optical Analysis of Transparent Polymeric Material Exposed to Ultraviolet Radiation," with 8th International Symposium on Materials in a Space Environment, Arcachon, France, 2000.
11. M.J. O'Neill et al., "The Stretched Lens Array (SLA), an Ultralight Concentrator for Space Power," 36th IECEC, Savannah, 2001.

34% EFFICIENT InGaP/GaAs/GaSb CELL-INTERCONNECTED-CIRCUITS FOR LINE-FOCUS CONCENTRATOR ARRAYS

L.M. Fraas, W.E. Daniels, H.X. Huang, L.E. Minkin, J.E. Avery
JX Crystals Inc., Issaquah, WA
C. Chu, P. Iles
Tecstar, Inc., City of Industry, CA
M.J. O'Neill, A.J. McDanal
ENTECH, Inc., Keller, Texas
Mike Piszczor
NASA Glenn, Cleveland, OH 44135

ABSTRACT: While monolithic multi-junction cells are preferred for flat plate arrays, mechanically stacked multi-junction cells are superior for solar concentrator applications. Reasons for this are that the mechanical stacked configuration with high efficiency Gallium Antimonide cells allows utilization of a much wider range of the solar energy spectrum, and the ability to use voltage matched interconnects results in full use of low bandgap cell currents. Herein, data are presented for simple two terminal voltage-matched circuits using InGaP/GaAs/GaSb stacked cells showing 34% average circuit efficiency for a lot of 12 circuits given prismatic covers. These circuits have been designed to fit into the ultralight Stretched Lens Array being developed by NASA. With these new cell-interconnected-circuits, we project that the power density at GEO operating temperature can be increased from 296 W/m^2 to 350 W/m^2 while maintaining the specific power at 190 W/kg at the full wing level.

Introduction

In 1989, Fraas and Avery (1) demonstrated a world-record 31% efficient AM0 GaAs/GaSb mechanically stacked dual junction solar cell (measured at 25° C at 100 suns with prismatic cover). However, the GaAs/GaSb mechanical-stacked cell was designed to work with concentrated sunlight and at that time, the space community had no experience with concentrated sunlight solar arrays. So, the aerospace photovoltaic community continued to work primarily on improving flat plate cell efficiencies for satellite power systems. This work led to the adoption of the InGaP/GaAs/Ge monolithic dual junction cell with an efficiency of 23% (AMO, 25° C , 1 sun, no prismatic cover). Meanwhile in 1992, Fraas and Avery fabricated GaAs/GaSb cells and Entech supplied lenses for a concentrator mini-module that was flown on the Photovoltaic Advanced Space Power (PASP) satellite. This mini-module performed well with high power density, excellent radiation resistance, and with no problems tracking the sun. The success of the PASP module then led to the successful use of a 2.5 kW line-focus concentrator array as the main power source on Deep Space I. Deep Space I was launched in 1998.

Meanwhile, work on flat plate monolithic multijunction cells continued. It became clear that the GaAs/GaSb cell outperformed the dual junction InGaP/GaAs/Ge cell because it responded to a much wider spectral range. This led to efforts to put an active junction in the Ge wafer in order to create a monolithic triple junction cell. These efforts have been successful, leading to an improvement in efficiency to 26% for flat plate cells (AMO, 25° C , 1 sun, no prismatic cover). It has been observed that the efficiencies of these triple junction cells increases to 30% with concentrated sunlight (AMO, 25° C , 8 suns, with prismatic covers). This is almost as high as the GaAs/GaSb record efficiency recorded 12 years ago with the GaAs/GaSb dual junction mechanically stacked cell, but not quite. Unfortunately, the currents are not matched in the InGaP/GaAs/Ge cell. Millions of dollars have now been spent trying to rectify this problem by going to four junction monolithic cells. However, these efforts have not been successful to date.

Herein, we observe that the current matching problem that is inherent in the InGaP/GaAs/Ge monolithic triple junction cell does not exist in a triple junction InGaP/GaAs/GaSb mechanically stacked circuit where voltage matching can be used. We report here the design and fabrication of voltage matched circuits where InGaP/GaAs dual junction cells are stacked on GaSb cells. The InGaP/GaAs cells used here are made transparent in the

infrared by growing the active layers on a thin GaAs substrate. Twelve circuits have been fabricated. The lot average circuit efficiency is 34% and the best of the lot circuit efficiency is 35% (AMO, 25° C, 15 suns, prismatic covers). Herein, we also observe that in the future by mechanically stacking a dual junction top cell on a dual junction bottom cell, efficiencies as high as 39% are achievable (AMO, 25° C, 15 suns, prismatic cover).

These very high cell conversion efficiencies can be very important for space satellites if the required concentrator array technology is developed and demonstrated. NASA has realized this and has been developing the ultralight Stretched Lens Array (SLA) for space power (2). In the following sections, we first describe in more detail why mechanically stacked cells outperform monolithic cells. We then present in more detail our triple-junction mechanical-stacked cell-interconnected-circuit (TJ-MS-CIC) design, fabrication, and performance results. Finally, we discuss the potential impact of higher performance TJ-MS-CICs on SLA space power.

Monolithic vs. Mechanical Stacked Multijunction Cells

Table I summarizes the various multijunction cell efficiency numbers discussed in the previous section.

Table I: Summary of AMO Concentrator Cell Efficiencies

Cell Type	# Junctions	Efficiency	# Suns
<u>Monolithic</u>			
InGaP/GaAs/Ge	2	27.5%	15 x
InGaP/GaAs/Ge	3	30%	15 x
InGaP/GaAs/GaInAsN/Ge	4	< 20% QE in GaInAsN	
<u>Mechanical Stack</u>			
GaAs/GaSb	2	31%	100 x
InGaP/GaAs/GaSb	3	35%	15 x

Over the past ten years, monolithic tandem cells have been used exclusively because they are preferred over stacked cells for flat plate arrays. However, it is noteworthy that stacked cells still out-perform the monolithic cells by a substantial margin. First with reference to dual junction cells, the reason why the GaAs/GaSb stacked cell out-performs the InGaP/GaAs/Ge monolithic dual junction (DJ) cell is really quite straightforward. The monolithic DJ cell only uses the energy in the sun's spectrum between 0.4 and 0.9 microns while the GaAs/GaSb DJ cell uses the much larger spectral range between 0.4 and 1.8 microns.

Given the state of the art today, the most appropriate comparison to make is between the monolithic and mechanical-stacked triple junction cells. Table II shows this direct comparison.

Table II: Efficiency Comparison for Triple-Junction PV Cells
at 15 Suns Concentration

	Monolithic InGaP/GaAs/Ge	Mechanical Stack InGaP/GaAs/GaSb
InGaP/GaAs Efficiency	27.5%	27.5%
IR Cell I_{mp}	15x16 mA/cm ² (series limited)	15x30 mA/cm ² (not limited)
IR Cell V_{mp}	0.25 V (Ge bandgap lower than GaSb bandgap)	0.35 V
IR Cell Efficiency	2.5% (from present SBIR contract)	6.5%
Triple-Junction Efficiency	<u>30%</u>	<u>34%</u>

Both the monolithic and mechanically stacked triple-junction (TJ) cells use the same InGaP/GaAs DJ top cell. In the monolithic cell case, the third junction is placed in the Ge and automatically connected in series with the DJ cell. In the mechanically stacked case, the third junction is in GaSb and the stacked cells allow voltage matching to be used instead of current matching. The most serious problem with the monolithic TJ cell is that the Ge cell is automatically series connected with the DJ cell. This means that while the DJ cell only produces a 1-sun current of 16 mA/cm^2 , both the GaSb and Ge cells are capable of producing 33 mA/cm^2 . In the series connected configuration, the current in excess of 16 mA/cm^2 is wasted. This is not a problem in the voltage-matched configuration used in mechanical-stacked circuits. A secondary problem with Ge vs. GaSb is that the lower bandgap of Ge leads to a lower voltage for the Ge cell and consequently worse performance at higher temperature relative to GaSb cells. Referring to table II, the result of the above two problems is that the boost efficiency from a Ge cell in the monolithic configuration is only 2.5% while the GaSb cell in the voltage matched configuration adds 6.5% to the final circuit performance. Thus, the 30% efficiency demonstrated for the InGaP/GaAs/Ge monolithic triple-junction (TJ) cell still falls short of the 34% efficiency achievable with a mechanically stacked TJ cell.

Practical triple-junction voltage-matched circuits

When there are two solar cell chips, one begins with 4 terminals, 2 per chip. How does one end up with a 2 terminal circuit? Figure 1 shows how this is done. When the cells are arrayed in a line, one simply connects the cells with the higher voltage in parallel while connecting the cells with the lower voltage in series until one obtains a voltage match. The example shown in figure 1 shows seven GaSb cells wired in series. In the circuit shown, the GaSb cells are wired in series to traces to the right of the circuit while the InGaP/GaAs cells are wired in parallel to traces at the left of the circuit. We refer to this as a 7 to 1 voltage match because it takes 7 GaSb cells in series to produce the voltage that 1 InGaP/GaAs cell produces. This is the appropriate interconnection for a circuit operating at 15 suns at room temperature. In that case, seven times the V_{mp} of GaSb ($7 \times 0.375 \text{ V} = 2.63 \text{ V}$) slightly exceeds the V_{mp} of 2.4 V for the InGaP/GaAs cell.

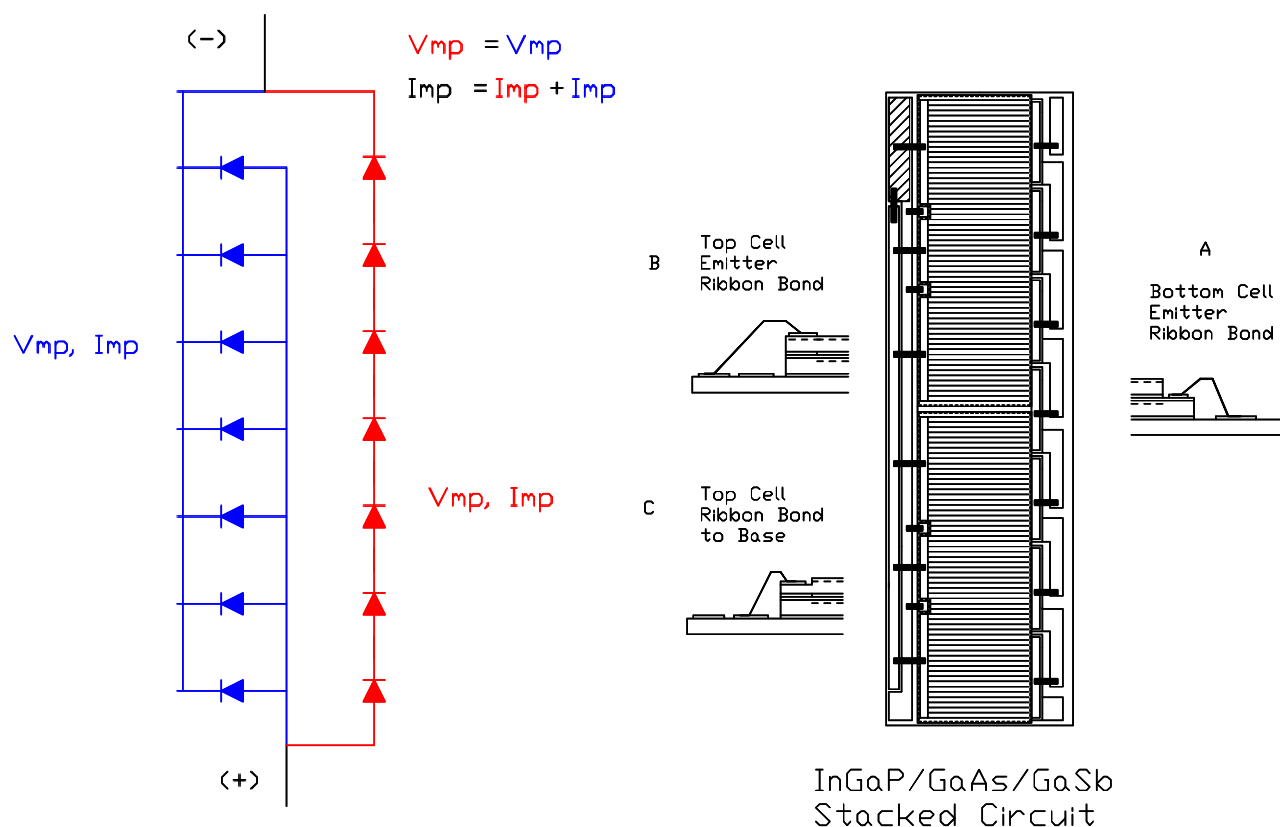
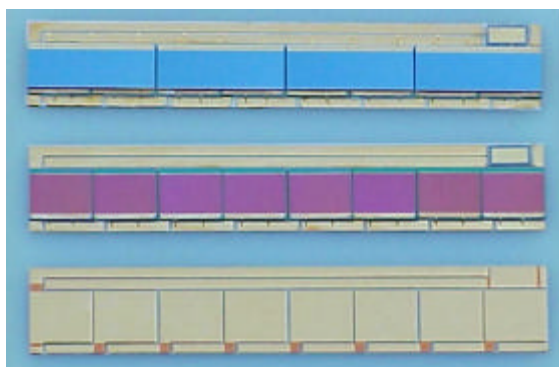


Figure 1. Voltage matching concept and mechanical circuit design.

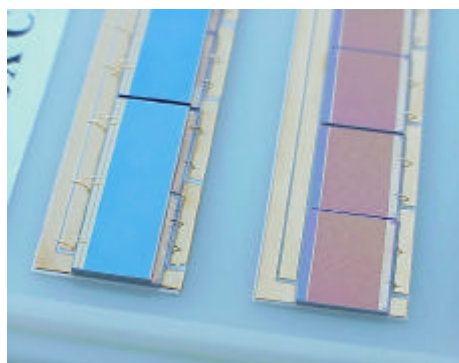
In addition to the voltage match concept, figure 1 also shows some detail related to mechanical assembly. There is a challenge in mechanical stacked circuits. How does one connect to the hidden base layer for the top cell? Figure 1 shows a drawing of a CIC assembly with schematic details of the wire bonds for each of three contact types.

The (a) interconnect connects the front GaSb cell contact, the positive contact, to an appropriate circuit board trace. The (b) interconnect is from the top surface contact of the InGaP/GaAs cell, also positive, to the circuit board. The (c) interconnect is the negative GaAs to circuit connection. Notice that (c) is shown on the frontside of the InGaP/GaAs cell. This is a new approach for front cell interconnects that allows all lead bonding to be done from the top side down, with no need to flip the top cells over as we have done previously to connect to the GaAs backside contact. A window is etched in the frontside epi layers and an isolated metal bonding pad is formed that electrically contacts the GaAs substrate. In this configuration, current is collected as usual by a grid on the backside of the GaAs wafer and transported to a bus underneath the topside base contact pad. This current then flows through the GaAs wafer thickness to the topside base contact pad. Since the electron mobility in N-type GaAs is high, for a wafer doping density of $3 \times 10^{17}/\text{cc}$ and a pad area of 1 mm^2 , the through-the-wafer resistance is only 2 milliohms. At 15 suns AMO, the top cell current will be 0.23 Amps per cm^2 . So the voltage drop through the wafer will be less than 1 mV.

In actuality, we have used an 8 to 1 voltage match in our fabricated circuits because we have designed for an operating temperature of 80°C for GEO. Photographs of these InGaP/GaAs/GaSb circuits are shown in figure 2.



Top: Completed InGaP/GaAs/GaSb Circuit
Middle: Circuit with GaSb IR Cells
Bottom: Substrate with Metal Traces



Close-up showing ribbon bonds
(Patent pending)

Figures 2a and 2b. Mechanically stacked triple junction cell-interconnected-circuits.

TJ-MS-CICs are made simply as follows. First, thin GaSb cells ($0.8 \text{ cm} \times 1 \text{ cm}$) are positioned. This is done rapidly with an automated pick-and-place machine which first writes a solder pattern on the evaporated metal pattern on the alumina substrate. The diode is placed followed by furnace solder attach. Then these cells are connected to the circuit traces shown at the right of the circuits in figure 2b using an automated ribbon bonder. The DJ cells are supplied with the backside negative contacts fed through to front side bonding pads, enabling front top bonding of both polarity contacts. These cells are adhesive-bonded on top of the GaSb cells with silicone adhesive and are then ribbon bonded to the circuit traces shown to the left on the circuits in figure 2b.

The DJ cell lead bonding is done with the same automated ribbon bonder that was used previously for the GaSb cell ribbon bonding. While the TJ-MS-CICs shown here in figure 2 is novel, this assembly procedure is similar to that used in fabricating the first concentrator PASP module flown in space in 1994. However, there is one notable improvement. Note that all of the ribbon bonds are made to the top side of the stack.

Experimental Results

As of this writing, Tecstar has just delivered 138 top cells, 24 with efficiencies over 26% (AMO) and 87 with efficiencies in the 25% to 26% range. JX Crystals had previously designed the circuit substrates and fabricated GaSb cells and populated circuits with GaSb series strings. JX Crystals has now fabricated 12 circuits complete with GaSb series strings and InGaP/GaAs parallel strings. Circuit outputs measured for these cell-interconnected-circuits range from 3.07 W to 3.25 W. Given an input power of $0.6 \times 8 \times 0.1353 \times 15 = 9.74 \text{ W}$, the

resultant circuit efficiency for the best circuit with an output of 3.25 W should be 33.4%. Given that the top cell grid shading is 7%, this efficiency could potentially increase to over 35% with the use of prismatic cover slides. Validation of these efficiency measurements at NASA is still required. However, it should be noted that NASA verified GaSb cell boost efficiencies (1) behind GaAs as high as 7% in flight experiments in 1990. Given this and the fact that the dual junction cell is a well-characterized cell, these high circuit efficiencies follow, and should not be surprising. The surprising fact is really that these high efficiency stacked concentrator cells have been ignored for so long.

Figure 3 shows the illuminated current vs. voltage curve for one of these circuits and tables III and IV summarize the performances for these 12 circuits.

Table III: TJ MSCIC Performance Summary

		<u>Without prismatic cover</u>	<u>With prismatic cover*</u>
Best Circuit	Pmax	3.25 W	3.41 W
Best Circuit	Effic	33.4%	35.1%
12 Circuit Ave	Pmax	3.15 W	3.31 W
12 Circuit Ave	Effic	32.5%	34.1%

*Projection

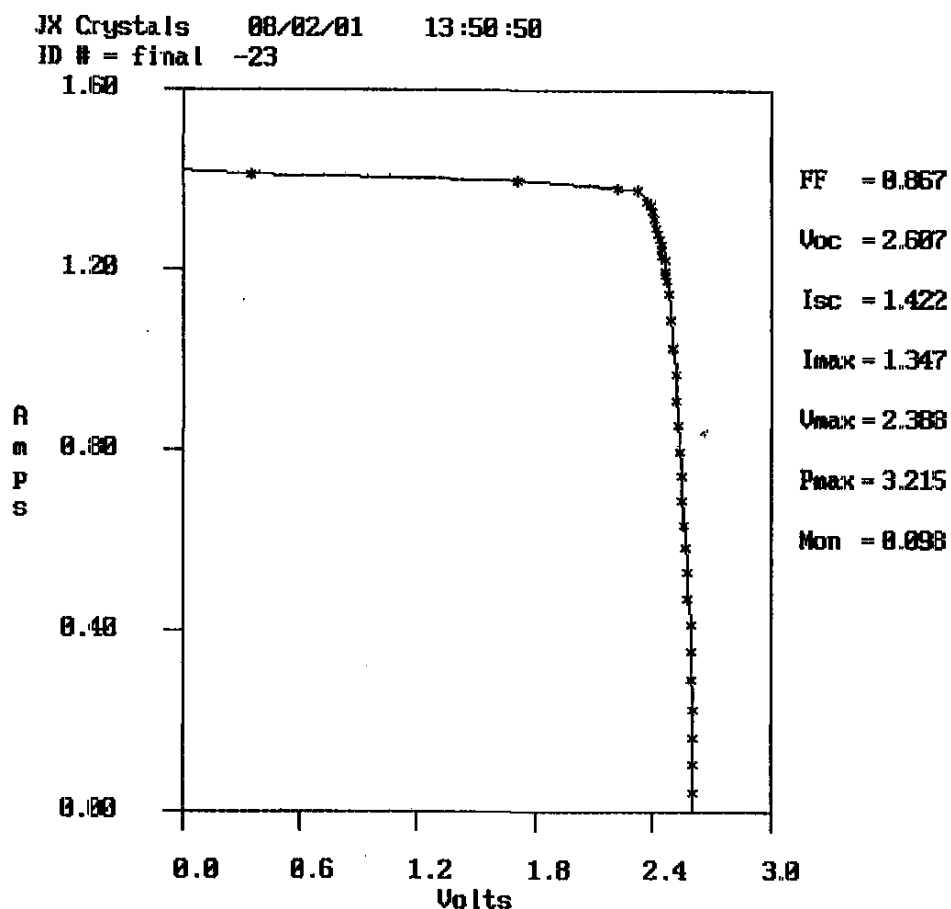


Figure 3. The illuminated current vs. voltage power curve for one of JX Crystals' satellite power circuits.

Table IV: Measured* JX Crystals' TJ MSCIC Performance Parameters**

ID	FF	Voc	Isc	I _{max}	V _{max}	P _{max}	Effic
23	0.872	2.617	1.424	1.356	2.397	3.252	33.4%
24	0.848	2.607	1.412	1.3	2.402	3.122	32.1%
25	0.864	2.617	1.34	1.256	2.412	3.03	31.1%
26	0.86	2.607	1.385	1.32	2.354	3.106	31.9%
3	0.862	2.617	1.397	1.307	2.412	3.152	32.4%
10	0.879	2.602	1.391	1.324	2.402	3.181	32.7%
11	0.87	2.602	1.385	1.321	2.373	3.136	32.2%
12	0.866	2.593	1.415	1.321	2.407	3.18	32.7%
13	0.881	2.603	1.386	1.322	2.402	3.176	32.7%
14	0.87	2.613	1.394	1.328	2.388	3.171	32.6%
15	0.87	2.598	1.394	1.31	2.407	3.153	32.4%
18	0.878	2.593	1.394	1.32	2.402	3.172	32.6%

*Without prismatic covers

**BMDO/NASA contract

As of this writing, we have sent the lowest performance circuit, #25, and the highest performance circuit, #23, to ENTECH for incorporation into mini-modules for further testing. In order to check out assembly procedures, ENTECH has initiated testing using the lowest performance circuit first. Figure 4 shows a photograph of this circuit in outdoor testing. Their initial performance testing on a very hot day showed a module efficiency of 27.3%. The outdoor temperature during this test was 42° C. Based on these results, a mini module efficiency of 30% should be achievable in the very near future.

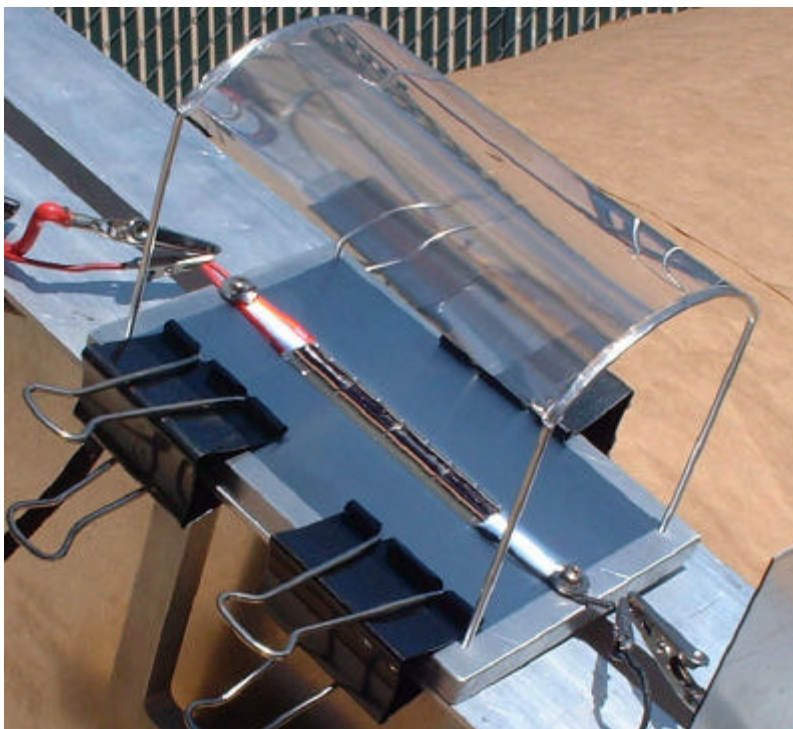


Figure 4. Mini-module with stretched lens and InGaP/GaAs/GaSb circuit.

Improved array performance

NASA has been developing the ultralight Stretched Lens Array (SLA) for space power (2). The baseline cell for this array to date has been the monolithic TJ cell. Very respectable array performance has been predicted for this SLA, as is shown in the first column in table V. In this section, we discuss the potential impact of mechanically stacked multijunction cells and circuits on the performance of this array. There will be an impact on both array weight and array power.

We first discuss the impact on array power density. The baseline SLA is designed to operate at 8 suns concentration and in GEO with cells operating at 80° C. Given a lens optical efficiency of 92%, the array efficiency using Monolithic TJ cells is anticipated to be 22% (column 1 in table V). For this reason, we measured the efficiency of circuit #15 at 8 suns and 80° C. We measured an efficiency of 27.2%. With lens losses, we anticipate an increase in array efficiency at operating temperature using mechanically stacked TJ cells from 22% to 25%. This will increase the array power density from 296 W/m² to 336 W/m². We also measured the efficiency for circuit #15 at 15 suns and 80° C and found the efficiency to increase from 27.2% to 28.1%. The array power density could then increase to 350 W/m². However, operation at 15 suns would require a tighter pointing tolerance (perhaps 1 degree instead of 2 degrees).

In the last two columns in table V, we note that still further improvements are theoretically possible. These improvements include improvements in the DJ and GaSb cells as well as the potential realization of four active junctions by making a stack consisting of 2J + 2J. This 2J + 2J will be much easier to achieve than a monolithic 4J because of relaxed material constraints.

What about the impact of our InGaP/GaAs/GaSb circuits on array weight? In a real array, we would not use the alumina substrates but we would use flex circuits instead. Given this, then the additional weight for the stacked cell comes about through the additional bottom cell and an increase in thickness in the DJ cell. If we assume 200 micron thick top and bottom cells as opposed to a 140 micron monolithic TJ cell, we find that additional weight is added to the array. However, because of the small sizes of the cells, this additional weight is not large and is compensated by the increase in power density such that the mass specific power at 8 suns remains nearly unchanged at 191 W/kg. As one goes to 15 suns, the mass specific power actually improves.

Finally, we briefly discuss costs. Without going into detail, if we assume an array final cost of \$500 per Watt, then the additional value associated with each GaSb cell would be approximately \$30 per cm². GaSb cells are made via simple diffusions without toxic gases and can easily be made at costs well below this value.

Table V: Stretched Lens Array Performance Projections

Cell Type	3J Mono	2J+1J Mech	2J+1J Mech	2J+1J Mech	2J+2J Mech
Cell supplier	Spectrolab	JXC	JXC	JXC	Tecstar
Conc. Ratio	8x	8x	15x	15x	15x
Cell Effic.(RT)*	Demo	Demo	Demo	Theory	Theory
2J	27.5%	27.5%	28%	30%	30%
Boost	2.5%	6.0%	6.5%	7%	9%
Total	30%	33.5%	34.5%	37%	39%
Operational @ 80° C Array Efficiency	22%	25%	26%	28%	30%
Areal Power (W/m ²)	296	336	350	377	403
Areal Mass (kg/ m ²)	1.54	1.76	1.54	1.54	1.54
Specific Power (W/kg)	192	191	227	245	262

*With prismatic cover

Conclusions

Transparent InGaP/GaAs Dual Junction solar cells were fabricated at a qualified aerospace solar cell production company. Efficiencies of over 26% were measured. These concentrator cells were mechanically stacked on top of GaSb booster cells that added over 6% efficiency for a total of over 32% at 15 suns. This high number results from the benefits of mechanical stacking. The solar energy spectrum is utilized out to 1.8 microns and the full current potential of the lower bandgap back-cells is realized by voltage matched interconnects.

A new stacked cell CIC design is being implemented that provides for voltage matching and bypass diode protection in a basic two-terminal array building block configuration. This Triple-Junction Mechanically-Stacked configuration can increase the real power density for the Stretched Lens Array dramatically to 350 W/m^2 without a penalty in the mass specific power density.

References:

- 1.) J.E. Avery, L. M. Fraas, et. al. 21st IEEE PVSC (1990) p. 1277.
- 2.) Mark J. O'Neill, Michael F. Piszczor, et. al., 36th IECEC (2001) IECEC2001-AT-39.

CARRIER RECOMBINATION AND ESCAPE IN P-I-N MULTIQUANTUM WELL SPACE SOLAR CELLS

A. Alemu, C. Monier*, L. Williams, A. Freundlich

Space Vacuum Epitaxy Center, University of Houston, Houston, Texas 77204-5507

* Present address: Sandia National lab., Albuquerque, New Mexico 87185-0753

The addition of quantum wells (QWs) in the intrinsic region of a p-i-n solar cell can boost the current output of a cell. The absorption region of the cell is extended towards the infrared by the incorporation of wells that have, by definition, a band gap lower than the host material. In order to have as much current improvement as possible, one will try to collect as much carriers as possible from the wells and minimize the loss of carriers. Both recombination and escape of photogenerated carriers occur in the i-region. Understanding recombination and escape mechanisms will help the optimization of the QW region for better performances. Recent studies showed the dependence of the carriers collection efficiency from the wells on the built-in electric field. A critical electric field was identified as necessary for the achievement of high collection efficiencies. Photocurrent and photoluminescence studies were carried out at different temperatures and bias in order to identify the main mechanisms involving carriers from the QW region. Samples included in this study are a large variety of InP-InAsP MQW solar cells which differ from one another by their arsenic composition and their QW region geometry. A qualitative analysis of the results is included in this work which identifies radiative recombination as the main carrier loss channel for non-collected carriers in a device with a relatively weak electric field.

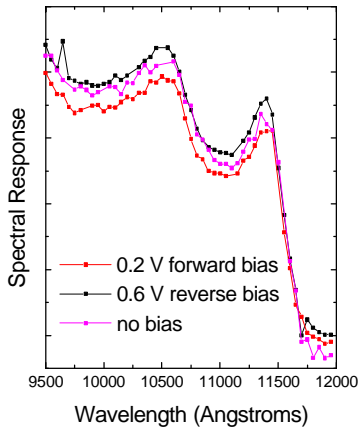
I. INTRODUCTION

The addition of quantum wells for solar cells used in space applications [1] results in increased efficiency and improved radiation hardness [2]. In a recent study [3], it was shown that the photocurrent output of some of the InP-InAsP MQW solar cells increases with increasing reverse bias while there is no variation for some others (saturation regime attained at zero bias). The later were found to have a strong built-in electric field as compared to the earlier. The built-in electric field, due to differences in doping between the p-emitter and n-base, is necessary to collect carriers coming from the emitter (or base, depending on the nature of the carrier) and carriers escaping from the quantum wells in the i-region. Its' value also depends on the geometry of the intrinsic region. For electric fields inferior to a critical value, reduced collection efficiency and a severe degradation of solar cell performance were observed [3]. This is mainly due to a reduced number of carriers collected from the wells as shown on figure 1.

Details concerning the structural parameters of the MQW solar cells are given in table I of reference 2. The dependence of the saturation regime (no photocurrent improvement at reverse bias) as a function of the open circuit voltage/total MQW thickness is presented in figure 2. The saturation conditions have been reached for samples having high open circuit voltage ($V_{oc} > 0.69$ V). The non-saturated samples exhibit smaller voltages. The reduction of the V_{oc} is a consequence of carrier recombination. The main objective of our present work is to identify the loss mechanisms that involve these carriers. This goes hand in hand with the understanding of the escape mechanisms of carriers confined in the wells. There are only two ways for a carrier to escape from a well: thermionic escape or quantum mechanical tunneling. A combination of both can also be considered. Similarly there are only two loss channels: radiative or non-radiative. In a radiative recombination, an electron and a hole recombine by emitting a photon. This can be measured by using an appropriate measurement setup like photoluminescence. A non-radiative recombination is not as straightforward as a radiative one. It is a dark process that can involve defect or impurity states, interaction with phonons (lattice vibration), scattering on impurities etc... Its evaluation is an indirect one and increases with temperature due to higher phonon population (higher vibration).

In the prevailing paradigm, non-radiative recombination is considered as the main carrier loss mechanism that leads to open circuit voltage reduction in MQW solar cells [4]. Nevertheless, in a theoretical analysis, Anderson et al. [5] found that open circuit voltage reductions resulting from the introduction of quantum wells stem directly from additional radiative recombination in the quantum wells and the corresponding increase in dark current in InP-based quantum well solar cells. Their study included samples grown at the University of Houston which are the subject of the present work. Their results are consistent with our experimental observations detailed below.

SR of a non-saturated MQW solar cell
(weak built-in electric field)



SR of a saturated MQW solar cell
(strong built-in electric field)

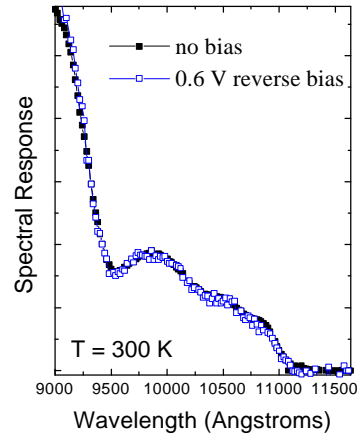


Figure 1: Room temperature photocurrent spectra of sample 712 (a) and sample 708 (b) under different values of electrical applied bias. Under a reverse bias the photocurrent from sample 712 improves while the one of sample 708 seems to have already saturated.

At room temperature, thermionic emission from the wells is considered by researchers in the literature as the only escape mechanism [4,6] even from wells many times deeper than kT (available thermal energy, k is boltzmanns' constant and T is the temperature in Kelvin) [6].

For a better analysis and understanding of our results we have roughly identified three different temperature ranges: low temperature (under 100 K), intermediate temperature range (between 100 and 250 K) and high temperature (above 250 K). This sectioning is purely for the purpose of this study and its boundaries have no exact physical meaning.

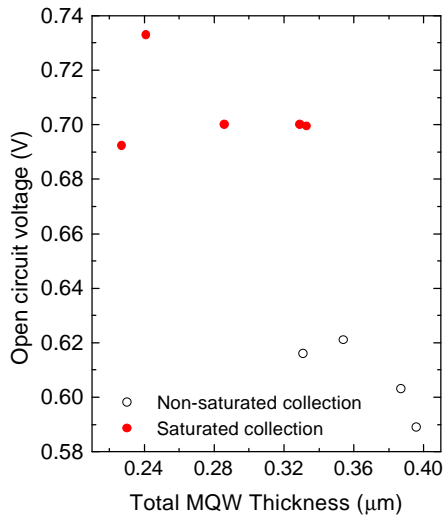


Figure 2: Open circuit voltage for samples with saturated (solid circles) or non-saturated open circles carrier collection efficiency from the multi-quantum wells

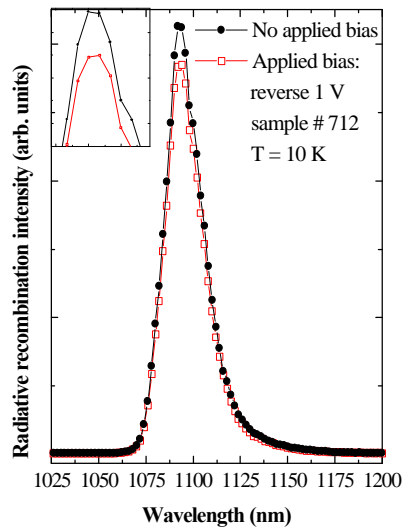


Figure 3: Photoluminescence (radiative recombination) intensity variation vs. bias at 10 K for sample 712. The decrease of the intensity at an applied bias of 1 V coincides with an increase of current read on an ammeter.

II. EXPERIMENT

Both photoluminescence and photocurrent studies were undertaken for different temperatures and applied bias. The samples studied are multi-quantum well (MQW) solar cells, grown by chemical beam epitaxy (CBE) at 510°C on (100) S-doped InP (001) substrates. Ten periods of not intentionally doped $\text{InAs}_x\text{P}_{1-x}\text{-InP}$ were incorporated in the intrinsic region of InP p-i-n structures for different arsenic composition and well/barrier thickness. Details concerning the optimization of growth sequences and characterization of p-i(MQW)-n heterostructures have been previously reported elsewhere [7,8]. The structural parameters were obtained by high-resolution x-ray diffraction; capacitance voltage (C-V) profiling measurements provided an evaluation of p- and n-doping levels from which the built-in electric field value in the MQW region was calculated by solving Poisson's equation. All structures have comparable doping levels for the emitter and base. For the photoluminescence experiments the MQW solar cells were placed in helium cooled cryostat (10 K) with contacts at its emitter and base in order to apply bias from a DC power supply. A temperature controller was used to bring the sample at the desired temperature. A voltmeter and ammeter are used to determine the applied bias and see the change in the resulting photocurrent. The applied bias rarely extends over 1 V in absolute value. The photoluminescence signal induced by the 514.5 nm wavelength of an argon laser was dispersed by a 0.25 m focal length monochromator and detected by a cooled InGaAs detector. For the photocurrent measurements, the MQWs cells were placed in a nitrogen cooled MMR cryostat and a 100 W tungsten halogen white lamp was used as an excitation source. The results from both experiments were used in combination for the understanding of the mechanisms involved in the loss and collection of the carriers from the QWs.

III. RESULTS AND DISCUSSION

III. a) Low temperatures

At very low temperatures (~ 10 Kelvin) any thermionic escape is inhibited and non-radiative recombination are minimized due to the low temperature. At 10 K, the decrease of the photoluminescence (PL) intensity (radiative emission) (see figure 3) and the increase of the photocurrent output, as measured on an ammeter, when a reverse bias is applied, show us that carriers do escape from the wells. Our low temperature PL results imply that tunneling does occur in our samples because it is the only escape mechanism available at that temperature. The application of a small forward bias decreases the electric field in the MQW region. When such a small forward bias is applied on our devices during a PL measurement, it results in the increase of the PL signal due to increased radiative emission from the wells. This suggests that the recombination of carriers, that did not escape due to a weak electric field, is mainly radiative. At low temperatures tunneling and radiative recombination are the main carrier escape and loss mechanisms, respectively. Which is also consistent with the findings of Zachariou et al. [4] for low temperatures.

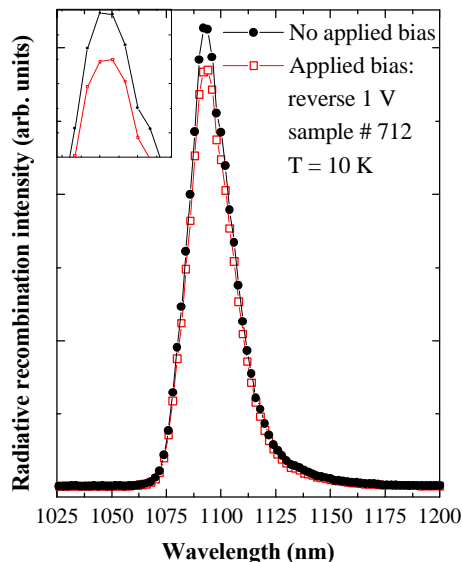


Figure 3: Photoluminescence (radiative recombination) intensity variation vs bias at 10 K for sample 712. The decrease of the intensity at an applied bias of 1 V coincides with an increase of current read on an ammeter.

III b) Intermediate temperatures

As the temperature increases there is an increasing availability of thermal energy (kT). This translates into the lowering of the barrier that the carriers have to overcome in order to escape from the QWs. Even if the temperature is not high enough for the thermionic emission to be predominant, this enhances the tunneling effect. The barrier through which the carriers are tunneling is seen thinner by the carriers at 100 K than at 10 K due to the greater thermal energy available at higher temperatures. Hence, tunneling is enhanced in the intermediate temperature range (~ 100 K to 250 K). For this temperature range, the application of a reverse 1 V bias on the cells in our PL measurement setup induces the highest PL peak reduction compared to a signal taken without applied bias (see Figure 4). The great variation of the PL signal at reverse 1 V bias, which is only 55 % of the signal without applied bias (at 150 K), shows that the escape is mainly through tunneling. The occurrence of the maximum reduction of the PL signal at these temperatures and not at lower temperatures shows that tunneling at this temperature range is thermally assisted. This is a temperature range where thermally assisted tunneling is dominant and therefore built-in electric field dependency is the strongest. The PL intensity decreases with temperature. This can be explained by the increase of non-radiative recombination processes due to the increase in temperature. Temperature has two opposite effects on device operation. On one hand, it can facilitate the escape of carriers through thermionic emission or/and thermally assisted tunneling. On the other hand, it increases the carriers' loss through the enhancement of non-radiative recombination by the availability of an increasing number of phonons. These phonons are used to facilitate the transfer of carriers to defect and impurity levels thereby increasing the dark process. All of our samples reach their maximum light conversion efficiency in the intermediate temperature range (figure 5). These means that at these temperatures, escape and collection of carriers are more favored than recombination in general. The maximum collection of carriers occurs at 150 K for the non-saturated sample 712, which is in the intermediate temperature range. This maximum is found in the intermediate temperature range for all saturated and non-saturated samples (about 180 K for the saturated sample 708).

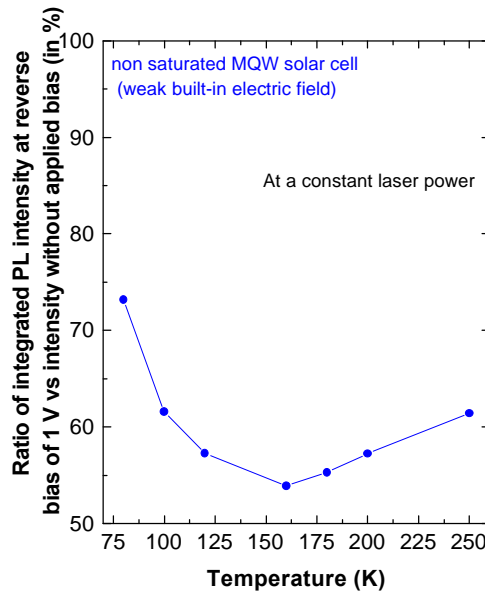


Figure 4: Integrated Photoluminescence intensity ratio between a signal taken under a reverse applied bias of 1V and a signal taken without applied bias for different temperatures (sample No. 712)

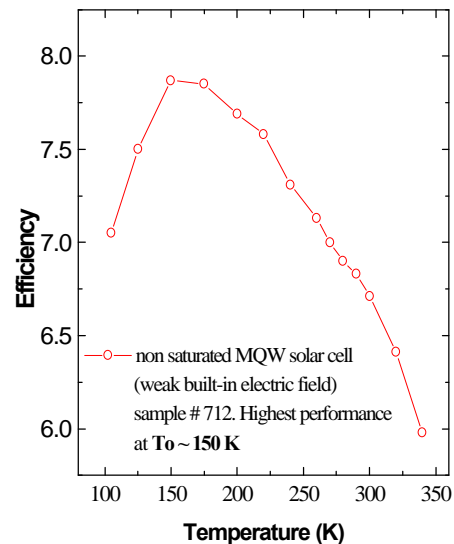


Figure 5: Efficiency variation vs temperature for sample 712.

If we consider the ratio between the number of collected carriers over the number of recombined carriers, it reaches its maximum in this temperature range. At these temperatures the balance between collection and recombination is more in favor of collection compared to lower or higher temperatures. The main carrier escape mechanism is a thermally assisted quantum mechanical tunneling of carriers. This can

be verified by the fact that the biggest reduction of radiative emission (PL) intensity under a reverse bias of 1 V occurs at this temperature. If the escape was purely thermionic then the change in bias wouldn't have affected the radiative emission this much. Most of the carriers would have anyway escaped thermally from the well. The escape is not purely by tunneling either because then the results would have not been temperature dependent. The strong link between applied bias and radiative emission intensity shows that under a weak electric field carriers are lost through the radiative recombination channel, for this temperature range.

Electric field in a quantum well tends to spatially separate electrons and holes. This results in the weakening of direct optical transition, which in turn favors escape. In general, the smaller energy barrier of light holes in a QW make them the first to escape thermally from the wells thereby creating space charges in the QWs. The study of space charge effects in carrier escape is beyond the scope of the present work; the reader can refer to the work of McFarlane et al [9]. The broadening of a PL peak is an indirect measure of the strength of non-radiative recombinations. This broadening stays almost constant under different applied bias but varies slightly with temperature. This suggests that non-radiative process is very low in the QWs. This is in accordance with results by other researchers who found that it mainly occurs in the barrier material during escape and is not much sensitive to reasonable changes in bias [4]. As temperature increases the efficiency starts declining because non-radiative recombination gains importance at the expense of collection.

III.c) High temperatures

In the high temperature range, above 250 K, the thermal processes are dominant. The PL peaks reduction with temperature shows that non-radiative recombinations are the dominant carrier loss mechanism. A comparison of results given for the same non-saturated sample on figure 1-a and figure 6 shows that collection still competes with radiative recombination. Thermionic emission becomes dominant but there is no evidence that tunneling should be negligible. Radiative recombination is still the main loss channel for non-collected carriers from the QWs. Therefore, radiative recombination is responsible for the reduction in V_{oc} (figure 2) for non-saturated solar cells. This experimental result is in accordance with theoretical results on open circuit voltage at the radiative limit of the ideal theory [5, 10].

The non-radiative recombination process acts as a virtual reservoir of carriers: as the temperature decreases, there are more and more carriers available for either radiative recombination or collection depending on the strength of the built-in electric field and MQW region geometry.

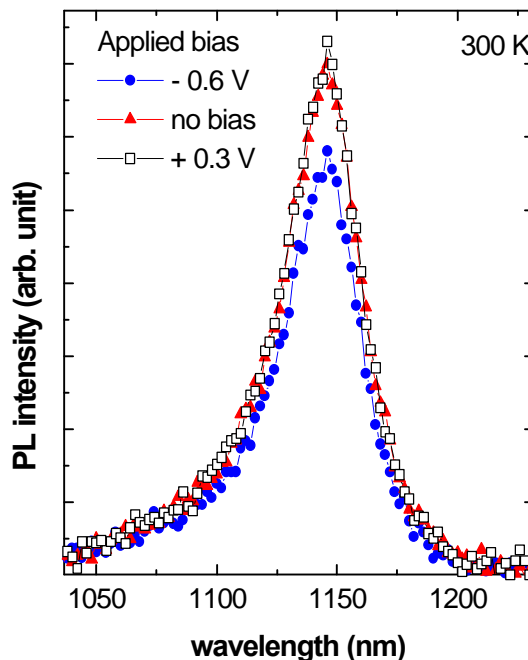


Figure 6: Photoluminescence (radiative recombination) intensity variation vs bias at 300 K for sample 712. The decrease of the intensity at an applied bias of 1 V coincides with an increase of photocurrent as shown in on figure 1

At high temperatures the loss of carriers occurs by both radiative and non-radiative recombination process. The non-radiative process is important due to the increased number in phonons at these temperatures. Thermionic emission is the main carrier escape mechanism but quantum mechanical tunneling should not be neglected especially for samples having high internal electric field. The invariance of the broadening of the photoluminescence peaks with applied bias, at any given temperature, shows that non-radiative recombination in the wells does not play a direct role in the bias dependence of the collection efficiency. At low temperature, the main carrier loss channel is the radiative recombination process and quantum mechanical tunneling is the only carrier escape mechanism from the wells. The dependence of the collection efficiency upon the built in electric field at low temperature (10 K) shows that radiative recombination is the main carrier loss channel under a weak electric field. This dependence has the same variation at 300 K, which means that the improvement in collection efficiency at higher electric fields comes to the expense of radiative recombination at 300 K.

IV. CONCLUSION

A strong electric field is needed to collect most of the carriers from the MQWs. At all temperatures, the reduced collection efficiency is found to correspond to a reduced built-in electric field and an increased radiative recombination. Open circuit voltage reduction in the non-saturated MQW solar cells is directly related to increased radiative recombination. Shallower wells (i.e. low As content) in InP/InAsP MQW solar cells that will minimize radiative recombination, are one way of getting efficient radiation resistant space solar cells.

References:

- ¹ A. Freundlich, et al "United States patent # US05851310 and #US06,147,296
- ² R. J. Walters, G. P. Summers, A. Freundlich, C. Monier, M. Vilela, and S. R. Messenger, 2nd World Conference on Photovoltaic Energy Conversion, Vienna, Austria, 1998, p. 3723
- ³ I. Serdiukova, C. Monier, M. F. Vilela, and A. Freundlich, Applied Physics Letters 74 (19), pp. 2812-2814, 1999
- ⁴ A. Zachariou, J. Barnes, K. W. J. Barnham, J. Nelson, and E. S. M. Tsui, "A carrier escape study from InP/InGaAs single quantum well solar cells", J. Appl. Phys. **83**, 877 (1998)
- ⁵ Neal G. Anderson and Steven J. Wojtczuk "Open-circuit voltage characteristics of InP-based quantum well solar cells", J. Appl. Phys. **79**, 1973 (1996)
- ⁶ Y. Yazawa, T. Kitatani, J. Minemura, K. Tamura and T. Warabisako, "Carrier generation and transport in InGaAs/GaAs MQW solar cells", Proceedings of the 24th Photovoltaics Specialists Conference, 1st WCPEC proceedings, pp. 1878-1881, 1994.
- ⁷ A. Freundlich, A. H. Bensaoula, and A. Bensaoula, J. Cryst. Growth **127**, 246 (1993).
- ⁸ C. Monier, M. F. Vilela, I. Serdiukova, and A. Freundlich, Appl. Phys. Lett. **72**, 1587 (1998).
- ⁹ S. C. McFarlane, J. Barnes, K. W. J. Barnham, E. S. M. Tsui, C. Button and J. S. Roberts, "Space charge effects in carrier escape from single quantum well structures", J. Appl. Phys., Vol. 86, No. 9, 5109 (1999)
- ¹⁰ Robert J. Walters, G. P. Summers, S. R. Messenger, M. J. Romero, M. M. Al-Jassim, R. Garcia, D. Araujo, A. Freundlich, F. Newman, and M. F. Vilela, "Electron beam induced current and cathodoluminescence study of proton irradiated InAs_xP_{1-x}/InP quantum-well solar cells", J. Appl. Phys., Vol. 90, Issue 6 pp. 2840-2846, (September 15, 2001)
- ¹¹ N. G. Anderson, "Ideal theory of quantum well solar cells", J. Appl. Phys. **78** (3), 1850 (1995)

Procedures at NREL for Evaluating Multi-junction One Sun and Concentrator Cells

Tom Moriarty, Keith Emery and Don Dunlavy
National Renewable Energy Laboratory
1617 Cole Blvd., Golden, CO

ABSTRACT

The procedures for evaluating the performance of multi-junction one sun and concentrator cells at NREL are described. The accurate measurement of the performance of multi-junction cells requires relative quantum efficiency measurements for each junction, reference cells for each junction, and a spectrally adjustable solar simulator. The quantum efficiency for each junction is measured by light biasing the other junctions to insure that the junction of interest is current limiting. The quantum efficiencies are used to calculate the spectral mismatch for each junction under the simulator and the simulator spectrum is adjusted until each is operating at its correct photocurrent.

Quantum Efficiency

To measure the performance of a multi-junction device under a simulator, the intensity and spectral content of a simulator must be adjusted so that each junction of the device operates at the same photocurrent it would experience under the desired reference spectrum. It is necessary to know the quantum efficiency of each of those junctions to make the proper simulator spectral adjustments.

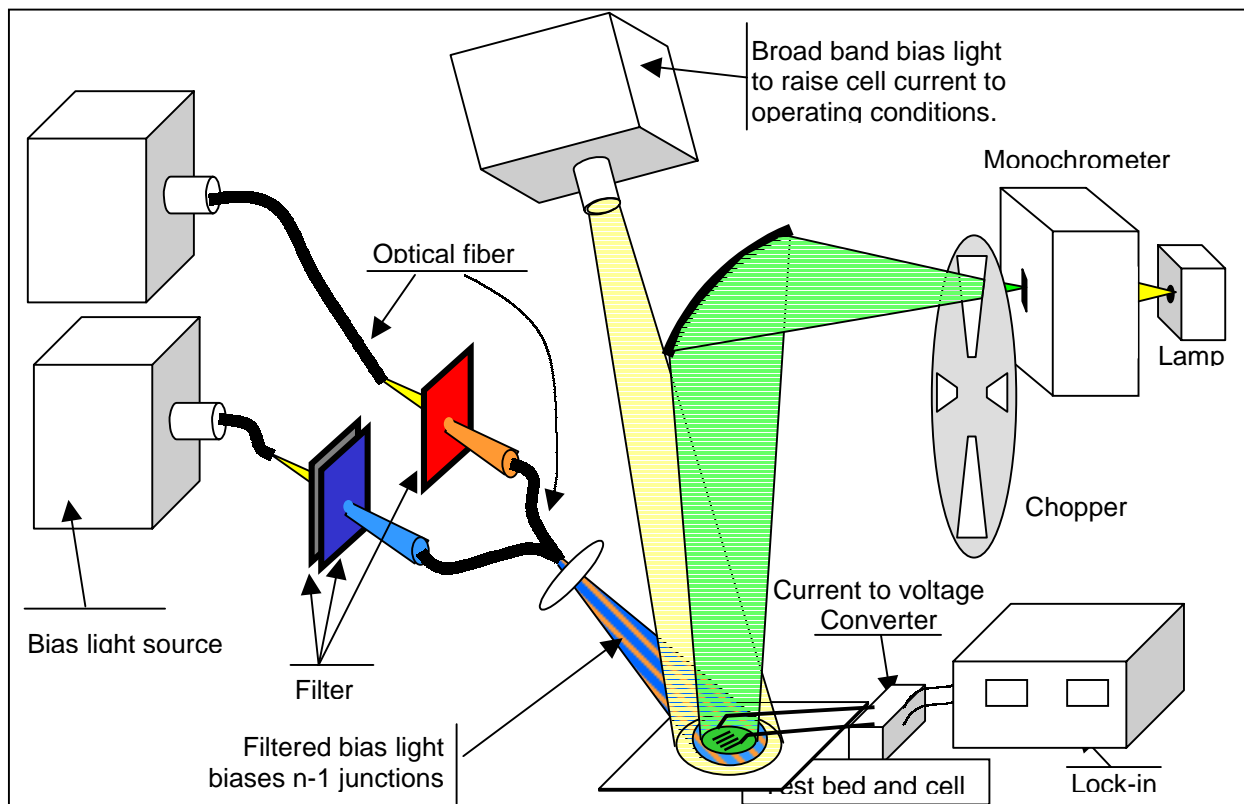


Figure 1. Filters in series tailor bias light to wavelength response range of only one junction. Groups of filters in parallel allow light biasing of all junctions but one, insuring that the excluded junction is current limiting. The chopped, monochromatic beam is only detected by the lock-in amplifier when its wavelength is in the response range of the non-light biased, current limiting junction.[4]

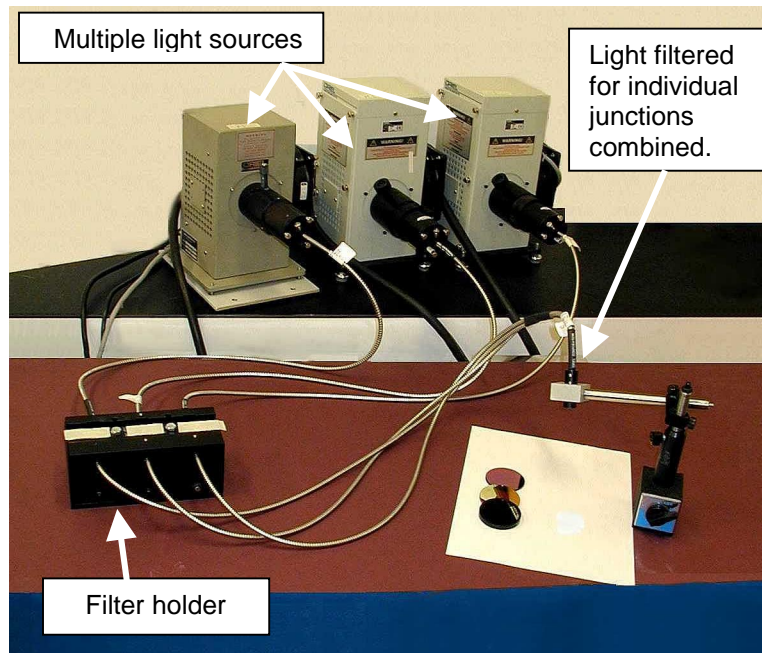


Figure 2. Several 250 W and 400 W light sources are available for light biasing the non-current limit junctions during a quantum efficiency measurement. Each source is coupled to the filter holder by optical fiber bundle where it tailored to the response range of single junction. Then, each filtered beam combined to a single optical fiber bundle and focused on the test device.

The quantum efficiency of each junction is measured by light biasing all other junctions to insure that they are not current limiting. To this end, we employ a set of independent light sources, each of which can be filtered to provide bias light in the wavelength response range of one junction. The light from each source and filter combination is collected and combined into a fiber optic cable to yield a continuous beam that is applied to the test device. A less intense monochromatic beam in the wavelength response range of the desired junction is simultaneously applied (figure 1). The continuous sources are iteratively increased until the chopped signal, as detected by a lock-in amplifier, no longer increases. A voltage bias may be applied to insure that the desired junction is operating near zero volts. Figure 2, above, shows the hardware used to provide the light bias to the non-current limiting junctions.

ONE SUN CURRENT VERSUS VOLTAGE MEASUREMENT

The NREL method for measuring the one sun current versus voltage focuses on modifying the simulator spectrum so that the photocurrent for each junction exactly (to within 1%) matches the photocurrent that would be expected under the desired reference spectrum, and then collecting a single set of current versus voltage data.

NREL adapted the single junction measurement procedures developed in 1984 [1], and subsequently adopted by various groups, and simultaneously applies them to each junction of a multi-junction device [2]. The procedure calls for adjusting the spectrum of the solar simulator, with the aid of a spectral mismatch correction, M_i , for each junction, until the each junction is operating at its proper photocurrent [3].

If the relative spectral response for each junction of the test device and a corresponding matched reference cell are known, and the relative spectral irradiance of the simulator is known, then the following equation holds for each test device junction or reference cell under the reference or simulator spectrum:

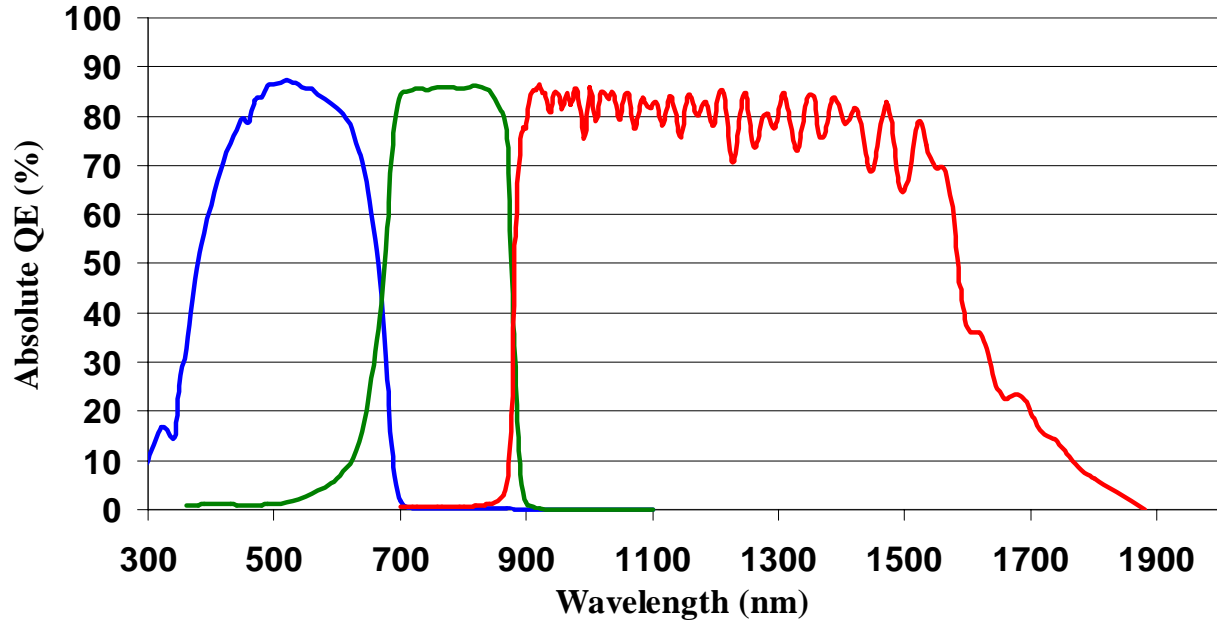


Figure 3. Absolute QE of GaInP/GaAs/Ge measured using light bias apparatus shown if figure 2.

$$I_{junction}^{spectrum} = \phi^{spectrum} \xi_{junction} \int_{\lambda 1}^{\lambda 2} \tilde{\Phi}^{spectrum}(\lambda) \tilde{Q}_{junction}(\lambda) d\lambda \quad (1)$$

where Φ is the photon flux, Q is the quantum efficiency, *spectrum* refers to either the simulator spectrum (*sim*) or reference spectrum (*refspec*), *junction* refers to a particular junction of the device under test (*test, j*) or a reference cell corresponding to a particular junction (*ref, j*). Symbols with a tilda (~) are relative so that scaling factors give

$$\Phi = \phi \tilde{\Phi} \quad \text{and} \quad Q = \xi \tilde{Q} . \quad (2)$$

The aim is to generate the same photocurrent under the simulator spectrum as under the reference spectrum for each junction, j , so from equation 1,

$$\frac{\phi^{sim}}{\phi^{refspec}} = \frac{\int_{\lambda 1}^{\lambda 2} \tilde{\Phi}^{refspec}(\lambda) \tilde{Q}_{test,i}(\lambda) d\lambda}{\int_{\lambda 1}^{\lambda 2} \tilde{\Phi}^{sim}(\lambda) \tilde{Q}_{test,i}(\lambda) d\lambda} . \quad (3)$$

The reference cell current may be different under the reference spectrum and simulator spectrum, so

$$\frac{I_{ref,i}^{sim}}{I_{ref,i}^{refspec}} = \frac{\phi^{sim}}{\phi^{refspec}} \frac{\int_{\lambda 3}^{\lambda 4} \tilde{\Phi}^{sim}(\lambda) \tilde{Q}_{ref,i}(\lambda) d\lambda}{\int_{\lambda 3}^{\lambda 4} \tilde{\Phi}^{refspec}(\lambda) \tilde{Q}_{ref,i}(\lambda) d\lambda} . \quad (4)$$

Substituting equation 3 into equation 4 gives

$$I_{ref,i}^{sim} = I_{ref,i}^{refspec} / M_i \quad (5)$$

where

$$M_j = \frac{\int_{\lambda_2}^{\lambda_1} \tilde{\Phi}^{sim}(\lambda) \tilde{Q}_{test,i}(\lambda) d\lambda \int_{\lambda_3}^{\lambda_4} \tilde{\Phi}^{refspec}(\lambda) \tilde{Q}_{ref,i}(\lambda) d\lambda}{\int_{\lambda_2}^{\lambda_1} \tilde{\Phi}^{refspec}(\lambda) \tilde{Q}_{test,i}(\lambda) d\lambda \int_{\lambda_3}^{\lambda_4} \tilde{\Phi}^{sim}(\lambda) \tilde{Q}_{ref,i}(\lambda) d\lambda} \quad (6)$$

for each junction.

Satisfying equation 5 for all junctions simultaneously is an iterative process. First, adjust the simulator spectrum. Second, measure the simulator spectrum and calculate the spectral mismatch, M_i for each test device junction. Third, measure the currents for each junction's corresponding reference cell. Repeat until equation 5 is satisfied. When equation 5 is satisfied, current versus voltage data representing the reference spectrum conditions may be generated under the simulator spectrum.

The simulator spectrum is adjusted by placing filters in front of the nineteen lenses at the exit of our Spectrolab model X25 lamp housing. Each filter or stack of filters for a particular port is carefully selected to transmit light in the response range of only one junction. If the filters are selected improperly then an attempt to adjust the beam intensity for one junction may change the intensity in another junction, greatly increasing the number of iterations and time required for the measurement. The shattering of filters due to the heat load is a serious problem. Many of the colored glass filters are specially tempered and the filters are cooled by blowing N_2 on the back and blowing a fan on the front.

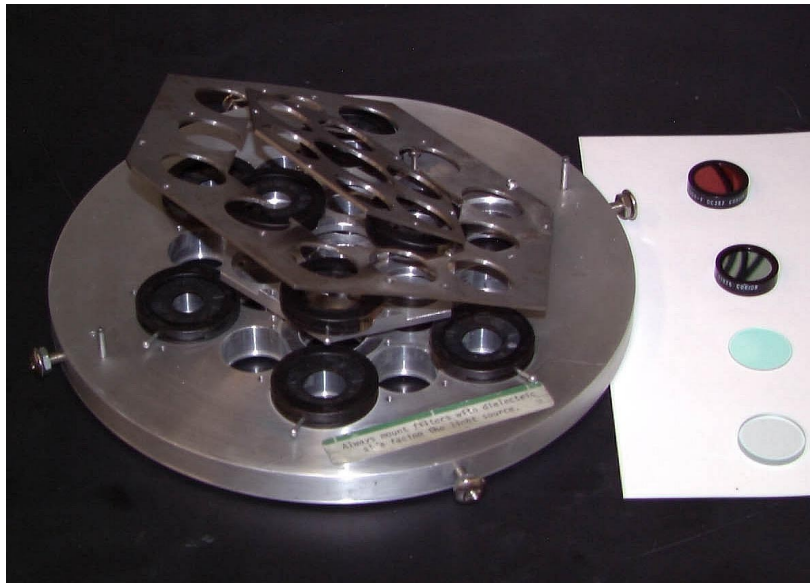


Figure 4. This filter holder fits over the exit of the Spectrolab X25 light source. Filters or stacks of filters may be placed over the nineteen exit lenses. Apertures can be placed over a maximum of ten of the filter stacks. Stacks of filters are chosen so that the transmitted light falls in the wavelength response range of only one junction.

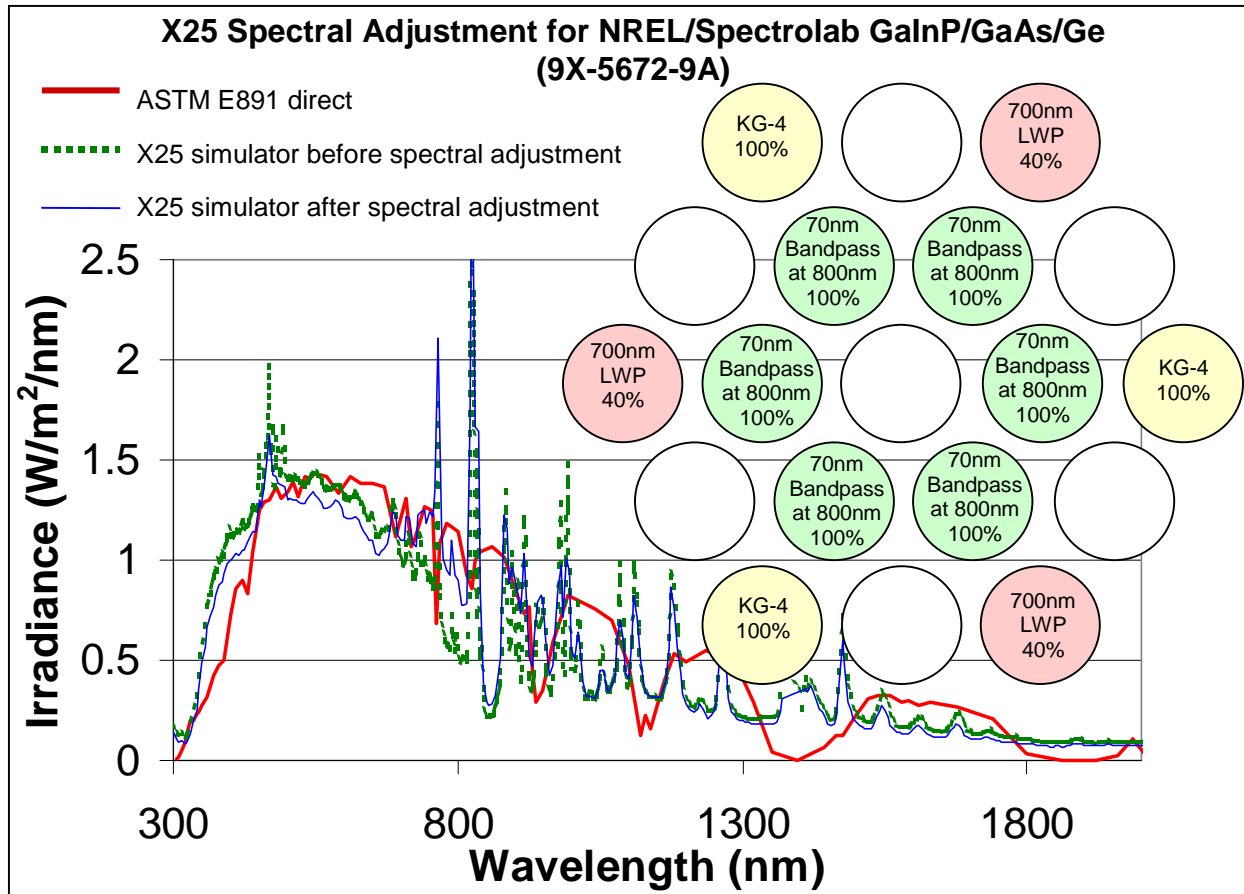


Figure 5. Filter layout for the nineteen X25 exit ports for a GaInP/GaAs/Ge cell and the resulting spectrum change. In this case only one filter was used per port. In some cases as many as three filters are stacked over some ports. [4]

CONCENTRATOR MEASUREMENTS

NREL uses a Spectrolab High Intensity Pulsed Solar Simulator (HIPSS) for concentrator measurements. It can generate up to 2000 suns during its approximately 1ms pulse. Concentration is adjusted by apertures below the lamps and by varying the lamp voltage.

At present concentration is not directly measured with a reference cell, but rather, linearity is assumed and concentration is approximated by $I_{sc}/(\text{one sun } I_{sc})$. Then, efficiency is given by:

$$\eta = \frac{I_{SC(1sun)}}{I_{SC}} \times \frac{P_{max}}{P_{max(1sun)}} \times \eta_{(1sun)} \quad (9)$$

Without calibrated reference cells, linearity is verified by noting that if device I_{sc} is proportional to E_{tot} , then

$$\frac{I_{SC,i}}{I_{SC,j}} = \alpha = \frac{E_{tot,i}}{E_{tot,j}} \quad (10)$$

where $E_{tot,j}$ is the integrated irradiance at the j^{th} intensity. So, for a given α , a plot of $I_{sc,i}/I_{sc,j}$ vs $I_{sc,j}$ should be a line with zero slope and intercept α . A non-zero slope would serve as an indicator of non-linearity. In

practice, α is set by selecting two lamp voltages, while i and j are varied by changing the flash housing shutter width. Or alternatively, α is set by selecting two flash housing shutter widths, while i and j are varied by changing the lamp voltage. Note that this procedure is not a correction for non-linearity, only an indicator of its presence. Figure 3 shows a sample of linearity check data from a Spectrolab GaInP/GaAs/Ge cell.

LIMITATIONS OF CURRENT METHODS AND PLANNED IMPROVEMENTS

Ideally, when the test device quantum efficiency is used to adjust the simulator spectrum (by satisfying equation 5 for each junction) it should be measured with an additional light bias that puts the DC current near that expected during the current versus voltage measurement. At this time NREL does not add that additional bias light. This is a problem if the quantum efficiency is a function of total irradiance. There are multiple reasons why adding this additional light bias is difficult.

All the problems of measuring the current versus voltage of a cell under continuous concentration as well as problems unique to the quantum efficiency measurement pertain. The first difficulty is simply achieving, say, 100 suns continuous concentration over a square centimeter while maintaining a reference temperature (usually 25° C). The noise component of a bias light at 100 suns may be hundreds of times stronger than the desired monochromatic signal, consuming lock-in dynamic reserve. There is also the problem of preventing any of the bias light from making its way back to the chopper and ultimately being mistakenly detected as part of the chopped monochromatic beam. At NREL we are working on a new quantum efficiency measurement system to deal with these problems. It will include a high throughput for the monochromatic beam and a low noise bias light system.

Current versus voltage measurements under concentration is another place where we have limitations and plans for improvement. Unlike the one sun measurements using the Spectrolab X25, we do not currently adjust the spectrum of our flash simulator so that each junction of a multi-junction device

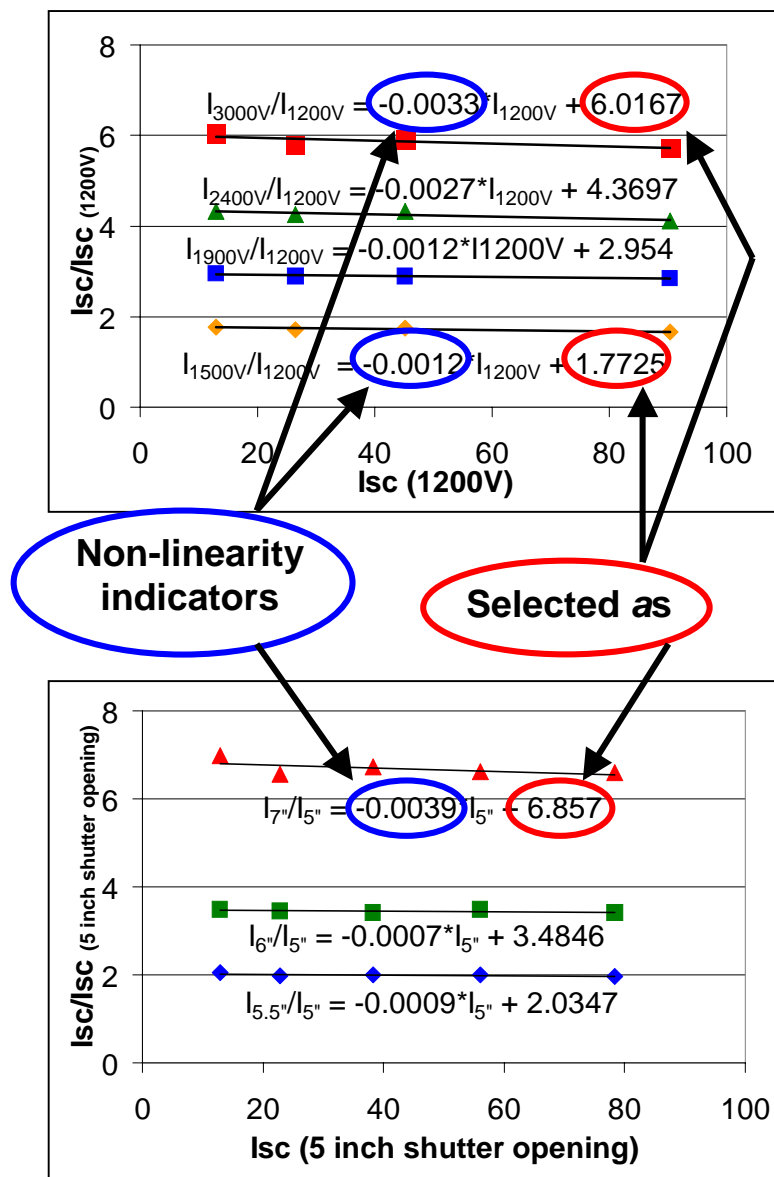


Figure 6. Two sets of linearity data for the same triple junction device. Each line on the top graph was generated by measuring I_{sc} at a set of different shutter openings but always at the same two lamp voltages. Each line in the bottom graph was generated by measuring I_{sc} at a set of different lamp voltages but always at the same two shutter openings. [4]

generates its expected photocurrent under the reference spectrum at the desired total irradiance. We are considering methods of placing filters near the flash lamps to adjust the spectrum while maintaining spatial uniformity. Even if we had the ability to adjust the spectrum of the flash simulator we could not carry out a concentrator version of the iterative process, mentioned above for the one sun measurements, because we have not found a practical way to measure the spectrum of the 1ms flash simulator pulse out to 2 microns with adequate wavelength and temporal resolution in a reasonable amount of time. At a minimum, the simulator spectrum could be adjusted to insure the proper junction was current limiting. Matched reference cells (one is needed for each junction of the test devices) calibrated as a function of total irradiance would allow us to bypass measurement of the simulator spectrum with each filter adjustment because the spectral mismatches (equation 6) would all be unity. However, calibration of the matched reference cells as a function of total irradiance introduces its own set of problems.

CONCLUSION

The methods for determining the quantum efficiency and current versus voltage characteristics for one sun multi-junction devices are well established at NREL. Given enough lead time to acquire the proper filters for each junction, a one sun measurement requires about two man days. Concentrator devices pose greater problems. We can perform accurate concentrator measurements of devices that do not exhibit changes in quantum efficiency with total irradiance and for which the current limiting junction under the reference spectrum is the same as the current limiting junction under the flash simulator spectrum. Light bias current densities need to be increased during quantum efficiency measurements to levels the device would see under concentration. A technique for adjusting the flash simulator's spectrum and a process for calibrating reference cells matched to each of a test devices junctions out to the total irradiances of interest needs to be implemented.

REFERENCES

- [1] K.A. Emery, C.R. Osterwald, T.W. Cannon, D.R. Myers, J. Burdick, T. Glatfelter, W. Czubytyj, and J. Yang, "Methods for Measuring Solar Cell Efficiency Independent of Reference Cell or Light Source," *Proc. 18th IEEE Photovoltaic Spec. Conf.*, Las Vegas, NV, October 21–25, 1985, pp. 623–628, IEEE, New York, 1985.
- [2] T. Glatfelter and J. Burdick, "A Method for Determining the Conversion Efficiency of Multiple-Cell Photovoltaic Devices," *Proc. 19th IEEE Photovoltaic Spec. Conf.*, New Orleans, LA, 1987, pp. 1187–1193
- [3] K.A. Emery, "Multi-Junction Amorphous Silicon Solar Cell Calibrations and Testing," *Proc. of the 1989 Amorphous Silicon Contractors Review meeting*, June 19-20, 1989, pp. 253-262
- [4] Moriarty, T.; Emery, K. (2000). Procedures at NREL for Evaluating Multi-junction Concentrator Cells. Program and Proceedings: NCPV Program Review Meeting 2000, 16-19 April 2000, Denver, Colorado. BK-520-28064. Golden, CO: National Renewable Energy Laboratory; pp. 71-72
- [5] Cotal, H. L.; Lillington, D. R.; Ermer, J. H.; King, R. R.; Karam, N. H.; Kurtz, S. R.; Friedman, D. J.; Olson, J. M.; Ward, S.; Duda, A.; Emery, K. A.; Moriarty, T. (2000). Highly Efficient 32.3% Monolithic GaInP/GaAs/Ge Triple Junction Concentrator Solar Cells. Program and Proceedings: NCPV Program Review Meeting 2000, 16-19 April 2000, Denver Colorado. BK-520-28064. Golden, CO: National Renewable Energy Laboratory; pp. 111-112
- [6] Emery, K; et al., "Efforts Underway to Measure the Efficiency of a Multi-junction Concentrators with an Uncertainty of Less Than $\pm 3\%$," First International Conference on Solar Electric Concentrators, 29-31 October 2001, Marbella, Spain. To be published.

UPDATE ON THE DISPLACEMENT DAMAGE DOSE MODEL FOR PROTON DAMAGE IN GALLIUM ARSENIDE SOLAR CELLS

S. R. Messenger and E.A. Burke
SFA, Inc., Largo, MD 20774

G.P. Summers and R.J. Walters
Naval Research Laboratory, Code 6818, Washington, DC 20375

ABSTRACT

An update is given of some details of the displacement damage dose (D_d) approach for predicting solar cell degradation in space, with the emphasis being on proton damage effects in GaAs solar cells, especially at very high and very low energies. High energy protons with $E > 15$ MeV and low energy protons with $E < 0.1$ MeV are found to give relatively small contributions to the overall device degradation.

INTRODUCTION

The use of the displacement damage dose (D_d) model for correlating radiation effects [1,2] is finding wide use in the space solar cell community. The power of the approach is that the energy dependence of the relative damage coefficients can be determined from a calculation of the nonionizing energy loss (NIEL) rather than from time-consuming and expensive experiments. Once the characteristic degradation curve is determined for a particular solar cell technology from measurements made at only one or two energies, damage predictions can be made for any other particle energy or for a spectrum of energies, such as that found in space.

Figure 1 shows data taken from the GaAs Solar Cell Radiation Handbook [3] for the relative proton damage coefficients (RDCs), normalized at 10 MeV, for the short circuit current (I_{sc} , denoted by solid squares) and both the maximum power and open circuit voltage (P_{max} and V_{oc} , respectively, denoted by solid triangles). The data points in Fig. 1 were determined from actual radiation measurements, while the lines through them were obtained by interpolation and extrapolation. It should be noted that these data are for normally incident protons on uncovered cells.

Also plotted in Fig. 1 are results for nonionizing energy loss (NIEL) calculations for protons in GaAs. It can be seen that the energy dependence of the NIEL and the RDCs is similar from ~ 0.05 MeV to ~ 15 MeV. However, at lower energies the RDCs appear to deviate from the NIEL and decrease rapidly towards zero. At higher energies an interesting divergence occurs, with the RDCs for P_{max} and V_{oc} being larger than those for I_{sc} . The continuous line in Fig. 2 shows the total NIEL, which includes contributions from both elastic and inelastic interactions, whereas the broken curve shows only the contribution from elastic interactions. It can be seen that the RDCs for P_{max} and V_{oc} track the total NIEL curve, while the RDCs for I_{sc} track the curve elastic NIEL curve. It should be noted that several recent calculations of the NIEL for protons in GaAs have been made by other groups using more sophisticated models for the cross sections, etc. for both the elastic and inelastic parts of the calculation. These calculations give results that are in close agreement with our original calculations over the whole energy range shown in Fig. 1 [4].

HIGH ENERGY PROTONS

The deviation of the relative damage coefficients from the NIEL in GaAs solar cells at high energies shown in Fig. 1 has also been seen in certain other parameters for other GaAs-based opto-electronic devices, as shown in Fig. 2 [5]. The data set in Fig. 2 represented by X's are normalized lifetime damage coefficients for GaAs diffused junction LEDs [6]. This data set, showing the energy dependence of the RDCs to be less than that which the total NIEL predicts, has been reproduced several times on similar devices. The data set represented by solid circles are recent lifetime damage coefficients for GaAs-based quantum well laser diodes (QW LEDs) [7].

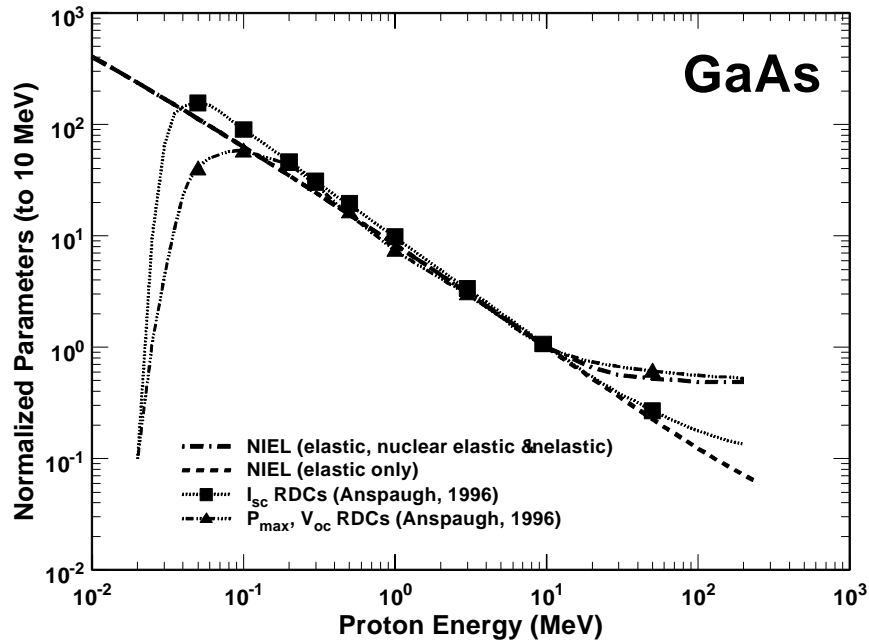


Figure 1. GaAs solar cell proton relative damage coefficients (RDCs) [3] and normalized NIEL calculations [1] plotted as a function of proton energy. The NIEL and RDCs are in close agreement over a large proton energy range. The deviations between the RDCs and the NIEL at very high and very low energies are discussed in the text. Note that the RDCs are for the incident proton energy.

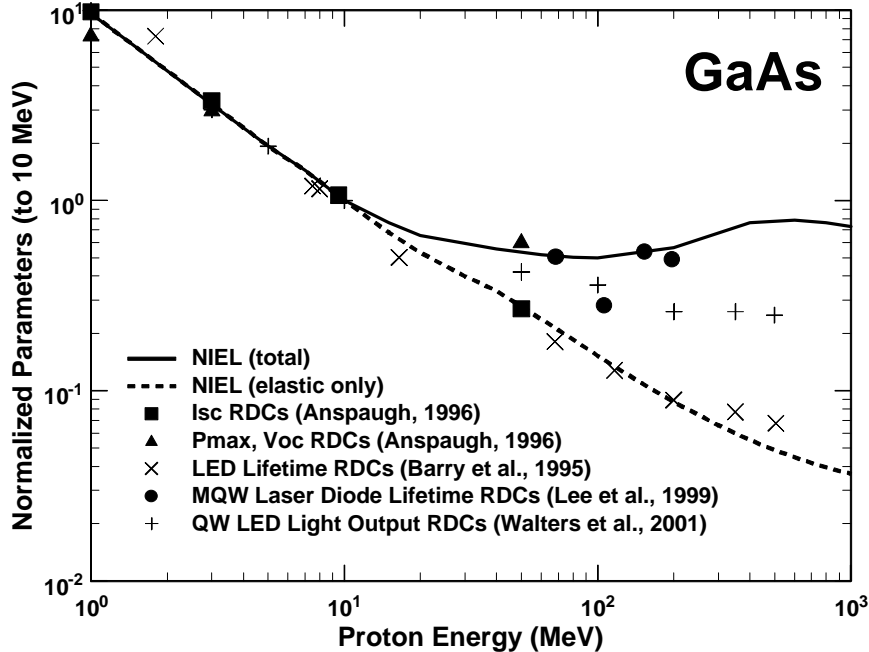


Figure 2. Comparison of proton damage coefficients measured in various opto-electronic devices with the calculated NIEL, normalized at 10 MeV. All the data shown at proton energies >10 MeV are bounded by the curve representing the total NIEL (including elastic and inelastic interactions, solid line) and the elastic NIEL (broken line).

The new data for the relative damage coefficients for the light output of QW LEDs [5] is very interesting in that they fall in between the curves for the total and elastic NIEL. Whether this behavior is related to the particular way that charge motion leads to radiative recombination in these particular devices is presently under investigation.

The results presented above raise an important question about how much high energy protons contribute to the overall degradation of solar cells in a typical space mission. This is important because, if the energy dependence of the damage coefficients at high energies for a particular parameter cannot be determined with certainty from a measurement made at a lower energy, the overall calculation of the displacement damage dose, and hence the overall expected cell degradation, could be in error. To investigate this question we calculated the expected D_d and expected end-of-life (EOL) degradation for a particular mission using both the total NIEL and the elastic NIEL in the integral. The case chosen was for a 5000 km circular, 60° inclination, orbit and for a mission lasting one year. Five different thicknesses of silica coverglass were considered ranging from 3 to 30 mils. The results are shown in Table I. It can be seen in Table 1 that the calculated values for the EOL fractional degradation in cell efficiency in all cases are different only in the third significant figure, i.e., at most less than one part in 350.

Table I. Effect of NIEL on GaAs D_d calculation for 5000 km, circular, 60° , 1 year mission. Difference in the D_d are negligible when using either the total or elastic NIEL. The units of D_d are MeV/g.

SiO ₂ Thickness(mils)	D_d (total NIEL)	Fractional Degrad. (total NIEL)	D_d (elastic NIEL)	Fractional Degrad. (elastic NIEL)
30	4.774e9	0.800	4.750e9	0.800
20	1.209e10	0.698	1.213e10	0.697
10	4.422e10	0.539	4.457e10	0.538
6	9.068e10	0.448	9.146e10	0.447
3	1.958e11	0.349	1.975e11	0.348

Figure 3 shows the cumulative fraction of the total D_d plotted as a function of proton energy. Note that the energy here is the slowed-down energy of a proton emerging from the back of the coverglass into the active region of the cell. When plotted in this way, one can see how different energies contribute to the total value of D_d . For variety, the space proton spectrum used for Fig. 3 is for a large solar proton event such as occurred in October, 1989. Three silica coverglass thicknesses were chosen in the analysis (3, 12, and 60 mils). For the 3 mil coverglass case, proton energies having $E > 10$ MeV contribute less than 2% to the total D_d . In general, for typical coverglasses used in space missions, proton energies greater than about 15 MeV can be seen to contribute very little to the total value of D_d .

LOW ENERGY PROTONS

The contribution of low energy protons to the total value of D_d can also be seen in Figure 3. Again, for the 3 mil coverglass case, protons having $E < 0.1$ MeV are shown to contribute ~25% of the total D_d . For 12 mil coverglasses, the contribution is only ~12%. Protons of these energies are, thus, not the most damaging part of the spectrum contributing to the cell degradation. It should be recalled that these results include protons that actually stop in the cell. Even though such particles individually produce substantial damage (due to higher NIEL values), in total they contribute relatively little to the overall cell degradation.

CONCLUSIONS

In the D_d methodology for determining space solar cell degradation, there are several components. One needs: 1) the space radiation spectrum of interest, 2) the slowed-down spectrum, 3) values of the NIEL, and 4) the characteristic radiation degradation curve for the parameter of interest, eg. P_{max} . Of these four components, the NIEL calculation was the one that this paper addressed. This was due primarily to investigate the behavior at high proton energies where the energy dependences of the damage coefficients for various device parameters were different. A trend exists suggesting a possible explanation for the results, i.e., that the energy dependence

of the damage coefficients for the depletion region related parameters track the total NIEL, while those for bulk related parameters track the elastic NIEL. Regardless, the effect of protons having $E > 15$ MeV involved in the D_d model for GaAs space solar cell degradation for typical missions was shown to be very small, only contributing a few percent to the total degradation. This fact will greatly simplify future calculations in the D_d analysis, since only the simple, elastic interaction needs to be included in the NIEL calculation.

Similarly low energy protons ($E < 0.1$ MeV) also contribute only a small amount to the overall cell degradation.

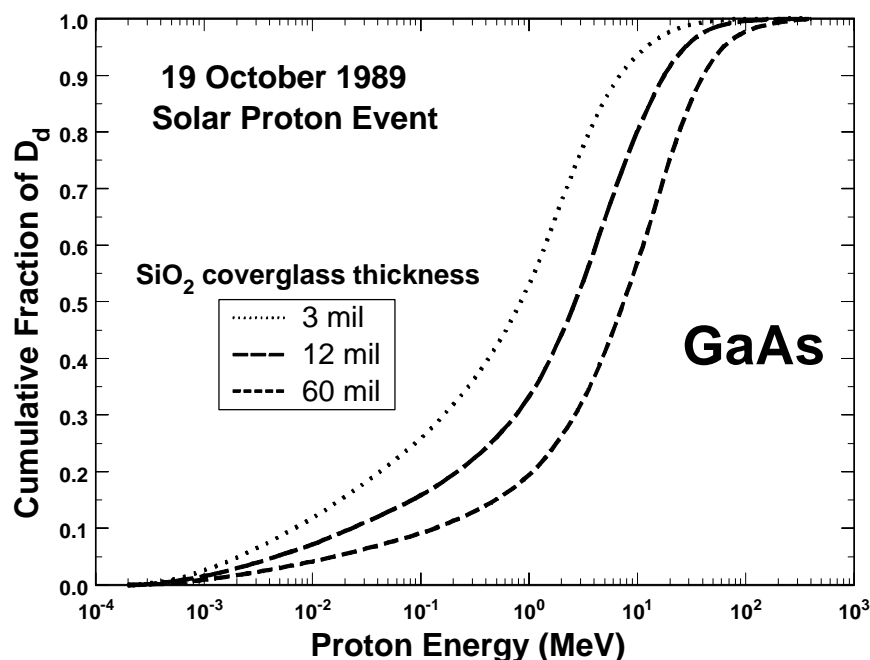


Figure 3. Energy dependence of the cumulative fraction of the displacement damage dose (D_d) in GaAs due to slowed-down protons exposed to a solar proton event like that of October 1989 after passing through silica coverglasses of thickness 3, 12, and 60 mils, respectively.

REFERENCES

- [1] G.P. Summers *et al.*, "A New Approach to Damage Prediction for Solar cells Exposed to Different Radiations", *Proceedings of the 1st IEEE World conference on Photovoltaic Energy Conversion*, Waikoloa, Hawaii, 2068-2075, December 1994.
- [2] S.R. Messenger *et al.*, "Modeling Solar Cell Degradation in Space: A Comparison of the NRL Displacement Damage Dose and the JPL Equivalent Fluence Approaches", *Progress in Photovoltaics: Research and Applications*, Vol. 9, 103-121 (2001).
- [3] B. E. Anspaugh, *GaAs Solar Cell Radiation Handbook*, JPL Publication 96-9, July 1, 1996
- [4] A. Akkerman *et al.*, "Updated Niel Calculations for Estimating the Damage Induced by Particles and Gamma-Rays in Si and GaAs", to be published in *Radiation Chemistry and Physics*, 2001.
- [5] Walters *et al.*, "Correlation of Proton Radiation Damage in InGaAs/GaAs Quantum Well Light Emitting Diodes", *IEEE Trans. Nucl. Sci.*, December 2001 issue.
- [6] A.L. Barry *et al.*, "The Energy Dependence of Lifetime Damage Constants In GaAs LEDs for 1-500 MeV Protons", *IEEE Trans. Nucl. Sci.*, Vol. 42, 2104-2107 (1995).
- [7] Lee *et al.*, "Comparison of Lifetime and Threshold Current Damage Factors for Multi-Quantum-Well (MQW) GaAs/AlGaAs Laser Diodes Irradiated at Different Proton Energies", *IEEE Trans. Nucl. Sci.*, **42**, 1797 (1995)

BOEING'S HIGH VOLTAGE SOLAR TILE TEST RESULTS

Brian J. Reed and David E. Harden;
Boeing Phantom Works; Seattle WA 98124

Dr. Dale C. Ferguson and Dr. David B. Snyder;
NASA Glenn Research Center; Cleveland, OH 44135

Abstract

Real concerns of spacecraft charging and experience with solar array augmented electrostatic discharge arcs on spacecraft have minimized the use of high voltages on large solar arrays despite numerous vehicle system mass and efficiency advantages. Boeing's solar tile (patent pending) allows high voltage to be generated at the array without the mass and efficiency losses of electronic conversion. Direct drive electric propulsion and higher power payloads (lower spacecraft weight) will benefit from this design. As future power demand grows, spacecraft designers must use higher voltage to minimize transmission loss and power cable mass for very large area arrays. This paper will describe the design and discuss the successful test of Boeing's 500-Volt Solar Tile in NASA Glenn's Tenney chamber in the Space Plasma Interaction Facility. The work was sponsored by NASA's Space Solar Power Exploratory Research and Technology (SERT) Program and will result in updated high voltage solar array design guidelines being published.

I. Introduction

The power source for virtually all satellites is photovoltaic solar arrays. They are critical to the satellite's operation and often are a limiting parameter in a satellite's mission capability and operational lifetime. The solar array's intrinsic fragility, exposure to harsh free-space environment, and a desire for minimizing solar array mass, stowage volume, and deployed area all place severe constraints on solar array design. As future power demands grow spacecraft designers must use higher voltage to minimize transmission loss and power cable mass for very large area solar arrays. Spacecraft mass and cost sensitivity encourages large area solar arrays to generate as well as distribute high-voltage.

High-voltage, high-power arrays in various earth orbits are subject to continuous arcing, which can destroy conductors and lightweight substrates. Arcing can become catastrophically augmented by solar array string currents to physically destroy solar array strings. Space plasma charging, auroral charging, electrodynamic effects, and sputtering or electron heating cause discharge arcs that waste power and can lead to power surges and solar array destruction. In the past 5 years, the loss of several spacecraft from on-orbit solar array failures and more recent evidence of electrostatic-discharge-induced, solar array augmented, arc failures demonstrates the importance of robust high voltage solar array design. Recently, interactions between high voltage solar arrays and their space environment has led to an increased understanding of spacecraft charge arcing on the solar array. Higher spacecraft cost, longer duration environmental exposure, and higher mission criticality has resulted in a higher reliability requirements being placed on each subsystem. Designers have (correctly) responded with more conservative approaches including lower voltages, below Paschen Law voltages, or by incorporating added system elements, such as the plasma contactor to "ground" the Space Station. This paper reports on one of an increasing body of work that pushes technology to solve the high voltage design issue.

II. Project Overview

The work reported here is a result of collaboration between engineers at NASA Glenn Research Center and Boeing, Seattle working under NASA's Space Solar Power Exploratory Research and Technology (SERT) Program. SERT focused well beyond 100kW to develop enabling technologies for new applications in space science, exploration, and commercial applications. Specifically, space solar power (SSP) generation and transmission to earth electric power users. The economic viability of very high power in space depends on the successful development of various new technologies, such as high-voltage solar arrays. These solar arrays are not only required for SSP, but could also be used for large high-power spacecraft, distributed spacecraft concepts, solar electric propulsion systems (SEPS), space-based radar, and space-based laser systems. This contract entitled "Advanced High Voltage Solar Array Design Guidelines from Solar Tile Testing" uses a Boeing solar tile design to characterize and extend high voltage design guidelines for the industry. Specifically, The Boeing/GRC team used a previously produced 34-Volt solar tile (ST) to perform plasma interaction tests using the NASA GRC Tenney vacuum chamber in the Plasma Interaction Facility. The results were used to design a high voltage tile. A new 500V solar tile was designed and manufactured, and has been tested in the Tenney chamber. These results will be used to update the solar array design guidelines. This paper reports the test results prior to the development and publication of those design guidelines.

III. Solar Tile Features

Boeing's solar tile, typically about 1 ft², features tightly packed, multi-junction solar cells, under a common coverslide, interconnected with Kapton®/copper flexible circuitry. Robotics allows solar cells to be rapidly and precisely placed, with very small cell-to-cell gaps, resulting in a very high cell packing factor (98%). Batch vapor phase soldering simplifies cell interconnection; development of coplanar cell contacts allows use of Kapton®/copper flexible circuitry instead of fragile discrete interconnects. Along with lower fabrication cost, the single coverslide provides superior plasma charge, atomic oxygen, and radiation protection during on-orbit operation. The solar tiles can be produced over a wide range of voltages and sizes, using various solar cell types. In addition to supporting standard spacecraft voltages, the tiles are ideally suited for high-voltage applications such as direct-drive electric propulsion. Since the solar tiles can be built to supply full bus voltage, the power ratings for the solar arrays can be achieved by connecting the required number of solar tiles in parallel.

Because it's single coverslide covers entire (bus voltage) circuits and it's coverglass is conductively coated and grounded, the Solar Tile offers excellent protection to high voltage arcing and from any environmental interaction. It is "cell-technology independent", utilizes high production-rate robotics cell placement for low assembly and no tooling cost. Boeing's Solar Tile concept is shown in figure 1. It illustrates the front and rear side of a typical solar tile. Mechanical cells were used in this early production version. It has been low-earth orbit qualified in acoustic, shock, thermal cycle and thermal vacuum cycling tests.

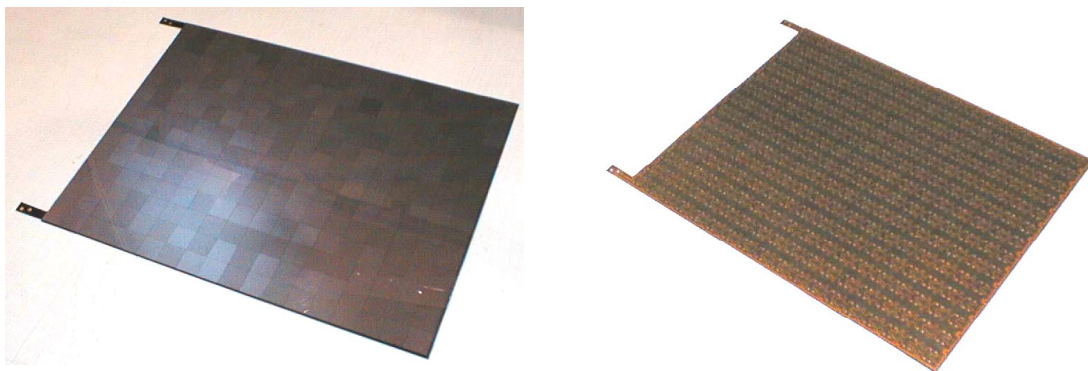


Figure 1: Front and Back views of a typical solar tile

IV. Methodology

The Boeing/GRC team utilized models of the existing 34V solar tile design to assess high-voltage susceptibility. A NASA Glenn team then performed plasma interaction tests on the Solar Tile using the NASA GRC Tenney vacuum chamber in the Plasma Interaction Facility. During testing, we will introduce a high-voltage electrostatic discharge (ESD) event-driven failure of the high-voltage solar tile. A fast switching shunt or other undefined device may be able to isolate or discharge the failure mechanism before the fault has a chance to cause permanent damage. Figure 2 shows the test facility. The background chamber was used and had the physical test setup as shown in Figure 3.



Figure 2. The Tenney Plasma Interaction Facility

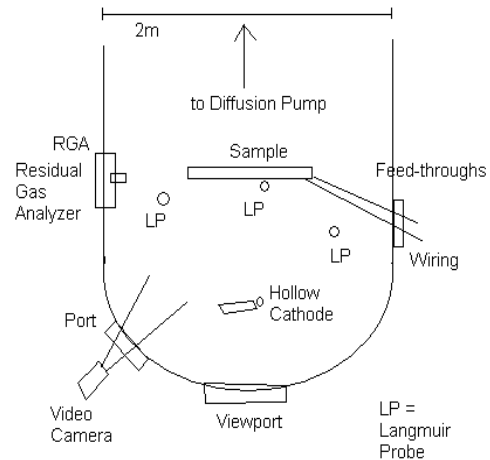


Figure 3. Chamber Test Setup

The results were used to expand and update our knowledge regarding high-voltage solar array design guidelines. The Boeing/GRC team tested the existing 34V solar tile design to assess high-voltage susceptibility. The Solar Tile design features of a large single conductively coated coverslide, large coverslide overhang. Coverglass grounding to the substrate provide a substantial improvement to high voltage solar array space environment tolerance. It is pictured in Figure 4.

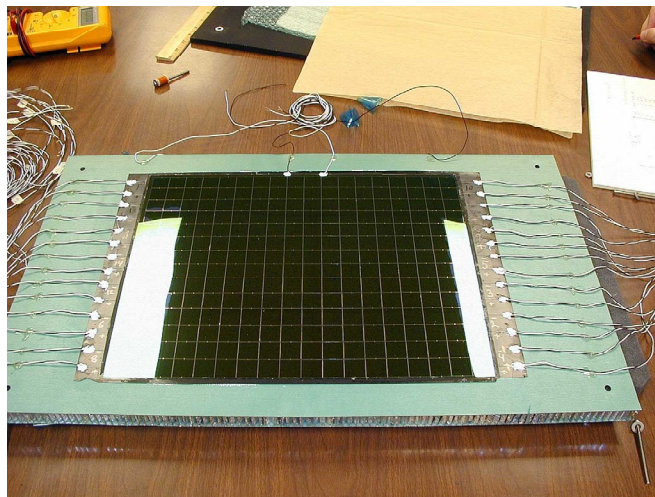


Figure 4: The 34-volt Test Article

The test article is a single solar tile measuring 11 by 14 inches mounted on a lightweight rigid substrate. There were four overhang dimensions on the test article, and the least damage at very high plasma voltage exposure was the largest overhang. The overhang was “filleted” to the substrate with coverglass bonding adhesive in each case.

V. Test Results

The plasma test results with high offset cell string voltages indicate that these 34-volt solar arrays will work at the -850-Volt plasma voltage. Two isolated plasma flashovers occurred up to -950 volts and continuous arcing commenced around -1000volts.

The observations during testing can be summarized as follows. The 34-Volt test sample arced once at -300 V on right-hand coverslide edge. Later, the sample arced once at -650 V somewhere on right hand coverslide (flash was so bright it blinded the video). In over six hours of additional testing at voltages between -300 V and -950 V, no arcs occurred anywhere. At -1000 V, numerous small arcs occurred at the edge of the kapton backing. Currents between biased and unbiased strings were greater than anticipated, although no arcs were seen. When biased at -1000 V, cells in many solar array strings glowed from forward bias current.

It must be noted that the coverslide lay-up not standard, left side of coverslide cracked under rapid vacuum pumpdown. Figure 5 shows the coverslide crack and the -650V arc event sites.

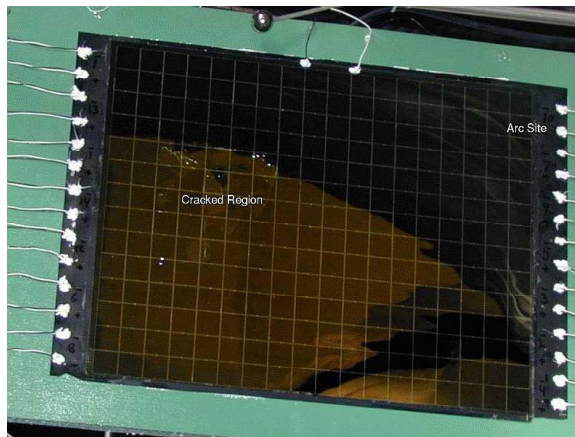


Figure 5: 34-Volt Tile after plasma testing

An extensive development effort isolated the multiple root causes. Boeing built many samples and tiles to both demonstrate causality and to verify the process steps needed to prevent the reoccurrence and “qualified” the new manufacturing steps and resulting tile. The new steps were incorporated into the 500-Volt solar tile processing and no coverglass debonding or cracks occurred at any time. Figure 6 shows the 500-Volt tile.

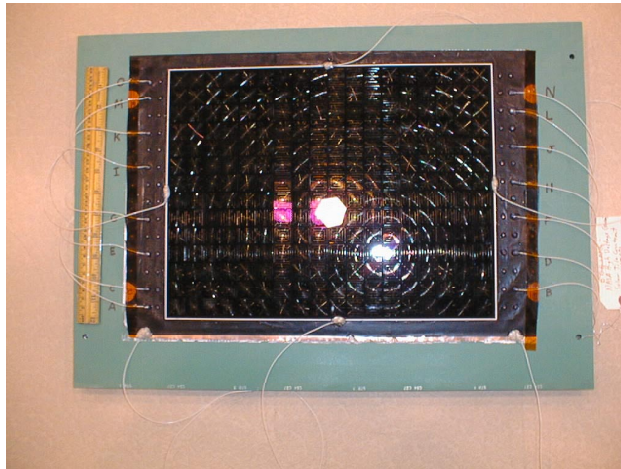


Figure 6: 500-Volt solar tile prior to plasma testing

The results of the 500-Volt Solar Tile test are summarized as follows. The sample arced once at –600 Volts. Figure 7 shows the sequence of four video frames that show the arc occurrence at –600 Volts. The top left frame is the pre-arc condition and the three other frames show the flashover and quench in clockwise direction. Some halo discharges became visible at approximately –750Volts. Leakage current was observed on the face of the Kapton®/copper flex circuit. No electrical performance degradation was measured or physical damage observed following exposure up to the (approximate) -1100Volt test limit.

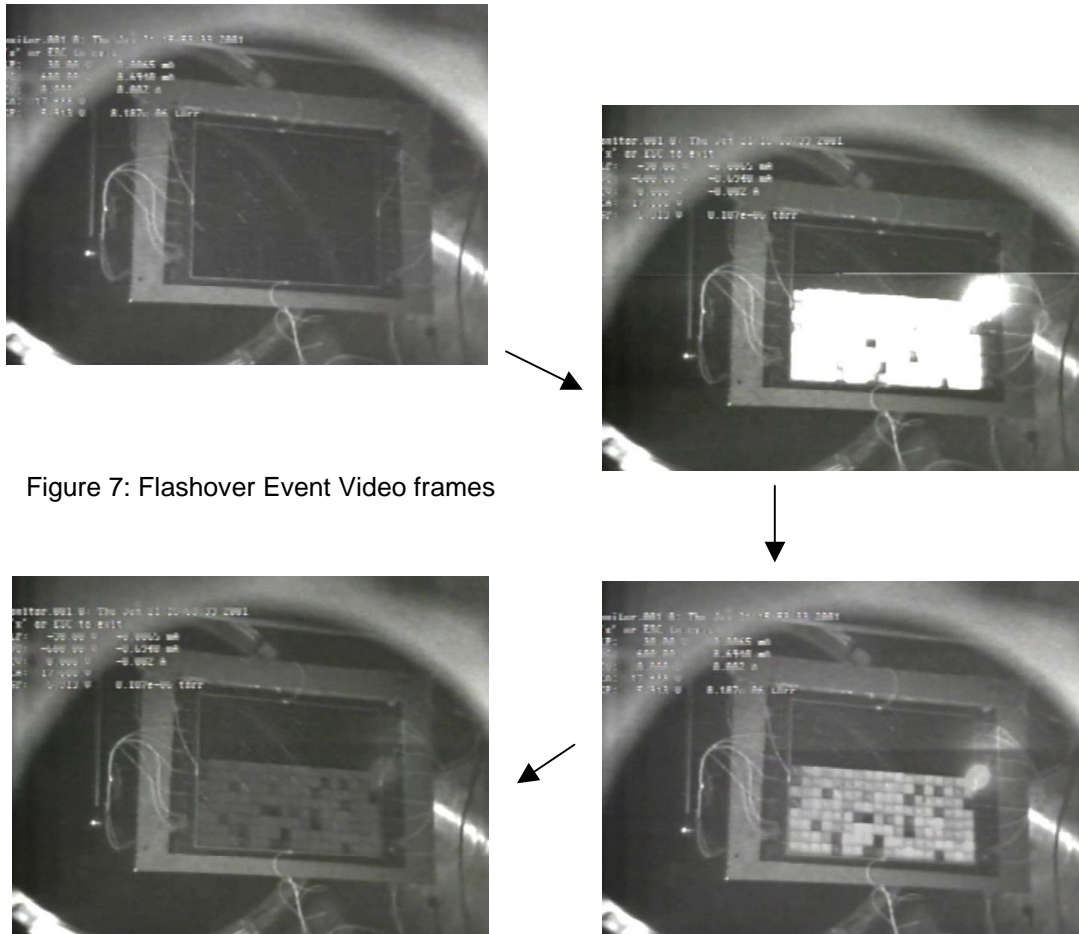


Figure 7: Flashover Event Video frames

VI. Conclusion

In conclusion, the high voltage solar tile design exceeded our 500-Volt testing goals because the solar tile withstood a worst-case low earth orbit (LEO) potentials between surfaces of the solar tile using simulated space plasma in GRC Plasma Interactions Facility. Determined the arc thresholds for Solar Tile at voltages of 600 V or more, relative to the plasma. We demonstrated 500-Volt solar tile tolerance to plasma charging

The one-time arcs may be attributed to H₂O evolution from adhesive or defect burning because they only occurred once.

Lastly, the solar tile is “flight ready” for direct drive electric propulsion applications.

In summary, the design and successful test of Boeing’s 500-Volt Solar Tile in NASA Glenn’s Plasma chamber indicates that the road to very high space power and direct drive electric propulsion is clearly open to further successful development.

PROTON AND ELECTRON RADIATION DATA AND ANALYSIS OF GaInP₂/GaAs/Ge SOLAR CELLS

P. R. Sharps, D. J. Aiken, M. A. Stan, C. H. Thang, and Navid Fatemi
EMCORE Photovoltaics
10420 Research Road SE
Albuquerque, NM 87112

ABSTRACT

We present electron and proton radiation data for our GaInP₂/GaAs/Ge triple junction solar cell. An analysis of the data is also done with both the “relative damage coefficients” (RDC) method developed at NASA-JPL [1], as well as the “displacement damage dose” (D³) method developed by the Naval Research Lab [2]. We also discuss radiation tolerance of cells in the light of our development of an advanced triple junction cell.

INTRODUCTION

A space solar cell's end-of-life (EOL) performance is a key parameter for array designers. The EOL performance depends on both the beginning-of-life (BOL) performance, as well as the degradation that the cell undergoes due to exposure to a radiation environment. Development programs for space solar cells should always focus on optimizing for EOL performance. At EMCORE Photovoltaics, we have been working for the last three years not only on improving III-V multi-junction cell BOL performance (i.e., achieve the highest BOL efficiency), but also on improving the EOL/BOL performance ratio. A separate talk in this conference will present performance data from our GaInP₂/GaAs/Ge advanced triple junction cell. In this paper we present an analysis of radiation data on our GaInP₂/GaAs/Ge triple junction cell, as well as thoughts on developing radiation tolerant advanced cells. We previously have presented an analysis of radiation data for our initial GaInP₂/GaAs dual junction cell, using both the JPL RDC approach and the NRL D³ approach [3]. While both methods have been shown to be equivalent [4], there are advantages and disadvantages to each approach. This paper is an extension of that work. Based on the lessons learned in the radiation testing of the dual junction cell, we modified the radiation testing of the current triple junction cell. The number of irradiations using low energy mono-energetic protons was increased, as was the energy range for the electrons.

EXPERIMENT

Figure 1 shows a schematic of the GaInP₂/GaAs/Ge triple junction cell that was used in this study. The cell has been in commercial production for about a year. The cell has the n-on-p polarity, and was designed for optimized performance at EOL, defined as exposure to 1 MeV electrons to a fluence of 1×10^{15} e/cm². At beginning of life (BOL), the cell is current limited by the GaInP₂ junction, while at EOL, the two junctions are current matched. As will be seen from quantum efficiency measurements, we actually optimized the cells for a fluence of 2×10^{15} e/cm², indicating that we were too limited by the GaInP₂ junction at BOL. The cells tested were 4 cm² in area, and did not have coverglasses.

The cells were measured at EMCORE Photovoltaics before and after irradiation with a calibrated, dual source solar simulator. The cells were irradiated to five fluences at each of 50 keV, 100 keV, 200 keV, 400 keV, 1 MeV, 2 MeV, and 10 MeV protons, and 1 MeV, 2 MeV, and 12 MeV electrons. All of the proton irradiations and the 1 and 12 MeV electron irradiations were done by JPL, while the 2 MeV electron irradiation was done by NRL. At least 12 cells were irradiated at each of the electron and proton energies and fluences. After

irradiation and prior to measurement in the solar simulator, the cells were annealed for 20 hours at 60 °C. All of the irradiations were done with unidirectional protons and electrons. We increased the low energy proton exposures, as well as the energy range of the electron exposures, compared to our dual junction radiation testing, in order to further test the applicability of the D³ approach.

Metal Grid	
n ⁺⁺ -GaAs Cap	AR Coatings
n ⁺ -AlInP ₂	Window
n ⁺ -GaInP ₂	Emitter
p-GaInP ₂	Base
p ⁺ -AlGaInP ₂	BSF
p ⁺⁺ -n ⁺⁺ High Bandgap Tunnel Diode	
n ⁺ -AlInP ₂	Window
n ⁺ -GaAs	Emitter
p-GaAs	Base
p-AlGaAs	BSF
p ⁺⁺ -n ⁺⁺ Tunnel Diode	
n-GaAs Buffer	
n ⁺ -Ge Emitter	
p-Ge Base and Substrate	
Back Contact	

Figure 1. Schematic of the GaInP₂/GaAs/Ge triple junction cell examined in this study.

RESULTS AND DISCUSSION

The degradation in the V_{oc} , I_{sc} , and P_{max} caused by the proton irradiation are shown in Figures 2, 3, and 4, respectively. The relative damage coefficients (RDCs) relative to 10 MeV protons are contained in Figure 5.

Voc Degradation vs. Proton Fluence

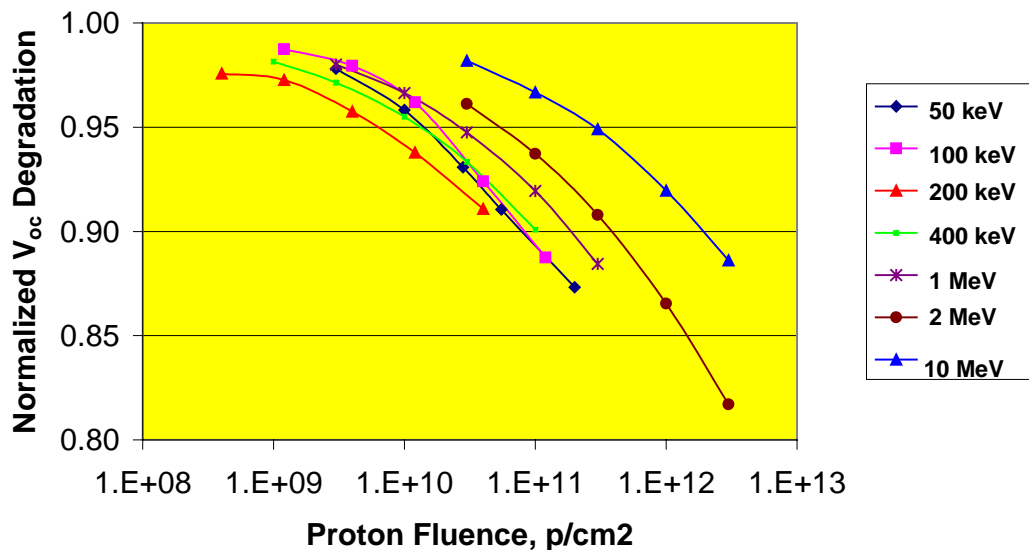


Figure 2. Degradation of the V_{oc} as a function of proton fluence, for various protons energies.

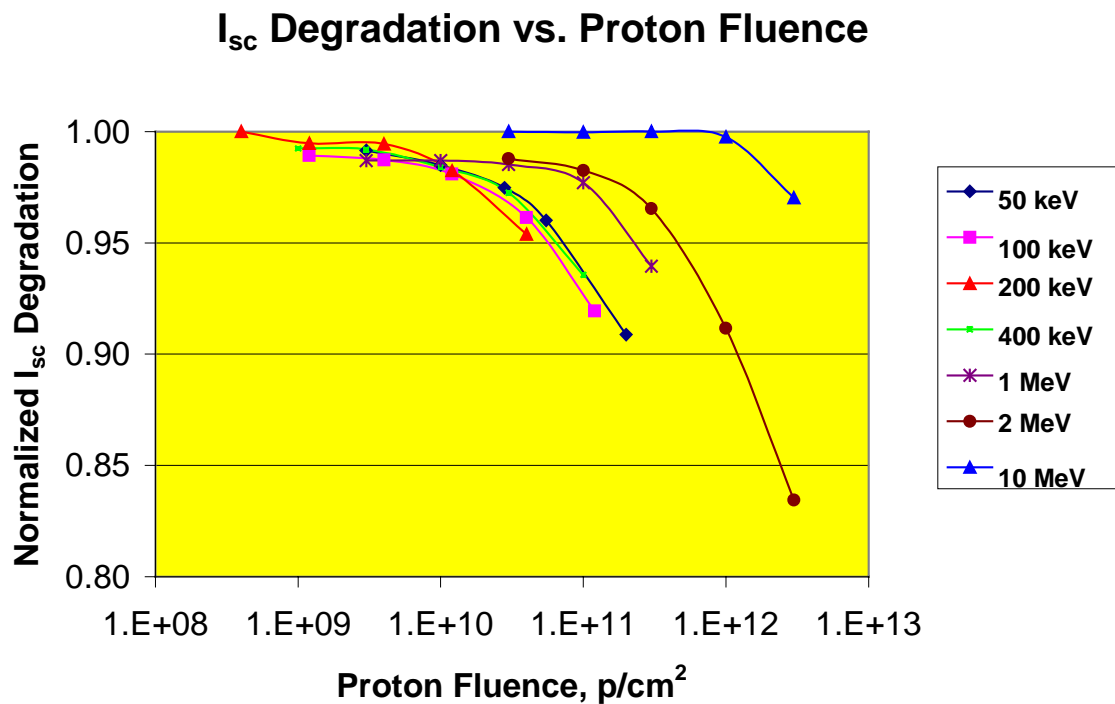


Figure 3. Degradation of the I_{sc} as a function of proton fluence, for various protons energies.

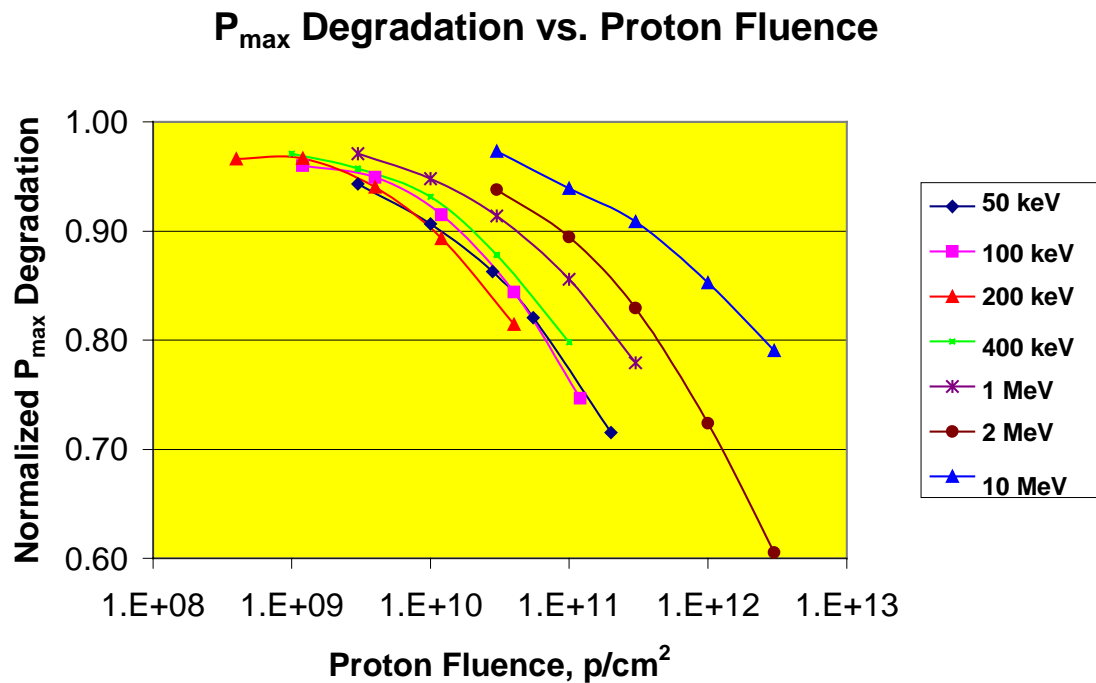


Figure 4. Degradation of P_{max} as a function of proton fluence, for various protons energies.

The RDC curves in Figure 5 show more detail than that for our previously published dual junction cell, particularly for the low energy protons. As can be seen, a single maximum in the RDC for V_{oc} , I_{sc} , and P_{max} occurs at a proton energy of 0.2 MeV. We do not see the dual maximum presented in a previous work [5].

We associate the single maximum with the 0.2 MeV energy to be due to the protons of this energy creating most of their damage in the GaInP₂ p-type base. The RDCs for the V_{oc} and P_{max} are similar to the numbers presented previously for an n-on-p triple junction cell, but our I_{sc} value at the peak is about 3 times as high as a previously published number. We believe that the difference is due to the present triple junction cell's design, particularly it's improved radiation hardness.

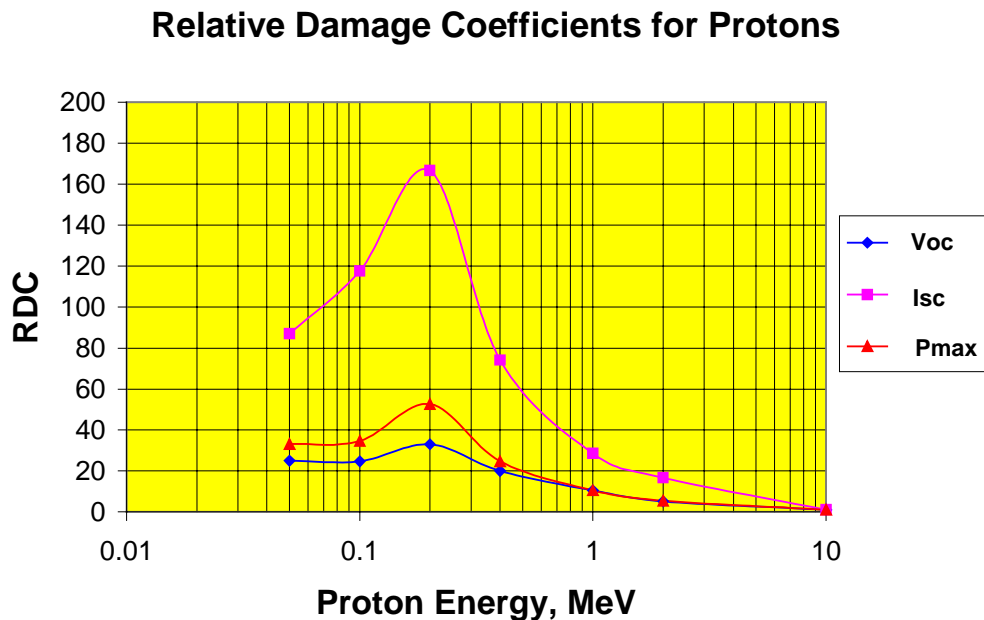


Figure 5. Relative damage coefficients for proton degradation of the triple junction cell.

The data from Figure 4 was converted to the displacement damage dose using the NIEL values and the formula presented in [2]. In order to make the calculation for the triple junction cell several assumptions had to be made. First, the triple junction cell was treated as a single entity, i.e., no special allowance was made for the three separate junctions. Some justification for this assumption comes from the cell being current limited by the GaInP₂ junction at beginning-of-life (BOL). Secondly, the NIEL value for GaAs was used, as there are no values for GaInP₂. The NIEL values for GaAs and InP are fairly close, hence the NIEL value for GaInP₂ should also be close to that for GaAs.

Figure 6 shows the reduction in P_{max} as a function of absorbed dose, for the proton radiation. All of the data for proton energies from 200 keV to 10 MeV collapses to a single curve. As noted previously [3], there is a divergence from the single curve for protons with energies less than 200 keV. The divergence occurs for energies lower than the maximum in the RDC curve, meaning that less relative damage occurs for energies below 200 keV. Part of the issue may be associated with the structure of the solar cell, i.e., there is an n-on-p junction in the device. The lower energies would have more of an effect on the emitter as compared to the base, and the damage generation in the n-type emitter may be different than that for the p-type base. The NIEL values are calculated for bulk material, and so the NIEL may not fully take into account nuances of structure. One solution may be fold in structure considerations in the calculation of the NIEL. Overall, it should be kept in mind that the discrepancy with the lower energy protons at most leads to a P_{max} degradation overestimation of about 1% [3].

Figure 7, 8, and 9 contain the degradation results for the V_{oc} , I_{sc} , and P_{max} as a function of electron fluence, for three different energies. There is independent confirmation of the 1 MeV electron radiation results. The Japanese Space Agency NASDA independently measured, irradiated, and remeasured a number of EMCORE triple junction cells. A comparison between NASDA's results and EMCORE's results is shown in Figure 10 for V_{oc} , I_{sc} , and P_{max} . There is quite good agreement over the fluence ranges that overlap. Note the P_{max} degradation numbers of 91% and 87% for 1 MeV electrons at fluences of 5×10^{14} and 1×10^{15} e/cm².

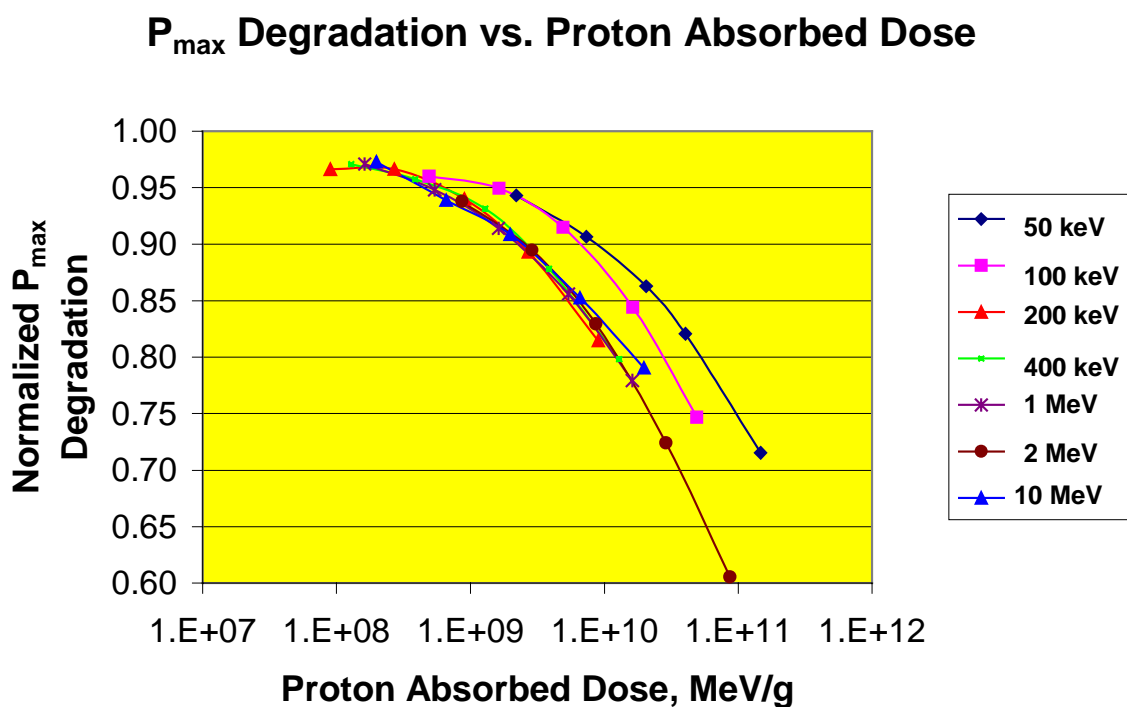


Figure 6. Power loss of GaInP₂/GaAs/Ge triple junction cell as a function of absorbed dose, for various proton energies.

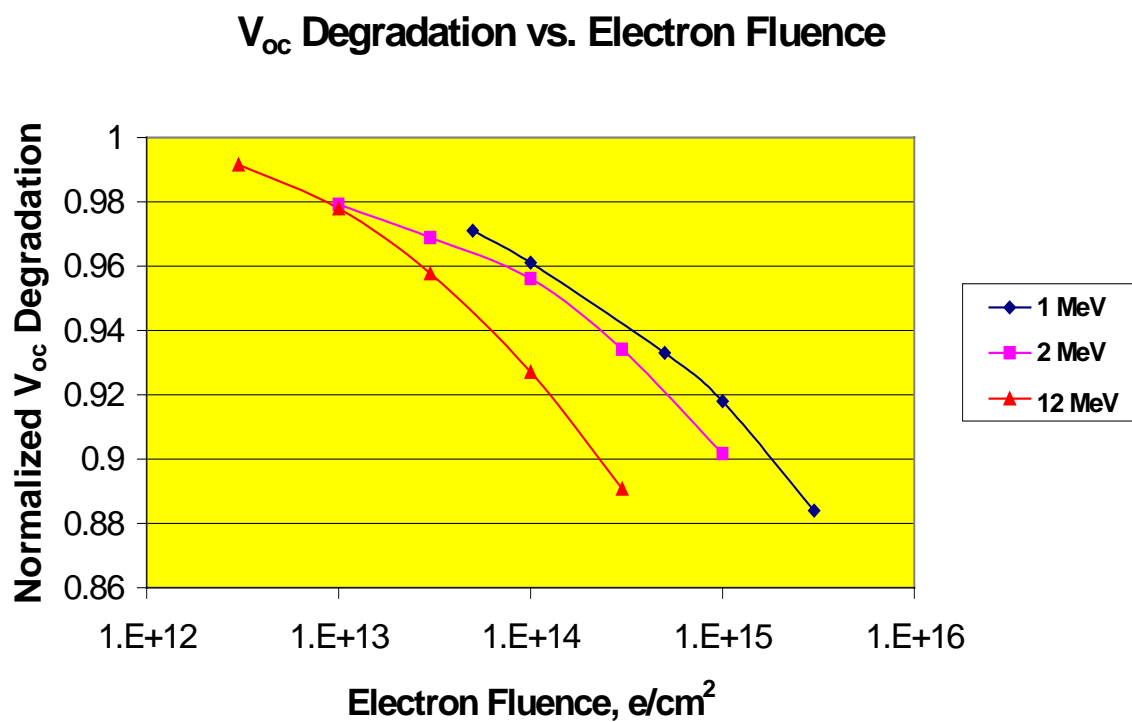


Figure 7. Degradation of the V_{oc} as a function of electron fluence for three electron energies.

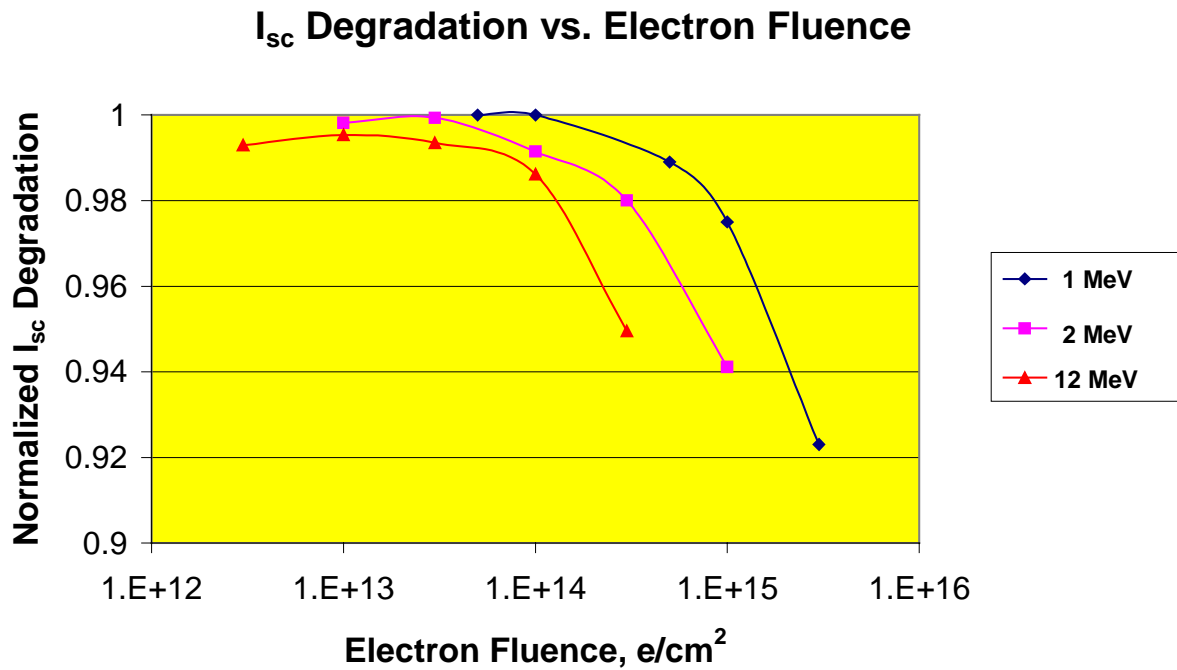


Figure 8. Degradation of the I_{sc} as a function of electron fluence for three electron energies.

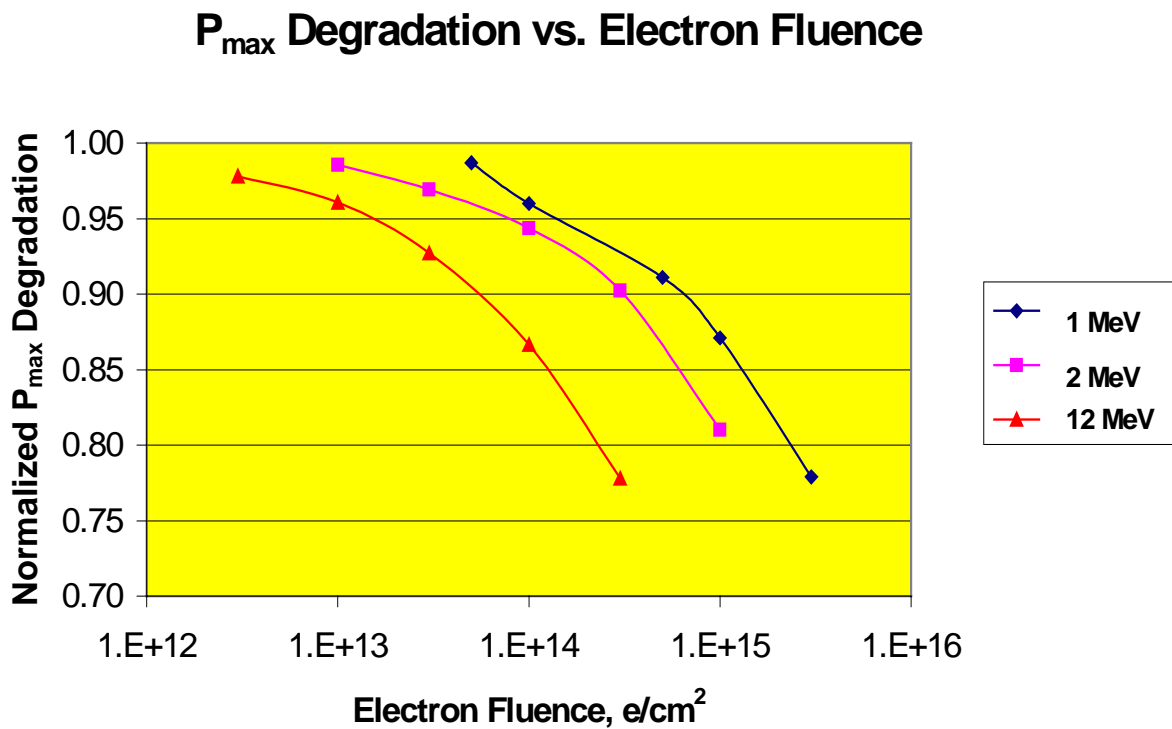


Figure 9. Degradation of P_{max} as a function of electron fluence for three electron energies.

Comparison of 1 MeV Electron Radiations

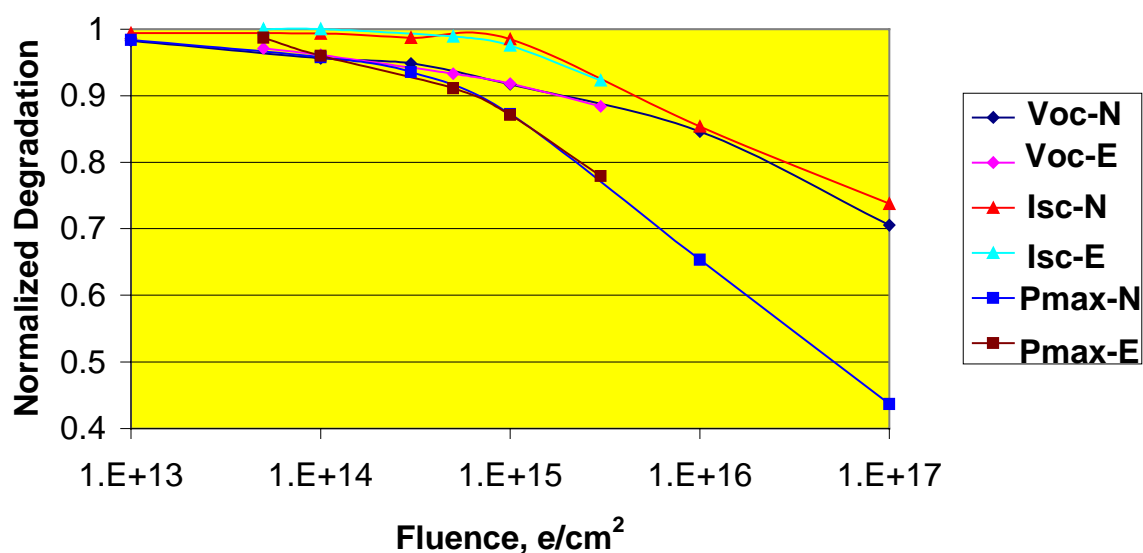


Figure 10. Comparison of EMCORE and NASDA V_{oc} , I_{sc} , and P_{max} degradation for the EMCORE triple junction solar cell.

Junction Current vs. Electron Fluence

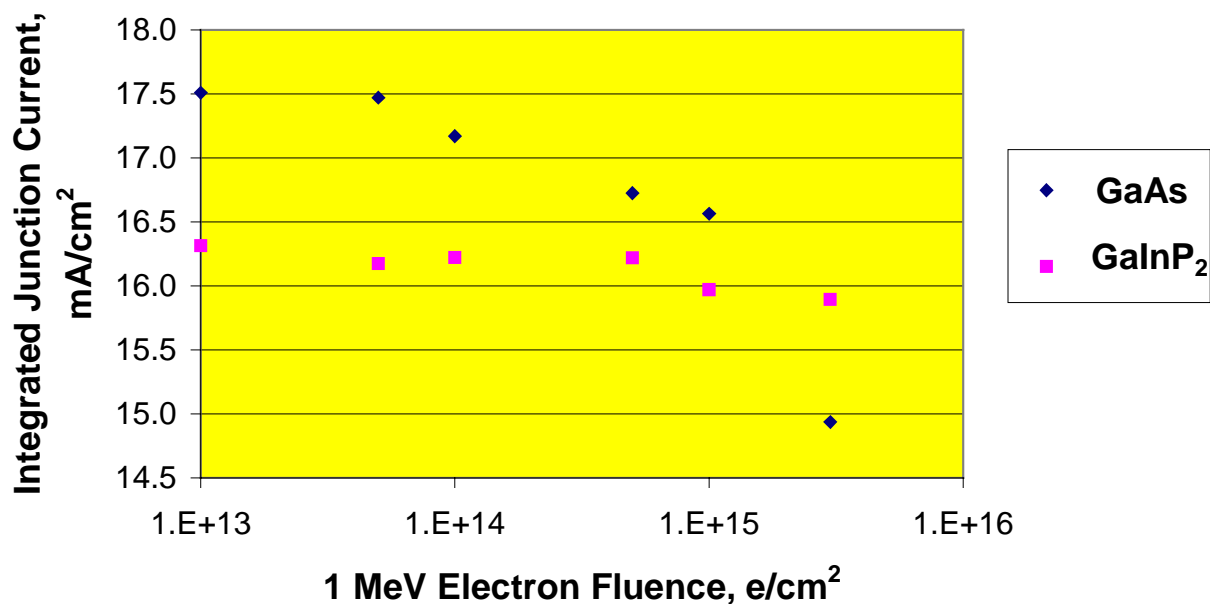


Figure 11. Current generated by GaInP₂ and GaAs junctions as a function of 1 MeV electron fluence.

Relative Damage Coefficients for Electrons

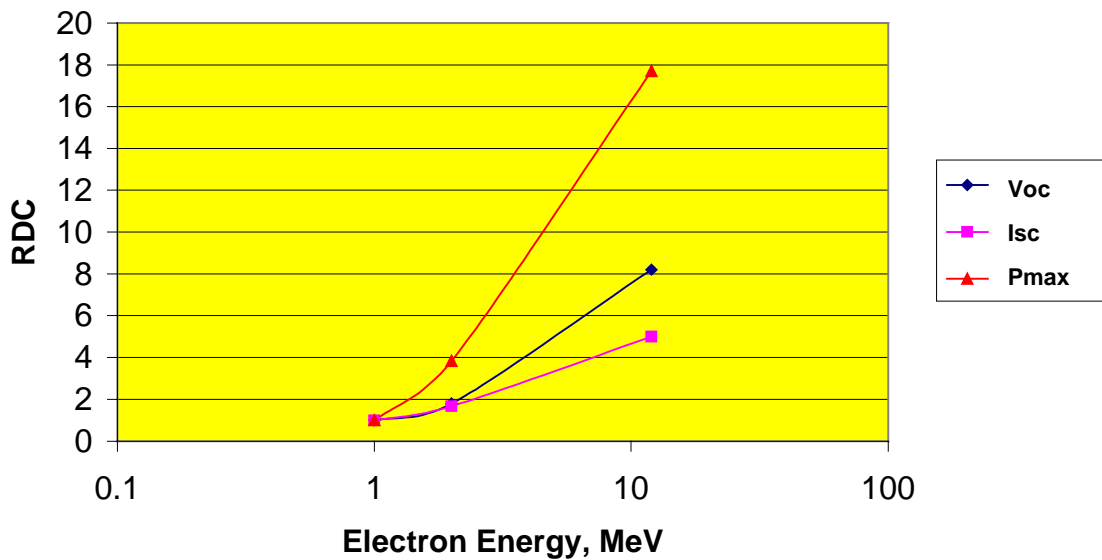


Figure 12. Relative damage coefficients for electron degradation of the triple junction cell.

Voc	Isc	Pmax
900	210	271

Table 1. Equivalent fluence factors for 1 MeV electrons and 10 MeV protons. The results are for 10% degradation of V_{oc} and I_{sc} , and for 20% degradation of P_{max} .

We have also further characterized the degradation of the cells irradiated with 1 MeV electrons by quantum efficiency measurements. In particular, we were interested in determining at what point the GaInP_2 and GaAs junctions are current matched. The results are shown in Figure 11. Each point in the plot is an average of measurements for three separate cells. The cross over from being top cell current limited to being bottom cell current limited occurs at about $2 \times 10^{15} \text{ e/cm}^2$, for the 1 MeV electrons. As mentioned previously, we had originally targeted the EOL as being at a fluence of $1 \times 10^{15} \text{ e/cm}^2$. The result is helpful in the design of the advanced triple junction (ATJ) cell, in determining the exact GaInP_2 junction base thickness. Thus we were able to reduce the amount of BOL current mismatch, which in turn increased our BOL efficiency for the ATJ.

RDCs for V_{oc} , I_{sc} , and P_{max} are shown in Figure 12. The 1 MeV electron/10 MeV proton damage equivalent fluence factors for 10% degradation of V_{oc} and I_{sc} , and for 20% degradation in P_{max} , are in Table 1, and are consistent with the results previously presented for our dual junction cell [3].

Using the displacement damage dose method for electron damage is more complicated than that for protons. This is because of the need to convert to an effective 1 MeV displacement damage dose [2]. Based on the lessons learned from the dual junction D^3 analysis, for the triple junction analysis we purposely chose three electron energies, at a wider spread in energy. Using the data from Figure 9, and through curve fitting (see [2]), we determined that the curve fit exponent “n-1” is 0.70. The resulting P_{max} degradation as a function of

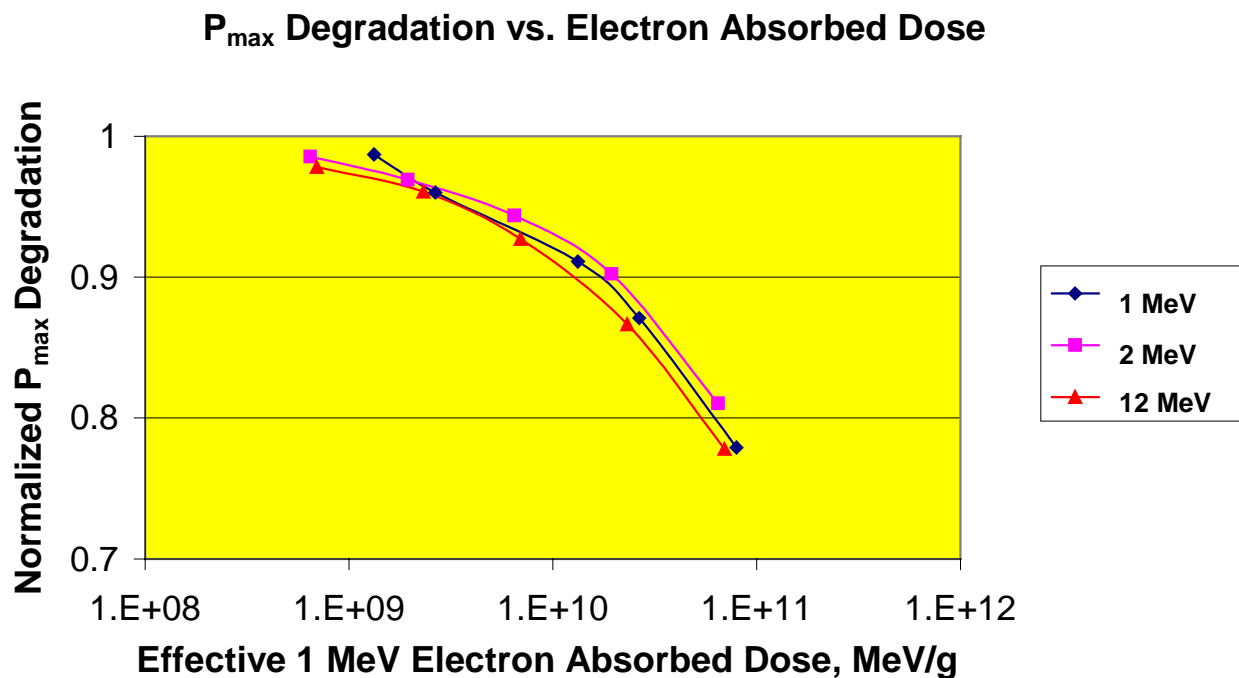


Figure 13. Degradation of P_{max} as a function of effective 1 MeV electron absorbed dose.

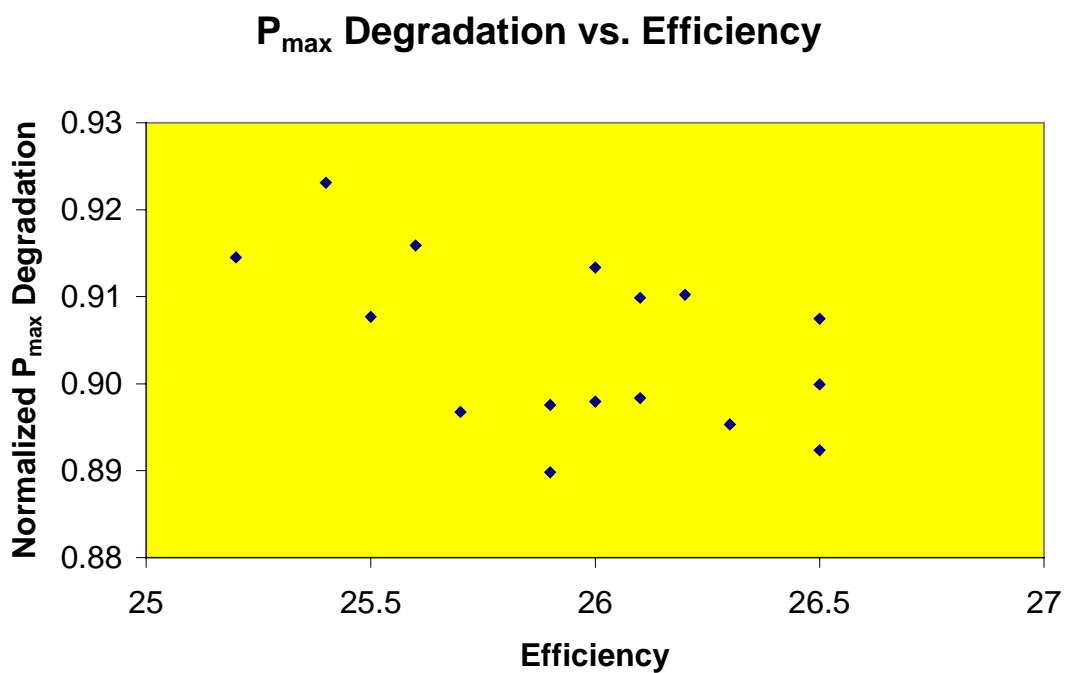


Figure 14. Variation of P_{max} as a function of efficiency, for exposure to 1 MeV electrons to a fluence of $5 \times 10^{14} \text{ e/cm}^2$.

effective electron absorbed dose is shown in Figure 13, using the effective 1 MeV electron absorbed dose. The curves for the electron energies do not merge as “nicely” as the curves for the proton energies greater than or equal to 200 keV. However, we estimate that using a “composite” curve for all of the energies, rather than the individual curves, would introduce about $\pm 1\%$ error, for the energy ranges in this study. While not large, we would like to see a further explanation of the variance for the different energies.

In the development of our ATJ, we have been mindful of the need to optimize for EOL performance. The improvements in BOL efficiency that are made to a device also have an effect on the radiation tolerance of a cell. For example, in going from a triple to a four junction device through addition of a 1.05 eV junction, the radiation tolerance of the 4J cell would stay the same relative to the 3J cell, provided that the fourth junction was as radiation tolerant as the GaInP_2 junction. On the other hand, if the efficiency of the 3J cell were improved through material quality improvements in the GaInP_2 junction, the radiation tolerance of the improved 3J device would be less than the radiation tolerance of the old 3J device. Incoming radiation would have a larger relative damage effect the better the quality of the material. An example of that can be seen for our current triple junction device. Figure 13 shows the degradation in P_{max} as a function of efficiency, for an exposure to 1 MeV electrons to a fluence of $5 \times 10^{14} \text{ e/cm}^2$. There is a general trend for the radiation tolerance to decrease as the efficiency of the device increases. This also points out the need when determining radiation degradation for a particular cell type to use representative cells from across the spectrum of the efficiency range.

For the ATJ, some areas of efficiency improvement have no effect on radiation hardness, while some improvements do. The overall goal, however, is to include the improvements that increase the EOL performance.

CONCLUSIONS

We have done a thorough study of the effect of electron and proton radiation on our $\text{GaInP}_2/\text{GaAs}/\text{Ge}$ triple junction solar cell. We have demonstrated a P_{max} EOL/BOL ratio of 91% and 87%, for exposure to 1 MeV electrons at a fluence of 5×10^{14} and $1 \times 10^{15} \text{ e/cm}^2$, respectively. The data was analyzed using both the NASA-JPL and NRL approaches. The method of analysis depends on the preference of the end users of the cells. The displacement damage dose method has advantages, but there are still issues, such as low energy protons, that need further resolution.

ACKNOWLEDGEMENTS

The authors would like to thank Dr. Bruce Anspaugh and Bob Weiss of JPL and Dr. Rob Walters of NRL for their assistance in irradiating samples.

REFERENCES

- [1]. B. E. Anspaugh, “Solar Cell Radiation Handbook-Addendum 1: 1982-1988”, *JPL Publication 82-69, Addendum 1*, 1989.
- [2]. G. P. Summers et al., Proceedings of the 1st World Conference of Photovoltaic Energy Conversion, 1994, pp. 2068-2075.
- [3]. P. R. Sharps et al., presented at the 27th IEEE PVSC, Anchorage, AK.
- [4]. G. P. Summers et al., 16th SPRAT Conference, August 1999.
- [5]. D. C. Marvin, “Assessment of Multijunction Solar Cell Performance in Radiation Environments”, *Aerospace Report No. TOR-2000(1210)-1*, 2000.

Comparison of the Electrical Performance of Various Amorphous Silicon Thin Film Solar Cells Produced for the PowerSphere Concept

Edward J. Simburger, Jasen Ross, James Matsumoto, Jean Baer and Nathan Presser

**The Aerospace Corporation
P.O. Box 92957 Mail Station M2-275
Los Angeles, Ca. 90009
(310) 336-7126 Fax: (310) 336-5846
E-mail: edward.j.simburger@aero.org**

**Frank R. Jeffery
Iowa Thin Film Technologies, Inc.
2337 230th. St.
Boone, IA 50036
(515) 292-7606 Fax: (515) 292-1922**

Abstract

The Aerospace Corporation has independently developed conceptual designs for microsatellites and nanosatellites. This development of microsatellites and nanosatellites for low earth orbits requires the collection of sufficient power for onboard instruments with a low weight, low volume spacecraft. Because the overall surface area of a microsatellite or nanosatellite is small, body-mounted solar cells are incapable of providing enough power. Deployment of traditional, rigid, solar arrays necessitates larger satellite volumes and weights, and also requires extra apparatus needed for pointing. One potential solution to this "power choke" problem is the deployment of a large, spherical, inflatable power system. This power system, termed the "PowerSphere", would offer a high collection area, low weight, and low stowage volume, and eliminate the need for a pointing mechanism.^{[1][2][3]} Figure 1 is a laboratory model of a PowerSphere populated with Iowa Thin Film Technologies (ITFT) Amorphous Silicon Solar Cells.

Development of a thin film amorphous silicon solar cell for the PowerSphere concept has focused on the impact that the size of an individual cell and top contact design has on the electrical performance of these cells. PowerSpheres ranging in size from approximately 7 inches in diameter to 2 feet in diameter are under investigation. Aerospace Corporation contracted with ITFT to produce amorphous silicon solar cells in hexagonal and pentagonal shapes with the sides of individual pentagons and hexagons ranging from 1 inch to 5 inches. These cells were fabricated with three different grid patterns using the stan-

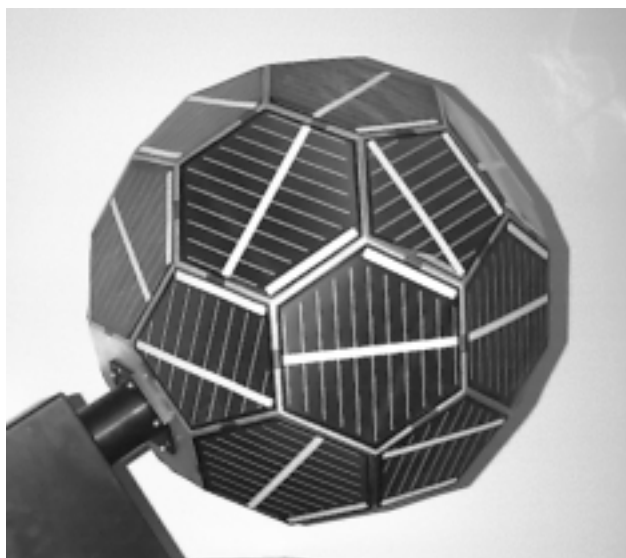


Figure 1. Laboratory Model of a PowerSphere Populated with ITFT Thin Film Solar Cells

Copyright 2001 The Aerospace Corporation. Printed with permission.

standard printed silver ink used for ITFT's standard terrestrial product.^{[4],[5]} In addition a number of cells were produced on which Aerospace vapor deposited silver metal contacts.

ITFT Thin Film Solar Cell Design and Fabrication

The ITFT thin film amorphous silicon solar cell is fabricated on a 2 mil thick Kapton substrate. The steps in the ITFT process are as follows:

1. Sputter aluminum on front side of kapton substrate and stainless steel on backside in roll-to-roll process.
2. Deposit amorphous silicon layers to produce a two-junction solar cell in a roll-to-roll process.
3. Laser scribe amorphous silicon solar cell to isolate individual cells.
4. Apply in a printing process an insulator to isolate individual cells.
5. Sputter zinc oxide on top of amorphous silicon layers as transparent top contact in a roll-to-roll process.
6. Laser scribe zinc oxide layer over insulator material to isolate front and back contacts.
7. Apply front contact.
8. Laser weld back contact pads on front of cell to back contact.
9. Encapsulate cells in a roll-to-roll process.
10. Cut out individual modules of series connected cells.

The cells produced with this process are capable of being series connected with a monolithic interconnection as shown in Figure 2.

Design Modifications of the ITFT Solar Cell for the PowerSphere

The PowerSphere in its present configuration is a Soccer Ball or Buckey Ball.^[6] The maximum dimension of one side of an individual hexagon or pentagon, which make up the PowerSphere, is five inches. This size of hexagon fits well on the 12-inch wide web used in the ITFT process. The full 12-inch width of the web cannot be used and ITFT recommends that the one-inch along each edge of the web not be used for best performance.

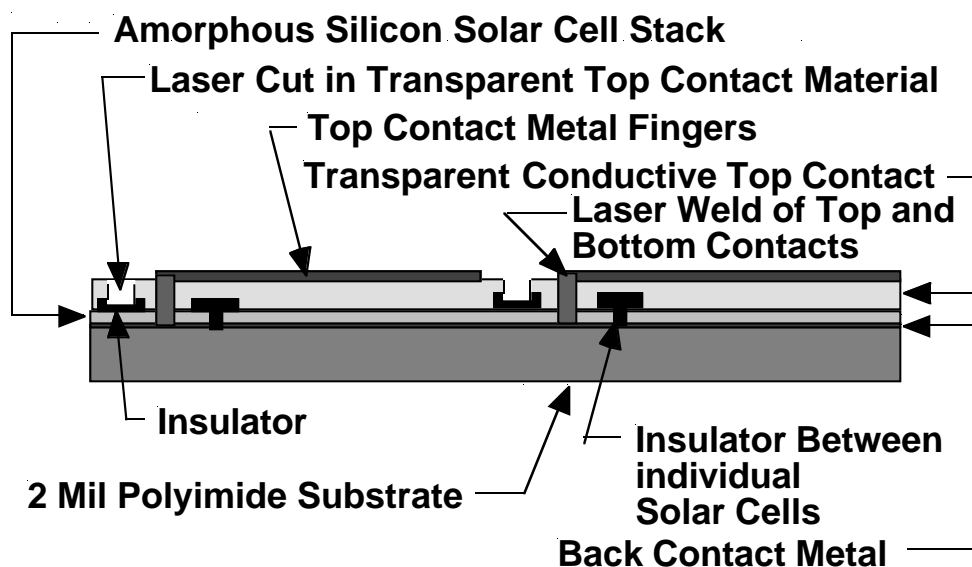


Figure 2. Thin Film Solar Array with Monolithic Interconnects

Since each of the 32 hexagonal and pentagonal panels will be receiving different levels of insolation, series connection of cells from different panels is not possible. With the monolithic integration scheme offered by the ITFT process it would be possible to divide up an individual hexagon or pentagon into cells of equal area and connect them in series. However, again due to the differences in insolation the peak power point for each of these series connected modules would be different. In addition the monolithic interconnection will reduce the active area for each of the panels and additional losses would be incurred in the blocking diode that would be required to prevent reverse biasing modules that were receiving no insolation. To overcome these issues the power system architecture for the PowerSphere calls for an individual DC-DC converter for each of the 32-panels which make up a PowerSphere.^[2] Small DC-DC converters are available which utilize a single chip which can boost current from a single solar cell with a peak power voltage of around one-volt and deliver a regulated five-volts to the power bus. This configuration eliminates the need to subdivide a single panel since the ITFT dual junction product has a peak power point around the one-volt level. The converter would also provide isolation for cells, which receive no insolation. Thus an individual panel would contain only one cell. The configuration for this cell is shown in Figure 3.

Thermal design considerations were important drivers in the development of the design of a thin film solar cell for the PowerSphere.^[3] The need to keep the maximum operating temperature of the thin film solar cells at approximately 80°C resulted in a requirement that the thermal emissivity of the front and back surface of the cells be 0.8. To accomplish this, aluminum is substituted for the stainless steel that ITFT applies to the back of the kapton substrate. The metalized layer on the back of the substrate is required for static charge bleed off during the roll-to-roll deposition of the amorphous silicon layers. It is not needed for the functioning of the cell. Aerospace and ITFT developed a process for removing the aluminum after completion of roll-to-roll processing of the cells leaving the 2 mil kapton substrate as the

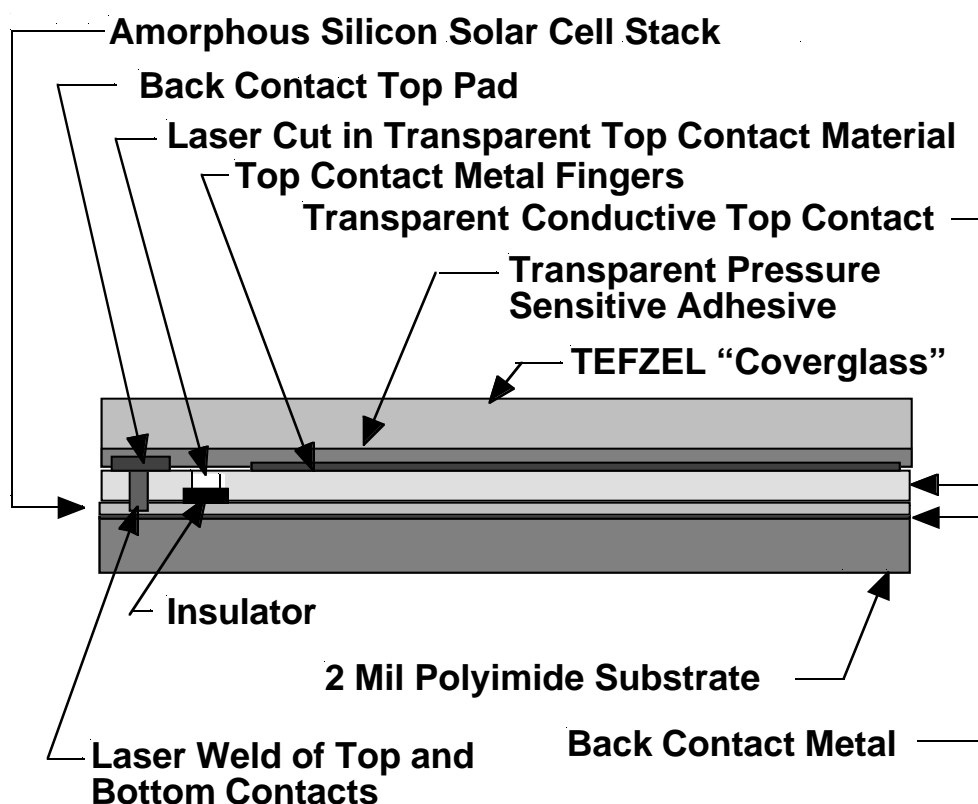


Figure 3. Design of Thin Film Solar Cell for PowerSphere

thermal emitting surface for the back of the cell. For the front of the cell a 1.5-mil sheet of TEFZEL with a 0.5 mil pressure sensitive adhesive layer is applied. The measured back surface thermal emissivity of completed cells was 0.76 and the front surface was 0.8.

Thin Film Solar Cell Performance Measurements

At present the AMO performance of the ITFT product provides efficiencies ranging from 1% to 3% for the large area cells produced for this project. The concept of using large area thin film solar cells produced in a low cost roll-to-roll process will require an understanding of what parameters in the design of the cells or the fabrication process have an impact upon the performance of the cells. The actual size of an individual cell or module cannot be a factor in cell efficiency performance of the resultant product. To investigate this on a statistical basis two different sizes of hexagonal and pentagonal cells were fabricated in 2000. The cells were fabricated with the standard ITFT terrestrial process. The cells were fabricated as hexagons and pentagons for use on a laboratory model of a PowerSphere. The large cells were 11.8 cm on a side and the small cells were 3.2 cm. The electrical performance of both cell sizes was measured and summarized in Table 1. These measurements were made on the bare cells produced by ITFT before any

Table 1. Comparison of Electrical Performance of Large and Small Thin Film Solar Cells Produced in 2000

Electrical Performance of Large (11.8 cm on A Side) Pentagonal Solar Cells									
S/N	Grid Spacing	Open Circuit Voltage	Short Circuit Current	Peak Power	Fill Factor	Voltage @ Peak Power	Current @ Peak Power	Temp. Degrees C	Cell Efficiency @ AM0
231-5	2	1.5353	0.7448	0.3880	33.93%	0.8570	0.4528	28.83	1.279%
232-5	2	1.6204	0.7482	0.4864	40.12%	1.0555	0.4608	29.17	1.603%
233-5	2	1.3879	0.7266	0.3282	32.55%	0.7530	0.4359	28.70	1.081%
234b-5	2	1.5833	0.6132	0.3228	33.25%	1.0085	0.3201	29.40	1.064%
235-5	2	1.4615	0.7592	0.3600	32.44%	0.8086	0.4452	29.50	1.186%
236-5	2	1.6259	0.7526	0.5033	41.13%	1.0834	0.4646	29.55	1.658%
237-5	2	1.4969	0.7452	0.3715	33.30%	0.8322	0.4464	29.42	1.224%
238-5	2	1.5537	0.7247	0.3567	31.68%	1.0056	0.3547	29.20	1.175%
239-5	2	1.5467	0.7137	0.3264	29.57%	0.9394	0.3475	29.00	1.076%
240b-5	2	1.6571	0.7493	0.5562	44.79%	1.1020	0.5047	29.45	1.833%
241-5	2	1.6298	0.7267	0.4487	37.89%	1.0337	0.4341	28.98	1.479%
average		1.5544	0.7277	0.4044	35.51%	0.9526	0.4243	29.2000	1.332%
std dev		0.0816	0.041	0.08103	4.75%	0.12121	0.05744	0.28976	0.267%
median		1.5537	0.7448	0.3715	33.30%	1.0056	0.4452	29.2000	1.224%

Electrical Performance of Small (3.2 cm on A Side) Pentagonal Solar Cells									
S/N	Grid Spacing	Open Circuit Voltage	Short Circuit Current	Peak Power	Fill Factor	Voltage @ Peak Power	Current @ Peak Power	Temp. Degrees C	Cell Efficiency @ AM0
A5-211		1.6949	0.0581	0.0529	53.75%	1.2503	0.0423	29.55	2.375%
B5-212		1.6400	0.0580	0.0421	44.28%	1.0562	0.0399	29.55	1.890%
C5-213		1.6675	0.0563	0.0395	42.13%	1.1115	0.0356	29.30	1.773%
D5-214		1.7007	0.0568	0.0554	57.38%	1.3052	0.0425	29.48	2.487%
A5-215		1.6809	0.0554	0.0472	50.64%	1.2074	0.0391	29.25	2.119%
B5-216		1.4408	0.0569	0.0324	39.50%	0.8400	0.0385	29.22	1.455%
C5-217		1.6021	0.0568	0.0307	33.69%	0.9481	0.0323	29.47	1.378%
D5-218		1.7024	0.0571	0.0552	56.87%	1.3060	0.0423	29.42	2.478%
average		1.6412	0.0569	0.0444	47.28%	1.1281	0.0391	29.4050	1.994%
std dev		0.0879	9E-04	0.00985	8.68%	0.17116	0.00362	0.13169	0.442%
median		1.6742	0.0569	0.0447	47.46%	1.1595	0.0395	29.4450	2.004%

Table 2. Electrical Performance of Bare Thin Film Solar Cells with Plated Silver Contacts produced in 2000

Electrical Performance of Large (11.8 cm on A Side) Pentagonal Solar Cells									
S/N	Grid Spacing	Open Circuit Voltage	Short Circuit Current	Peak Power	Fill Factor	Voltage @ Peak Power	Current @ Peak Power	Temp. Degrees C	Cell Efficiency @ AM0
05-26	1	1.5293	0.6820	0.4039	38.73%	0.9278	0.4354	29.63	1.331%
05-28	1	1.5236	0.7005	0.4394	41.17%	0.9330	0.4709	29.58	1.448%
05-38	1	1.6112	0.7000	0.4551	40.35%	1.0018	0.4543	29.65	1.500%
05-201B	1	1.6868	0.7918	0.6740	50.46%	1.1821	0.5701	29.58	2.221%
05-202	1	1.6914	0.7973	0.6850	50.80%	1.1930	0.5742	29.48	2.257%
05-203B	1	1.6831	0.8009	0.6732	49.94%	1.1782	0.5714	29.73	2.218%
05-204B	1	1.6693	0.7948	0.6190	46.66%	1.1590	0.5341	29.75	2.040%
05-245	1	1.6432	0.7383	0.4954	40.84%	1.0343	0.4790	28.22	1.632%
average		1.6297	0.7507	0.5556	44.87%	1.0762	0.5112	29.4525	1.831%
std dev		0.069	0.0511	0.1188	5.12%	0.1146	0.0576	0.50545	0.392%
median		1.6563	0.7651	0.5572	43.92%	1.0967	0.5066	29.6050	1.836%

Electrical Performance of Small (3.2 cm on A Side) Pentagonal Solar Cells									
S/N	Grid Spacing	Open Circuit Voltage	Short Circuit Current	Peak Power	Fill Factor	Voltage @ Peak Power	Current @ Peak Power	Temp. Degrees C	Cell Efficiency @ AM0
A5-S01		1.6576	0.0523	0.0377	43.49%	1.1619	0.0325	28.73	1.692%
A5-S02		1.2413	0.0577	0.0258	35.97%	0.6973	0.0370	28.85	1.158%
B5-S02		1.5473	0.0574	0.0357	40.19%	0.9276	0.0385	29.03	1.603%
C5-S02		1.6864	0.0544	0.0410	44.70%	1.1830	0.0347	28.67	1.841%
D5-S02		1.7294	0.0542	0.0546	58.17%	1.3067	0.0418	28.38	2.451%
average		1.5724	0.0552	0.0390	44.50%	1.0553	0.0369	28.7320	1.749%
std dev		0.197	0.0023	0.0104	8.36%	0.2426	0.0036	0.24004	0.468%
median		1.6576	0.0544	0.0377	43.49%	1.1619	0.0370	28.7300	1.692%

further processing at Aerospace. At this time, there is substantial variability in the data for this production run, but the average efficiency is greater for the small cells. This difference is attributed to increased series losses in the top and bottom contacts for the large cells.

Some of the cells from the same production run were delivered to Aerospace by ITFT without the printed ink top contacts. Top contacts were vapor deposited on these cells at Aerospace. The vapor deposited top contacts consist of 100Å of titanium followed by 1000 Å of palladium and lastly by 15000 Å of silver. The titanium was needed to provide good mechanical adhesion to the zinc oxide layer. The palladium layer provides a barrier layer between the titanium layer and the silver layer and bonds well with both. Before the plating process the cells were subjected to the sodium carbonate bath to remove the aluminum on the back of the kapton substrate. The electrical performance of the bare cells is presented in Table 2.

A set of cells was fabricated in 2001 with a thicker aluminum back contact. These cells are of an intermediate size, which are hexagons and pentagons, which are 6.5 cm on a side. As one can see by comparison with the data contained in Table 1, the electrical performance data for these cells has improved over that of the cells produced earlier. The fill factor has increased from an average of 35.5% for large cells and 47.28 % for small cells produced in 2000 to 49.10% for the cells produced in 2001. Part of this improvement is better control of the deposition process at ITFT. The electrical performance of the bare cells is presented in Table 3.

Table 3. Electrical Performance of Mid Sized Cells produced in 2001

Electrical Performance of Medium (6.5 cm on A Side) Pentagonal Solar Cells									
S/N	Grid Spacing	Open Circuit Voltage	Short Circuit Current	Peak Power	Fill Factor	Voltage @ Peak Power	Current @ Peak Power	Temp. Degrees C	Cell Efficiency @ AM0
05-400		1.7220	0.2069	0.1691	47.46%	1.1300	0.1496	29.85	1.829%
05-403		1.7143	0.2037	0.1639	46.93%	1.2728	0.1287	29.73	1.772%
05-406		1.7377	0.2129	0.1926	52.04%	1.1938	0.1613	29.58	2.083%
05-409		1.7320	0.2130	0.1862	50.50%	1.2015	0.1550	29.47	2.014%
05-412		1.7222	0.2142	0.1841	49.90%	1.1399	0.1615	29.25	1.991%
05-415		1.7206	0.2180	0.1808	48.21%	1.1577	0.1562	29.28	1.955%
05-418		1.7114	0.2146	0.1730	47.13%	1.2181	0.1421	29.30	1.871%
05-421		1.7329	0.2159	0.1865	49.84%	1.2186	0.1530	29.10	2.017%
05-425		1.7432	0.2242	0.2024	51.78%	1.1894	0.1701	28.92	2.189%
05-427		1.7282	0.2175	0.1727	45.93%	1.1755	0.1469	28.80	1.868%
05-430		1.7278	0.2181	0.1735	46.04%	1.1615	0.1494	28.25	1.876%
05-433		1.7606	0.2251	0.2120	53.49%	1.2215	0.1736	27.17	2.293%
average		1.7294	0.2153	0.1831	49.10%	1.1900	0.1540	29.0583	1.980%
std dev		0.013	0.0061	0.0141	2.52%	0.04	0.012	0.736735	0.153%
median		1.7280	0.2153	0.1825	49.03%	1.1916	0.1540	29.2650	1.973%

Comparison of Electrical Resistance of Printed Ink and Plated Silver Contacts

The electrical resistance of the thin film solar cell current collector traces were measured using a Hewlett Packard HP4338B Milliohmeter. This instrument uses a four-probe resistance method (two probes for excitation, and two for measurement). The method of excitation is a 1000 Hz AC signal, which makes it

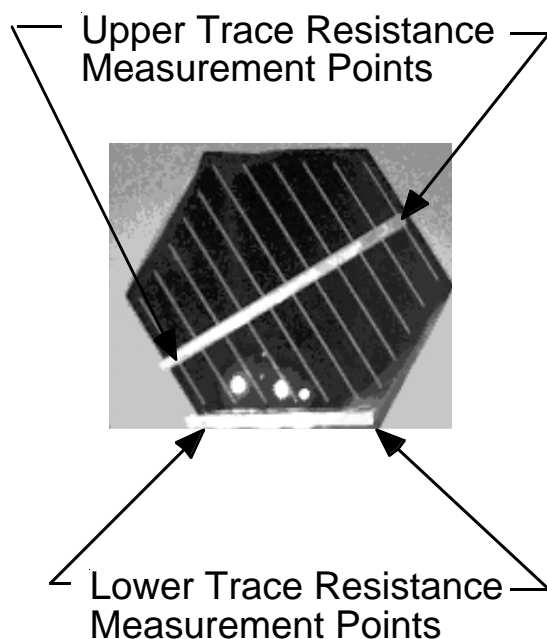


Figure 4. Location of Probes for Measuring Resistance of Thin Film Solar Cell Contacts

ideal where DC voltages from, for example, batteries or illuminated solar cells, would interfere with a DC ohmmeter measurement. The HP4338B is capable of measuring resistance from 10 mΩ to 100 kΩ. For each of the measurements, the probes were placed at each end of the respective current collector trace, and the length of the traces was measured.

Measurements were made on Large Pentagons and Hexagons fabricated in 2000. A method was devised to make an assessment of the resistance of the back contact of the cells using a normalized impedance of the top contact busbar. The lower trace is actually a parallel combination of the surface trace that has been laser stitched, or electrically connected to the solar cell back contact. By using the measured electrical resistivity of the top contact busbar and adjusting the differences in length the electrical resistance of the surface trace could be calculated. This resistance is in parallel with the electrical resistance of the solar back contact. The measurements made were of the parallel connection of these two conductors. The resistance of the back solar cell contact was then calculated. The results of these measurements and calculations are contained in Table 4. The assumption that the thickness and therefore the electrical resis-

Table 4. Electrical Resistance Measurements of Large Cells with Printed Ink and Plated Silver Contacts Produced in 2000.

Plated Silver Top Contacts					Silver Conductive Ink Top Contacts				
Cell ID	Measured Resistance	Length cm	Normalized Resistance Long Bus Bar Ohms	Normalized Resistance Back Contact Ohms	Cell ID	Measured Resistance	Length cm	Normalized Resistance Long Bus Bar Ohms	Normalized Resistance Back Contact Ohms
5251	0.3265	18.7198	0.0163915		5206	1.849	18.7198	0.0928263	
	0.2805	11.7348		-0.354851		0.4913	11.7348		0.3996826
5254	0.1721	18.7198	0.00864		5207	1.948	18.7198	0.0977965	
	0.1454	11.7348		-0.195968		0.5475	11.7348		0.4651686
5255	0.1708	18.7198	0.0085748		5208	1.969	18.7198	0.0988507	
	0.1454	11.7348		-0.190353		0.4703	11.7348		0.3561145
5256	0.1699	18.7198	0.0085296		5209	1.952	18.7198	0.0979973	
	0.1513	11.7348		-0.168601		0.4385	11.7348		0.3203043
5245	0.2793	18.7198	0.0140218		5210	1.99	18.7198	0.099905	
	0.127	11.7348		0.2167401		0.4795	11.7348		0.365059
6243	0.3322	20.32	0.0153643		5211	2.054	18.7198	0.103118	
	0.1145	11.684		0.4971169		0.4949	11.7348		0.3767735
					5215	1.958	18.7198	0.0982985	
						0.5821	11.7348		0.5189292
					5218	1.955	18.7198	0.0981479	
						0.455	11.7348		0.3391832
Average			0.0119	-0.0327				0.0984	0.3927
Standard Deviation			0.0037	0.3215				0.0028	0.0673

tivity of the two top busbars is the same proved to hold for the printed ink contacts but was not valid for the plated silver contacts. The vacuum metal evaporation chamber used to deposit the plated silver contacts on the cells is just large enough to hold the large cells. Thus deposition thickness drops near the edges of the large cells which is where the back contact surface contact is located. Thus, when the resistance of the back contacts of the silver plated cells was calculated using this method, negative values resulted.

The back contact thickness of cells produced in 2000 was measured to be approximately 150 nm. The measurement was made by first using Aerospace's Focused Ion Beam (FIB) milling machine to cut a section in the thin film solar cell. A Scanning Electron Microscopy (SEM) image of the section was made of

Table 5. Electrical Resistance Measurements of Printed Ink Contacts of Medium Cells Produced in 2001

Conductive Ink Top Contacts				
Cell ID	Measured Resistance	Length cm	Normalized Resistance Long Bus Bar Ohms	Normalized Resistance Back Contact Ohms
06-400	2.041	11.049	0.07037931	
	1.086	6.2738		30.399748
06-402	1.97	11.049	0.067931034	
	0.96	6.2738		11.924511
06-404	1.86	11.049	0.064137931	
	0.934	6.2738		14.223591
06-406	1.725	11.049	0.059482759	
	0.896	6.2738		18.514002
06-408	1.956	11.049	0.067448276	
	1.02	6.2738		22.009464
06-410	1.994	11.049	0.068758621	
	1.021	6.2738		18.304057
06-412	1.978	11.049	0.068206897	
	1.056	6.2738		31.110528
06-414	2.008	11.049	0.069241379	
	0.98	6.2738		12.285585
06-416	2.009	11.049	0.069275862	
	1.041	6.2738		20.967676
06-417	2.105	11.049	0.072586207	
	1.033	6.2738		13.401704
Average			0.0677	19.3141
Standard Deviation			0.0036	6.9808

this cut and the thickness of the back contact was determined. This process was repeated with the cells produced in 2001 and the back contact thickness was measured to be 40 nm. Figures 5 and Figure 6 provide the SEM images of the FIB cuts. The electrical resistance of the cells produced in FY 2001 was measured and the results are provided in Table 5. The measured increase in the electrical resistivity of the short busbar for cells produced in 2001 verses cells produced in 2000 is consistent with the measured decrease in the thickness of the aluminum metal used for the back contact.

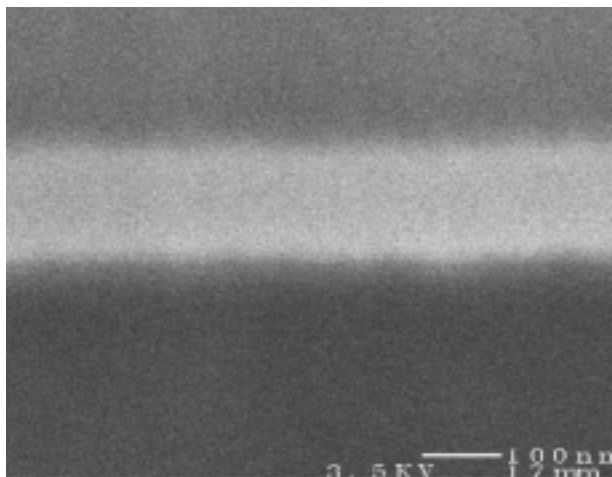


Figure 5. SEM of Thin Film Solar Cell Produced in 2000

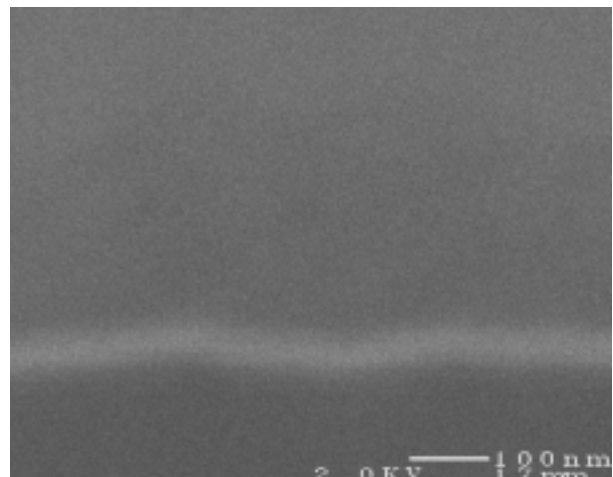


Figure 6. SEM of Thin Film Solar Cell Produced in 2001

Summary and Conclusions

Work to date to develop a Thin Film Amorphous Silicon Solar Cell has resulted in a physical configuration for the solar array blanket which meets the thermal requirements for space applications of the PowerSphere. The present design uses the kapton substrate as the rear thermal radiator and a clear TEFZEL "coverglass" as the front surface thermal radiator. This design provides the required thermal properties to ensure optimum operating temperatures. The improved performance due to the seven-fold reduction in electrical resistance afforded by the plated silver contacts over the ITFT printed ink contacts warrants the use of this contact type for space applications. Likewise, an increase in the thickness of the back contact of the cells improved the performance by lowering the series resistance of the cells. Simple measurements of the electrical resistivity of the busbar welded to the back contact can give some indication of the actual thickness of the back contact metal layer.

Acknowledgment

This work was supported by The Aerospace Corporation's IR&D Program.

References

- [1] E. J. Simburger, "PowerSphere Concept", The Aerospace Corporation, Proceedings of Government Microcircuit Applications Conference, 8-11 March 1999.
- [2] Alonzo Prater, Edward J. Simburger, Dennis Smith, Peter J. Carian, and James Matsumoto, The Aerospace Corporation, "Power Management and Distribution Concept for Microsatellites and Nanosatellites", Proceedings of IECEC 1-5 August 1999.
- [3] David G. Gilmore, Edward J. Simburger, Michael J. Meshishnek, David M. Scott, Dennis A. Smith, Alonzo Prater, James H. Matsumoto and Margot L. Wasz, The Aerospace Corporation, "Thermal Design Aspects of the PowerSphere Concept", Proceedings of Micro/Nano Technology for Space Applications Conference, 11-15, April 1999.
- [4] Edward J. Simburger, David Scott, Dennis Smith, David Gilmore, Mike Meshishnek, and Meg Abraham, The Aerospace Corporation and Frank R. Jeffery, Iowa Thin Film Technologies, Inc. "Development of a Thin Film Amorphous Silicon Space Solar Cell for the PowerSphere Concept", 16th Space Photovoltaic Research and Technology Conference, 30 August - 2 September 1999.
- [5] E. Simburger, J. Matsumoto, A. Garcia III, D. Smith, J. Ross, M. Meshishnek, M. Abraham, F. Jeffery (Iowa Thin Film Technologies, Inc), and P. Gierow (SRS Technologies Group), "Advancements in the Development of Thin Film Amorphous Silicon Space Solar Cell for the PowerSphere Concept," 28th IEEE Photovoltaic Specialists Conference, Anchorage, AK, 20 September 2000.
- [6] Edward J. Simburger, James Matsumoto, David Hinkley, David Gilmore, Thomas Giants, and Jasen Ross, "Multifunctional Structures for the PowerSphere Concept," 42ND AIAA/ASME/ASCE/AHS/ASC Structures, Structural Dynamics, and Materials Conference & Exhibit, Seattle, Washington 16-19 April, 2001

THIN-FILM SOLAR ARRAY EARTH ORBIT MISSION APPLICABILITY ASSESSMENT

David J. Hoffman
Thomas W. Kerslake
Aloysius F. Hepp
NASA Glenn Research Center, Cleveland, OH.

Ryne P. Raffaele
Rochester Institute of Technology, Rochester, New York

ABSTRACT

This is a preliminary assessment of the applicability and spacecraft-level impact of using very lightweight thin-film solar arrays with relatively large deployed areas for representative Earth orbiting missions. The most and least attractive features of thin-film solar arrays are briefly discussed. A simple calculation is then presented illustrating that from a solar array alone mass perspective, larger arrays with less efficient but lighter thin-film solar cells can weigh less than smaller arrays with more efficient but heavier crystalline cells. However, a proper spacecraft-level systems assessment must take into account the additional mass associated with solar array deployed area: the propellant needed to desaturate the momentum accumulated from area-related disturbance torques and to perform aerodynamic drag makeup reboost. The results for such an assessment are presented for a representative low Earth orbit (LEO) mission, as a function of altitude and mission life, and a geostationary Earth orbit (GEO) mission. Discussion of the results includes a list of specific mission types most likely to benefit from using thin-film arrays. NASA Glenn's low-temperature approach to depositing thin-film cells on lightweight, flexible plastic substrates is also briefly discussed to provide a perspective on one approach to achieving this enabling technology. The paper concludes with a list of issues to be addressed prior to use of thin-film solar arrays in space and the observation that with their unique characteristics, very lightweight arrays using efficient, thin-film cells on flexible substrates may become the best array option for a subset of Earth orbiting missions.

BACKGROUND

Photovoltaic (PV) solar arrays using thin-film solar cell technology have much promise for future Earth-orbiting space missions. The most attractive features of thin-film solar arrays include the following:

- | | |
|-----------------------|---|
| Extremely lightweight | – enabling the highest solar array mass specific power, W/kg. |
| Low cost | – enabled by large scale “roll-to-roll” thin-film manufacturing processes. |
| Good packageability | – solar cell and blanket flexibility increase stowage options. |
| Radiation tolerant | – amorphous and polycrystalline thin-film cells are inherently resistant (1). |

However, the projected efficiency of thin-film PV cells is currently about one-third to one-half of advanced thin-crystal silicon (Si) and multi-junction (or multi-band gap, MBG) gallium arsenide (GaAs) based cells. Consequently, for Earth orbiting missions, especially those in low Earth orbit (LEO), spacecraft-level impacts associated with the large deployed array area required for thin-film arrays can offset or even negate their lower array-level mass and cost benefits. The less attractive features of thin-film solar arrays are summarized below:

- | | |
|---------------------------|--|
| Large deployed areas | – two or three times the size of high-efficiency crystalline cell arrays.
– increased propellant required for CMG desaturation and drag makeup.
– possible instrument field-of-view impacts.
– larger, potentially less stiff arrays may have lower first fundamental frequencies with potential attitude control system impacts and are more sensitive to propulsion system thrust levels. |
| Potentially less reliable | – more complicated deployment and support systems as compared to standard rigid panel arrays. |

Recognizing the less attractive features of thin-film arrays, it is easy to conclude that unless dramatic gains are made in thin-film cell efficiency, these arrays will not fully replace high-efficiency cell arrays in the foreseeable future. Each type of array will support missions that take advantage of their unique characteristics. Figure 1

depicts the characteristics of solar arrays using either high-efficiency crystalline cells or thin-film cells by plotting cell efficiency and array power density (or area specific power, W/m^2) versus area density (or area specific mass, kg/m^2). Flexible planar, concentrator or inflatable arrays of moderate area density ($1-2.5 kg/m^2$) using either relatively heavy but very efficient multi-junction solar cells, or relatively lighter but less efficient thin silicon cells, could obtain an array-level specific power approaching $300 W/kg$. To get to this level from the current state-of-the-art $\sim 70 W/kg$, new solar array substrates, support structures and deployment concepts may be needed in conjunction with improved cell technology (2)

Ultra-lightweight arrays ($0.25-1.0 kg/m^2$) using lightweight thin-film solar cells of moderate efficiency may enable the attainment of even greater array-level specific power. As the plot in figure 1 implies, very lightweight thin-film arrays may be the most feasible means of approaching the very high specific power necessary to enable missions with very high power requirements, such as space solar power satellites, manned Mars or lunar surface missions and some high-power solar electric propulsion (SEP) concepts (3, 4).

THIN-FILM ARRAY MASS BENEFITS

Array mass specific power, W/kg , is a key metric featured in Figure 1 and is often discussed, in many cases without full consideration of what is accounted for in its numerator and denominator. Further, the mass of the solar array alone is just one component in one subsystem of the entire spacecraft. To perform a proper systems assessment, the mass of other subsystems must be included, especially the mass of these subsystems that result from aspects of the original subsystem being assessed. This will be discussed further later. For this section, array mass alone serves as a starting point to illustrate the promise thin-film arrays.

From a solar array alone mass perspective, larger arrays with less efficient but lighter thin-film solar cells can weigh less than smaller arrays with more efficient but heavier crystalline cells. Array mass specific power can be obtained by dividing the area specific power (W/m^2) by the array's area density (kg/m^2). Area specific power is a function of the cell efficiency and array packing factor, which is the ratio of solar cell area to total array area. Area density is a function of the cell material density and thickness and the array substrate, wiring, support structure and mechanisms. To a first order, the cell efficiency required to match the specific power of an array of a given type but using different cells can be estimated with the following equation,

$$\eta_{TF} = \eta_2 \left(\frac{PF_2}{PF_{TF}} \right) \left(\frac{Array + Cell_{TF}}{Array + Cell_2} \right) \quad (\text{Eq. 1})$$

where η is the cell efficiency, PF is the array packing factor, $Array$ is the area density (kg/m^2) of the array, including its wiring, substrate, support structure and mechanisms, and $Cell$ is the cell area density. While the array area density is held constant in this first order approximation, in actuality, it would decrease with the use of lighter cell technology.

Figure 2 shows the approximate thin-film cell efficiency required to match the specific power of a high efficiency cell array using equation 1. Cell material densities, including the coverglass, of $0.50 kg/m^2$ for the Si cell, $1.0 kg/m^2$ for the multi-junction GaAs cells, and $0.2 kg/m^2$ for the thin-film cells are assumed in figure 2. In practice, the actual cell efficiency required to match array specific mass will also depend on the cell operating temperature and degradation of the cell efficiency from environmental effects over the mission life. Nevertheless, figure 2 can be used to discern trends. For example, the figure shows that for very lightweight arrays (area densities from 0.25 to $0.75 kg/m^2$), only moderate thin-film cell efficiencies are required to match the specific power of arrays using much higher efficiency, but heavier cells. Improvements in thin-film cell efficiencies may still be necessary in order to reduce the size of thin-film arrays in order to minimize attitude control system impacts and to reduce array stowed volume and deployment complexity for missions with these concerns.

While the potential array mass benefit is evident for thin-film arrays, it is mitigated, in some cases more than others, when spacecraft-level mass impacts are included.

PAST SYSTEMS STUDIES

A number of past studies have assessed the spacecraft-systems level impacts of solar cell and array technologies for Earth orbiting missions. In 1999, Eugene Ralph performed system trades for crystalline and thin-film cells on rigid, flexible and concentrator arrays in Low Earth Orbit (LEO) and Geostationary Earth Orbit (GEO) (5, 6). Ralph's results in reference 5 indicate that GEO arrays using high efficiency MBG GaAs-based cells have mass and cost advantages over alternatives, especially when the area penalty (increased attitude control fuel) of arrays using the less efficient thin-film cells is included. With Ralph's assumptions, thin-film cell efficiency needs to be at least 12.6% to be competitive in GEO. For LEO, Ralph concluded that while the most efficient multi-junction cell array has the lowest mass, arrays with 9% to 12.6% efficient thin-film cells have competitive area-adjusted costs.

The paper by Bell outlines a model developed by the Aerospace Corporation to "determine optimal power subsystem suites as a function of spacecraft design and total system cost" (7). Example model results are reported for a 100 satellite high-power (15kW) LEO constellation and a small, single-mission 1 kW LEO satellite. Study results for both cases favored high efficiency cell solar arrays. Because satellites in the LEO constellation were delivered to a low parking orbit and then transferred to the final 1852 km orbit, the large area of the 8%-10% efficient thin-film arrays led to significant attitude control system impacts, and ultimately higher mission costs. For the single-mission low power LEO case, the Aerospace model favored mature, low nonrecurring cost array technologies using 16% efficient Si and 21.5% efficient GaAs cells.

Each of the studies reviewed above looked at near-term thin-film cell technology on flexible, but not necessarily lightweight arrays for Earth orbiting applications. Only when the cell efficiency of a thin-film array was greater than 10% did they compare favorably with crystalline cell arrays for some of the missions studied.

EARTH ORBITING MISSIONS SYSTEMS ASSESSMENT

The objective of the present assessment is to perform a spacecraft-systems level assessment similar to the ones just reviewed, but assuming higher-performing cell and array technology in order to determine the "crossover" points in terms of systems mass. While small-area thin-film cells developed in the laboratory have exceeded 17% AM1.5 efficiency, thin-film cell efficiency of 10% (AM0) can be considered state-of-art for this technology. In this study, the performance of very lightweight thin-film arrays with assumed cell efficiencies of 10% and 15% (AM0, 28° C) sized for a representative LEO mission over a range of altitudes and mission lifetimes is evaluated. In addition, the spacecraft-level mass impacts of array size for a representative GEO mission is also assessed.

The NASA Glenn Array Design Assessment Model (ADAM) was used to perform the assessments. ADAM was developed at Glenn to support evaluation of array design alternatives (8). ADAM includes several integrated array design modules, databases to manage input set alternatives for running the design modules, and a user interface with input forms and model outputs. Outputs include over 100 items representing solar array, power system and spacecraft characteristics and performance. The spacecraft characteristics include estimates of the propellant required for reboost (drag makeup) and to desaturate CMGs or reaction wheels as a result of environmental disturbance torques (due to aerodynamic drag, gravity gradient, solar radiation pressure and magnetic moments).

For both LEO and GEO assessments, the baseline to which all mass results are normalized is an array using 30% GaAs-based multi-band gap (MBG) high-efficiency solar cells on rigid panels. While 30% MBG cells are not yet widely available commercially, high-efficiency MBG cells on rigid panels are a commonly used type of array for NASA Earth-orbiting missions. The first alternative array design assumes use of the same MBG cells but now on a flexible array substrate with a deployable coilable lattice boom, similar to the design of the International Space Station solar arrays. The next two alternatives are flexible thin-film cell array designs: one assumes 10% efficient thin-film cells and the other assumes 15% efficient cells. Both thin-film PV blanket area densities are 0.23 kg/m², which can be obtained if the thin-film cells are deposited on a plastic substrate or a very thin metal foil. All flexible array coilable lattice deployment booms are sized for ≥ 0.25 Hz minimum first fundamental frequency. For both LEO and GEO missions, the spacecraft is assumed to be Earth nadir-pointing with two single axis sun-tracking solar arrays. Average atmospheric density is assumed throughout the mission life.

Specific assumptions for the representative LEO and GEO cases are summarized in the following table:

LEO Mission Assumptions	GEO Mission Assumptions
400 km to 1200 km altitude; 5 year life	10 kW EOL Bus Power
0.25 to 5 year life at 500 km altitude	10 year mission life
2 kW EOL Bus Power	Constant maximum value of secular components of solar array radiation pressure torques
2500 kg Spacecraft Dry Mass	

RESULTS

LEO Mission Altitude Study –

Figure 3 shows mass as a function of altitude for the three alternative solar array designs alone as well as including the propellant mass required for impacts directly associated with solar array area - momentum wheel desaturation and drag makeup performed by hydrazine thrusters. In each case, the mass is normalized to the 30% efficient MBG cell rigid array, either alone or including its associated propellant mass.

The plot indicates that the mass of each type of solar array is constant over the range of altitudes. The flexible 30% MBG cell array is half the mass of the same cells on a rigid array. The 10% thin-film cell array has slightly greater mass, 0.57 of the baseline, while the 15% thin-film cell array has the least mass at 0.45 of the rigid baseline.

When including the propellant mass required as a result of array area, figure 3 shows that for the assumptions in this study the total mass increases rapidly below 700 km. At 600 km, the mass of the 10% thin-film cell array and its associated propellant equals the mass of the baseline rigid array and its associated propellant. This occurs at approximately 550 km for the 15% thin-film cell array. The reason for this is that the aerodynamic torque rapidly increases as the atmospheric density increases as altitude decreases.

Beyond 800 km, gravity gradient and solar pressure become the dominant disturbance torques, but are much less severe than the aerodynamic torques experienced at lower altitudes. At these higher altitudes, the propellant mass associated with solar array area is much less and approaches a negligible addition to the array mass alone.

LEO Mission Life Study –

The LEO altitude study clearly shows the severe impact of large array areas on propellant mass for lower LEO altitudes for a five-year mission duration. It also showed that flexible arrays using either 10% to 15% thin-film cells, or 30% MBG cells for that matter, offer a significant mass advantage (~50%) when considering the array alone. This implies that there will be a mission duration for which the alternative thin-film arrays should be competitive even when their associated propellant mass is included.

Figure 4 shows the mass of array plus propellant for the three flexible array options as compared to the rigid baseline for mission durations of three months to five years at an altitude of 500 km. For missions under three years, the 15% thin-film cell array and its propellant mass is less the 30% MBG cell rigid array baseline. Mission durations for the 10% thin-film cell array must be less than 1.5 years to preclude a mass penalty over the rigid array baseline when including propellant.

GEO Mission Study –

In GEO, the dominant environmental disturbance torque is a result of solar radiation pressure. The magnitude of this torque is directly related to the size of the solar arrays and the offset of the center-of-pressure that this force acts through and the spacecraft's center of mass. While radiation pressure is predominantly a cyclic torque for a nadir-pointing spacecraft, there are non-zero (secular) components that result in the need for momentum storage and subsequent desaturation via thrusters.

Figure 5 shows the mass breakdown of solar arrays sized to provide 10 kW to the spacecraft bus over a 10-year mission. Also included is a "worst case" estimate of the propellant needed to desaturate the momentum wheels as a result of solar pressure torques. The 30% MBG cell arrays have a significant portion of their mass in the cell and cover glass masses. The dominant mass for the 30% MBG cell rigid array is the rigid panels.

The flexible arrays offer significant mass savings over the rigid array, even when propellant mass is included. For the thin-film cell arrays, the major mass contribution comes from the flexible blanket substrate and the addition of the propellant mass. However, for the significantly higher power level of this GEO mission as compared the LEO mission in this assessment, the mass advantage of the 15% thin-film cell flexible solar array is so significant (its mass is about 1/4th of the rigid array) that its additional propellant mass burden does not yield its mass advantage even to the flexible 30% MBG cell array.

DISCUSSION

It is recognized that different assumptions for any number of the parameters assumed in the above analysis could lead to a different threshold (e.g. altitude or mission life) for which one array option results in a lower total system mass as compared with another. In other words, while the results above are meant to be representative to realistic classes of Earth-orbiting missions, results for actual, individual missions will no doubt vary.

That said, it is felt that the input assumptions and model fidelity is good enough to indicate more specifically the Earth-orbiting mission types which could make best use of the mass advantages thin-film solar arrays without mitigation from the spacecraft-level mass impacts associated with larger deployed areas.

Attractive Earth-orbiting applications for thin-film arrays include:

- LEO missions above 500 km to 800 km
- LEO missions of short duration, especially at lower altitudes
- LEO sun-synchronous missions with array normal perpendicular to velocity vector
- LEO-to-GEO transfer missions: good radiation tolerance.
- GEO missions, given thin-film cell efficiency $\geq 10\%$
- Very small micro/nanosat missions

While some of the types of missions in the preceding list were not addressed in this study, the benefits of thin-film solar arrays for these missions are at least intuitively obvious, and have been quantitatively explored in other studies (see reference 4 for SEP transfer missions).

THIN-FILM CELL DEVELOPMENT AT NASA GLENN

Among the desirable attributes in any space-bound component, subsystem or system are high specific power, radiation tolerance and high reliability, without sacrificing performance. NASA Glenn is currently developing space-bound technologies in thin film chalcopyrite solar cells and thin-film lithium polymer batteries (9). The thin-film solar cell efforts at Glenn are summarized below.

The key to achieving high specific power solar arrays is the development of a high-efficiency, thin-film solar cell that can be fabricated directly on a flexible, lightweight, space-qualified durable substrate. Such substrates include Kapton[™] (DuPont) or other polyimides or suitable polymer films. While the results of the present study indicate that lightweight thin-film cells with moderate efficiency on lightweight substrates can compete on a mass basis, higher cell efficiencies will be required to mitigate impacts associated with large array area. Current thin-film cell fabrication approaches are limited by either (A) the ultimate efficiency that can be achieved with the device material and structure, or (B) the requirement for high-temperature deposition processes that are incompatible with all presently known flexible polyimides, or other polymer substrate materials.

At Glenn, a chemically based approach is enabling the development of a process that will produce high-efficiency cells at temperatures below 400 °C. Such low temperatures minimize the problems associated with the difference between the coefficients of thermal expansion of the substrate and thin-film solar cell and/or decomposition of the substrate.

Polymer substrates can be used in low temperatures processes. As such, thin-film solar cell materials can be deposited onto molybdenum-coated Kapton, or other suitable substrates, via a chemical spray process using advanced single-source precursors. A single-source precursor containing all the required chemically-coordinated atoms such as copper, indium, sulfur and others, will enable the use of low deposition temperatures that are compatible with the substrate of choice (10).

A combination of low-temperature chemical vapor deposition and chemical bath deposition has been used to produce ZnO/CdS/CuInSe₂ thin-film photovoltaic solar cells on lightweight flexible plastic substrates, depicted in figure 6 (11)

CONCLUSION

Until thin-film PV is further developed, future Earth-orbiting missions will most likely keep using high efficiency silicon or MBG cell rigid planar arrays, and perhaps an occasional flexible MBG cell array or a concentrator array. In order for thin-film solar arrays to be more seriously considered, a number of issues need to be further addressed:

1. Thin-film **cell efficiencies increase** and/or **substrate mass decreases**.
Need economical large-scale production of large-area (e.g. >10-cm²) thin-film cells with stable efficiencies > 10% to 15% (1-Sun AM0) on low-mass substrates (1-mil metallic, 5-mil pre-preg composite ply, 2-mil polymer, open-weave polymer).
2. Thin-film **cell space qualification is completed**.
Need to demonstrate tolerance to radiation, thermal cycling (delamination), mechanical strain (packaging and blanket tensioning) and (for amorphous silicon) light-induced instability.
3. Thin-film **solar arrays** are **designed** and **space qualified**.
Need packaging, deployment systems and support structures tailored to thin-films.
4. **Appropriate missions** are **identified...**
...that would benefit from thin-film array attributes (high specific power, good packageability, radiation tolerance, low cost) and whose benefits are not mitigated by spacecraft-level operations issues associated with larger area, low-mass arrays (see the "Discussion" section for a list of Earth-orbiting mission candidates.)

Once available and space qualified, moderate to relatively high efficiency thin-film cells on lightweight flexible substrates will offer significant mass and cost benefits. This approach may even enable ultra-lightweight solar arrays to attain the very high specific mass required for future high-power missions and applications. Further, as thin-film cell efficiency improves, the packaging, deployment and attitude/control impacts of the larger array area will diminish. With these characteristics, very lightweight arrays using efficient, thin-film cells on flexible substrates may become a leading alternative for a large subset of Earth-orbiting missions.

REFERENCES

1. Woodyard, J., Landis, G., "Radiation Resistance of Thin Film Solar Cells", *Solar Cells*, Vol. 31, No. 4, pp. 297-329, 1991 (also NASA Technical Memorandum TM-103715).
2. Jones, P.A., White, Stephen F., Harvey, T.J., "A High Specific Power Solar Array for Low to Mid-Power Spacecraft", Proceedings of the Space Photovoltaic Research and Technology Conference (SPRAT XII), 1992, NASA CP-3210, pp. 177-187.
3. Landis, G., Hepp, A., "Applications of Thin-Film PV for Space", Proceedings of the 26th Intersociety Energy Conversion Engineering Conference, Vol. 2, pp. 256-261, Aug. 1991.
4. Kerslake, Thomas W., Gefert, Leon P., "Solar Power System Analyses for Electric Propulsion Missions", NASA/TM-1999-209289, SAE 99-01-2449, 34th IECEC, August 1999.
5. Ralph, E.L., Woike, T.W., "Solar Cell Array System Trades – Present and Future", AIAA, 1999.
6. Ralph, E.L., "High Efficiency Solar Cell Arrays System Trade-Offs", IEEE, 1994.
7. Bell, Kevin D., Marvin, Dean C., "Power Generation and Storage Technology Selection for an Optimal Spacecraft System Design", IECEC 1999-01-2531.
8. Hoffman, David J., Kerslake, Thomas W., Hepp, Aloysius F., Jacobs, Mark K., Ponnusamy, Deva, "Thin-Film Photovoltaic Solar Array Parametric Assessment", 35th Intersociety Energy Conversion Engineering Conference, Las Vegas, NV, July 24-28, 2000. "Thin-Film PV Solar Array Assessment for Satellites, Final Review Report," contract number NAS3-26565, Task Order 31.
9. Raffaele, R.P., Harris, J.D., Rybicki, G.C., Scheiman, D.A., Hepp, A.F., "A Facile Route to Thin-Film Solid State Lithium Microelectric Batteries", *J. of Power Sources*, in press, 2000.

10. Hollingsworth, J.A., Hepp, A.F., and Buhro, W.E., 'Spray CVD of Copper Indium Sulfide films: Control of Microstructure and Crystallographic Orientation', *Chemical Vapor Deposition*, Vol.3, pp. 105-108, 1999.
11. J.D. Harris, D.G. Hehemann, J.E. Cowen, A.F. Hepp, R.P. Raffaele, J.A. Hollingsworth, "Using Single Source Precursors and Spray Chemical Vapor Deposition to Grow Thin Film CuInS_2 ," *28th Photovoltaic Specialists Conference*, September 17-22, pp. 563-566, 2000.

Figure 1 - Lightweight solar array technology thrusts.

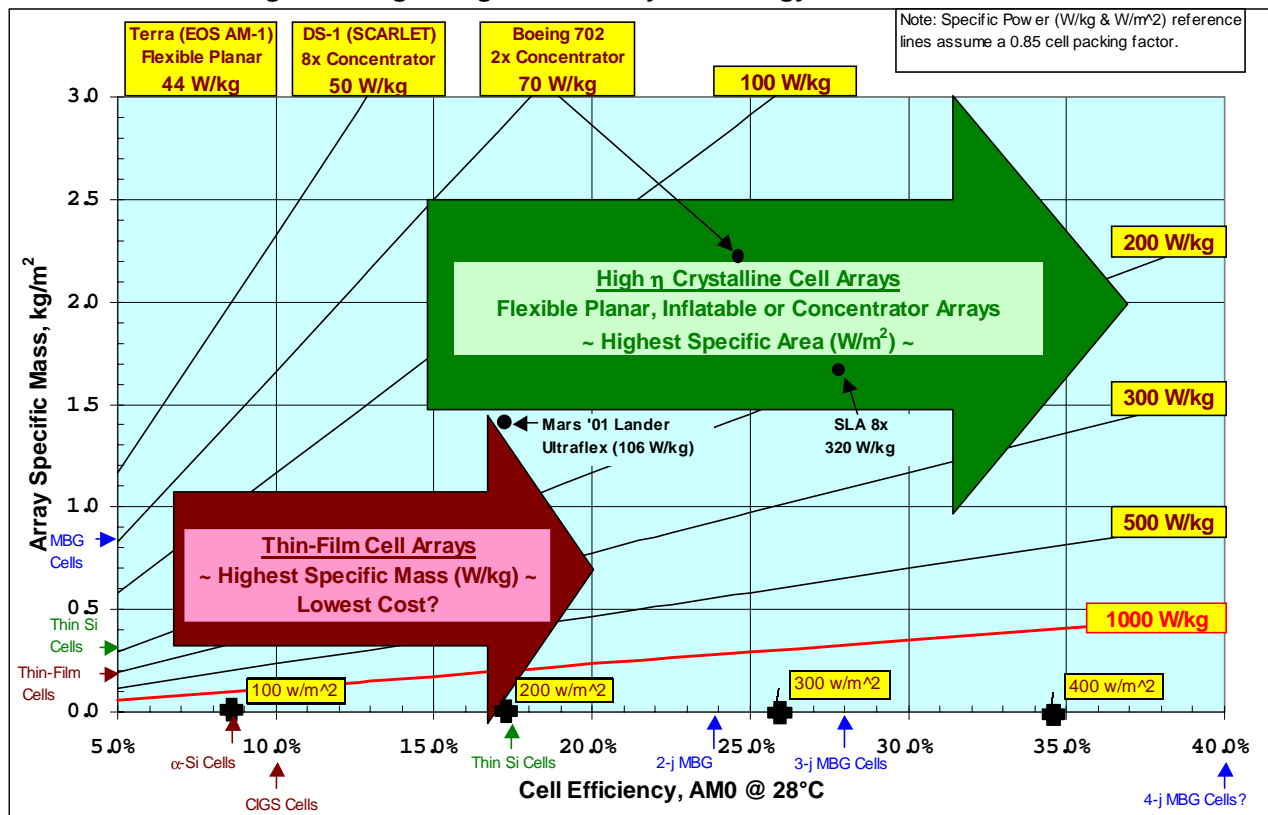


Figure 2 - Approximate thin-film cell efficiency required to match high efficiency cell array mass.

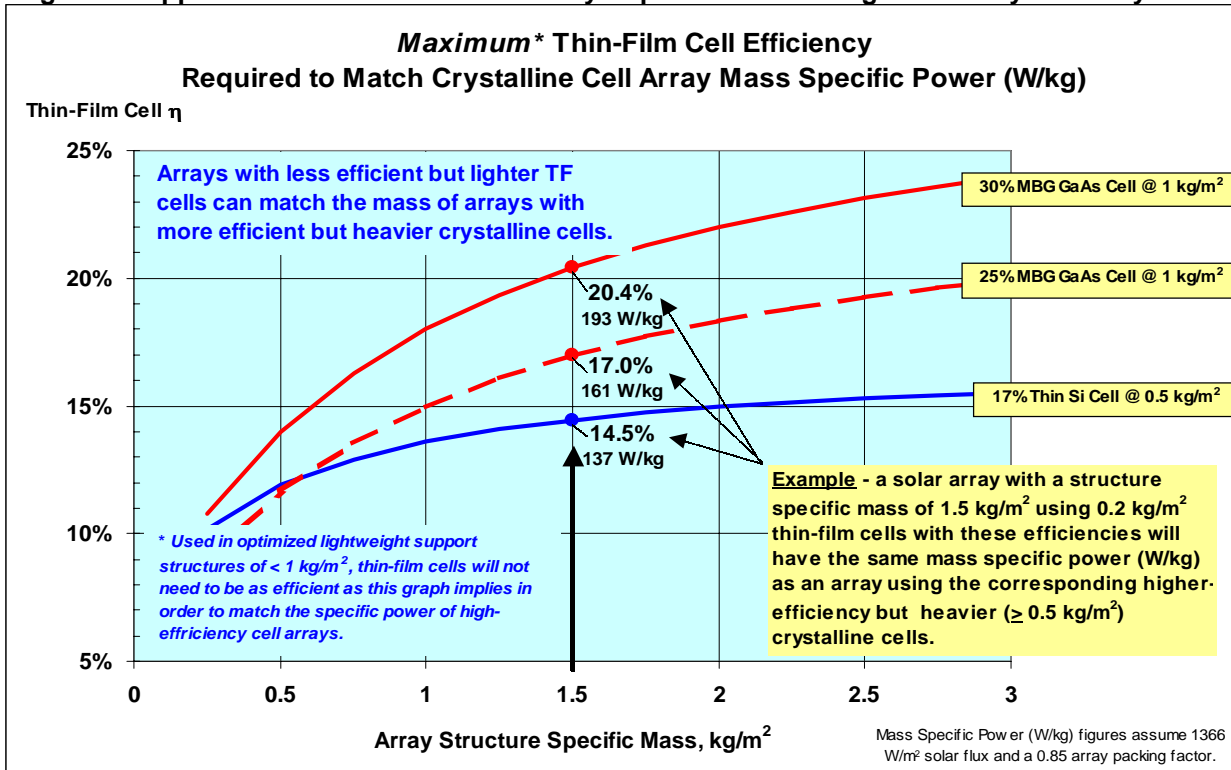


Figure 3 – Larger LEO arrays require in additional propellant.

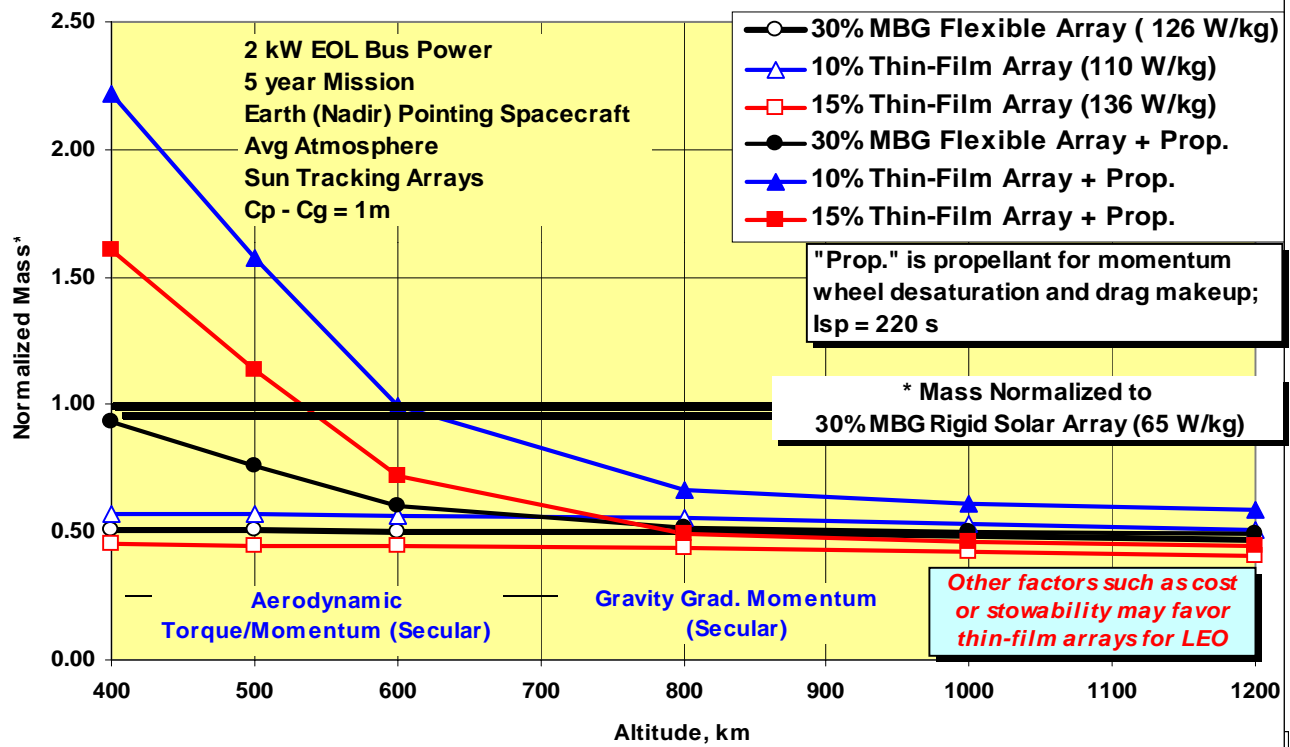


Figure 4 – Shorter mission life mitigates mass impact of larger solar arrays in LEO.

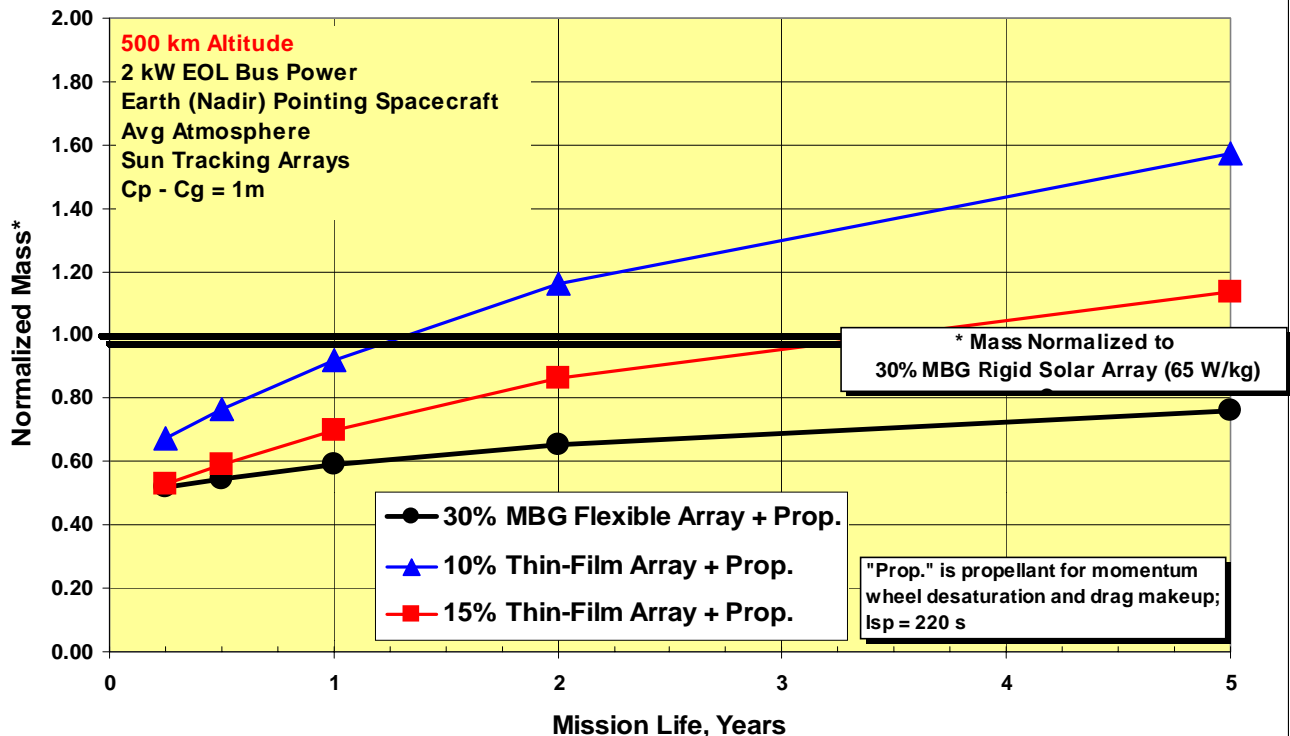


Figure 5 – Larger GEO solar arrays will require additional propellant.

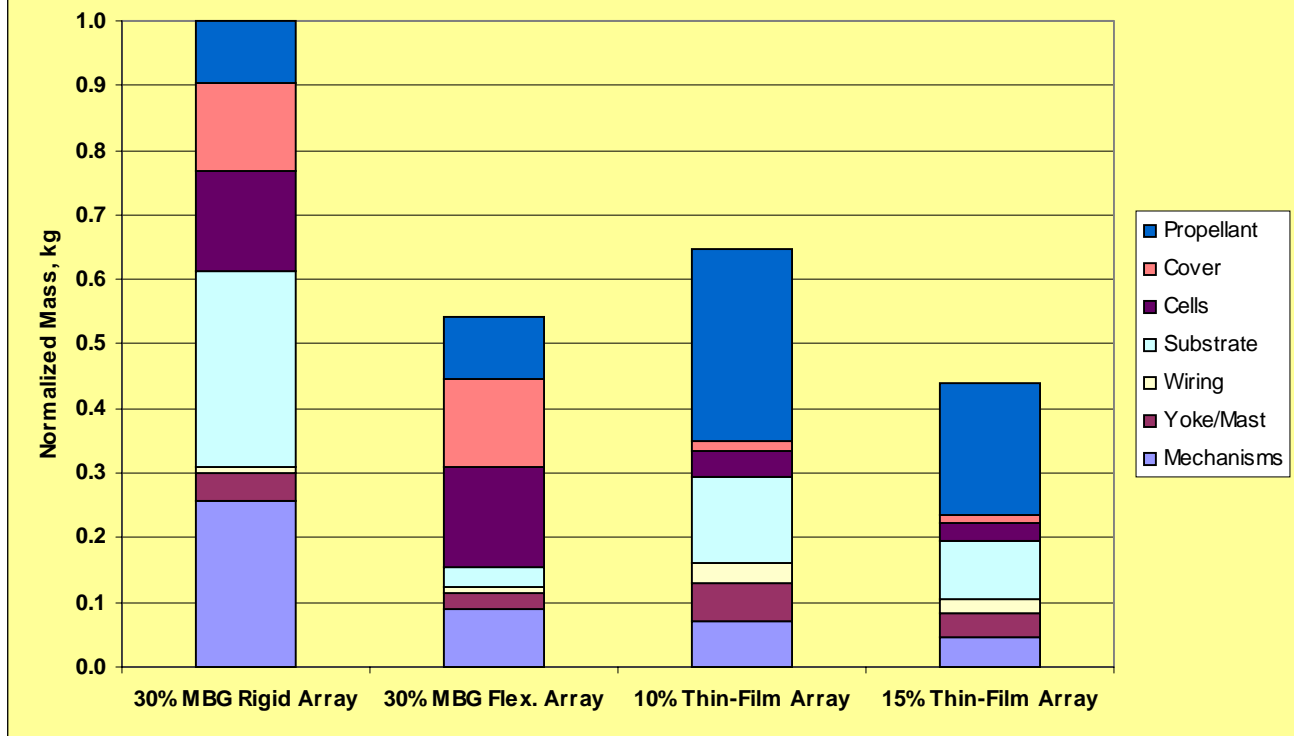
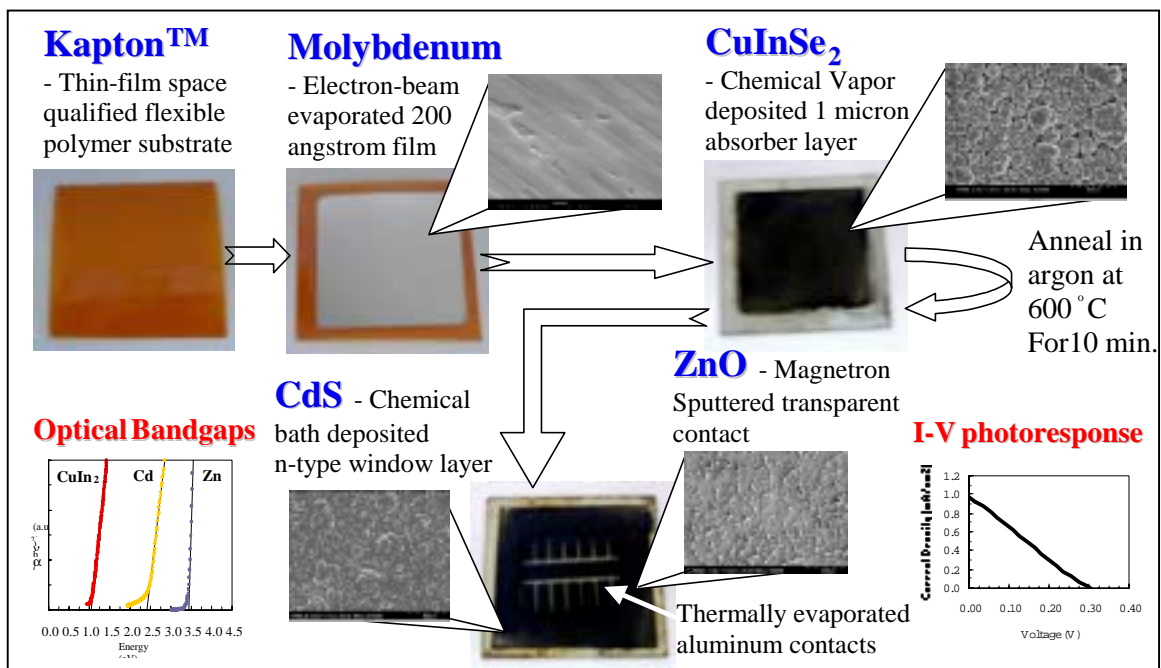


Figure 6 - NASA GRC thin-film cell approach.



ATMOSPHERIC PRESSURE SPRAY CHEMICAL VAPOR DEPOSITED CuInS_2 THIN FILMS FOR PHOTOVOLTAIC APPLICATIONS

J. D. Harris
Cleveland State University, Cleveland, OH 44115

R. P. Raffaele
Rochester Institute of Technology, Rochester, NY 14623

K. K. Banger, M. A. Smith and D.A. Scheiman
Ohio Aerospace Institute, Brookpark, OH 44142

A. F. Hepp
NASA Glenn Research Center, Cleveland, OH 44135

ABSTRACT

Solar cells have been prepared using atmospheric pressure spray chemical vapor deposited CuInS_2 absorbers. The CuInS_2 films were deposited at 390°C using the single source precursor $(\text{PPh}_3)_2\text{CuIn}(\text{SEt})_4$ in an argon atmosphere. The absorber ranges in thickness from 0.75 - 1.0 μm , and exhibits a crystallographic gradient, with the leading edge having a (220) preferred orientation and the trailing edge having a (112) orientation. Schottky diodes prepared by thermal evaporation of aluminum contacts on to the CuInS_2 yielded diodes for films that were annealed at 600°C . Solar cells were prepared using annealed films and had the (top down) composition of $\text{Al/ZnO/CdS/CuInS}_2/\text{Mo/Glass}$. The J_{sc} , V_{oc} , FF and η were 6.46 mA/cm^2 , 307 mV, 24% and 0.35%, respectively for the best small area cells under simulated AM0 illumination.

INTRODUCTION

The National Aeronautics and Space Administration is interested in developing low temperature deposition techniques for producing thin-film photovoltaics (1-5). Low temperature routes ($<400^\circ\text{C}$) allow devices to be deposited onto lightweight polymer substrates such as KaptonTM or polybenzobisoxazole (PBO). These lightweight devices would not only offer cost savings over present technologies, but in many cases would be mission enabling (6). One of the most promising family of materials for photovoltaic applications are the chalcopyrite $\text{Cu}(\text{Ga},\text{In})(\text{S},\text{Se})_2$ alloys. These materials exhibit high absorption coefficients in the visible to near IR spectrum range, are generally prepared as p-type but can also be prepared n-type by adjusting the stoichiometry of the material, have good electrical characteristics and terrestrial stability, and in the case of CuInSe_2 (2), has been demonstrated to be more radiation tolerant than crystalline silicon and gallium arsenide (7). Tests on laboratory scale CuInSe_2 based devices have achieved efficiencies approaching 18% (8). Likewise, CuInS_2 based devices have achieved conversion efficiencies over 11% and its direct band gap of 1.5 eV is near optimal for solar radiation utilization (9, 10). In addition, from an environmental standpoint, CuInS_2 is free from the toxicity concerns associated with the selenium containing analog, and thus may be a more suitable material for terrestrial applications.

To facilitate low temperature deposition, organometallic molecules are used because of their low decomposition temperatures. To avoid premature decomposition of the precursor, atmospheric pressure spray chemical vapor deposition (CVD) was used. Spray CVD combines the benefits of traditional MOCVD with those of spray pyrolysis, while avoiding the disadvantages of each. The technique not only offers film growth in inert

atmospheres, large area deposition and laminar flow over the substrate, which are features usually associated with MOCVD, but it also offers a low temperature solution reservoir, an advantage which comes with spray pyrolysis. The latter feature is an important benefit which can prevent premature precursor decomposition when using thermally sensitive precursor compounds. In addition, this technique allows low volatile precursors to be easily put into the vapor phase, without using high vacuum and/or elevated precursor temperatures, since the precursor solutions are sprayed as aerosols and then swept into the reactor.

In the early 1990's, Kanatzidis and coworkers reported the synthesis of a new family of single source molecular precursors for CuInQ_2 , (where $\text{Q} = \text{S}$ or Se) (11). Several compounds of the type $(\text{PPh}_3)_2\text{CuIn}(\text{QR})_4$ (where $\text{R} =$ ethyl or propyl) were structurally characterized, and it was observed that all the compounds decomposed at temperature below 300°C to yield CuInQ_2 . In follow on work, Hollingsworth and coworkers demonstrated that spray CVD and $(\text{PPh}_3)_2\text{CuIn}(\text{SEt})_4$ could be used to deposit high quality CuInS_2 , as characterized by SEM-EDS, Rutherford Backscattering Spectroscopy and X-ray diffraction (12, 13). However, the only electrical property that was measured for the films was sheet resistivity, which was less than $100 \Omega \text{ cm}$ for a $1 \mu\text{m}$ thick film. The work reported here demonstrates that photovoltaic device quality CuInS_2 can be deposited using single source precursors and atmospheric pressure spray CVD.

EXPERIMENTAL

All operations of moisture- and air-sensitive materials were performed under an argon atmosphere employing standard Schlenk techniques and a double-manifold vacuum line. Solids were manipulated in an argon filled glovebox. Solvents were freshly distilled from appropriate drying agents under Ar prior to use. The single source precursors, $(\text{PPh}_3)_2\text{CuIn}(\text{SEt})_4$ was prepared using a procedure reported elsewhere (11, 12, 14, 15). Precursor purity was monitored by nuclear magnetic resonance spectroscopy (NMR).

Using a spray CVD reactor similar to Hollingsworth's (12, 13), $1 \mu\text{m}$ thick films of CuInS_2 were deposited in 70-90 minutes from 150 ml of 0.01 M solution of $(\text{PPh}_3)_2\text{CuIn}(\text{SEt})_4$ in toluene. The solution was atomized by a 2.5 MHz nebulizer and swept into a two-zone hot-wall reactor by argon carrier gas (4 l/min) that was presaturated with the solvent. Zone one (evaporation zone) of the reactor was held at $128 \pm 1^\circ\text{C}$, and zone two (deposition zone) was held at $390 \pm 1^\circ\text{C}$ during depositions. For films given a post-deposition anneal at higher temperatures, the carrier gas was reduced to a minimal flow and both zones of the furnace were heated to $600 \pm 1^\circ\text{C}$ in 4 minutes, held isothermal for 8 minutes and then allowed to cool to room temperature.

Films were characterized by transmission spectroscopy (Perkin Elmer, Lambda-19), scanning electron microscopy (SEM) (Hitachi S-3000N), Energy Dispersive Spectroscopy (SEM-EDS) (EDAX), profilometry (KLA-Tencor HRP 75) and X-ray diffraction (Philips). Schottky barriers were prepared by thermally evaporating aluminum contacts onto the CuInS_2 films and the diode curves measured. Complete cells with the (top down) composition of $\text{Al/ZnO/CdS/CuInS}_2/\text{Mo/glass}$ were also prepared using the spray CVD deposited films. Films were etched in a 1.5 M KCN solution for one minute, prior to chemical bath deposition of CdS to form the heterojunction. A $1 \mu\text{m}$ thick layer of fluorine-doped ZnO_2 was sputtered on top of the CdS, followed by thermally evaporated aluminum contacts. Complete cells were characterized under a simulated AM0 solar spectrum and diode curves were measured (Tektronix 370A).

RESULTS AND DISCUSSION

As deposited, the well adhering CuInS_2 films were dark blue to black, depending on film thickness. The thickness for a typical film ranged from 0.75 to $1.0 \mu\text{m}$, with grain size for the films less than $0.5 \mu\text{m}$ (Figure 1). As evident from the SEM images, grain growth appears dense and columnar, despite the small grain size (Figure 2). The film thickness varies along the sample, with the thinner portion of the film growing in the "up stream" end of the substrate, and the thick portion of the film growing on the "down stream" end. It is believed this gradient is a

product of temperature inhomogeneity, carrier gas flow rate and incline angle of the substrate holder. Experiments are in progress to minimize the thickness gradient.

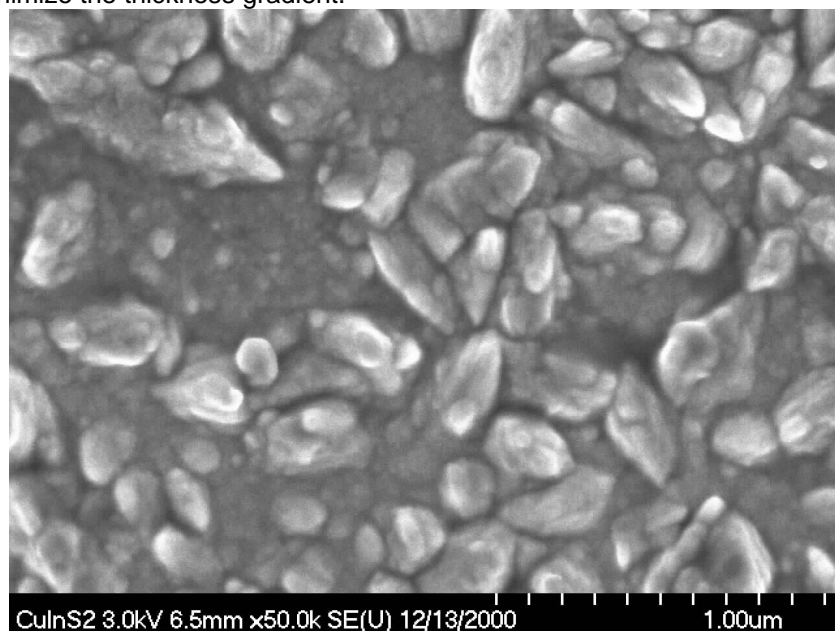


Figure 1. SEM image of CuInS₂ deposited on Mo foil at 390°C at a flow rate of 4 L/min.

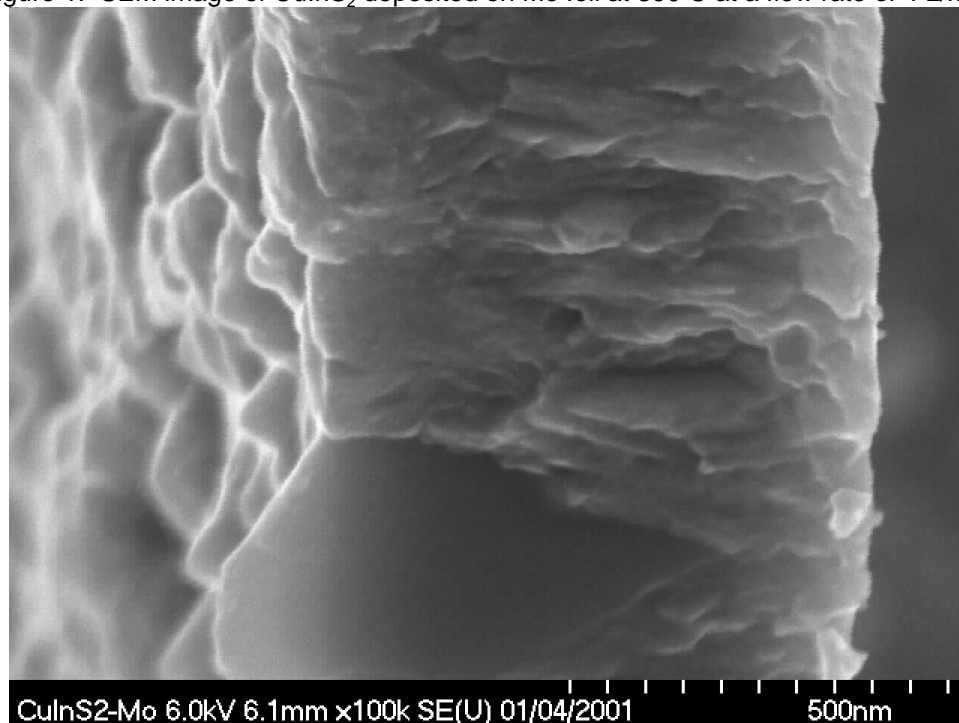


Figure 2. SEM edge-on view of a CuInS₂ film showing film thickness and columnar grain growth.

Along with the thickness gradient, there is also a gradient in the crystallographic orientation of the films. As deposited, the majority of the film is highly (112) oriented. Over the length of the 76 mm long substrate, the

leading 1/3 of the film is (220) oriented, whereas the downstream 2/3 of the film are strictly (112) oriented (Figure 3). Siemer and co-workers have demonstrated that devices prepared from preferred (112) oriented CuInS_2 films have better performance than photovoltaic devices fabricated from other oriented films due mainly to a lower series resistance (16). The reflection at $2\theta = 27^\circ$ in the front film, labeled with an * has been identified as arising from In_2S_3 and In_2Se_3 in films of CuInS_2 and CuInSe_2 , respectively, prepared by spray pyrolysis. However, spray pyrolyzed films only yield the spurious reflection when indium rich solutions were sprayed. For films grown by spray CVD, the reflection is only observed on the leading 1/3 of the film, yet as will be discussed later, composition of the films remain constant from front to back. Films deposited by spray CVD also lack the (101) reflection at $2\theta = 17.914^\circ$. It is unknown whether this is a product of preferred orientation or lack of long range order since chalcopyrite has the zinc-blend structure with a doubled c-axis and alternating Cu and In atoms replacing the Zn atoms. Using a similar spray CVD reactor, Hollingsworth demonstrated that crystal orientation is a function of both carrier gas flow rate and solution concentration (13). It is anticipated that experiments to reduce the thickness gradient will improve the orientation gradient as well.

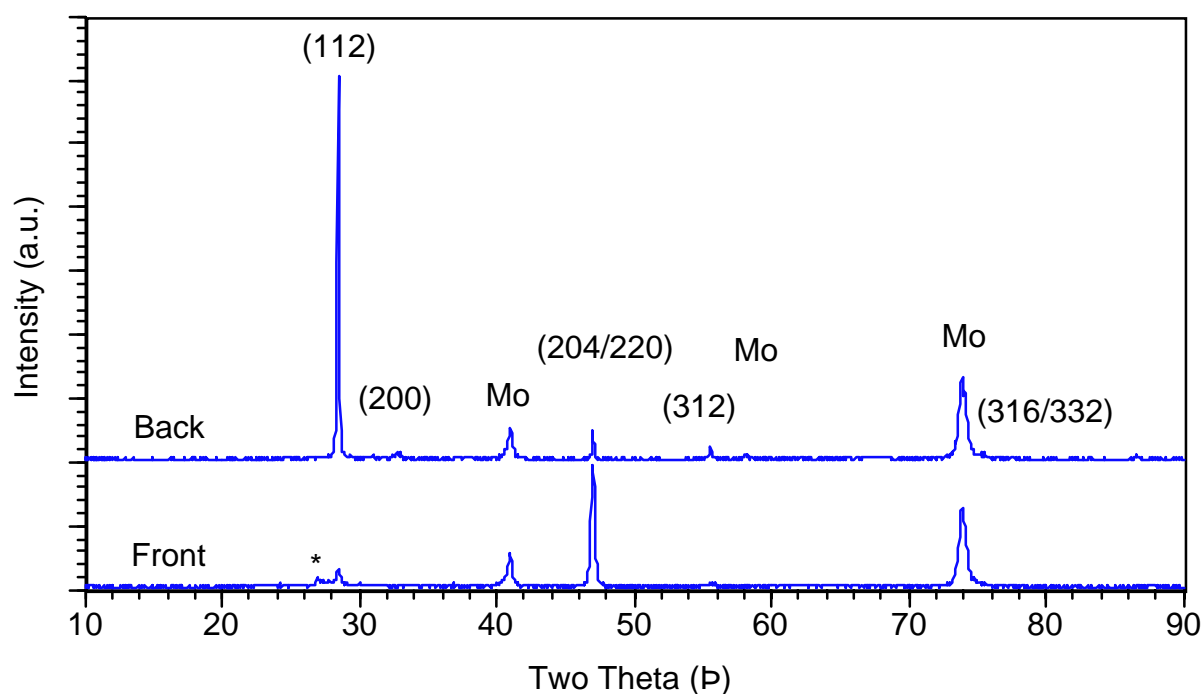


Figure 3. X-ray powder diffraction spectra of a CuInS_2 film on Mo coated glass.

Films were deposited onto a variety of substrates, including Ti, Mo and Ni foils, Kapton™, PBO, SiO_2 , and Mo coated glass. In all cases, SEM-EDS measurements revealed the films were nearly stoichiometric CuInS_2 , or only slightly indium and sulfur rich, (with atomic percents for Cu, In and S as 23%, 24% and 53%, respectively). Films deposited on all substrates, except nickel, show no evidence of phosphorous or carbon by SEM-EDS, indicating that the precursor molecules decompose cleanly. Within experimental error of SEM-EDS, the stoichiometry of the films remain constant along their length. SEM-EDS data for films deposited on nickel substrates revealed large quantities of phosphorous (16%) in the material. SEM-EDS measurements of as deposited films on nickel gave atomic percents for Cu, In, S and P as 24%, 17%, 43% and 16%, respectively. This implies that nickel substrates promote the cracking of the phosphine during deposition, and would thus be unacceptable for device preparation without a passivating layer.

To evaluate the electrical properties of the deposited films, current versus voltage (IV) measurements were recorded for the films using thermally evaporated aluminum point contacts ($10\text{ }\mu\text{m}^2$) to make Schottky barrier diodes. Many of the Schottky barriers were excellent diodes on films annealed at 600°C , with "turn on" voltages of 0.6 - 0.8 volts and little leakage when reverse biased. However, many of the contacts on the as-deposited films gave large reverse bias currents and nearly ohmic response. This behavior is indicative of degeneracy of the semiconductor due to a high carrier density resulting from native defects. The improvement in the diode behavior of the annealed films is attributed to enhanced crystallinity and reduction of defects, as considerable narrowing of the diffraction lines was observed in the annealed films.

Solar cells were prepared from annealed films deposited on Mo coated glass substrates. The $10\text{ mm} \times 76\text{ mm}$ cell was mechanically scribed into many smaller cells, with an IV curve for each being measured under a simulated AM0 light source. The maximum efficiency achieved by one of the small area cells was 0.35% (Figure 4), which was located on the back third of the substrate and had a total area of 0.15 cm^2 . The most obvious feature of the JV curve is the lack of a "knee," given that the curve is nearly linear. From the data near the open circuit voltage (V_{oc}), the device appears to have high series resistance. At this time it is unknown whether the series resistance is from the absorber layer, from the interfaces between the different layers or both. From the slope of the line near the short circuit current (J_{sc}), the film also has high shunt resistance. The mechanical scribing of the small area cells could have caused the shunting; future small area cells will be prepared lithographically.

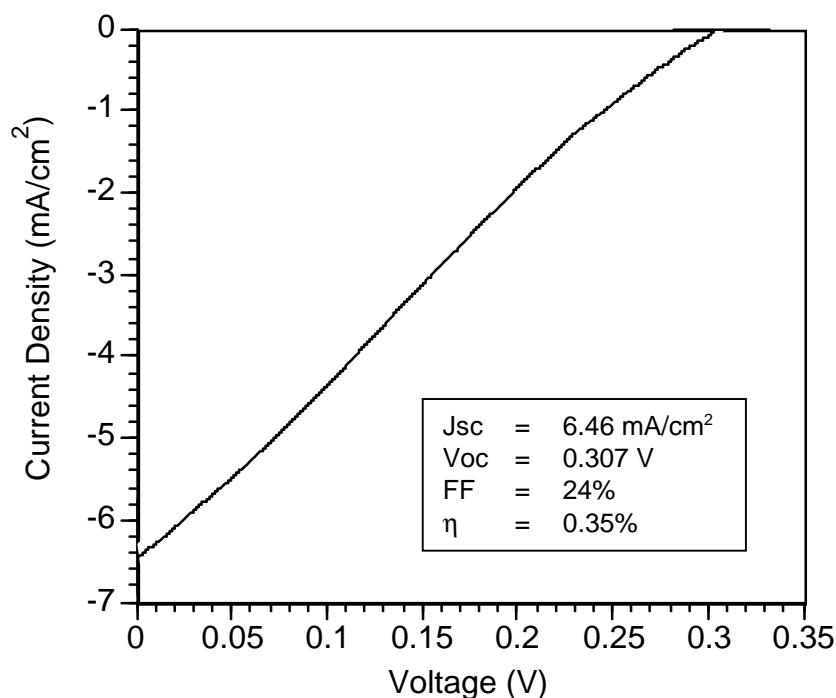


Figure 4. JV curve for small area CuInS_2 cell on Mo coated glass.

CONCLUSION

Working photovoltaic devices have been prepared from atmospheric pressure spray CVD deposited CuInS_2 thin films using the single source precursor $(\text{PPh}_3)_2\text{CuIn}(\text{SEt})_4$. Although the V_{oc} , J_{sc} and fill factor are low, it is anticipated that these will increase as deposition parameters are optimized. X-ray diffraction of the films reveals there is a preferred orientation gradient along the substrate, with only the back two thirds of the film having the

desired (112) crystal orientation. The films also range in thickness, with the leading edge being thinner than the trailing edge. Spray CVD is a promising technique for depositing CuInS_2 on to low temperature substrates such as Kapton™ and PBO and temperatures below 400°C. However, the films with the best electrical properties were annealed at 600°C following deposition.

REFERENCES

- [1] J. D. Harris, D. G. Hehemann, J. E. Cowen, A. F. Hepp, R. P. Raffaele, and J. A. Hollingsworth, "Using Single Source Precursors and Spray Chemical Vapor Deposition to Grow Thin-Film CuInS_2 ," Proc. of the 28th IEEE Photovoltaic Specialists Conference, pp. 563-566, Anchorage, AK, 2000.
- [2] R. P. Raffaele, J. G. Mantovani, S. G. Bailey, A. F. Hepp, E. M. Gordan, and R. Haraway, "Electrodeposited CuInSe_2 Thin Film Junctions," NASA Lewis Research Center, Cleveland, OH, NASA Technical Memorandum TM-97-206322, November 1997.
- [3] R. P. Raffaele, T. Potdevin, A. F. Hepp, and S. G. Bailey, "Electrochemical synthesis of CuInSe_2 for thin film devices," *Mat. Sci. Semi. Process.* 2, pp. 289-296, 1999.
- [4] R. Friedfeld, R. P. Raffaele, and J. G. Mantovani, "Electrodeposition of $\text{CuIn}_x\text{Ga}_{1-x}\text{Se}_2$ thin films," *Solar Energy Materials & Solar Cells*, **58**, pp. 375-385, 1999.
- [5] R. P. Raffaele, W. Juneke, J. Gorse, T. Thompson, J. D. Harris, J. Cowen, D. Hehemann, G. Rybicki, and A. F. Hepp, "Wet-Chemical Synthesis of Thin-Film Solar Cells," *Mat. Res. Soc. Symp. Proc.*, **606**, pp. 115-162, 2000.
- [6] D. J. Hoffman, T. W. Kerslake, A. F. Hepp, M. K. Jacobs, and D. Ponnusamy, "Thin-Film Photovoltaic Solar Array Parametric Assessment," Proc. of the AIAA 35th. Intersociety Energy Conversion Engineering Conference, pp. 670-680, Las Vegas, NV, 2000.
- [7] A. Rockett and R. W. Birkmire, " CuInSe_2 for photovoltaic applications," *J. Appl. Phys.*, **70**, pp. R81, 1991.
- [8] H. S. Ullal, K. Zweibel, and B. G. von Roedern, "Current Status of Polycrystalline Thin-Film PV Technologies," 26th IEEE Photovoltaic Specialists Conference, pp. 301-305, Anaheim, CA, 1997.
- [9] J. Klaer, I. Luck, K. Siemer, R. Klenk, and D. Bräunig, "Progress in CuInS_2 Submodules," Proc. of the 28th IEEE Photovoltaic Specialists Conference, pp. 559-562, Anchorage, AK, 2000.
- [10] C. Dzionk, H. Metzner, S. Hessler, and H.-E. Mahnke, *Thin Solid Films*, **299**, pp. 38, 1997.
- [11] W. Hirpo, S. Dhingra, A. C. Sutorik, and M. G. Kanatzidis, "Synthesis of Mixed Copper-Indium Chalcogenolates. Single-Source Precursors for the Photovoltaic Materials CuInQ_2 (Q = S, Se)," *J. Am. Chem. Soc.*, **115**, pp. 1597-1599, 1993.
- [12] J. A. Hollingsworth, W. F. Buhro, A. F. Hepp, P. P. Jenkins, and M. A. Stan, "Spray Chemical Vapor Deposition of CuInS_2 Thin Films for Application in Solar Cell Devices," *Mat. Res. Soc. Symp. Proc.*, **495**, pp. 171-176, 1998.
- [13] J. A. Hollingsworth, A. F. Hepp, and W. E. Buhro, "Spray CVD of Copper Indium Disulfide Films: Control of Microstructure and Crystallographic Orientation," *Chem. Vap. Deposition*, **5**, pp. 105-108, 1999.

- [14] G. J. Kubas, B. Monzyk, and A. L. Crumbliss, "Tetrakis(acetonitrile)Copper(I) Hexafluorophate," *Inorg. Synth.*, **19**, pp. 90-92, 1979.
- [15] J. Díez, S. Falagán, P. Gamasa, and J. Gimeno, "Preparation of New Mono and Polynuclear Bis(triphenylphosphine) Copper(I) Derivatives Containing Mono and Bidentate N-heterocycles, 8-hydroxyquinoline and Oxalate Ligands," *Polyhedron*, **7**, pp. 37-42, 1988.
- [16] K. Siemer, J. Klaer, I. Luck, and D. Bräunig, "Influence of Crystal Orientation on Device Performance of CuInS_2 Solar Cells," Proc. of the 28th IEEE Photovoltaic Specialists Conference, pp. 630-633, Anchorage, AK, 2000.

CIGS2 THIN-FILM SOLAR CELLS ON FLEXIBLE FOILS FOR SPACE POWER¹

Neelkanth G. Dhere, Shantinath R. Ghongadi, Mandar B. Pandit, Anant H. Jahagirdar
Florida Solar Energy Center, 1679 Clearlake Road, Cocoa, FL 32922-5703

David Scheiman

Ohio Aerospace Institute, NASA Glenn Research Center, Cleveland, Ohio 44135

$\text{CuIn}_{1-x}\text{Ga}_x\text{S}_2$ (CIGS2) thin-film solar cells are of interest for space power applications because of the near optimum bandgap for AM0 solar radiation in space. CIGS2 thin film solar cells on flexible stainless steel (SS) may be able to increase the specific power by an order of magnitude from the current level of 65 Wkg^{-1} . CIGS solar cells are superior to the conventional silicon and gallium arsenide solar cells in the space radiation environment. This paper presents research efforts for the development of CIGS2 thin-film solar cells on 127 μm and 20 μm thick, bright-annealed flexible SS foil for space power. A large-area, dual-chamber, inline thin film deposition system has been fabricated. The system is expected to provide thickness uniformity of $\pm 2\%$ over the central 5" width and $\pm 3\%$ over the central 6" width. During the next phase, facilities for processing larger cells will be acquired for selenization and sulfurization of metallic precursors and for heterojunction CdS layer deposition both on large area. Small area CIGS2 thin film solar cells are being prepared routinely. Cu-rich Cu-Ga/In layers were sputter-deposited on unheated Mo-coated SS foils from CuGa (22%) and In targets. Well-adherent, large-grain Cu-rich CIGS2 films were obtained by sulfurization in a $\text{Ar}:\text{H}_2\text{S}$ 1:0.04 mixture and argon flow rate of 650 sccm, at the maximum temperature of 475°C for 60 minutes with intermediate 30 minutes annealing step at 120°C . Samples were annealed at 500°C for 10 minutes without H_2S gas flow. The intermediate 30 minutes annealing step at 120°C was changed to 135°C . p-type CIGS2 thin films were obtained by etching the Cu-rich layer segregated at the surface using dilute KCN solution. Solar cells were completed by deposition of CdS heterojunction partner layer by chemical bath deposition, transparent-conducting ZnO/ZnO:Al window bilayer by RF sputtering, and vacuum deposition of Ni/Al contact fingers through metal mask. PV parameters of a CIGS2 solar cell on 127 μm thick SS flexible foil measured under AM 0 conditions at NASA GRC were: $V_{\text{oc}} = 802.9 \text{ mV}$, $J_{\text{sc}} = 25.07 \text{ mA/cm}^2$, $\text{FF} = 60.06\%$, and efficiency $\eta = 8.84\%$. For this cell, AM 1.5 PV parameters measured at NREL were: $V_{\text{oc}} = 788 \text{ mV}$, $J_{\text{sc}} = 19.78 \text{ mA/cm}^2$, $\text{FF} = 59.44\%$, efficiency $\eta = 9.26\%$. Quantum efficiency curve showed a sharp QE cutoff equivalent to CIGS2 bandgap of $\sim 1.50 \text{ eV}$, fairly close to the optimum value for efficient AM0 PV conversion in the space.

1. INTRODUCTION

Lightweight flexible thin film solar cells have many promising applications in space and terrestrial photovoltaic power systems [1]. Future space missions would include very large satellites such as solar power satellites and very small satellites. Long-term plans envisage swarms of distributed, autonomous, small satellites termed microsats or even nanosats to perform specific tasks. Some missions will use solar electric propulsion (SEP) instead of rockets. CIGS2 thin film solar cells on flexible stainless steel (SS) may be able to increase the specific power by an order of magnitude from the current level of 65 Wkg^{-1} . Thin-film technology could conservatively reduce the array-manufacturing cost of medium-sized five-kilowatt satellite from the current level of \$2000k to less than \$500k [2]. Weight benefits of higher efficiency cells are decreased and high costs become less affordable in the case of flexible thin-film blanket arrays that can be easily rolled out. Non-rigid cells also have an advantage in stability. Because of the low initial velocities and steady acceleration, SEP satellites must spend long periods in intense regions of trapped radiation belts. CIGS solar cells are superior to the conventional silicon and gallium arsenide solar cells in the space radiation

¹ This work was supported by the NASA Glenn Research Center and by the Air Force Research Lab through Jackson and Tull.

environment. The potential for improved radiation resistance of thin-film solar cells relative to single-crystal cells, could extend mission lifetimes substantially. Recent studies have shown that 12.6% efficient, thin film cells would start to become cost-competitive in GEO and LEO missions [3]. However, significant technological hurdles remain before thin-film technology could be implemented as the primary power source for spacecraft.

There is a recent interest in the development of CIGS2 solar cells on flexible substrates. Several groups have reported fabrication of polycrystalline $\text{CuIn}_{1-x}\text{Ga}_x\text{Se}_2$ (CIGS) solar cells on flexible foils substrates [4]. The CIGS cell with an efficiency exceeding 17% has been obtained using SS substrate [4].

The objective of the present research is to develop ultra-lightweight, radiation-resistant, highly efficient, high specific power $\text{CuIn}_{1-x}\text{Ga}_x\text{S}_2$ (CIGS2) thin-film solar cells for space electric power. Small proportion of gallium is being incorporated so as to obtain benefits of improved adhesion, slightly higher bandgap, and incorporation of back-surface field as has been done with CIGS cells. Initially CIGS2 thin film solar cells are being fabricated on 127 μm thick SS substrates. The main thrust is towards development of fundamental understanding and baseline processes rather than attaining the highest efficiencies.

2. EXPERIMENTAL TECHNIQUE

Bright annealed stainless steel foils with thickness of 127 μm and 20 μm were used as substrate. Copper, gallium and indium layers were sputtered in the ratio of $\text{Cu}/(\text{In}+\text{Ga}) \sim 1.4$. CIGS2 thin films were prepared using a two-step process. The first step involved deposition of alternate layers of (Cu+Ga) and In on molybdenum coated flexible substrate. This formed a stacked elemental layer sequence that produced a predominant $\text{Cu}_{11}\text{In}_9$ precursor phase. This layer was sulfurized in H_2S : Ar gas environment using a three zone furnace at temperatures in the range of 135 to 475° C. Sulfurization time was varied from 20 – 60 minutes. Samples were annealed at 500° C for 10 minutes without H_2S gas flow in Ar atmosphere. The initial dwell of 120° C for 30 minutes was changed to 135° C for 25 minutes without H_2S gas flow during sulfurization. It was found that the binary $\text{Cu}_{11}\text{In}_9$ precursor phase reacted in H_2S : Ar gas environment to form a good crystalline pseudo-quaternary phase of CIGS2 film. Some samples were sulfurized at 475° C for 30 minutes followed by annealing at 500° C for 10 minutes. This annealing step favored grain growth and recrystallization. The Cu-rich stoichiometry during the growth of CIGS2 films results in an improved morphology, i.e. enhanced grain sizes of the polycrystalline films. For selenide system, this phenomenon is attributed to CuSe liquid formed on top of Cu-rich films [5]. For the sulfur system, according to the phase diagram of Cu-S, the respective liquid phase is not expected in the substrate temperature range of $T_{\text{sub}} < 600^\circ \text{C}$. However, due to the high cation mobility in the Cu-S compounds, the cation lattice in a binary Cu-S phase at the surface of a growing CIS2 film behaves as a quasi-liquid. The Cu_xS phase was etched using 10% KCN. This was followed by deposition of CdS buffer layer by chemical bath method and ZnO window layer (Fig.1). Bright annealed stainless steel foils of 20 and 127 μm thickness respectively were evaluated as possible substrate materials for polycrystalline CIGS2 solar cell. The phases, surface morphologies and elemental depth profiles of the CIGS2 films prepared on stainless steel flexible foils substrates were characterized.

Films were examined visually for their appearance, color and any tendency of peeling. X-ray diffraction (XRD) was used to identify the crystalline phases using a RIGAKU diffractometer. The 2θ range for the diffractometer was set from 10 to 80° with a step size of 0.02°. Surface morphology study of the CIGS2 thin film was performed using Scanning electron microscopy (SEM). Chemical composition was analyzed by employing electron probe microanalysis (EPMA). Depth profiling was performed using secondary ion mass spectroscopy (SIMS) and Auger electron spectroscopy (AES) with simultaneous sputter etching. The substrate surface roughness was measured using DEKTAK³ surface profile measuring system.

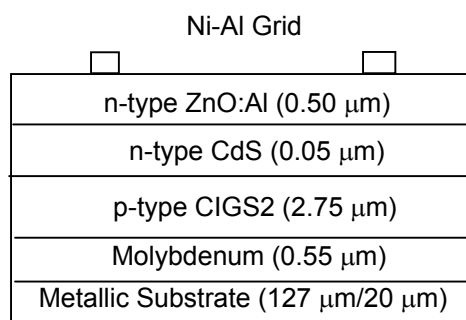


Figure 1. Layer sequence of CIGS2 thin film solar cell.

3. RESULTS AND DISCUSSION

To avoid the formation of voids before the initiation of sulfurization, the initial dwell of 30 minutes at 120° C was changed to 135° C, and the flow of H₂S gas was started after 25 minutes at 135° C [6]. The X-ray diffraction spectrum of the as-deposited (Cu+Ga)/In metallic precursors processed at 135° C indicated the presence of highly oriented Cu₁₁In₉ phase without any elemental or alloy phases. Figure 2 is the XRD pattern of a near stoichiometric, slightly Cu-poor, etched CIGS2 thin film. It showed (101), (112), (103), (004)/(200), (213), (204)/(200), (116)/(312), (008)/(400), and (332) reflections of CuIn_{0.7}Ga_{0.3}S₂ phase. The strongest reflection was from (112) set of planes at 27.62°. Mo peak was obtained 40.22°. The lattice parameters calculated were a 5.67 Å and c 11.34 Å. The spectra stayed well above the base line in between the (112)_{CuInS₂} and the (112)_{CuGaS₂} maxima indicating the pseudo-quaternary phase with varying Ga/(In+Ga) ratio. Ga diffused towards Mo back contact creating a compositional gradient that resulted in a localized Ga poor phase on the surface and in the bulk of material and Ga rich phase near back contact in polycrystalline CIGS2 thin film [7]. Because of the compositional gradient in Ga content with Ga/(Ga+In) ratio of 0.13 at the surface and 0.23 near the back contact, peaks were broad at the base line of the spectra showing reflection from (112) set of planes with Ga poor phase on the surface. In case of random orientation, the intensity ratio of (112) with respect to (220)/(204) peaks, should be 1.5. The intensity ratio of I₁₁₂/I_{220/204}, for these films, was remarkably very high, showing a very high degree of preferred orientation towards (112) reflection that was beneficial for good lattice matching with CdS for efficient device fabrication.

Despite the very Cu-rich film of unetched sample with Cu/(In+Ga) ratio up to 1.68 no secondary phases could be detected in the XRD pattern for unetched sample [8]. As discussed earlier a Cu-rich stoichiometry during the growth of CIGS2 films results in an improved morphology, i.e. enhanced grain sizes of the polycrystalline films. This excess Cu_xS was etched using 10% KCN.

The surface scanning electron micrograph (SEM) of a near stoichiometric, slightly Cu-poor, etched CIGS2 thin film is shown in figure 3. SEM image for the sample showed large, well faceted grains with slight porosity. The porosity was observed at the grain boundaries from where the Cu_xS phases have been etched. The grain size measured by intercept method was 3 µm i.e. comparable to film thickness.

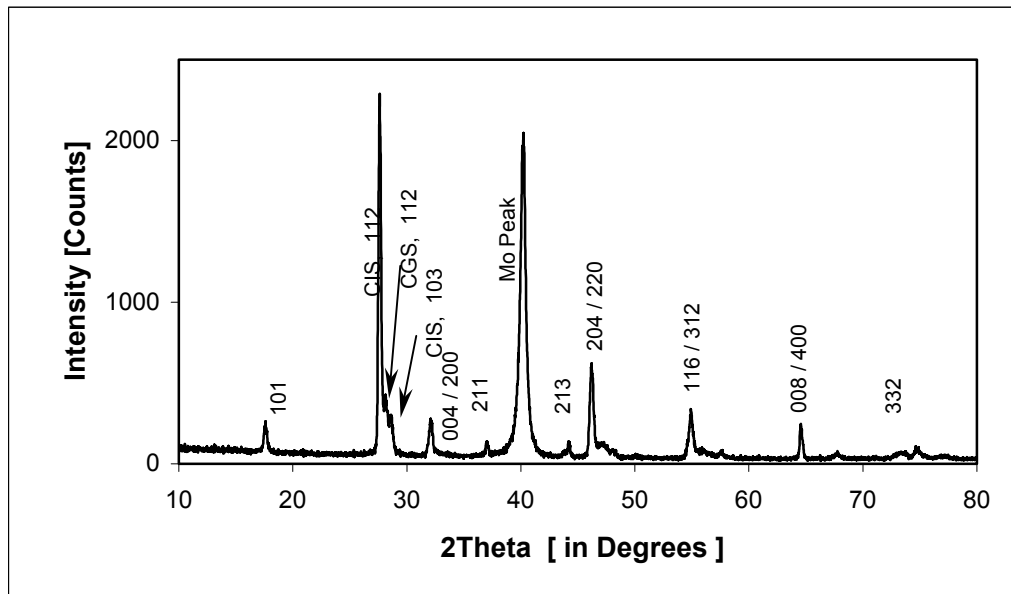


Figure 2. XRD pattern from a near stoichiometric, slightly Cu-poor, etched CIGS2 thin film.

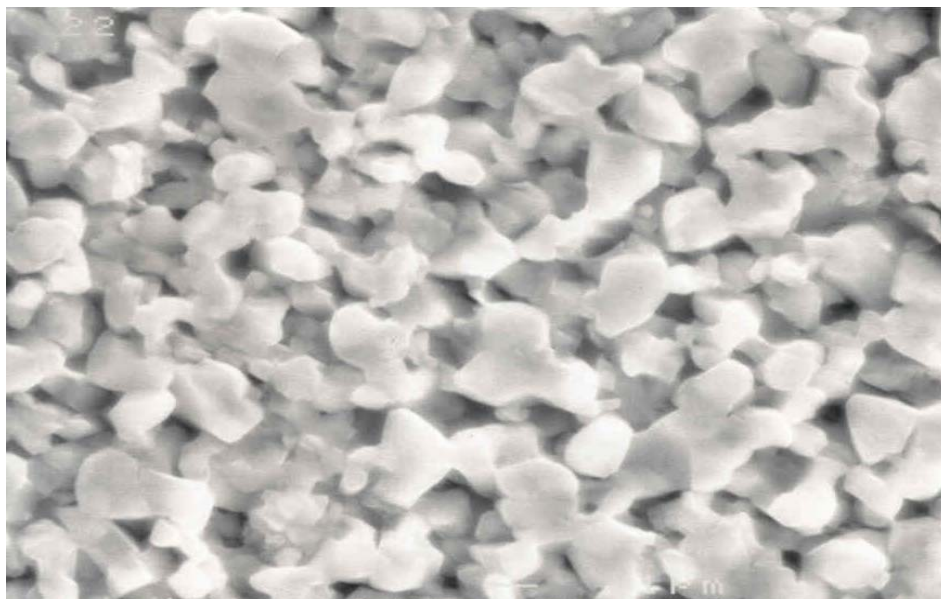


Figure 3. Surface SEM image of a near stoichiometric, slightly Cu-poor, etched CIGS2 thin film.

AES survey (Fig. 4) of near stoichiometric, slightly Cu-poor, etched CIGS2 thin film sample was performed over a range of kinetic energies of 50-2250 eV. The primary electron beam having energy of 5 keV was made incident on the sample surface for analysis. A representative area of sample was chosen and an AES survey was carried out at magnification of 1000x equivalent to an area of 102 μm x 102 μm . An AES survey over the selected area showed presence of copper at 60, 777, 850, and 924 eV, sulfur at 151, and 2131 eV, indium at 345, and 410 eV, gallium at 1071 eV, carbon at 273 eV, potassium at 252 eV and oxygen at 515 eV. The surface atomic concentrations calculated by using the peak-to-peak height from AES survey and relative sensitivities of the respective elements were as follows: copper 20.67 atomic (at.) %, sulfur 31.62 at. %, indium 12.63 at. %, gallium 6.92 at. %, potassium 7.72 at. %, oxygen 11.92 at. % and carbon 15.04 at. %.

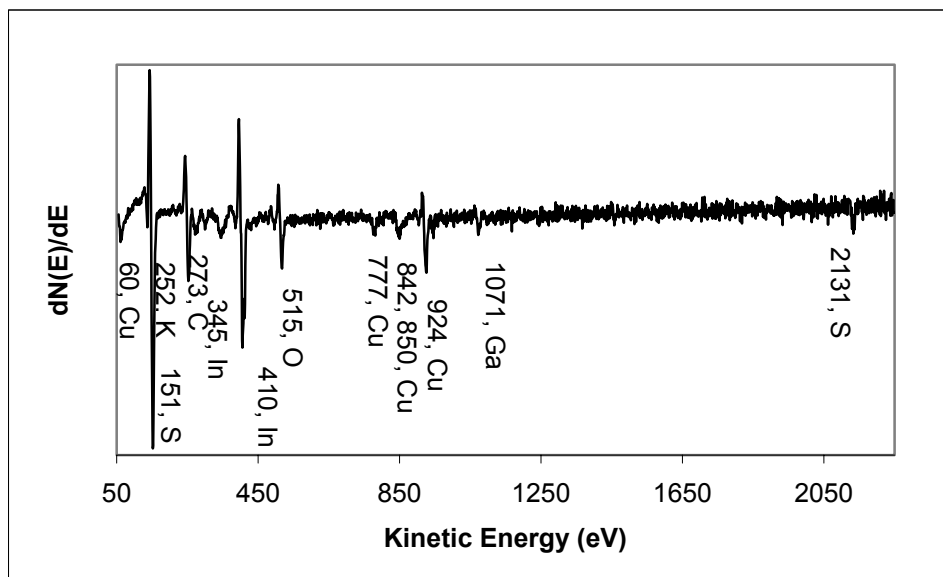


Figure 4. Surface AES survey of near stoichiometric, slightly Cu-poor, etched CIGS2 thin film.

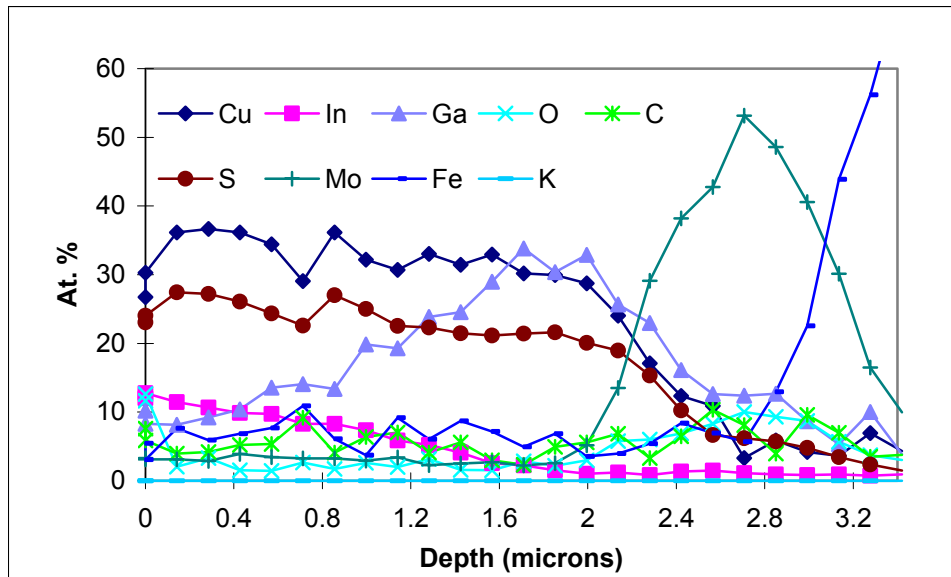


Figure 5. AES depth profile of near stoichiometric, slightly Cu-poor, etched CIGS2 thin film.

AES depth profile was obtained by sputtering an area of $1 \times 1 \text{ mm}^2$ with energetic argon ions at a rate of 475 Å/min for 72 minutes. Figure 5 shows peak heights at different depths (time) for different element. The peak heights were obtained for the following elements: copper, indium, gallium, oxygen, carbon, sulfur, molybdenum, iron and potassium. Copper and sulfur concentration showed the same trend. It decreased near the Mo back contact. Potassium was detected at the surface. Its concentration decreased rapidly in the bulk. Potassium was attributed to KCN treatment that was used to etch away excess Cu_xS phase. Indium concentration is constant in most of the thickness of CIGS2 layer and falls near the Mo back contact. Concentration of gallium at the surface was approximately 10% while at the CIGS/Mo interface it was 30%. This showed that Ga concentration increased towards the back Mo contact. Indium concentration decreased with depth and was negligible at CIGS/Mo interface. The apparent humps in the depth profiles are caused by a non-uniform sputter-etching rate. It can be seen that the film thickness of etched CIGS2 sample from depth profile was approximately 2.4 μm .

SIMS depth profiling (Fig.6) was performed on an etched samples by positive SIMS using CAMECA IMS – 3F system with oxygen primary beam current of 150 nA, impact energy of 5.5 keV angle of incidence of 42° , rastered over $250 \text{ μm} \times 250 \text{ μm}$ area, with source at 10 keV and sample at 4.5 keV. The corresponding unetched sample had $\text{Cu}/(\text{In}+\text{Ga}) \sim 1.4$ and was sulfurized at 475°C for 30 minutes and annealed for 10 minutes each at 475 and 500°C respectively. Slightly Cu-poor, etched CIGS2 thin film sample was monitored for eight species. To realize high sensitivity measurements secondary positive cluster ions such as ^{23}Na , ^{34}S , K , ^{54}Fe , ^{65}Cu , $^{69}(\text{Ga}+\text{O})$, ^{92}Mo , and $^{113}(\text{In}+\text{O})$ were used for detection of Na, S, K, Fe, Cu, Ga, Mo, and In respectively. Cu concentration was mostly constant over the depth of the film. Ga concentration remained constant till 1 μm and then increased till the Mo back contact. Indium concentration remained constant through most of film thickness and decreased near the Mo back contact. Na was not added intentionally. S concentration was uniform throughout film thickness. Na concentration at surface of substrate was attributed to residue left due to cleaning with soap solution. Potassium incorporation was due to etching of Cu_xS phase present on the grains and near the grain boundaries with KCN solution. No sharp interfaces were observed at CIGS2/Mo and Mo/Substrate respectively. This was probably because of the interdiffusion of species and porosity formed due to etching with 10% KCN treatment.

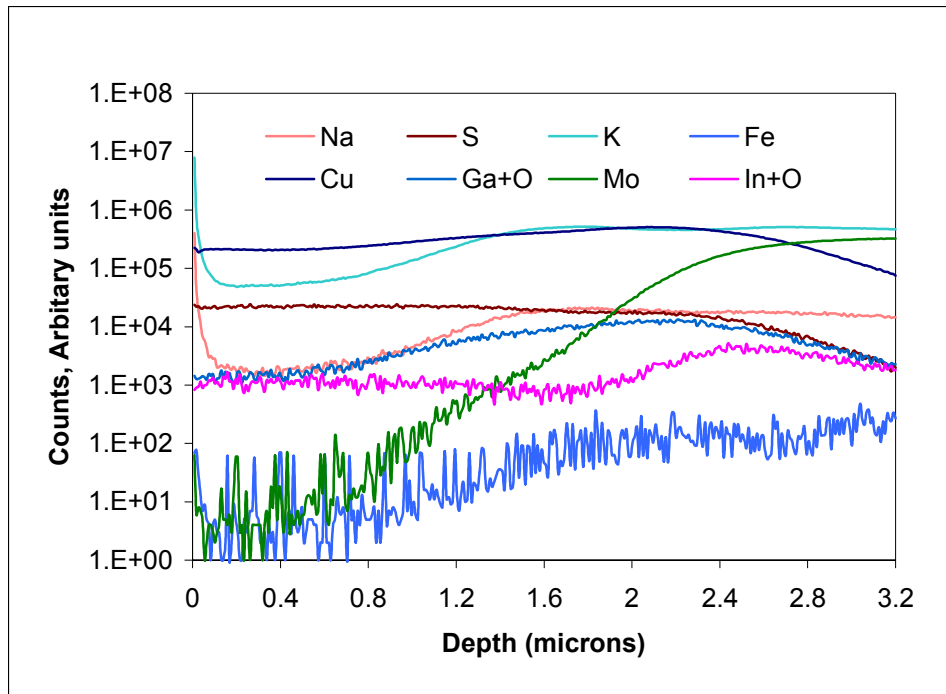


Figure 6. SIMS depth profile of near stoichiometric, slightly Cu-poor, etched CIGS2 thin film.

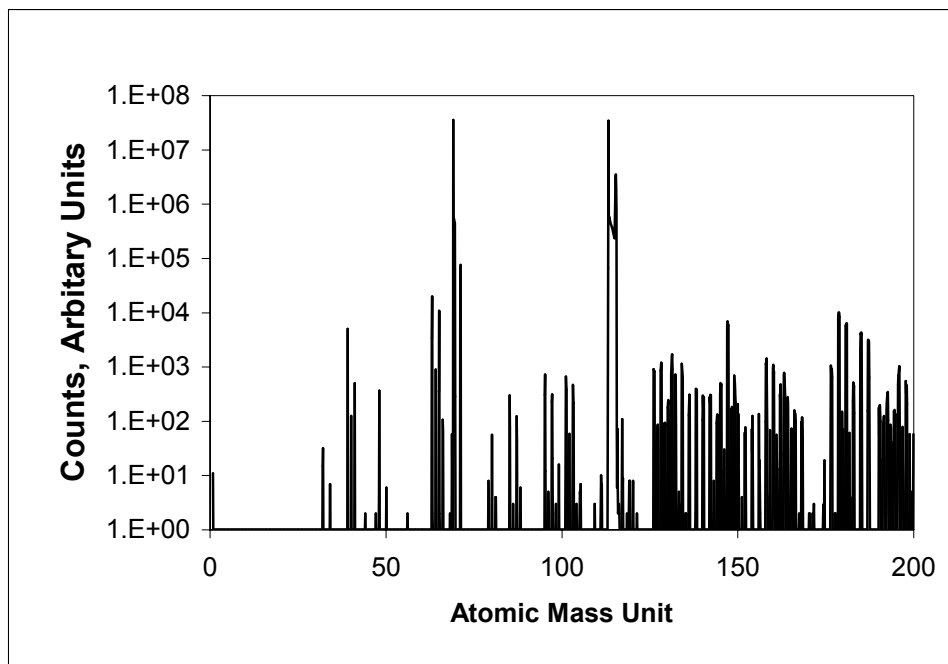


Figure 7. SIMS mass spectra of near stoichiometric, slightly Cu-poor, etched CIGS2 thin film.

The mass spectrum recorded from masses of 1 to 200 is shown in figure 7. Sharp peaks were observed for elemental and molecular species such as O_2^+ , S^+ , K^+ , Ca^+ , SO^+ , Cu^+ , Ga^+ , GaO^+ , CuO^+ , CuO^{++} , In^+ , InO^+ , and InO_2^+ . Na was not detected during analysis of mass spectra. Because of large number of isotopes of Cu, In, Mo, Ga, and S, a number of mass interferences were observed. The mass spectrum clearly indicated presence of Cu, In, Ga, S, Mo and K.

The chemical composition of CIGS2 films was analyzed by EPMA. Average atomic concentrations measured at 10 KV and 20 KV for an unetched sample showed Cu: In: Ga: S proportion of 51.52: 7.80: 1.83: 38.83 and 41.90: 10.92: 2.56: 44.63 respectively. The Cu: In: Ga: S atomic concentrations for the etched sample at 10 KV and 20 KV were found to be 27.38: 21.61: 3.30: 47.71 and 23.96: 19.36: 5.70: 50.99 respectively. The compound formulae were $Cu_{1.09}In_{0.87}Ga_{0.13}S_2$ and $Cu_{0.96}In_{0.77}Ga_{0.23}S_2$ respectively. The Cu: In: Ga: S atomic concentrations for the etched sample deposited on 20 μm thick SS foil at 20 KV were found to be 28.60: 14.90: 11.42: 45.10. The compound formula was $Cu_{1.10}In_{0.60}Ga_{0.40}S_2$.

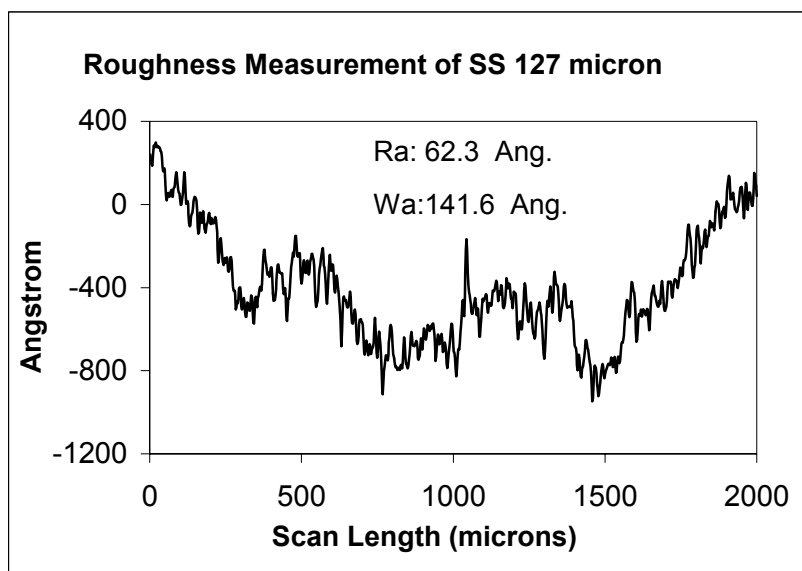


Figure 8. Surface roughness measurement of 127 μm thick SS foil.

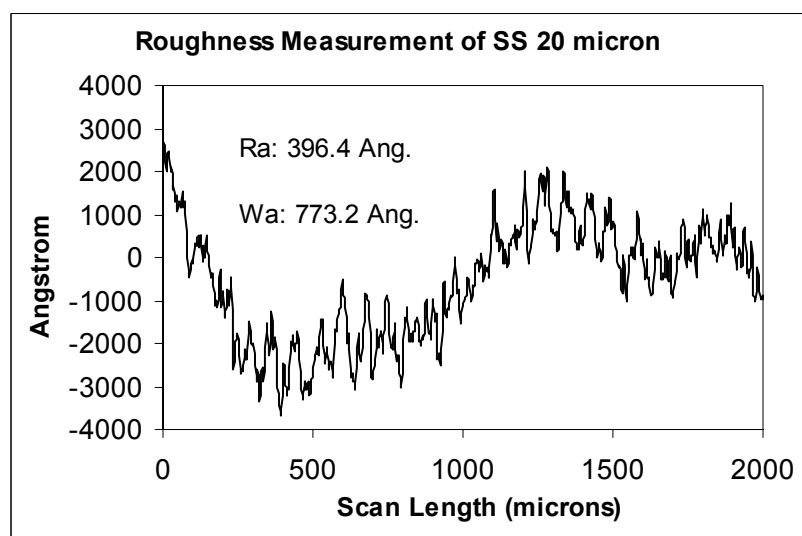


Figure 9. Surface roughness measurement of 20 μm thick SS foil.

Table I. Projected Specific Power in W/Kg.

Substrate	Projected Specific Power in W/Kg.	
	For $\eta = 10\%$ at AM 0.	For $\eta = 15\%$ at AM 0.
127- μm (5 mil) SS foil	133.03	199.55
20- μm (< 1mil) SS foil	768.75	1153.13
25.4- μm (1 mil) Ti foil	1015.76	1523.64

Surface roughness of the substrate was measured using DEKTAK³ surface profile measuring system. The average roughness (Ra) value measured of 127 μm thick SS foil (Fig. 8) was 62.3 Å and average waviness (Wa) was 141.6 Å. The average roughness (Ra) value measured of 20 μm thick SS foil (Fig. 9) was 396.4 Å and surface waviness (Wa) was 773.2 Å.

PV parameters of a CIGS2 solar cell on 127 μm thick SS flexible foil measured under AM 0 (Fig.10) conditions at the NASA GRC were: $V_{oc} = 802.9\text{ mV}$, $J_{sc} = 25.07\text{ mA/cm}^2$, $FF = 60.06\%$, and $\eta = 8.84\%$. For this cell, AM 1.5 PV parameters measured at NREL were: $V_{oc} = 788\text{ mV}$, $J_{sc} = 19.78\text{ mA/cm}^2$, $FF = 59.44\%$, $\eta = 9.26\%$. Quantum efficiency curve (Fig.11) showed a sharp QE cutoff equivalent to CIGS2 bandgap of $\sim 1.50\text{ eV}$, fairly close to the optimum value for efficient AM0 PV conversion in the space. PV parameters for cell fabricated on 20 μm thick SS foil measured at NREL under AM 1.5 conditions were: $V_{oc} = 740\text{ mV}$, $J_{sc} = 13.129\text{ mA/cm}^2$, $FF = 41.63\%$, efficiency $\eta = 4.06\%$.

Foils with high defect density in the form of surface roughness showed increase in Ga content in the bulk of material. Fill factor that is the measure of squareness of I-V curve also decreased with increase in defect density. Efficiency showed decreasing trend with increasing in surface roughness. The loss in efficiency was attributed to surface roughness of the substrate, increase in Ga content in the bulk of the material and decrease in fill factor.

The solar efficiency of a photovoltaic system depends critically on the spectral distribution of the radiation. At AM 0 the solar spectrum has 1353 W/m^2 value. At PV Materials Laboratory of FSEC, the proposed efficiency at AM 0 to be obtained is in the range of 10 to 15 %. Table I provides the projected specific power in W/Kg of flexible metallic substrate at AM 0 for 10 and 15 % efficient CIGS2 solar cells.

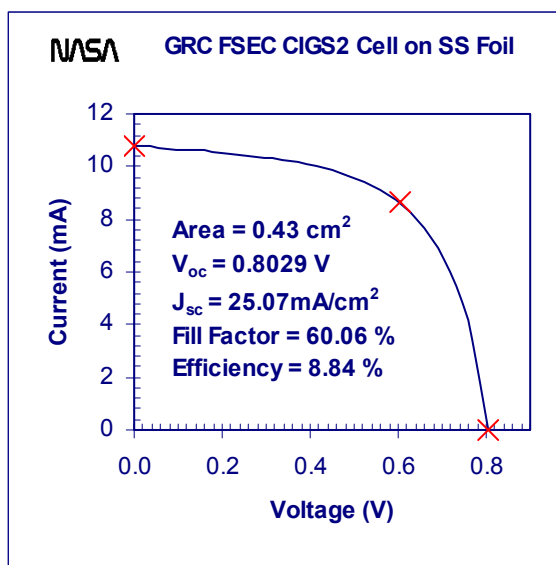


Figure 10. IxV curve of CIGS2 thin film solar cell.

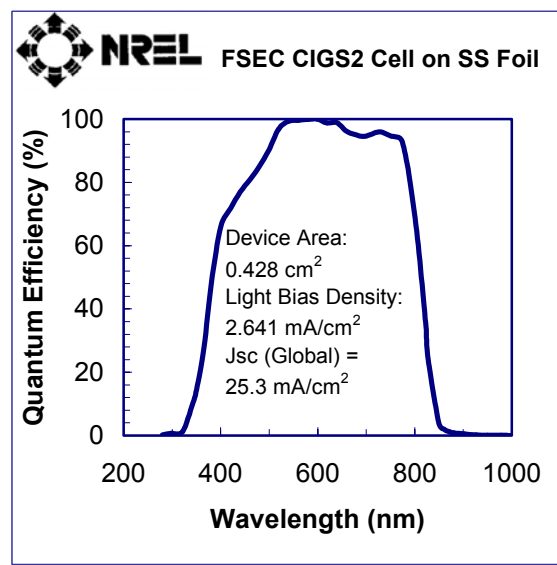


Figure 11. QE curve of CIGS2 thin film solar cell.

3.1. LARGE-AREA, DUAL-CHAMBER MAGNETRON-SPUTTERING AND SULFURIZATION SYSTEMS

Earlier, the substrate size was limited to 1" x 1". A large-area, dual-chamber magnetron-sputtering unit has been fabricated recently. The chambers are equipped with cryopumps, two-stage mechanical vacuum pumps, throttled-gate valves, mass-flow controllers for argon and oxygen, and convection and Bayard-Alpert ionization gauges (Fig.12). A large number of feed-thru ports have been provided to both the chambers for rotation and electrical feed-thru's. This will permit addition of "in situ" diagnostic tools. Three 4" x 12" DC magnetron sputtering sources have been installed for sputter deposition from molybdenum, indium, and copper, CuGa (22%) or CuGa (67%) targets in the larger chamber. Two 4" x 12" RF magnetron sputtering sources have been installed into the smaller chamber for ZnO and ZnO: Al bilayer window deposition.

The thickness uniformity along the 12" dimension is expected to be better than $\pm 2\%$ over the center width of 5" and better than $\pm 3\%$ over the center width of 6" for linear substrates motion along the 4" dimension. Moreover, the sputtering sources are expected to provide excellent (>40%) target utilization. A linear substrate movement set-up has been fabricated for "in line" deposition of molybdenum back contact and Cu-Ga/In metallic precursors. A four-hearth e-beam source has also been procured for vacuum evaporation of Ni/Al contact grids. The vacuum system and chambers were designed at the Florida Solar Energy Center (FSEC). Vacuum chambers were built elsewhere. Complete system was constructed at FSEC. Siemens Solar Industries will be donating a selenization-sulfurization furnace, reactor and control system for preparation of large (4"x4") CIGS2 thin films and solar cells.

4.CONCLUSION

Sputtered copper, gallium and indium precursors in the ratio of $\text{Cu}/(\text{In}+\text{Ga}) \sim 1.4$ formed a predominant $\text{Cu}_{11}\text{In}_9$ precursor phase, free from inhomogeneous secondary phases. The initial dwell of 120° C for 30 minutes was changed to 135° C for 25 minutes without H_2S gas flow during sulfurization. The binary $\text{Cu}_{11}\text{In}_9$ precursor phase reacted in H_2S : Ar gas environment to form a good crystalline pseudo-quaternary phase of CIGS2 film. After etching in KCN, CIGS2 films became stoichiometric, regardless of the ratio of $\text{Cu}/(\text{In}+\text{Ga})$ of unetched film. CIGS2 films grew with (112) texture of chalcopyrite structure. The compositional

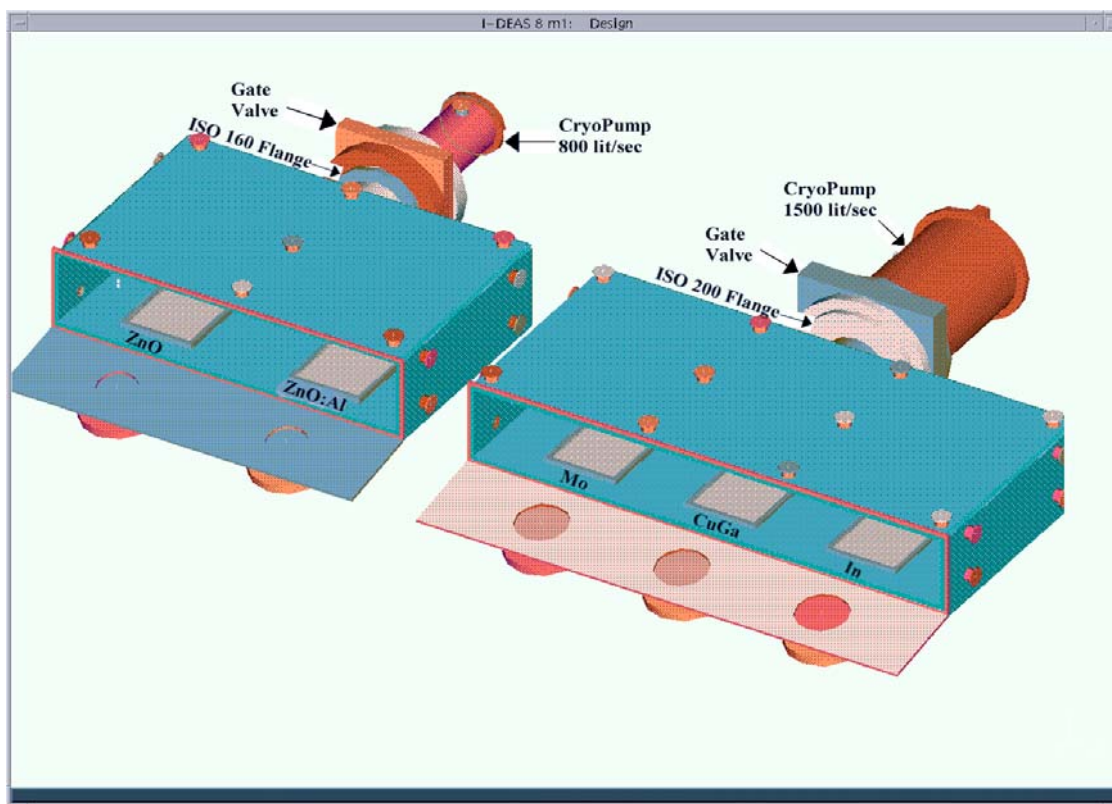


Figure 12. Large-area, dual-chamber magnetron-sputtering unit.

gradient in Ga content created localized Ga -poor phase in the electrical active part of the device and in the bulk of the film, and highly Ga-rich phase near the back contact. The band-gap of this film was narrow at the surface and gradually widened towards back contact leading to formation of back surface field. This built-in back surface electric field was expected to improve the solar cell performance [9,10].

PV parameters of a CIGS2 solar cell on 127 μ m thick SS flexible foil measured under AM 0 conditions at the NASA GRC were: V_{oc} = 802.9 mV, J_{sc} = 25.07 mA/cm², FF = 60.06%, and efficiency η = 8.84%. For this cell, AM 1.5 PV parameters measured at NREL were: V_{oc} = 788 mV, J_{sc} = 19.78 mA/cm², FF = 59.44%, η = 9.26%. Quantum efficiency curve showed a sharp QE cutoff equivalent to CIGS2 bandgap of ~1.50 eV, fairly close to the optimum value for efficient AM0 PV conversion in the space. PV parameters for cell fabricated on 20 μ m thick SS foil measured at NREL under AM 1.5 conditions were: V_{oc} = 740 mV, J_{sc} = 13.129 mA/cm², FF = 41.63 %, efficiency η = 4.06 %. Foils with high defect density in the form of surface roughness showed increase in Ga content in the bulk of material. Fill factor that is the measure of squareness of I-V curve also decreased with increase in defect density. Efficiency showed decreasing trend with increasing in surface roughness. The loss in efficiency was attributed to surface roughness of the substrate, increase in Ga content in the bulk of the material and decrease in fill factor.

With the construction of large-area, dual-chamber magnetron-sputtering unit, samples having thickness uniformity of ± 2 % over the central 5" width and ± 3 % over the central 6" width would be fabricated.

5. REFERENCES

1. S. G. Bailey and D. J. Flood, Space Photovoltaics, Prog. Photovolt. Res. Appl. 6, 1-14, (1998).
2. E. L. Ralph, and T. W. Woike, Solar Cell Array System Trades – Present and Future, Proceedings of 37th American Institute of Aeronautics and Astronautics Aerospace Sciences Meeting and Exhibit pp. 1-7, 1999.
3. J. Tringe, J. Merrill, and K. Reinhardt, Proc. 28th IEEE Photovoltaic Specialists Conference, Anchorage, Alaska, AK, 2000.
4. Takuya Satoh, Yasuhiro Hashimoto, Shin-ichi Shimakawa, Shigeo Hayashi and Takayuki Negami, CIGS solar cells on flexible stainless steel substrates, 28th IEEE Photovoltaic Specialists Conference, Anchorage, AK., pp. 567- 570, 2000.
5. R. Scheer, H. J. Lewerenz, Formation of secondary phases in evaporated CuInS₂ thin films. I.A Surface stoichiometry and phase segregation, J. Vac. Sci. Technology A 13(4), pp. 1924-1929, 1995.
6. R. W. Miles, K. T. Ramakrishna Reddy, and I. Forbes, Synthesis of CuInS₂ from magnetron sputtered Cu/In bilayers for use in thin film solar cells, 2nd WCEPVSEC, Vienna, 496 - 499, 1998.J. Klaer, J.
7. A. Neisser, I. Hengel, R. Klenk Th. W. Matthes, J. A. García, A. P. Rodríguez, A. R. Rodríguez, M. Ch. Stenier, Effect of Ga incorporation in sequentially prepared CuInS₂ thin film absorbers, Solar Energy Materials and Solar Cells 67, pp. 97-104, 2001.
8. Neelkanth G. Dhere, Shashank R. Kulkarni, Sanjay S. Chavan and Shantinath R. Ghongadi, Cu (In,Ga)S₂ thin – film solar cells prepared by H₂S sulfurization of CuGa-In precursor, SPRAT XVI, Cleveland OH, 1999.
9. Neelkanth G. Dhere, Shashank R. Kulkarni and Shantinath R. Ghongadi, PV characterization of CIGS2 thin film solar cells, 28th IEEE Photovoltaic Specialists Conference, Anchorage, AK., pp. 1046, 2000.
10. Neelkanth G. Dhere, Shashank R. Kulkarni and Pamela K. Johnson, Bandgap optimization of CIGS2 space solar cells, Proc. 16th European Photovoltaic Solar Energy Conference, Glasgow UK, pp. 1-4, 2000.
11. Bruns, R. Henninger, K. Topper, R. Klenk, K. Ellmer and D. Braunig, A tolerant two step process for efficient CuInS₂ solar cell, 2nd WCEPVSEC, Vienna, 537- 540, 1998.
12. H. W. Schock, Polycrystalline compound semiconductor thin films in solar cells, Springer Proceedings in physics, Vol. 35, pp. 246 – 256, 1989.

OVERVIEW OF PHOTOVOLTAIC CALIBRATION AND MEASUREMENT STANDARDS at GRC

Cosmo Baraona, David Snyder, David Brinker, Sheila Bailey, Henry Curtis, NASA GRC
David Scheiman, Phillip Jenkins, Ohio Aerospace Institute

Introduction

Photovoltaic (PV) systems (cells and arrays) for spacecraft power have become an international market. This market demands accurate prediction of the solar array power output in space throughout the mission life of the spacecraft. Since the beginning of space flight, space-faring nations have independently developed methods to calibrate solar cells for power output in low Earth orbit (LEO). These methods rely on terrestrial, laboratory, or extraterrestrial light sources to simulate or approximate the air mass zero (AM0) solar intensity and spectrum.

Background

Calibrated solar cells are needed to adjust the intensity of laboratory light sources (solar simulators) to the intensity of AM0. The NASA Glenn Research Center at Lewis Field has calibrated solar cells using an aircraft method since 1963. Between 1963 and 1975 a B57B aircraft performed 120 calibration flights. From 1975 to 1981 an F-106 aircraft performed 87 flights. A Lear 25 has been used since 1985 and has performed 324 flights. About 1200 different solar cells have been calibrated during this time, or about 2 cells per flight. Each flight includes 5 2x2 cm cells to be calibrated and one local standard or check cell. A cell is flown at least twice to determine its calibrated AM0 Isc.

The Langley Plot Method is used for these calibrations. With this method, solar cells are flown along 45 degrees north latitude (near Alpena Michigan) to an altitude of 50,000 feet. The airplane is aligned for normal sunlight incidence on the solar cells. Short circuit current (Isc) as well as pressure and temperature are recorded as the altitude is decreased to about 30,000 feet. Data below the tropopause is not used. The natural log of Isc is plotted and extrapolated to AM0 to obtain the calibrated outer space Isc.. Corrections for distance from the sun and for ozone absorption (~1%) are made. Because of the height of the tropopause and the sun angle, calibration flights can be performed only from late Oct. to late March each year. A typical flying season would allow about 30 flights of about 75 cells total.

The six 2x2 cm solar cells to be calibrated are in a collimation tube (4:1) without a window so that they are exposed directly to sunlight. The cells all have 4 wire instrumentation. A heater in the base plate maintains their temperature at 25 C. The sunlight is monitored with a thermopile and/or a spectrometer. Source meters, switches, and computers collect and record the data in flight. Two solar cells have been flown repeatedly between 1978 and 1997 and show a 1% standard deviation. Comparisons of the aircraft method with the Space Shuttle and with the JPL Balloon Method show agreement within 1%.

ISO Standards

Beginning in 1994, the PV community (national space agencies and industry) in Asia, Europe, and the Americas have been working together to develop an international standard for single junction cell AM0 short circuit current measurement and calibration. Annual workshops have been held since

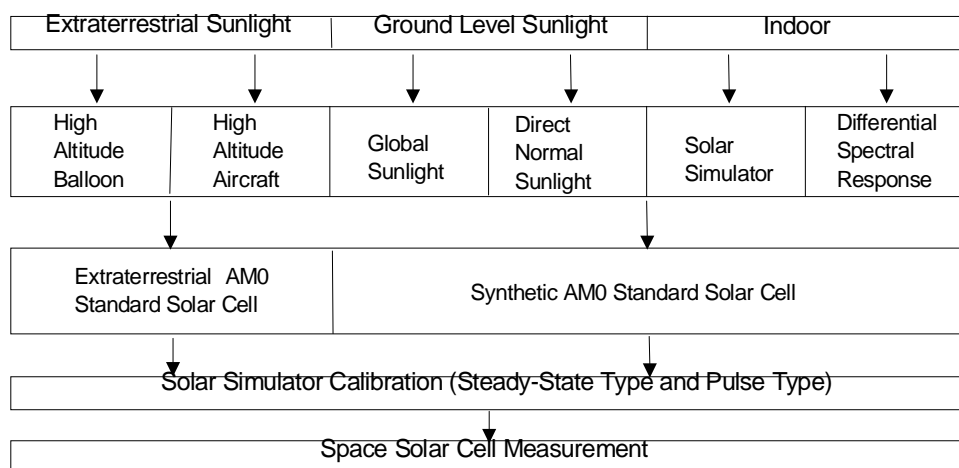
1994 to discuss and compare balloon, aircraft, direct terrestrial sunlight, and laboratory based methods for calibrating PV cells. These workshops have also discussed measurement of multi-junction cells and radiation damage testing and have also conducted measurement inter-comparisons (round robins) of the different calibration methods.

International standards for space solar cells are supported by the International Organization for Standardization (ISO). ISO Technical Committee (TC) 20 is for Aircraft and Space Vehicles, while ISO TC20 Subcommittee (SC) 14 focuses on Space Systems and Operations. ISO TC20 SC14 Working Group (WG) 1 is for Space Systems Design and Engineering. The US members of the Space Solar Cell Calibration and Measurement Workshop also serve as a Technical Advisory Group (TAG) to support the US delegation to the ISO TC20 SC14 WG1.

The most recent workshop, the 7th International Workshop on Space Solar Cell Calibration and Measurement, was held in Girdwood, Alaska on Sept. 25-27, 2000. Twenty-eight representatives from Argentina, Canada, Germany, Japan, The Netherlands, Spain, the UK, and the USA represented ESA, NASA, NASDA, and industry. This workshop had several working groups. One working group focused on single junction crystalline cell calibration, one on single crystal multi-junction cell measurement, one on round robin measurement inter-comparisons and one on irradiation damage testing.

Single Junction Cell Standard

A document entitled “Single Junction Space Solar Cell Measurement and Calibration Procedure” was first proposed by the Japanese in 1994 and became ISO working draft WD15387 in 1996 with inputs from the six Workshops which were held every year from 1995 through 2000. The six calibration methods described in this document include the NASA JPL and French CNES high altitude balloon methods, the NASA GRC high altitude aircraft method, ground level sunlight methods including global and direct normal, and synthetic sunlight methods including solar simulator or differential spectral response. The calibration results will have a standard deviation of +/- 1% using an AM0 solar constant of 1367 +/- 7W/m². Measurements are done at a cell temperature of 25 +/- 1 degree C. Further work with the error analysis for each of the methods is in progress. The document is a Draft International Standard and will be voted upon by the member nations this year. The six methods are shown in the figure below and are grouped by light source. The references in the bibliography give further information about the methods.



Round Robin Inter-Comparison

A series of round robin measurement inter-comparisons has been performed for each of the single junction calibration methods. A standardized cell holder that is compatible with each of the methods was developed. The latest round robin with three silicon and three gallium arsenide single junction cells will be completed by the end of this year. Because of the seasonal nature of some of the calibration methods, it takes a year or longer to complete a round robin intercomparison calibration at the seven laboratories worldwide. Future round robins will include multi-junction cell calibration.

Other Standards

The 7th Workshop reviewed an outline of a standard proposed by the Japanese participants on Electron and Proton Irradiation Test Methods. This document has been proposed to ISO as an official New Work Item (NWI) for their standards creation process. A favorable vote for its adoption as a NWI is anticipated.

A NWI on multi-junction solar cell calibration and measurement will be proposed to ISO this year.

The 8th International Workshop is being planned by ESA for October 29-31, 2001 in Freiburg, Germany. A partial bibliography of selected publications for some of the calibration methods is shown below.

Bibliography

- (1) Phillip Jenkins, David Brinker and David Scheiman, "Uncertainty Analysis of High Altitude Aircraft Air Mass Zero Solar Cell Calibration", 26th IEEE Photovoltaic Specialists Conference, Anaheim, CA, Sept. 29 - Oct. 3, 1997.
- (2) JPL Publication 95-23
B.E. Anspaugh and R.S. Weiss, "Results of the 1995 JPL Balloon Flight Solar Cell Calibration Program", Jet Propulsion Laboratory, California Institute of Technology, Pasadena, California, USA, December 1, 1995.
- (3) Brue Anspaugh, "Errors Estimates in the Calibration of Solar Cells on Jet Propulsion Laboratory High Altitude Balloon Flights", 5th International Workshop, Aldershot, UK, July 13-16, 1998.
- (4) RA/DP/EQ/QM/92-398
Cuquel and M. Roussel, "Calibration of Solar Cells Outside the Atmosphere", CNES, Toulouse, France, December 22, 1992.
- (5) R. Shimokawa, F. Nagamine, Y. Miyake, K. Fijisawa and Y. Hamakawa, "Japanese Indoor Calibration Method for the Reference Solar Cell and Comparison with the Outdoor Calibration", Japanese Journal of Applied Physics, Vol. 26, No. 1, January 1987, pp. 86-91.
- (6) O. Kawasaki, S. Matsuda, Y. Yamamoto, Y. Kiyota and Y. Uchida, "Study of Solar Simulator Calibration Method and Round Robin Calibration Plan of Primary Standard Solar Cell for Space Use", 1st World Conference and Exhibition on Photovoltaic Solar Energy Conversion (WCPEC), Hawaii, USA, Dec. 5-9, 1994.
- (7) Japanese Space Solar Cell Calibration Technical Committee, "Results of Uncertainty Analysis for AM0 Standard Solar Cells Calibration Methods", 4th International Workshop, Cleveland, USA, Oct. 6-9, 1997.
- (8) Klaus Bucher, "Calibration of Solar Cells for Space Applications", Progress in photovoltaics: Research and applications, Vol.5, pp.91-107, 1997

- (9) Trinidad J. Gomez, "Calibration of Space Solar Cells –Terrestrial Global Method-", 4th International Workshop, Cleveland, USA, Oct. 6-9, 1997.
- (10) CAST Technical Report, "Uncertainty Estimation of CAST Direct Normal Calibration Facility", 4th International Workshop, Cleveland, USA, Oct. 6-9, 1997.
- (11) Yang Yiqiang, Zeng Lingru and Ma Zong Cheng, "Calibration of AM0 Reference Solar Cells Using Direct Normal Terrestrial Sunlight", 9th International Photovoltaic Science and Engineering Conference (PVSEC), Miyazaki, Japan, Nov. 11-15, 1996.
- (12) (PTB Technical Report, "CD15387, Para.7.3.4, Differential spectral response calibration method", 5th International Workshop, Aldershot, UK, July 13-16, 1998.

RADIATION HARDNESS TESTS OF FLEXIBLE, THIN-FILM PHOTOVOLTAICS FOR SPACE APPLICATIONS¹

Pawel Tlomak and Kitt C. Reinhardt
Air Force Research Laboratory, Advanced Space Power Generation
Kirtland Air Force Base, NM 87117-5776

Robert J. Walters
U.S. Naval Research Laboratory, Washington, DC 20375

Scott R. Messenger
SFA, Inc. Largo, MD 20774

ABSTRACT

An overview of flexible thin-film photovoltaics (TFPV) radiation-testing program undertaken at the AFRL is presented. This effort has been initiated and supported by the AFRL to develop a space radiation qualification program for the state-of-the-art TFPV. Preliminary radiation studies concentrated on two state-of-the-art technologies, namely amorphous silicon (a-Si) and copper-indium-diselenide (CIS) TFPV. Proton and electron irradiation tests were carried out and the response of the a-Si cells has been characterized via illuminated I-V, dark I-V, and QE measurements. The cells demonstrated relatively high radiation resistance up to high Displacement Damage Dose (D_d) levels. The degradation of the FF, observed at high radiation doses was effectively removed by annealing.

INTRODUCTION

TFPV have recently enabled the design of next-generation lightweight space solar arrays that promise major performance improvements and cost reduction for space missions. TFPV are also more radiation-resistant than their crystalline counterparts, an important characteristic for use in radiation-rich space environment. These emerging technologies pose a need for the development of on-ground testing program addressing specifically TFPV. AFRL has initiated comprehensive space qualification program including both simulated space environment testing and development of space qualified protective coatings for state-of-the-art TFPV. Thermal annealing effects are well known in TFPV devices. A major step in understanding the role of annealing is the evaluation of post-radiation cell recovery under realistic conditions that simulate space environment. This work presents results of combined effects of radiation and annealing on a-Si and CIS thin-film solar cells. Also, we have initiated radiation damage analysis methodology based on D_d as applied to TFPV. The approach has already been successfully applied to crystalline multijunction solar cells and suitable methodology for predicting on-orbit cell performance has been established [1]. In this work we present preliminary results of this methodology as applied to TFPVs.

SOLAR CELLS

The triple-junction a-Si solar cells with an active area of approximately 1 cm² were supplied by United Solar Systems (USS). These cells were deposited via PECVD. The CIS cells with an active area of approximately 1 cm² were supplied by Global Solar Energy Systems (GSE). Both types of solar cells were deposited on flexible stainless steel substrates. The BOL characteristics of these cells are summarized in table 1. The data represent the average of three or more measurements made on each cell along with the value of standard deviation.

¹ Radiation test presented in this paper were carried out at the U.S. Naval Research Laboratory and were sponsored by the Air Force Research Laboratory

Table 1. BOL data measured for a-Si and CIS solar cells.

Cell Type	I_{sc} (mA/cm ²)		V_{oc} (V)		I_{mp} (mW/cm ²)		V_{mp} (V)		P_{mp} (mW/cm ²)		FF		E_{ff} (%)	
a-Si	9.78	0.24	2.296	0.005	8.41	0.13	1.79	0.03	15.07	0.17	0.671	0.016	11.03	0.13
CIS	20.32	2.46	0.487	0.013	15.16	2.45	0.36	0.02	5.52	0.93	0.556	0.045	4.03	0.68

The efficiencies of a-Si cells ranged from 11 to 12% with standard deviation of 0.13%, which is quite good for this technology. Also, these cells seem to be rather tightly grouped in terms of performance. The CIS cells displayed significantly worse performance than a-Si cells and in addition to this their BOL characteristics were much more scattered. The poor performance of these CIS cells is explained, at least in part, by the significantly higher dark current and a large variation in shunt current.

SOLAR CELLS ELECTRICAL TESTS

A Spectrolab X-25 Mark-II solar simulator equipped with Xe arc lamp was used to perform electrical measurements. Appropriate external filters were used for better spectral match to the AMO solar spectrum. The simulator light intensity was calibrated using three reference cells: a single-junction (SJ) GaInP cell, a SJ GaAs cell with a thick GaInP window layer, and a SJ crystalline Si cell. The first two cells were grown to mimic the top and the middle cells of a standard triple-junction (TJ) GaInP/GaAs/Ge solar cell, and they were calibrated by Tecstar, Inc. against balloon-flown standards. The Si reference cell was calibrated against an ARFL balloon-flown standard cell. The wavelength range of these reference cells, in aggregate, closely matches that of the test cells, and the simulator was adjusted so that the short-circuit current of each of the three reference cells was within 1% of its calibrated value. The I-V data both under illumination and in the dark were taken using a computer controlled Keithley 236 high current source unit. All I-V measurements were taken at 27 +/- 0.5°C. The dark current characteristic of the a-Si cells used in this work showed no sensitivity to light soaking. The QE measurements were made using the standard lock-in amplifier technique and a pyroelectric detector. Light-biases were applied in order to measure the response of each individual junction of the triple junction stack. The optimum conditions were achieved using a 400W Xe bulb with carefully selected filters.

RADIATION EXPERIMENTS

The cells were measured incrementally; irradiated and measured and then returned to the accelerator for another incremental fluence of particles. This irradiation/measurement sequence was repeated five times to produce a total of five fluence points. Irradiations were performed at three different proton energies, namely 100, 500, and 1000 keV and at three different electron energies, namely 0.5, 1.0, and 1.5 MeV. A different set of solar cells was exposed at each energy. Each set consisted of six solar cells. Half of the solar cells at each energy were exposed to a 24-hour, 70°C anneal, in the dark and at open circuit after each fluence increment. Full electrical characterization was performed before and after annealing. Another, nominally identical sample set, was not exposed to the annealing and used as control cells. These cells were stored in the same box and handled in the same manner as the irradiated cells. Prior to any measurement sequence, the IV curve of at least one of the control cells was measured. Control cell measurements showed variation of about 2.3% in I_{sc} , 0.5% in V_{oc} , 2.4% in FF, and 3.3% in P_{mp} and E_{ff} . These values give an indication of the uncertainty in the IV parameter data presented here. Both, the proton and electron irradiations were performed using the Van DeGraaff facility at NASA Goddard in Greenbelt, MD. For irradiation, the solar cells were mounted, using small strips of Scotch Tape, to a metal disk. During irradiation, the disk was constantly rotated thus allowing a large number of cells to be exposed in one irradiation run. In contrast to the proton irradiations, the electron irradiations were performed in air. Also, the sample disk was inserted significantly closer to the source in order to maximize the beam current. This was necessary to achieve high electron fluencies in a reasonable amount of time. However, special care was taken to ensure that the sample temperature remained near 21°C during the irradiations. Dosimetry was achieved using a Faraday cup with a measurement accuracy of 15%. In addition, InP solar cells were used as

control cells and irradiated with the a-Si solar cells. The degradation data measured in the InP cells matched the InP characteristic curve very well lending further confidence to the fluence numbers.

PROTON IRRADIATIONS TEST RESULTS

A summary of the normalized PV parameters measured in the unannealed a-Si cells irradiated with protons is plotted in figure 1. The data are plotted as a function of D_d , which is given by the product of the particle fluence and the nonionizing energy loss (NIEL). The NIEL values used in these calculations are given in table 1. There appears to be significant scatter in the radiation response of the normalized P_{mp} data from cell to cell directly linked to the FF. The I_{sc} and V_{oc} data, on the other hand, are very tightly grouped and show very little degradation except at very high levels of D_d .

Table 1. NIEL values in MeV-cm²/g for the two technologies under study at the three proton irradiation energies.

	100 keV	500 keV	1000 keV
a-Si	0.679	0.157	0.0819
CIS	0.474	0.118	0.0637

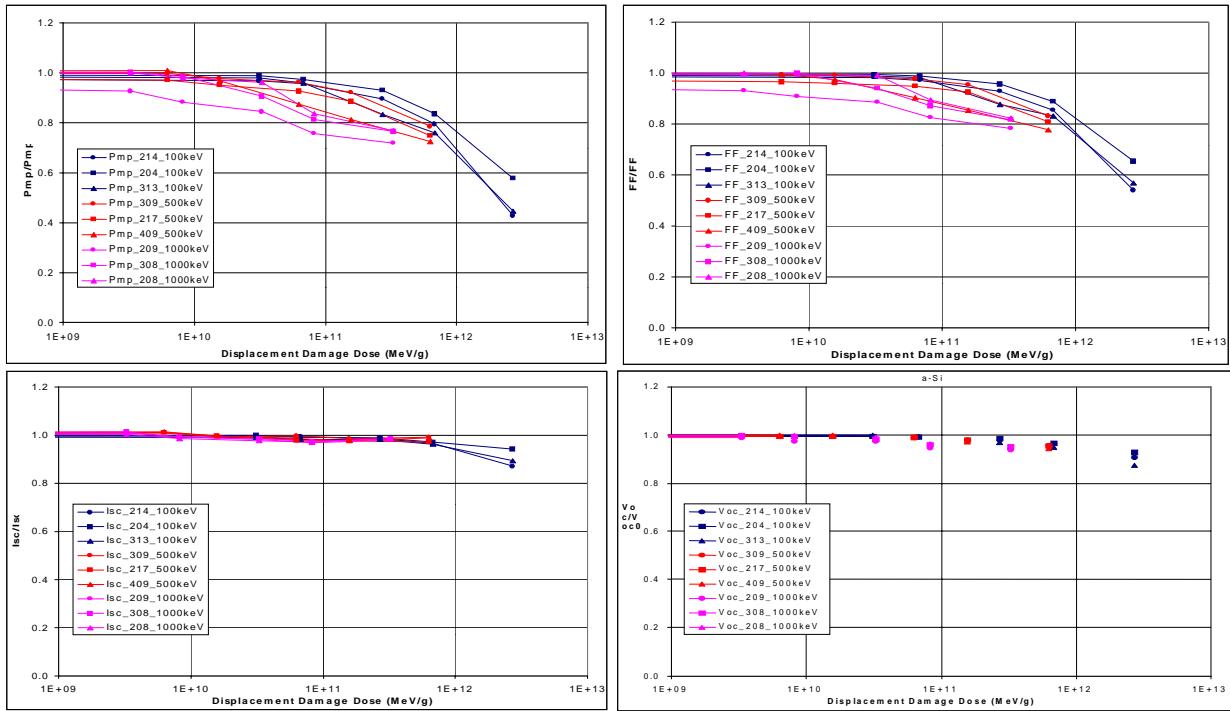


Figure 1. Normalized PV parameters measured on the a-Si cells after proton irradiation. These cells were not annealed.

The normalized PV data from some of the a-Si cells from the annealed group are shown in figure 2. Two points are plotted at each D_d value corresponding to measurements made after irradiation before and after annealing at 70°C for 24 hours. In agreement with the unannealed data shown above, only a very small amount of degradation of I_{sc} and V_{oc} was observed only at the highest D_d levels. The FF, on the other hand, degraded significantly, leading to P_{mp} degradation. The annealing resulted in partial recovery in all of the parameters, especially the FF and hence P_{mp} . The degradation pattern of FF for both the unannealed and annealed a-Si cells was further investigated using dark current measurements. The results suggested that some cells exhibit

anomalous FF degradation caused by weakness within the cells that is not directly linked to radiation effects. It could likely be a variable series resistance due to poor adhesion of top contacts or shunts caused by edge effects. These cells showed poor initial dark current characteristics and significant variability from measurement to measurement under proton irradiation. Data from these cells were not considered in the present analysis.

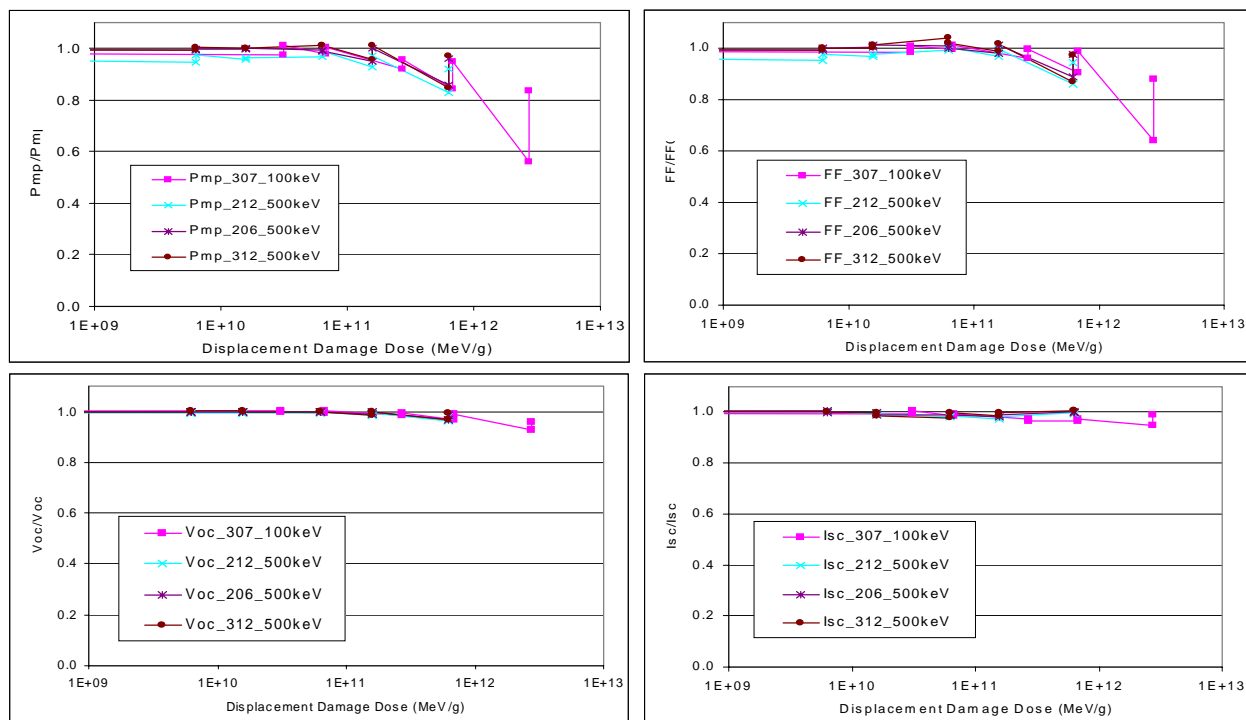


Figure 2. Normalized PV parameters of a-Si cells irradiated with protons and annealed at 70°C for 24 hours following each fluence increment. Two data points are shown at each fluence, before and after the annealing. Degradation of FF and P_{mp} is partially restored after the annealing.

The effect of proton irradiation on the spectral response of a-Si cells is shown in figure 3. No radiation-induced changes are evident for unannealed cells. This is consistent with the photovoltaic parameter data, as the majority of the radiation-induced damage was confined to the FF with little to no change being seen in I_{sc} , (see figure 1). In agreement with this data, no radiation-induced degradation of the QE was observed in annealed cells either.

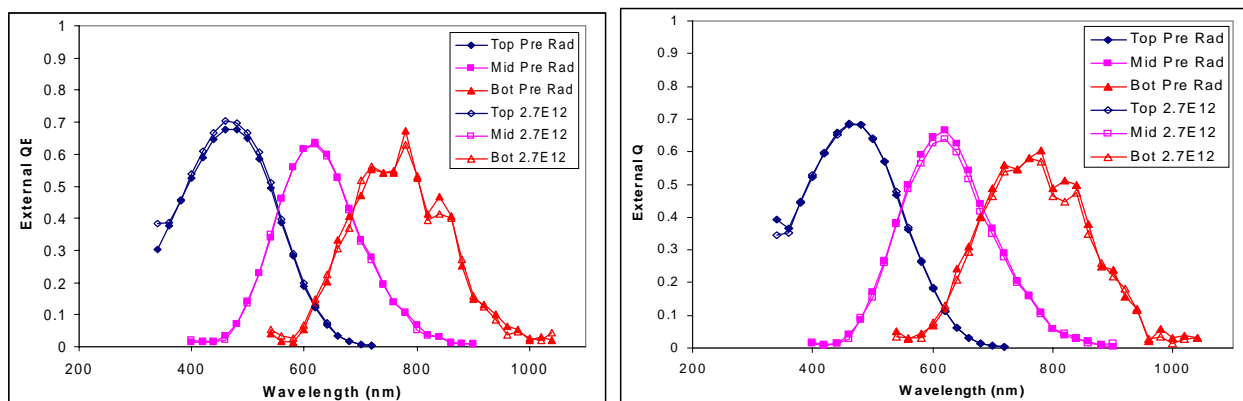


Figure 3. QE measurements for representative a-Si cell before and after 100 keV proton irradiation up to $D_d = 2.7 \times 10^{12}$ MeV/g; unannealed cells (left) and cells annealed at 70°C for 24 hours (right).

Normalized P_{mp} data measured for a-Si cells were replotted as a function of D_d using equation (1) [2]:

$$P(D_d) = P_0 - C \cdot \log \left(1 + \frac{D_d}{D_x} \right) \quad (1)$$

The replotted data fit one curve, represented by the lower curve in figure 4. The upper curve in this figure represents data obtained on somewhat similar a-Si cells [3,4] for comparison. The cells tested in this work seem to degrade more rapidly at higher D_d levels but it has to be kept in mind that in both cases data were scattered significantly. Therefore, further error analysis needs to be done before final conclusions are drawn. To show the effect of annealing both the unannealed (dashed curve) and annealed data (solid curve) were fitted into the equation (1) are replotted in figure 5. The significant benefit of the annealing is evident.

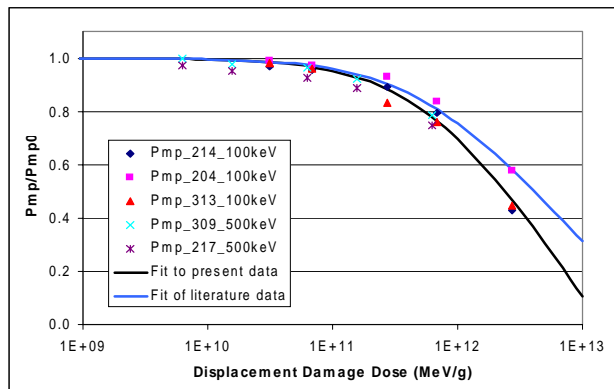


Figure 4. Normalized P_{mp} data measured for a-Si cells irradiated with protons and fit into equation (1): current data (lower curve) and data from [3,4] (upper curve).

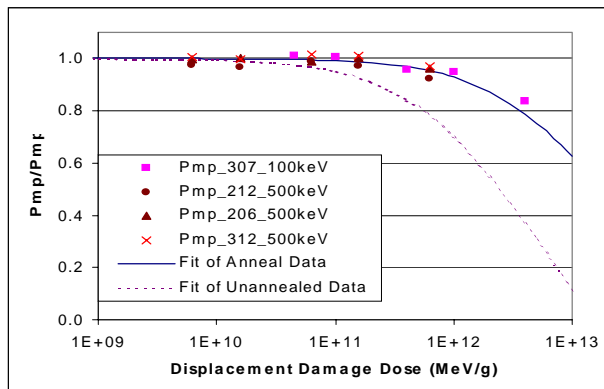


Figure 5. Normalized P_{mp} data measured for a-Si before (dashed curve) and after (solid curve) annealing.

Preliminary radiation experiments with CIS cells showed significant variation from cell to cell, and it was difficult to see any trends or draw any conclusions. It should be emphasized that these cells were of very poor quality with significant variation from cell to cell. In particular, the V_{oc} and FF do not seem to show any radiation-induced degradation, but the initial values of these parameters were so low, that such results were not surprising. The same applies to the QE and dark current data. The CIS cells showed poor initial performance and little to no change with irradiation.

ELECTRON IRRADIATIONS TEST RESULTS

A summary of the normalized PV parameters measured for a-Si solar cells irradiated with electrons is presented in figures 6 and 7, for both unannealed and annealed cells respectively. The treatment consisted of a 24 hour, 70°C anneal after each incremental fluence, except for the highest fluence point where the anneal time was 43 hours. Most of the degradation for unannealed cells appears in the FF although significant degradation in V_{oc} and I_{sc} was observed at the highest fluences. Also, the amount of damage increases with decreasing electron energy. A very similar degradation pattern was observed for annealed cells. The primary effect was a suppression of current flow through the junction apparent in a reduction in the dark current and the FF resulting in significant P_{mp} degradation, and the degradation was most severe after the lowest energy electron irradiations. The annealing produced a significant recovery in all of the solar cells. For example, for 0.5 MeV electrons at the highest fluence of $6 \times 10^{15} \text{ cm}^{-2}$, electron irradiation caused P_{mp} to degrade by approximately 80 %, but after annealing, the cell output was restored to within approximately 10% of the BOL value, for a net recovery of approximately 70 %, see figure 7. Furthermore, annealing for additional 19 hours after the highest fluence induced even higher recovery. This observation suggests that full recovery may be achieved with extended annealing times or perhaps higher annealing temperatures.

The effect of the electron irradiation on the spectral response is shown in figure 8 for 0.5 MeV electrons as an example. Despite the observed degradation in the PV parameters, the QE response appears to be quite insensitive to the irradiation. A small amount of degradation of the middle and the bottom junction was caused by electron irradiation, but this degradation was removed by annealing. The dark current analysis showed that the primary effect of radiation induced degradation was a suppression of both the photo-generated and the dark currents, which resulted in degradation of the PV response.

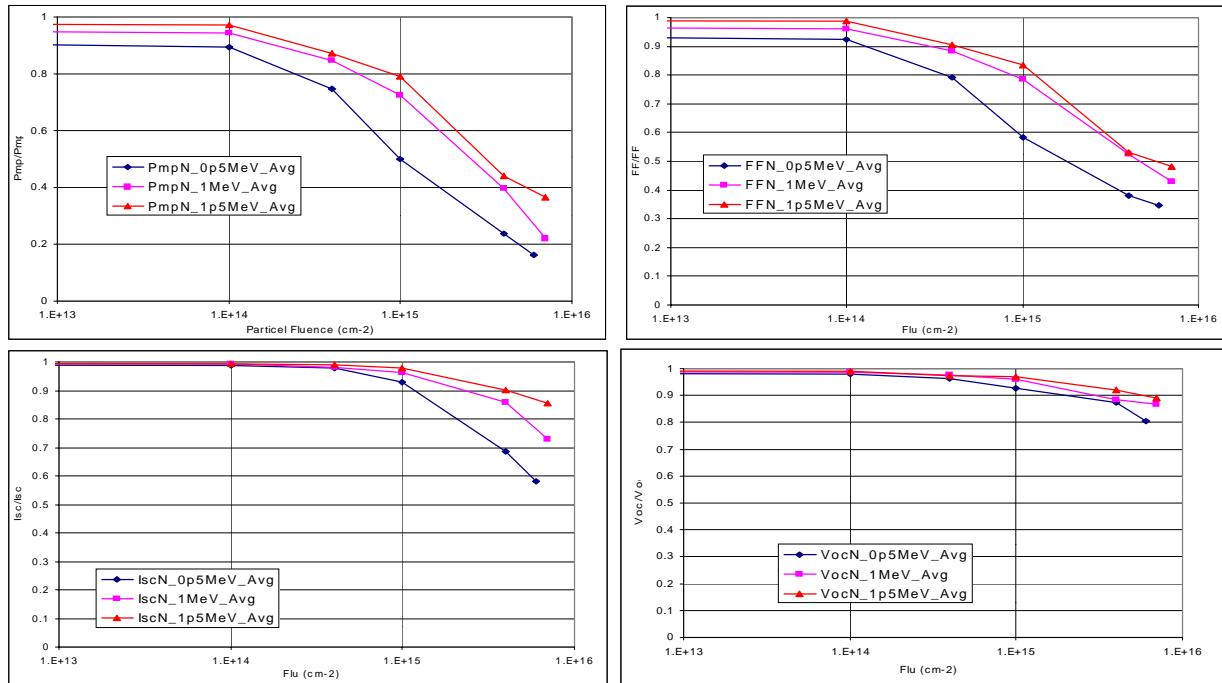


Figure 6. I-V parameters measured in the a-Si solar cells as a function of electron fluence.

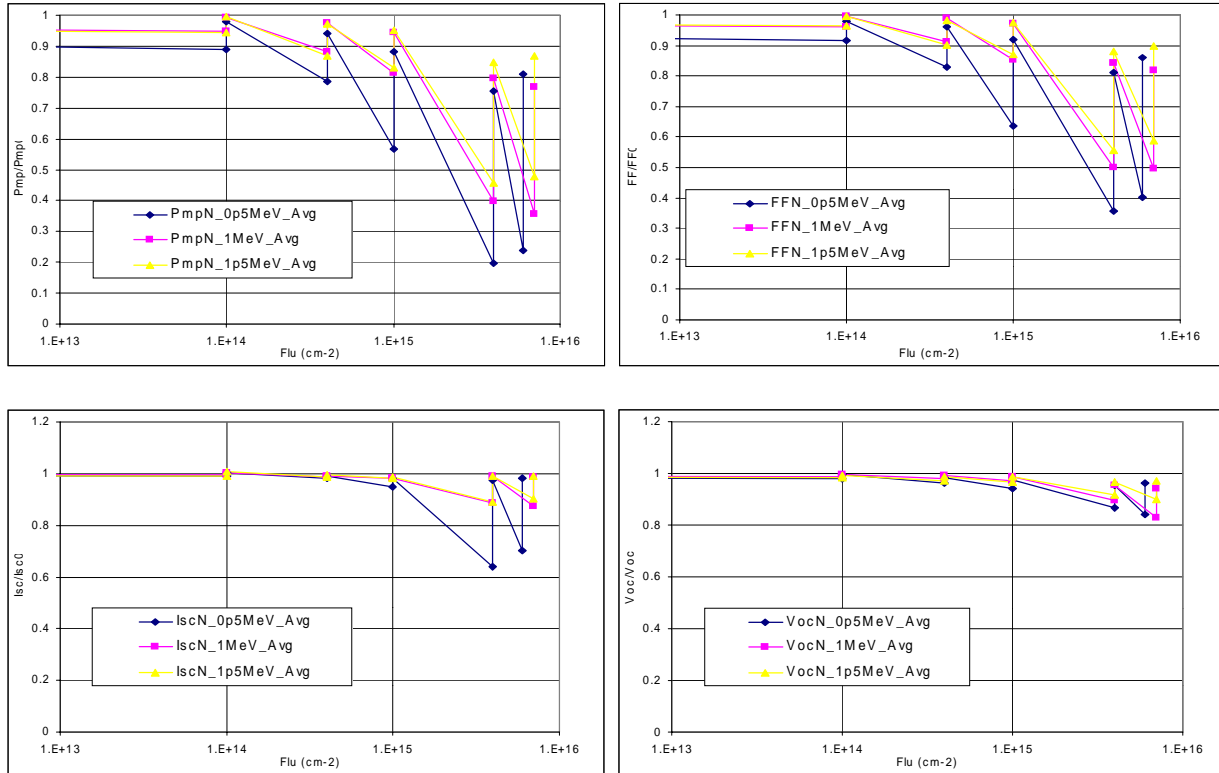


Figure 7. I-V parameters measured in the solar cells that experienced the annealing treatment. The irradiation caused considerable degradation, but the annealing results in significant recovery..

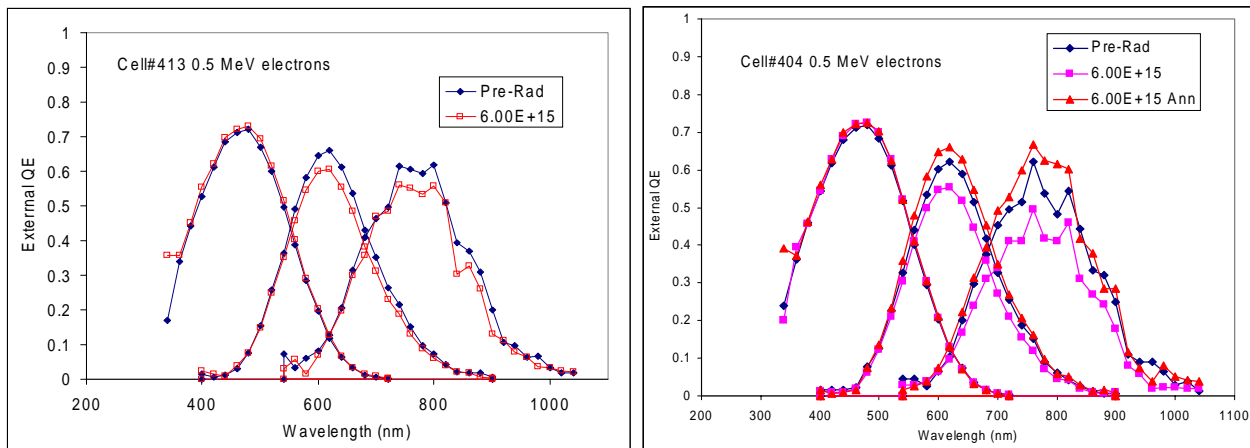


Figure 8. Representative QE curves measured in the a-Si solar cells before and after electron irradiation. The figure legend gives the particle fluence in units of cm⁻². QE data measured after the highest fluence increment (left) and then after the subsequent annealing treatment (right).

Annealing at 70°C has been shown to have tremendous effect on a-Si cells degraded by electron irradiation. Indeed, after experiencing 80% degradation in P_{mp} due to electron irradiation, a-Si solar cells recovered to within 10% of the pre-irradiation level, see figure 9. The data presented in this figure clearly shows how for any given fluence level, the annealed cells degrade much less than their unannealed counterparts and recover much of the degradation. Also, the increased recovery due to the extended anneal after the final irradiation (additional 19 hours) suggests that full recovery is attainable by annealing for longer times or at higher temperatures.

DISCUSSION AND CONCLUSIONS

Results of the present work produced a comprehensive data set for the proton and electron radiation responses of a-Si TFPV. The a-Si cells proved to be quite resistant to proton radiation up to high D_d levels, where degradation of the FF and the P_{mp} were observed. The I_{sc} and V_{oc} data on the other hand, show very little degradation except at very high D_d levels. Annealing at 70°C for 24 hours readily removed the degradation. The proton radiation data correlate reasonably well in terms of D_d . This is an important result because in these amorphous materials, in contrast to crystalline materials, it is not clear if the primary damage mechanism is ionizing or displacement damage. Indeed, the work of Srour et al. [5] suggests that the damage observed here should be due to ionizing damage and not displacements. Overall radiation response seems to be primarily controlled by radiation-induced changes in the junction dark current where a new current mechanism appears to be introduced by proton irradiation. Clarification of these issues with the emphasis on the investigations of the physical nature of radiation-induced current mechanisms will be a primary subject of continued investigations.

The dark current data measured on a-Si solar cells tested in this work provided a good data set for monitoring the effect of proton irradiation on the cell junction characteristics. The data measured at D_d higher than 6.8×10^{11} MeV/g showed dark current suppression at voltages above about 2 V. Since radiation-induced degradation is normally expected to cause an increase in dark current, the present results were somewhat surprising. These results are very similar to those presented by Wang et al. [6]. In that study, it was found that an increase in the series resistance alone did not accurately model these results. Instead, an additional current mechanism of the form bV^m (b and m are parameters) was considered, representing a real radiation-induced current mechanism, which physical nature has not yet been determined.

Results of electron irradiations have showed significant degradation of tested a-Si solar cells, which was effectively removed via annealing at 70°C for 24 hours. The primary degradation mechanism appeared to be a suppression of the flow of both the photo-generated and the dark current through the junction. This is a surprising result since in crystalline solar cells; irradiation causes the dark current to increase, which results in a decrease in photocurrent. In terms of the PV characteristics it was mostly evident in reduction of the FF. The simultaneous reduction in dark and photogenerated current might be explained by a radiation-induced increase in the resistivity of the a-Si material, as that would account for the degradation in FF and reduction in dark current without a significant change in QE. Our results are in good agreement with those of Wang et al. [6], where it was showed that the observed changes cannot be modeled by a simple increase in cell series resistance and a current generation mechanism that varies with V to a power was introduced to fit the data well. Physical nature of this mechanism has not been identified yet.

Comparison with irradiation data from literature shows that tested a-Si solar cells are extremely radiation resistant if the annealing process is employed, figure 10. The UniSolar data were measured on a-Si cells (nominally identical to those studied in this work) held at 70°C during the irradiations. The 2J TRW cells were annealed for 24 hours at 70°C after each fluence. The 3J Solarex a-Si cells were annealed at 60°C for approx. 20 hours after each fluence. The InP data was generated in the present study. The crystalline Si and GaAs/Ge data are from [2]. The a-Si cells show relatively poor radiation hardness without the annealing treatment. However, with suitable annealing treatment the a-Si cells may be expected to show virtually no degradation on-orbit. Although the a-Si solar cells are not inherently any more radiation resistant than their c-Si counterparts, it is the tremendous low temperature annealing capability that makes them attractive for space applications.

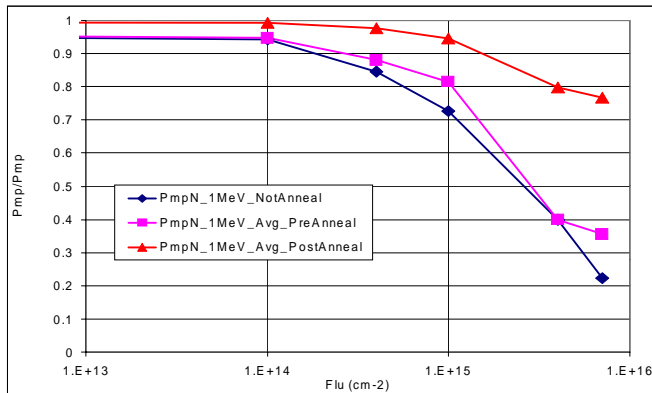


Figure 9. Normalized P_{mp} data for a-Si cells measured with and without the annealing.

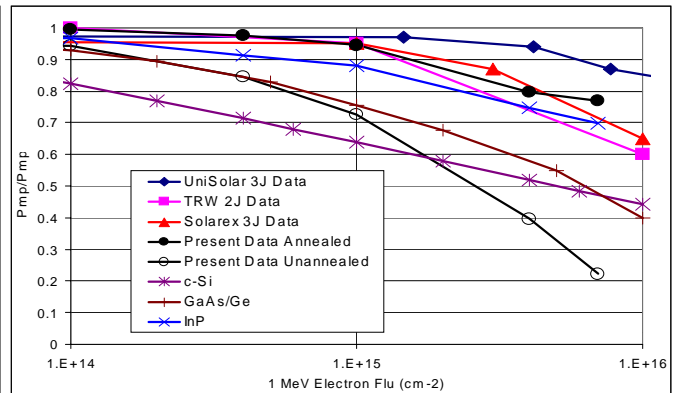


Figure 10. Comparison of the 1 MeV electron a-Si data with data from literature.

Dependence of the degradation of tested a-Si solar cells on the electron energy does not seem to follow D_d effects, figure 11. In crystalline solar cells, atomic displacement is the primary damage mechanism, higher energy electrons produce more atomic displacements, and therefore solar cell damage increases with increasing electron energy. However, exactly the opposite effect was observed here, where 0.5 MeV electrons produced the most damage. Similar results were presented in JPL studies [3]. The more recent study by Srour et al. [5]

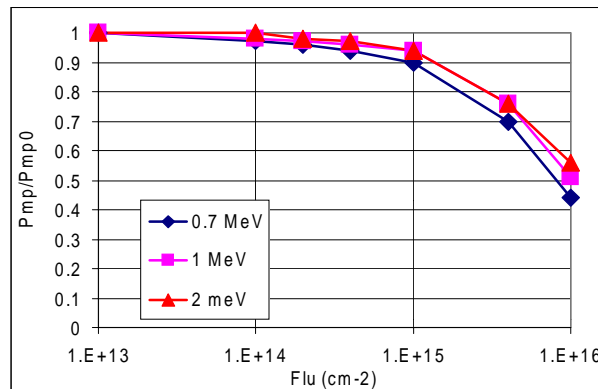


Figure 11. Data measured on Solarex 3J a-zSi solar cells after irradiation by electrons of different energies do not confirm displacement damage effects.

suggested that it is ionizing effects instead of displacement damage that controls the a-Si radiation response. It is hoped that more detailed analysis of the degradation mechanism will help to explain observed behavior of a-Si solar cells.

The primary conclusion drawn from the CIS data is that the cells displayed extremely poor initial performance with significant variation from cell to cell. As result the radiation data also showed significant variation and it was difficult to see any trends or draw any conclusions.

REFERENCES

- [1] R. J. Walters, G. P. Summers, and S. R. Messenger, "Analysis and Modeling of the Radiation Response of Multijunction Space Solar Cells", Proc. 28th IEEE Photovoltaic Specialists Conference – 2000, Anchorage, AK 15-22 September, 2000, pp 1092- 97.
- [2] B. E. Anspaugh, GaAs Solar Cell Radiation Handbook, JPL Publication 96-9 (1996).

- [3] R. L. Muller and B. E. Anspaugh, "Results of Some Initial Space Qualification Testing on Triple Junction a-Si and CuInSe₂ Thin Film Solar Cells", Proc. 12th Space Photovoltaic Research and Technology Conference, NASA Lewis Research Center, 1992.
- [4] G. J. Vendura, C. M. C. Toporow, and M. A. Kruer, "Irradiation and Annealing of Amorphous Silicon Space Solar Cells", Proc. IEEE 2nd World Conference on Photovoltaic Energy Conversion", Vienna Austria, July 1998.
- [5] J. R. Srour, G. J. Vendura, D. H. Lo, C. M. C. Toporow, M. Dooley, R. P. Nakano, and E. E. King, "Damage Mechanisms in Radiation-Tolerant Amorphous Silicon Solar Cells", IEEE Trans. Nuc. Sci, **45**, 2624 (1998)
- [6] Q. Wang, K. Lord, and J. R. Woodyard, "Effects of 40 keV Electron Irradiation on Dark I-V Characteristics of Single-Junction a-Si:H Solar Cells", Proc. IEEE 28th Photovoltaic Specialist Conference, Anchorage, AK, Sept. 2000.

A REVIEW OF SINGLE SOURCE PRECURSORS FOR THE DEPOSITION OF TERNARY CHALCOPYRITE MATERIALS

K. K. Banger

Ohio Aerospace Institute, Brookpark, OH 44142

J. Cowen, J. Harris, R. McClarnon, D. G. Hehemann, S. A. Duraj
Cleveland State University, Cleveland, OH 44115

D. Scheiman

QSS Inc, Cleveland, OH 44135

A. F. Hepp

NASA Glenn Research Center, Cleveland, OH 44135

ABSTRACT

The development of thin-film solar cells on flexible, lightweight, space-qualified durable substrates (i.e. Kapton) provides an attractive solution to fabricating solar arrays with high specific power, (W/kg). The syntheses and thermal modulation of ternary single source precursors, based on the $[(LR)_2Cu(SR')_2In(SR')_2]$ architecture in good yields are described. Thermogravimetric analyses (TGA) and Low temperature Differential Scanning Calorimetry, (DSC) demonstrate that controlled manipulation of the steric and electronic properties of either the group five-donor and/or chalcogenide moiety permits directed adjustment of the thermal stability and physical properties of the precursors. TGA-Evolved Gas Analysis, confirms that single precursors decompose by the initial extrusion of the sulphide moiety, followed by the loss of the neutral donor group, (L) to release the ternary chalcopyrite matrix. X-ray diffraction studies, EDS and SEM on the non-volatile pyrolyzed material demonstrate that these derivatives afford single-phase $CuInS_2/CuInSe_2$ materials at low temperature. Thin-film fabrication studies demonstrate that these single source precursors can be used in a spray chemical vapor deposition process, for depositing $CuInS_2$ onto flexible polymer substrates at temperatures less than 400°C.

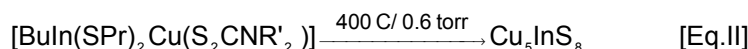
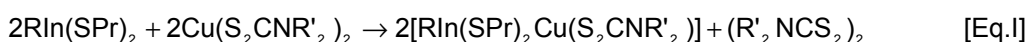
INTRODUCTION

Photovoltaic modules based on ternary chalcopyrite absorber layers, $(I-III-VI_2; Cu(In,Ga)(S,Se)_2)$ have been the focus of intense investigation for over two decades. The use of chalcopyrite absorber are highly appealing since their bandgaps correlate well for their use in terrestrial (AM 1.5), and low orbital space applications (AM0), whilst displaying long term stability and excellent radiation tolerance [1,2]. Additionally, by adjusting the percentage atomic composition of either Ga for In and/or S for Se, the bandgap can be tuned from 1.0 eV to 2.4 eV, thus permitting fabrication of high, or graded bandgaps [3]. One of the most promising technologies lies in the development of polycrystalline thin films, since their lightweight structure enables them to achieve higher specific power (WKg^{-1}), than alternative single crystalline devices [4]. Thus, a key step of device fabrication for thin film solar cells is the deposition onto flexible, lightweight, space-qualified substrates such as polyimides.

Current methods of choice for the depositing ternary crystallite compounds, i.e. co-evaporation of elements [5-7], or binary elements [8], electrodeposition [9], reactive-sintering [10], flash evaporation [11] involve toxic sulphurization/selenization steps, often at elevated temperatures. Furthermore, under these conditions loss of volatile In/Ga chalcogenides is reported [5,12]. The requirement of high temperature deposition makes this technique incompatible with all presently known flexible polyimides, or other polymer substrates. In addition, use of toxic reagents is a limiting factor. The use of multi-source inorganic/organometallic precursors in a CVD type process is more appealing due to milder process parameters. However, stoichiometry control of deposited films can be difficult to achieve, and film contamination is evident [13], or the use of toxic pyrophoric precursors are required [14]. A novel approach is the use of ternary single source precursors, (SSP), which have the I-III-VI₂ stoichiometry built in and are suitable for low temperature deposition. Although, a rich and diverse array of binary SSP are known, characterized, reviewed and tested, the number of reports for the preparation of ternary SSP are limited, in addition to their use in deposition processes [15].

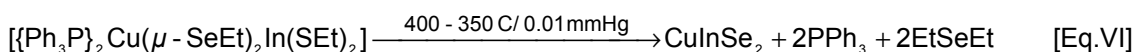
BACKGROUND

In early studies Nomura *et al*, reported that an equimolar mixture of $\text{Bu}'_2\text{InSPr}$ and $\text{Cu}(\text{S}_2\text{CNBu}_2)_2$ decomposed to afford CuInS_2 powders [16]. On this basis, solution pyrolysis of this mixture dissolved in *p*-xylene was used to deposit thin-film CuInS_2 at 350 °C onto glass substrates. Film composition was determined by XRD, which showed broad peaks. XRD revealed the ratios of In/Cu and S/Cu decreased with temperature, and a second phase to be present for films deposited at 350 °C. Grain size was estimated to be in the range of 50-100 nm as determined by SEM. It was later realized that the equimolar reaction mixture of $\text{Bu}'_2\text{InSPr}$ and $\text{Cu}(\text{S}_2\text{CNBu}_2)_2$ (as used in solution pyrolysis) afforded a single source precursor $[\text{Bu}_2\text{In}(\text{SPr}')\text{Cu}(\text{S}_2\text{CNPr}'_2)]$ before decomposing to the chalcopyrite matrix [17]. Analytical and spectral data confirmed that the mixture of $\text{Bu}'_2\text{InSPr}$ and $\text{Cu}(\text{S}_2\text{CNBu}_2)_2$ yielded a SSP. A number of analogous ternary CIS precursors were also synthesized by the reaction of alkyl indium thiolates with copper dithiocarbamates, [Eq.I] [18]. However, only $[\text{Bu}_2\text{In}(\text{SPr}')\text{Cu}(\text{S}_2\text{CNPr}'_2)]$ was successfully implemented for depositing pure CuInS_2 by low pressure MOCVD. In the case of $[\text{BuIn}(\text{SPr}')_2\text{Cu}(\text{S}_2\text{CNR}'_2)]$, tetragonal CuIn_5S_8 was deposited, [Eq.II] [19].



Although the structure of these SSP were unresolved, it can be envisaged that their utility could be extended for the deposition of Ga and or Se based ternary thin-films, by using gallium thiolates/selenolates with copper dithio/diseleno carbamates. Furthermore, careful molecular design by selectively introducing S or Se groups into only one of the Ga/In, or copper reagents may aid in determining the decomposition mechanism of the precursor, in addition to serving as a $\text{CuIn}(\text{S,Se})_2$ source, for example, $[\text{Bu}_2\text{In}(\text{SePr}')\text{Cu}(\text{S}_2\text{CNPr}'_2)]$.

In early 1990 Kanatzidis *et al* reported the preparation of hetro binuclear complexes consisting of tetrahedrally arranged Cu and In centers, with two bridging thiolato and selenolato groups, [Eq.III] [20]. Pyrolysis studies undertaken revealed that the Se derivative could be converted into CuInSe_2 at 400-450 °C @ 0.01 mm Hg [Eq.VI], but none of the precursors had been evaluated in a thin-film deposition study.



In continuing work, Buhro and Hepp were able to demonstrate that $[\{\text{PPh}_3\}_2\text{Cu}(\text{SEt})_2\text{In}(\text{SEt})_2]$ could be utilized in a spray CVD process, for depositing thin-film CuInS_2 below 400 °C [21-22]. Thin film where deposited using a dual solvent system of toluene and dichloromethane, (CH_2Cl_2) as the carrier solvent. Single phase 112 orientated CuInS_2 thin films were successfully deposited at a range of temperatures from 300 to 400 °C, whilst at elevated temperatures (500 °C), CuIn_5S_8 phase thin films could be deposited. RBS EDS and XPS analysis showed that the films were free from any detectable impurities and highly crystalline, thus concluding the precursor decomposes cleanly. During the course of the study, the morphology of the deposited thin films where found to be temperature, and carrier solvent dependent. Films deposited at 300 °C and 350 °C yielded grain size of 400-800 nm, with smaller finer particles of 50-200 nm resident on top. At higher deposition temperature of 400 °C, the films consisted of more angular and uniform grain size of approx 200 to 400 nm. Photoluminescence (PL) data and optical transmission measurements on the confirmed that deposited CuInS_2 thin films were direct bandgap semiconductors. In addition, the preparation of the first CuGaS_2 SSP, $[\{\text{PPh}_3\}_2\text{Cu}(\text{SET})_2\text{Ga}(\text{SET})_2]$ was also synthesized, although the structure was not elucidated [23]. XRD and RBS characterization of the pyrolysed material, (350-400 °C, 0.01 mmHg) and spray CVD deposited material confirmed the ternary Ga SSP to afford single phase CuGaS_2 .

Very recent research at NASA Glenn has successfully reported the fabrication of the first ternary chalcopyrite quantum dots synthesized from ternary single source precursors, hence further extending their utility [24].

In the course of our investigations for improved single source precursors for the spray CVD of chalcopyrite thin-films, to the ternary semiconductor $\text{Cu}(\text{Ga}/\text{In})(\text{Se}/\text{S})_2$, we have continued to expand the molecular design of SSP based on the $[\{\text{LR}_3\}_2\text{Cu}(\text{ER}')_2\text{In}(\text{ER}')_2]$ architecture [20]. Primarily due to the limited preparation and investigation for their use in a spray CVD process. Furthermore, the number of “tunable” sites within the complex allows for their utility in preparing a number of ternary chalcopyrites of varying composition, in addition to engineer the SSP to match a given spray CVD process.

EXPERIMENTAL

All manipulations were carried out under anaerobic condition using standard Schlenk-line techniques. Multinuclear NMR, Differential Scanning Calorimetry (DSC), and Thermogravimetric analyses (TGA) with evolved gas analysis, (EGA) were used to characterize and verify precursor formation and purity. The complexes are synthesized based on modification of the procedure reported by Kanatzidis [20], with the exception of the thiolate/selenoato anion being generated *in situ* by reaction of the conjugate acid with NaOEt in methanol. The thiolate/selenoate was prepared *in situ* by reaction of NaOEt (24.25 mmol) with thiol/senenol (23.01 mmol) in anhydrous methanol.

After 30 minutes, InCl_3 (1.27 g, 5.75 mmol) was added affording a clear solution and the mixture was stirred for 1hr. $[\text{Cu}(\text{CH}_3\text{CN})_2\text{L}_2]\text{PF}_6$ (5.75 mmol), dissolved in anhydrous CH_2Cl_2 (20 mL) was added dropwise to the reaction flask. The mixture was stirred (~1 to 2 d) resulting in the precipitation of a white solid. The reaction solution was then concentrated and the product extracted with anhydrous CH_2Cl_2 (50 mL,) and filtered through celite to remove the inorganic salts. The collected filtrate was concentrated via rotary evaporation. The solid precursors can then be used as is or further purified by washing with cold anhydrous diethyl ether, (3x 20 mL) and then finally anhydrous pentane, (2x10 mL). The multi-stage synthesis yields the desired products in good yields, (> 65 %) as opaque liquids, or solids with varying stability in air.

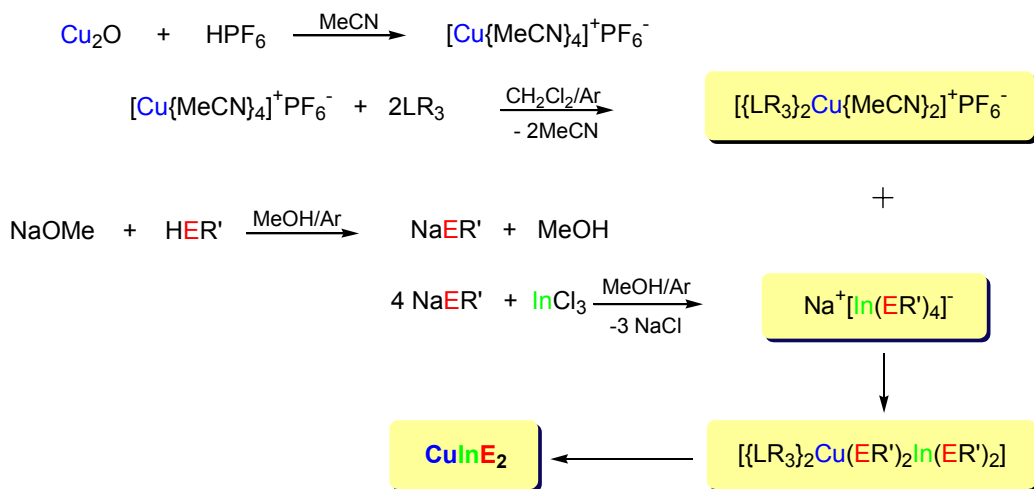
Films of CuInS_2 were deposited on molybdenum substrates using a spray CVD reactor similar to those described elsewhere, [23,25]. For a typical deposition, 1.5 g of the SSP was dissolved in 150 ml of toluene. The solution was atomized by a 2.5 MHz nebulizer and swept into a two-zone hot-wall reactor by a carrier gas (argon) that was pre-saturated with the solvent. The temperature of the first zone (evaporation zone) was $128 \pm 1^\circ\text{C}$ and the temperature of the second zone (deposition zone) ranged from $390 \pm 1^\circ\text{C}$. Carrier gas flow rate was 4 L/min.

Where possible deposited films were characterized by transmission spectroscopy (Perkin Elmer, Lambda-19), scanning electron microscopy (SEM) (Hitachi S-3000N), Energy Dispersive Spectroscopy (SEM-EDS) (EDAX), profileometry (KLA-Tencor HRP 75) and X-ray diffraction Philips PW3710, ($\text{Cu K}\alpha$, 1.541 Å). Reported SEM-EDS measurements are accurate to $\pm 3\%$. Thermal analyses were performed on TA Instruments TGA 2950 using Platinum pans under a dinitrogen atmosphere, (ramp $10^\circ\text{C}/\text{min}$) and TA Instruments DSC 910/MDSC 2910 under a dinitrogen atmosphere, in hermetically sealed aluminum pans.

RESULTS & DISCUSSION

The SSP are prepared by the reaction of a stabilized Cu(I) cation, with an Indium(III) chalcogenide anion prepared *in situ* by reaction of the conjugate acid of the thiol or senenol with NaOEt in methanol. An advantage of this method is no adverse side products are produced, in addition to an “activated” thiolate/selenonate anion. During the course of the reaction the more labile MeCN ligands are displaced in preference to the thermodynamically stable chalcogenide-Cu bond formation, (Scheme I).

Scheme I. Synthesis of ternary single source precursors



L = P, As, Sb; E = S, Se; R' & R = alkyl, aryl

The versatility of this synthetic pathway can be illustrated by ability to modulate the physical properties of the precursor and composition at any of the intermediate synthetic steps by either;

- Adjusting the Lewis acid-base interaction (L→Cu)
- Adjusting the accessibility of the lone pair of electrons on the neutral donor ligand by variation of R
- Adjusting the bond strength between the chalcogenide with either In/Ga and Cu metal centers
- The ability to prepare analogues of group 16, (S, Se, Te)
- The ability to prepare either indium or gallium derivatives

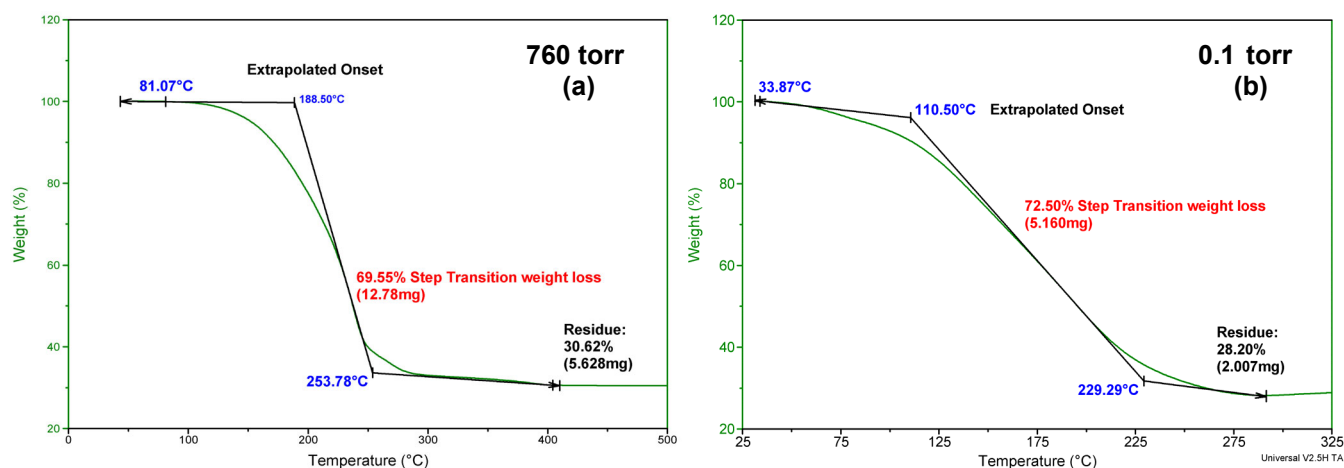
The Lewis acid-base interaction is a valuable component to the overall stability of the molecule, given that the ability of the Lewis base to dissociate from the cation at lower energies is pertinent to the degradation of the precursor at reduced temperatures. Hence, the Drago-Wayland approximation, [26] can be used for ternary single source precursor design, to quantitatively estimate the strength of the Lewis acid-base interaction between the copper center and the neutral donor. The cleavage of chalcogenide-R' bond also plays an important role, since this allows the chalcogenide to be released for incorporation into the ternary chalcopyrite matrix. Hence, the use of a sterically demanding R' group of good "leaving ability", would promote the facile release of the chalcogenide.

Initial studies focused on basic modification of the SSP, and their influence on precursor stability. Multinuclear NMR data demonstrated that the precursors were free from any starting reagents. Thermogravimetric analyses (TGA) were performed at ambient pressure in platinum pans on samples of the precursors, heated at a rate of 10 °C / min under a dinitrogen atmosphere. Weight loss was associated with decomposition of the complexes. Calculation of the derivative maximum rate of weight loss (%/°C), listed as MRW in Table I, shows a range from a low of 225 °C for **8** to a high of 325 °C for **5**. Calculation of the precursor efficiency to afford CIS/Se as the final product, based on the residual material from the TGA experiments found the samples to be within 5 % (Figure Ia).

Table I. Thermal data for ternary Single Source precursors.

Single Source Precursors	TGA			DSC	
	Extrap. Onset °C	MRW °C / %	Residue %	M.P. °C	Decomp. °C
1 $[\{\text{PPh}_3\}_2\text{Cu}(\text{SEt})_2\text{In}(\text{SEt})_2]$	236	269	25	122	266
2 $[\{\text{AsPh}_3\}_2\text{Cu}(\text{SEt})_2\text{In}(\text{SEt})_2]$	205	233	18	47	276
3 $[\{\text{SbPh}_3\}_2\text{Cu}(\text{SEt})_2\text{In}(\text{SEt})_2]$	212	239	26	45	271
4 $[\{\text{PPh}_3\}_2\text{Cu}(\text{SPr}^i)_2\text{In}(\text{SPr}^i)_2]$	215	254	29	163	260
5 $[\{\text{PPh}_3\}_2\text{Cu}(\text{SPh})_2\text{In}(\text{SPh})_2]$	261	325	22	117	280
6 $[\{\text{PPh}_3\}_2\text{Cu}(\text{SePh})_2\text{In}(\text{SePh})_2]$	223	253	22	53	219
7 $[\{\text{P}(\text{Bu}^n)_3\}_2\text{Cu}(\text{SEt})_2\text{In}(\text{SEt})_2]$	189	238	31	-	264
8 $[\{\text{P}(\text{Bu}^n)_3\}_2\text{Cu}(\text{S}(\text{Pr}^n))_2\text{In}(\text{SPr}^n)_2]$	171	225	29	-	239

Preliminary Vacuum-TGA studies for the “smoothed” profile for the SSP **7**, shows the extrapolated onset can be lowered by approx 80 °C thus lowering the degradation temperature window and making these precursors model candidates for use in low temperature/pressure spray CVD on space qualified substrates such as Kapton™ (Figure Ib).

Figure I. TGA profiles for $[\{\text{P}(n\text{-Bu})_3\}_2\text{Cu}(\text{SEt})_2\text{In}(\text{SEt})_2]$, **7**.

A further example of the flexibility of the $[\{\text{ER}_3\}_2\text{Cu}(\text{YR}')_2\text{In}(\text{YR}')_2]$ architecture to direct adjustment of these precursors are the SSP **7** and **8**, which have a liquid solid-state phase. Low temperature DSC was used to investigate the liquid phase for **7** and **8**. In separate studies, samples **7** and **8** were subjected to both quench cooling and slow controlled cooling before being heated at 10 °C/min and 5 °C/min. The higher heating rates were chosen since this is preferable to enhance resolution for the observation of a finite onset point assignable to melting [27]. In low temperature DSC experiments using controlled cooling, both samples **7** and **8** were found not to show an endotherm assignable to a melting phase transition (Figure II).

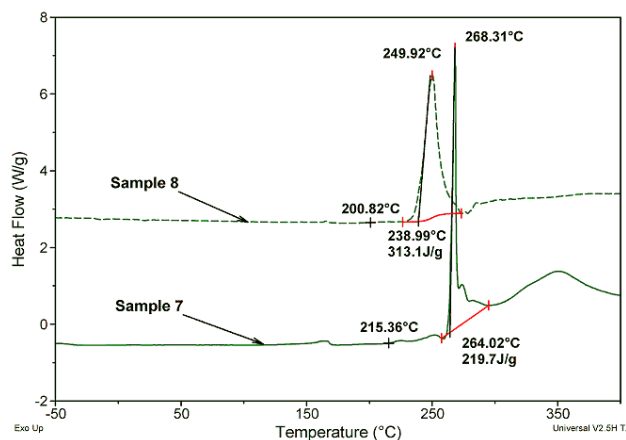


Figure II. Low temperature DSC for $[\{P(Bu^n)_3\}_2Cu(SET)_2In(SET)_2]$ **7** and $[\{P(Bu^n)_3\}_2Cu(S(Pr^n))_2In(SPr^n)_2]$ **8**.

In similar quench cooling experiments, an endothermic phase change assignable to a melt was also not observed. Although Modulated-DSC is known to provide greater sensitivity to deconvolute small phase transitions, studies using this technique also demonstrated the absence of an endothermic phase transition assignable to a melt. This may be attributed to the fact that MDSC uses a sinusoidal heat flow, hence the “resident time” during control cooling may not be sufficient to allow the material to undergo cold crystallization. Therefore, under these various test conditions it can be validated that sample **7** and **8** have a liquid phase at ambient temperatures. Examination of the other phase transitions reveal the main exothermic events for **7** and **8** begin with extrapolated onset temperatures of 264 °C and 239 °C, which can be assigned to the decomposition of the samples. The lower decomposition temperature of **8** can be explained, since an increase in chain length and/or steric “bulk” of the alkyl groups is known to decrease the stability of a complex [15].

Thermal analysis experiments demonstrate that the physical and chemical properties of these complexes are easily controlled by directed adjustment on one, or more of the “tunable” sites within the complex. Analysis of the thermal data shows that precursors stability can be modified by even minor adjustment of either the electronic or steric effects of the peripheral groups of the precursors. A more detailed interpretation of how the thermal properties of these materials can be modulated is presented elsewhere [28]. To verify the mechanism of decomposition for the precursors, TGA-Evolved Gas Analysis via FTIR and mass spectrometry was investigated. The real time FTIR spectrum for **7** and **8** shows absorptions at approx 3000, 1460, 1390, 1300 and 1250 cm^{-1} (Figure III).

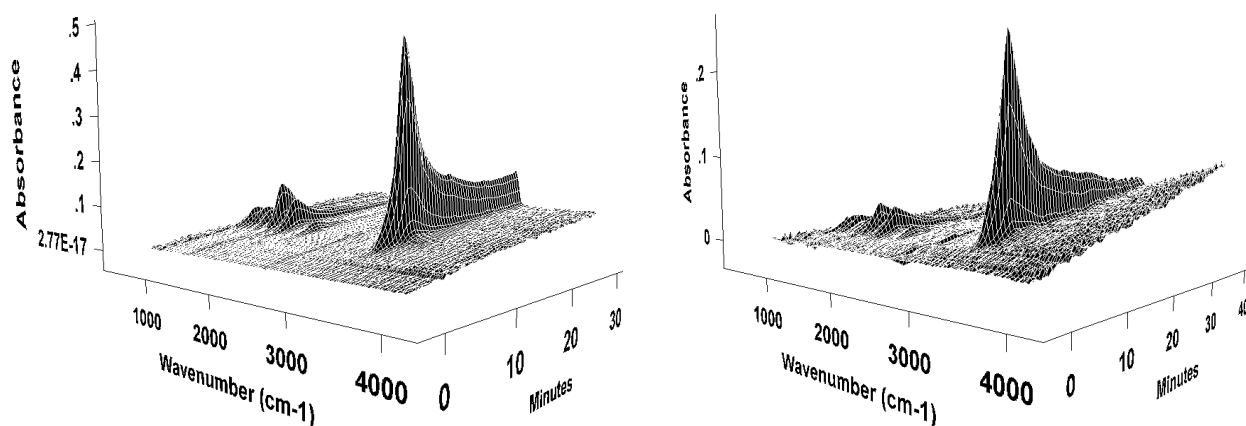


Figure III. EGA-FTIR spectra for $[\{P(n-Bu)_3\}_2Cu(SET)_2In(SET)_2]$ **7** and $[\{P(n-Bu)_3\}_2Cu(SPr)_2In(SPr)_2]$ **8**.

Correlation with the EGA-mass spectra allows for the assignment to the initial loss of diethyl sulphide, as supported by the library fit and from the assignment of the fragment and parent ions ($m/z = 90$) (Figure IVa). After approximately 15 minutes mass-spec EGA shows the absence of peaks assignable to Et_2S and the occurrence of fragment ions with a mass to charge ratio (m/z) greater than 90 with an intense peak at $m/z = 202$. These can be assigned to the successive loss of PBU_3 on the basis of its library fit of 92 % and assignment of the fragment ions (Figure IVb). In similar experiments, EGA for the *n*-propyl derivative **8** gave analogous results, however for samples **1-6**, EGA was only able to confirm the extrusion of the dialkyl/diaryl sulphide moiety. The inability to detect the neutral group V donors may be attributed to their lower volatility.

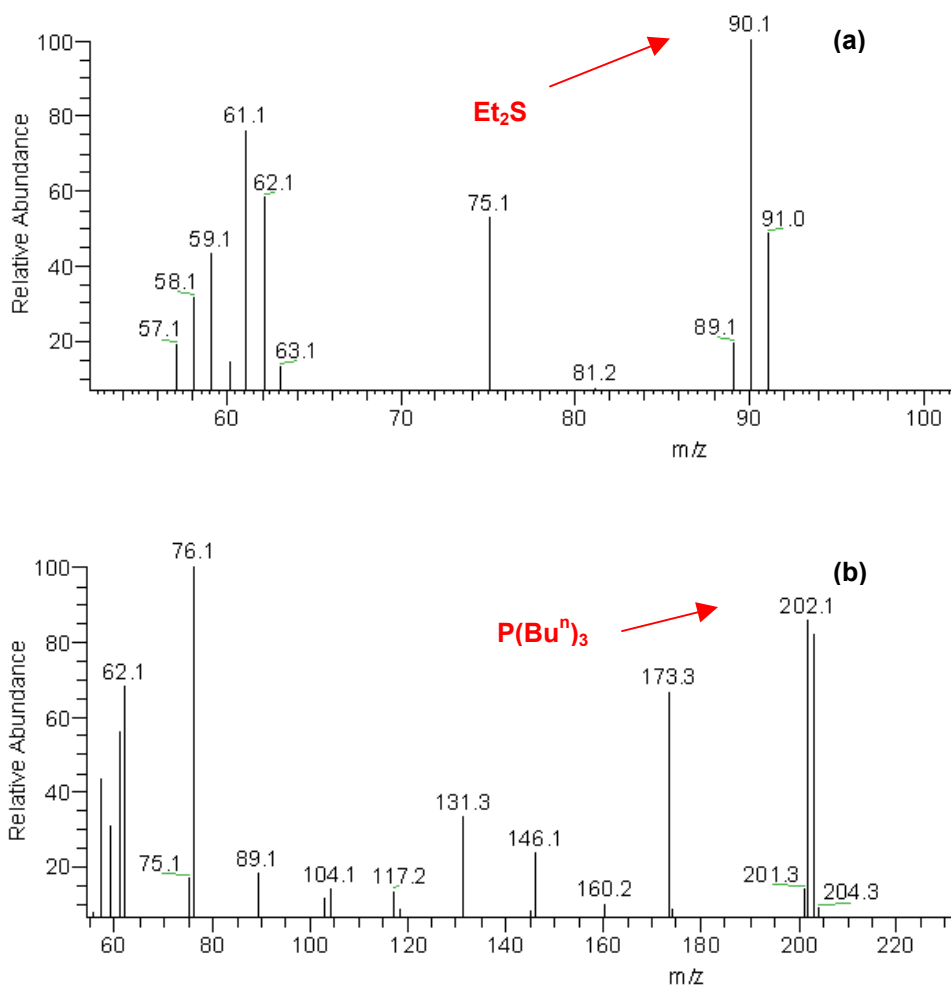


Figure IV. EGA: Mass Spec data from TGA for $[\{\text{P}(n\text{-Bu})_3\}_2\text{Cu}(\text{SET})_2\text{In}(\text{SET})_2]$, **7**.

Thus, the use of TGA-EGA provides conclusive evidence for the mechanism of decomposition for the single source precursors to occur via the loss of a sulphide moiety, followed by loss of the neutral donor ligand.

The ability of the new precursor to thermally decompose to yield single-phase CIS was investigated by powder X-ray diffraction (XRD) analysis and Energy Dispersive Spectroscopy, (EDS) on the non-volatile solids from the TGA experiments of selective compounds. XRD spectra for the non-volatile material produced from the pyrolysis of **7** with the JCPDS reference patterns for CuInS_2 (27-0159), confirmed it to be single-phase CuInS_2 (Figure V).

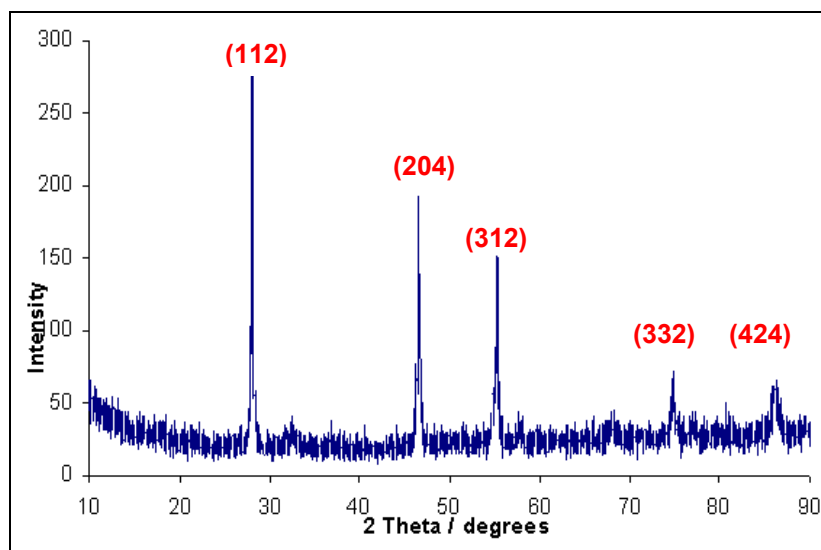


Figure V. XRD Powder Diffraction for non-volatile residue from pyrolysis of $[\{P(n\text{-Bu})_3\}_2\text{Cu}(\text{SEt})_2\text{In}(\text{SEt})_2]$, (Cu $K\alpha$, 1.541 Å).

Examination of the EDS spectra for the same samples shows predominant emissions due to Cu, In, and S edges, with the approximate percentage atomic composition of 27, 23 and 50 for **7** and 28, 23 and 49 for **8** respectively, thus supporting the formation of CuInS_2 . SEM images of the non-volatile residue (CuInS_2) from the TGA experiments for sample **7** and **8** show grain size of $\sim 1\mu\text{m}$ (Figure VI).

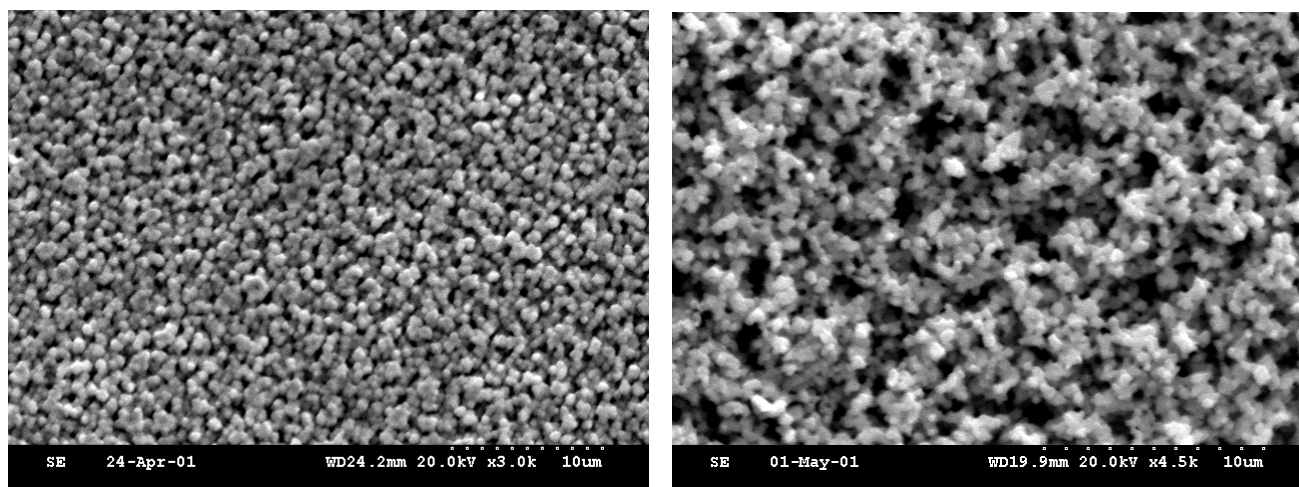


Figure VI. SEM of non-volatile residue from TGA for $[\{P(n\text{-Bu})_3\}_2\text{Cu}(\text{SEt})_2\text{In}(\text{SEt})_2]$, **7**, Grain size $\sim 1\mu\text{m}$; $[\{P(n\text{-Bu})_3\}_2\text{Cu}(\text{SPR}^n)_2\text{In}(\text{SPR}^n)_2]$, **8**.

The suitability of some of these single source precursors for the fabrication of thin-film CIS absorber has been investigated, and these results are reported in detail elsewhere [25,29]. Herein we report the first studies in the attempt to use the liquid precursor in a Spray CVD process. Well adhering films of CuInS_2 were deposited on a Molybdenum substrate by spray CVD at 390°C using $[\{P\text{Bu}_3\}_2\text{Cu}(\text{SEt})_2\text{In}(\text{SEt})_2]$, which were dark blue/black, due to variation in film thickness. Unfortunately due to the limited quantities of liquid precursor for thin-film deposition studies, film thickness was too low to obtain an adequate SEM image. However, XRD and EDS data were recorded.

As deposited, the majority of CuInS₂ film is highly (112) oriented (Figure. VII), which is ideal since the preferred orientation for CIS films used in photovoltaic devices is (112) as these films have a low series resistance [30].

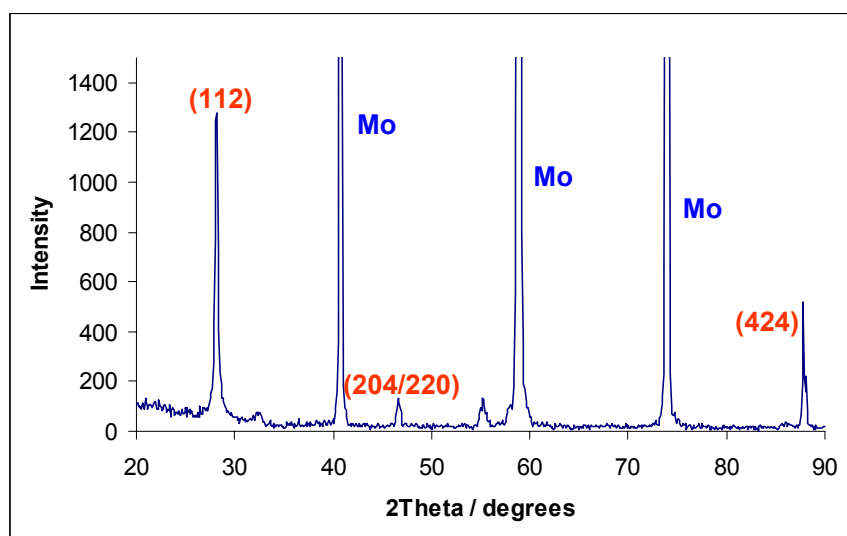


Figure VII. X-ray powder diffraction spectra of a CuInS₂ film on Mo (back half of the substrate).

Since the EDS emissions for sulfur and Molybdenum overlap, measurements were limited to recording emissions for only the Cu and In edges. SEM-EDS data on a number of regions on the thin film gave atomic percents representative of CuInS₂ (Table II), in addition, no evidence of phosphorous or carbon contamination could be detected, verifying that the precursor decomposes cleanly as evidenced in EGA-TGA studies.

Table II. Atomic composition of CIS thin-film deposited using SSP 7.

	Atomic %, (± 3 %)		
	Front 1	Front 2	Back
Cu	50	51	50
In	50	49	50

No electronic properties of the film could be preformed since film thickness was insufficient for device fabrication. However, the electrical properties of deposited films using SSP 1 were suitable for current versus voltage (IV) measurements to be recorded using thermally evaporated aluminum to make Schottky barriers. Many of the Schottky barriers exhibited excellent diode behavior (Figure VIII), furthermore, rapid thermal annealing of the films at 600°C for five minutes, more then doubled the current density of the diodes at 0.9 Volts and improved the reverse bias leakage. The improvement in the diode behavior is attributed to enhanced crystallinity and reduction of defects in the annealed films, as considerable narrowing of the diffraction lines was observed in the annealed films. Unfortunately, the higher annealing temperature is not compatible with deposition onto space qualified polymer substrates. It is hoped that by use of more labile single source precursors, improved electrical properties can be achieved without annealing.

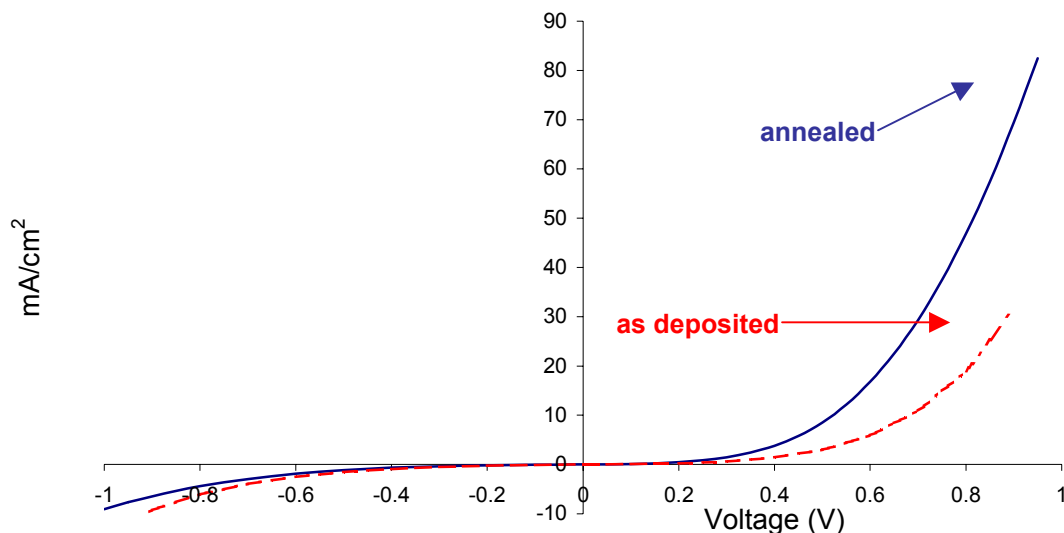


Figure VIII. Current density vs. voltage plot of Schottky barrier made from evaporated Al on CuInS_2 on Mo foil for both as-deposited and annealed films using SSP 1, (Al contacts $\sim 0.04 \text{ mm}^2$)

SUMMARY

Thermal analysis data substantiates that even minor adjustment of the steric and electronic properties on either the neutral donor, or chalcogenide groups, permits adjustment of the solid-state phase and stability of the precursor. Evolved gas analysis via mass-spec FTIR spectroscopy, confirms the mechanism of decomposition for the SSP proceeds by the loss of the sulphide group, followed by loss of the neutral donor. XRD and EDS show that the non-volatile materials from pyrolysis studies afford single-phase CuInS_2 and CuInSe_2 . Thin-film fabrication studies successfully demonstrate that by using a single source organometallic precursor in conjunction with spray chemical vapor deposition, CuInS_2 can be deposited on flexible polymer substrates at temperatures less than 400°C .

REFERENCES

- [1] S. G. Bailey, D. J. Flood, "Space photovoltaics", Prog. Photovoltaics Res. Appl., **6**, p.1, 1998. ; (b) H. W. Schock, R. Noufi, "CIGS-based solar cells for the next Millennium", Prog. Photovolt. Res. Appl., **8**, 151-160
- [2] H. W. Schock, K. Bogus, "Development of CIS solar cells for space applications", Proc. 2nd World Conf. On Photovolt. Energy Conf., Eds. J. Schmid, H. A. Ossenbrink, P. Helm, H. Ehmann and E. D. Dunlop, 3586, E. C. Joint Res. Center, Luxembourg, 1998.
- [3] D. Tarrant, J. Ermer, I-III-VI₂ multinary solar cells based on CuInSe_2 , Proceedings 23rd IEEE Photovoltaic Specialist Conference, Louisville, KY, IEEE, New York, pp. 372, 1993.
- [4] D. Hoffman, T. Kerslake, A. Hepp, R. Raffaele, "Thin-Film Solar Array Earth-Orbit Mission Applicability Assessment", XVII Space Photovoltaic Research and Tech. Conf., 2001.
- [5] B. M. Basol, V. K. Kapur, A. Halani, C. Leidholm, J. Sharp, J. R. Sites, A. Swartzlander, R. Matson, H. Ullal, "Cu(In,Ga)Se₂ thin films and solar cells prepared by selenization of metallic precursors", Journal of Vacuum Science and Technology A, **14A**, p. 2251, 1996.

- [6] V. Probst, W. Stetter, W. Riedl, H. Vogt, M. Wendl, H. Calwer, S. Zweigart, K. Ufert, B. Freienstein, H. Cerva, F. H. Karg, "Rapid CIS-process for high efficiency PV-Modules: development towards large area processing", *Thin Solid Films*, **387**, p. 262, 2001.
- [7] B. Dimmler, H. W. Schock, "Scalability and pilot operation in solar cells of CuInSe₂ and their alloys", *Prog. Photovolt. Res. Appl.*, **6**, p. 193, 1998.
- [8] S. C. Park, D. Y. Lee, B. T. Ahn, K. H. Yoon, J. Song, "Fabrication of CuInSe₂ films and solar cells by sequential evaporation of In₂Se₃ and Cu₂Se binary compounds", *Sol. Energy Mater. Sol. Cells*, **69**, p. 99, 2001.
- [9] C. Guillen, J. Herrero, "Recrystallization and components redistribution processes in electrodeposited CuInSe₂ thin films", *Thin Solid Films*, **387**, p.57, 2001
- [10] C. Eberspacher, C. Fredric, K. Pauls, J. Serra, "Thin-film CIS alloy PV materials fabricated using non-vacuum, particles-based techniques", *Thin Solid Films*, **387**, p.18, 2001.
- [11] M. Klenk, O. Schenker, V. Alberts, E. Bucher, "Properties of flash evaporated chalcopyrite absorber films and solar cells", *Thin solid Films*, **387**, p. 47, 2001.
- [12] C. Dzionk, H. Metzner, S. Hessler, H. E. Mahnke, "Phase formation during the reactive annealing of Cu-In films in H₂S atmosphere". *Thin Solid Films*, **299**, p. 38, 1997.
- [13] M. Krunk, V. Mikli, O. Bijakina, H. Rebane, A. Mere, T. Varema, E. Mellikov, "Composition and structure of CuInS₂ films prepared by spray pyrolysis", *Thin Solid Films*, **361-362**, p.61, 2000.
- [14] M. C. Artaud, F. Ouchen, L. Martin, S. Duchemin, "CuInSe₂ thin films grown by MOCVD: characterization, first devices", *Thin Solid Films*, **324**, p. 115, 1998.
- [15] A. C. Jones, P. O'Brien, "CVD of Compound Semiconductors: Precursors Synthesis, Development & Application", VCH Press, 1997.
- [16] R. Nomura, K. Kanaya, H. Matsuda, "Preparation of Copper-Indium-Sulfide thin films by solution Pyrolysis of organometallic sources", *Chem. Let.*, p. 1849, 1988.
- [17] R. Nomura, S. Fujii, K. Kanaya, H. Matsuda, "Oxygen- or sulphur- containing organoindium compounds for precursors of indium oxide and sulphide thin films", *Polyhedron*, **9**, p. 361, 1990.
- [18] R. Nomura, Y. Seki, H. Matsuda, "Preparation of copper indium sulfide (CuInS₂) thin films by single-source MOCVD process using Bu₂In(SPr-iso)Cu(S₂CNPr-iso₂)", *J. Mater. Chem.* **2(7)**, p.765, 1992.
- [19] R. Nomura, Y. Seki, H. Matsuda, "Preparation of copper indium sulfide (CuIn₅S₈) thin films by single-source organometallic chemical vapor deposition", *Thin Solid Films*, **209(2)**, p. 145, 1992.
- [20] W. Hirpo, S. Dhingra, A. C. Sutorik, M. G. Kanatzidis, "Synthesis of mixed Copper-Indium chalcogenolates. Single Source Precursors for the photovoltaic material CuInQ₂ (Q = s, Se)", *J. Am. Chem. Soc.*, **115**, p. 597, 1993.
- [21] J. A. Hollingsworth, A. F. Hepp, W. E. Buhro, "Spray CVD of Copper Indium Disulfide Films: Control of Microstructure and crystallographic orientation", *Chem. Vap. Deposition*, **5**, p. 105, 1999.
- [22] J. A. Hollingsworth, W. E. Buhro, A. F. Hepp, P. P. Jenkins, M. A. Stan, "Spray chemical vapor deposition of CuInS₂ thin films for application in solar cell devices", *Mat. Res. Soc. Symp. Proc.*, **495**, p 171, 1998.
- [23] J. A. Hollingsworth, "Chemical routes to nanocrystalline and thin-film III-VI and I-III-VI semiconductors" PhD Thesis, Supervisor W. E. Buhro, Washington University 1999.
- [24] R. Raffaele, S. Castro, S. G. Bailey, "Quantum Dots Solar Cells", XVII Space Photovoltaic Research and Tech. Conf., 2001.
- [25] J. D. Harris, D. G. Hehemann, J. E. Cowen, A. F. Hepp, R. P. Raffaele, J. A. Hollingsworth, "Using single source precursors and spray chemical vapor deposition to grow thin-film CuInS₂", *Proc. Of the 28th IEEE Photovoltaic Specialists Conference*, Anchorage, AK, p. 563, 2000.
- [26] R. S. Drago, N. Wong, C. Bilgrien, G. C. Vogel, "E and C parameters from Hammett substituent constants and use of E and C to understand cobalt-carbon bond energies", *Inorg. Chem.* **26(1)**, p. 9, 1987.
- [27] TA Instruments, "Thermal Analysis & Rheology; Chapter 3 Running Experiments: Preparing Samples", p.3, 1998.
- [28] J. E. Cowen, A. Riga, A. F. Hepp, S. Duraj, K. K. Banger, R. McClaron, NATAS Conference Session: Thermal Application of Materials; NATAS Conference St. Louis, MO (2001).
- [29] K. K Banger, J. Harris, J. Cowen, A. F. Hepp, E-MRS Spring Meeting, Symposium P: Thin Film Materials for Photovoltaics, Strasbourg, France, 2001.
- [30] K. Siemwe, J. Klaer, I. Luck, D. Braunig, "Influence of crystal Orientation on Device Performance of CuInS₂ solar cells", *Proc. Of the 28th IEEE Photovoltaic Specialists Conference*, Anchorage, AK, p. 630, 2000.

SOLAR FLIGHT ON MARS AND VENUS

Geoffrey A. Landis
NASA John Glenn Research Center
Cleveland, OH 44135

Christopher LaMarre
University of Illinois

Anthony Colozza
Analex
NASA John Glenn Research Center

Solar powered aircraft are of interest for exploring both Mars and Venus.

The thin atmosphere of Mars presents a difficult environment for flying. It is clear that a new approach is needed. By making a totally solar airplane, we can eliminate many of the heavy components, and make an airplane that can fly without fuel. Using high efficiency solar cells, we can succeed with an airplane design that can fly for up to 6 hours in near-equatorial regions of Mars (4 hours of level flight, plus two hours of slow descent), and potentially fly for many days in the polar regions. By designing an airplane for a single day flight. In particular, this change means that we no longer have to cope with the weight of the energy storage system that made previous solar powered airplanes for Mars impractical). The new airplane concept is designed to fly only under the optimal conditions: near equatorial flight, at the subsolar point, near noon. We baseline an 8 kg airplane, with 2 kg margin. Science instruments will be selected with the primary criterion of low mass.

Solar-powered aircraft are also quite interesting for the exploration of Venus. Venus provides several advantages for flying a solar-powered aircraft. At the top of the cloud level, the solar intensity is comparable to or greater than terrestrial solar intensities. The atmospheric pressure makes flight much easier than on planets such as Mars. Figure 1 shows the atmospheric pressure on Venus. From an altitude of approximately 45 km (pressure = 2 bar), to approximately 60 km (pressure = 0.2 bar), terrestrial airplane experience can be easily applied to a Venus airplane design. At these flight altitudes, the temperature varies from 80 °C at 45 km, decreasing to -35 °C at 60 km. Also, the slow rotation of Venus allows an airplane to be designed for flight within continuous sunlight, eliminating the need for energy storage for nighttime flight. These factors make Venus a prime choice for a long-duration solar-powered aircraft.

Fleets of solar-powered aircraft could provide an architecture for efficient and low-cost comprehensive coverage for a variety of scientific missions. Exploratory planetary mapping and atmospheric sampling can lead to a greater understanding of the greenhouse effect not only on Venus but on Earth as well.

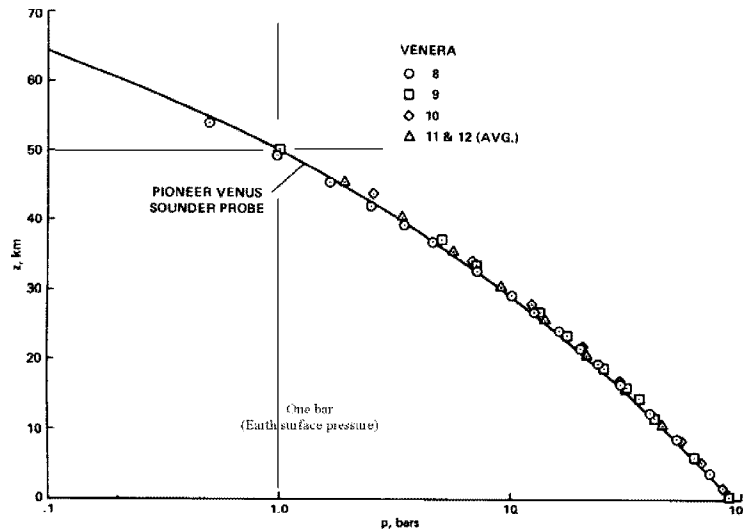


Figure 1. Atmospheric pressure (horizontal axis) as a function of altitude (vertical axis) in the Venus atmosphere. (Data from Venera 8-12 and Pioneer Venus missions).

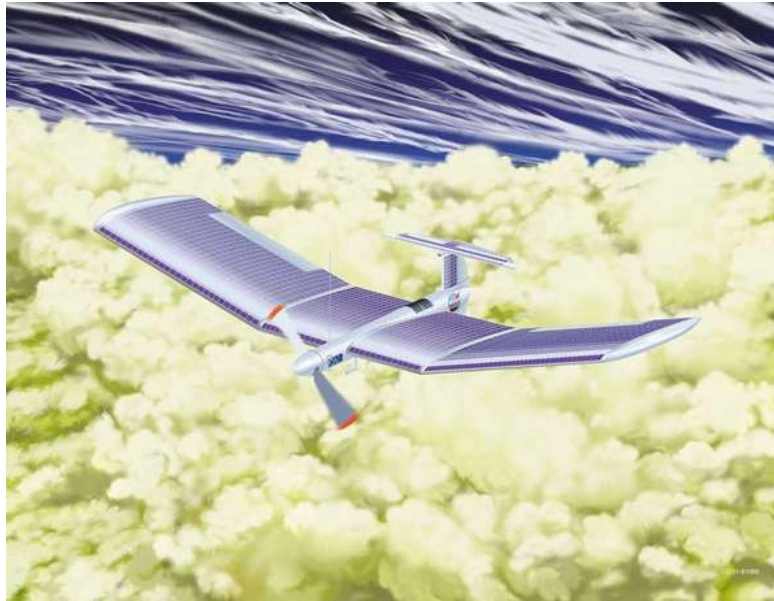


Figure 2. Concept for a Venus airplane design

REFERENCES:

1. Geoffrey A. Landis, "Exploring Venus by Solar Airplane," presented at the STAIF Conference on Space Exploration Technology, Albuquerque NM, Feb. 11-15, 2001. *AIP Conference Proceedings Volume 552*, pp. 16-18.
2. Anthony J. Colozza, "Preliminary Design of a Long-Endurance Mars Aircraft," *NASA CR 185243*, April 1990.
3. Paul B. MacCready, P. Licsaman, W. R. Morgan, and J. D. Burke, "Sun Powered Aircraft Design," *AIAA 81-0916*, May 1981.
4. D. M. Hunten, L. Colin, T. M. Donahue, and V. I. Moroz, *Venus*, University of Arizona Press 1983.

MEASURED AND SIMULATED DARK J-V CHARACTERISTICS OF a-Si:H SINGLE JUNCTION p-i-n SOLAR CELLS IRRADIATED WITH 40keV ELECTRONS¹

Kenneth Lord and James R. Woodyard
Wayne State University, Detroit, MI 48202

ABSTRACT

The effect of 40 keV electron irradiation on a-Si:H p-i-n single-junction solar cells was investigated using measured and simulated dark J-V characteristics. EPRI-AMPS and PC-1D simulators were explored for use in the studies. The EPRI-AMPS simulator was employed and simulator parameters selected to produce agreement with measured J-V characteristics. Three current mechanisms were evident in the measured dark J-V characteristics after electron irradiation, namely, injection, shunting and a term of the form CV^m . Using a single discrete defect state level at the center of the band gap, good agreement was achieved between measured and simulated J-V characteristics in the forward-bias voltage region where the dark current density was dominated by injection. The current mechanism of the form CV^m was removed by annealing for two hours at 140 °C. Subsequent irradiation restored the CV^m current mechanism and it was removed by a second anneal. Some evidence of the CV^m term is present in device simulations with a higher level of discrete density of states located at the center of the bandgap.

INTRODUCTION

Thin-film a-Si:H solar cells are prime candidates for space applications because investigations show that they have good radiation resistance [1]. The fabrication technology may be automated and has the potential for solar arrays with low cost per watt. The a-Si:H-based solar cell technology permits deposition on ultra-thin flexible substrates, thus offering high specific power density. To take advantage of the high specific power density, cells must be flown without a cover glass, thereby requiring that the nude device structure have good radiation resistance. In order to predict the radiation resistance of solar cells in space environments, particle irradiations are generally carried out in the laboratory with monoenergetic particle beams at normal incidence. In space environments there is a wide energy distribution of particles with a range of incident angles. Hence, the fundamental radiation resistance mechanisms must be understood if laboratory measurements are to be used to predict solar cell performance in a variety of space environments.

The goal of our program is to acquire a detailed understanding of the effect of particle irradiation on thin-film solar cells. We have carried out studies on the effect of MeV proton irradiation on single and multi-junction a-Si:H cells; dark current mechanisms have been identified in both virgin and irradiated cells [2]. The proton irradiation studies have shown that dark J-V characteristics are orders of magnitude more sensitive to radiation effects than light J-V characteristics. Woodyard and Landis reviewed the published literature on electron irradiation studies on thin-film devices [3]; materials and device structures have improved since the review was published. Cells are thinner and more efficient than those studied in earlier work. It is important to study and characterize the effect of particle irradiation on state-of-the-art cells if current technology is to be advanced. The AE8MAX model [4] predicts a ten-year integrated electron flux of $1.7E16 \text{ cm}^{-2}$ for electrons in the 50 keV to 10MeV range incident on a surface in geosynchronous orbit. The model does not include flux from solar flares and fluxes are questionable at the lower electron energies. The flux of electrons in the model increases at lower energies. It is for this reason that our initial electron irradiation work was carried out with electron beam energies of 40keV and fluences of about $1E17 \text{ cm}^{-2}$.

¹ This work was supported under NASA Grant NAG 3-2180.

A single-junction a-Si:H p-i-n device structure was selected for this work. Single-junction p-i-n cells without back reflectors, as opposed to multi-junction cells with back reflectors, were studied for two reasons. The single-junction p-i-n device structure is the basic structure employed in multi-junction a-Si:H solar cells. An understanding of the single-junction a-Si:H p-i-n device structure may make it possible to predict the performance of multi-junction device structures. Additionally, the analysis of measured dark J-V characteristics of a single-junction p-i-n device structure is considerably easier than those of multi-junction devices structures.

The study of the fundamental radiation resistance mechanisms in devices is complex. It is for this reason that both J-V measurements of irradiated cells and device simulations of J-V characteristics were employed in this work. In order to gain experience with available device simulators in calculating dark J-V characteristics, two simulators were used to study a two-sided step p-n junction. The free electron densities, electric field and dark J-V characteristics of a two-sided step p-n junction can be calculated using an analytical model [5]. The simulators selected were EPRI-AMPS [6] and PC-1D [7]. Parameters were selected for each simulator to produce identical electron densities, electric field and dark J-V characteristics. The premise for this approach was, if two simulators developed independently and employing different algorithms could produce the same p-n junction characteristics, and the characteristics agree with an analytical model, then simulations of p-i-n structures, which cannot be modeled analytically, may have some validity. Agreement between the simulators and analytical would also insure that we had an adequate understanding of the simulators to use them effectively.

Following irradiations with 40 keV electrons, dark J-V characteristics were measured. Simulations of dark J-V characteristics of p-i-n solar cells were carried out and parameters selected to fit the simulations to the measurements. The parameters that resulted in good fits to the measured J-V characteristics in the various forward-bias ranges were used to develop an understanding of current mechanisms in both virgin and irradiated a-Si:H p-i-n solar cells.

p-n JUNCTION SIMULATIONS

A p-n junction device structure with Si material parameters was investigated with both PC-1D and EPRI-AMPS simulators and the results compared with each other and an analytical model for a two-sided p-n step junction. The p-type and n-type layers were each 5000 μm thick. A doping level of $1\text{E}18\text{ cm}^{-3}$ was used for both acceptors in the p-layer and donors in the n-layer. For simplicity, a mobility of $1000\text{ cm}^2\text{V}^{-1}\text{s}^{-1}$ was chosen for both electrons and holes. In working with the simulators, we learned there are two major differences between the simulators. First, PC-1D is a transient simulator, and EPRI-AMPS is a steady-state simulator. Therefore, stepping times for sweeping device voltages must be considered when using the PC-1D simulator. Secondly, the PC-1D simulator uses a lifetime model and the EPRI-AMPS simulator employs an electronic density of states, DOS, model. In order to calculate free electron carrier densities from lifetimes with the EPRI-AMPS simulator, a lifetime subroutine is provided by the developer for calculating a DOS from carrier lifetimes. The PC-1D and EPRI-AMPS simulators produced vastly different free electron densities with the lifetime approach. It was concluded that the EPRI-AMPS simulator does not produce correct free electron densities when the lifetime approach is employed. The next approach was to use the DOS feature of EPRI-AMPS and to calculate a lifetime using a model that relates the DOS to a lifetime that could be used in the PC-1D simulator.

Figure 1 shows the simulated and calculated free electron concentration in the p-n junction under a forward bias of 0.5 V. The front of the device is located at a position of 0 μm and the metallurgical junction at 5,000 μm . The front p-type layer is within positions of 0 to 5,000 μm and the rear n-type layer is within positions of 5,000 to 10,000 μm . The front and rear contacts in the simulators are located at 0 and 10,000 μm , respectively. Electrons are minority carriers in the p-type layer and the free carrier densities are about $1\text{E}2\text{ cm}^{-3}$ near the front contact of the device. Electrons are majority carriers in the n-type layer and have free carrier densities of about $1\text{E}18\text{ cm}^{-3}$ near the back contact. Figure 1 shows that both PC-1D and EPRI-AMPS simulators produce a diffusion electron current density due to electron injection at the metallurgical junction. Electron injection is evidenced by the exponential decrease in the free electron carrier densities from the metallurgical junction forward into the p-type layer. The PC-1D simulator free electron density versus position was calculated using a Shockley Read Hall, SRH, recombination lifetime of 10 μs . The band-to-band recombination coefficient was set to an unrealistically low number for simplicity so that the recombination is entirely dominated by SRH recombination. The EPRI-AMPS simulator free electron density versus position shown in Figure 1 was calculated with a DOS distribution. The DOS distribution used was constant both with respect to position in the device as well as with respect to

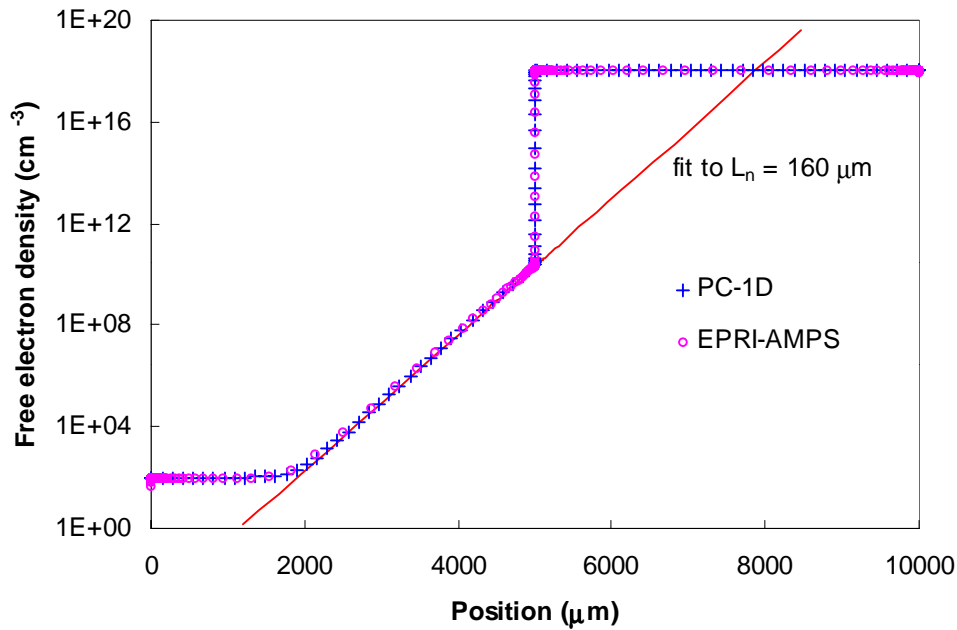


Figure 1. Simulated free electron density of a p-n junction with a forward bias of 0.5 V.

energy in sub-band-gap region of the energy band. The DOS used in the EPRI-AMPS simulation, n_E , was $1E14 \text{ cm}^{-3}\text{eV}^{-1}$; the cross section for the states, σ_t , was $1E-16 \text{ cm}^2$. The thickness of the layers, $5,000 \text{ μm}$, was chosen to insure that all recombination occurs in the bulk of the material and not at the contacts.

The exponential decay of minority carriers in the p-type layer can be fit by an exponential with two parameters, namely, the injected excess electron minority carrier density, $\Delta n_p = 1E10 \text{ cm}^{-3}$ at $5,000 \text{ μm}$, and an electron diffusion length, $L_n = 160 \text{ μm}$. The fit of the excess electron carrier density, $\delta n(x_p)$, to the exponential behavior in the p-type layer with $x_p < 5000 \text{ μm}$ is shown as the solid line in Figure 1; it was obtained using:

$$\delta n(x_p) = \Delta n_p \exp[(x_p - 5000 \text{ μm})/L_n] . \quad (1)$$

The electron diffusion length can be calculated from the electron mobility, μ_n , and lifetime, τ_n , using:

$$L_n = \sqrt{(kT/q) \mu_n \tau_n} \quad (2)$$

where k is the Boltzman constant, T the temperature, q the electronic charge, and τ_n the electron recombination lifetime. Substituting $\mu_n = 1000 \text{ cm}^2\text{V}^{-1}\text{s}^{-1}$ and $\tau_n = 10 \text{ μs}$ into Equation (2) yields $L_n = 160 \text{ μm}$. Hence the lifetime model employed in the PC-1D simulation is in agreement with the analytical theory.

An equivalent DOS lifetime for comparison with the PC-1D simulator was calculated from the parameters used in the EPRI-AMPS DOS simulation using [8]:

$$\tau_n = (n_E \Delta E \sigma_t v_t)^{-1} \quad (3)$$

where ΔE is the energy width of the DOS distribution for states serving as recombination centers and v_t is the carrier thermal velocity. Using $n_E = 1E14 \text{ cm}^{-3}\text{eV}^{-1}$, $\Delta E = 0.1 \text{ eV}$, $\sigma_t = 1E-16 \text{ cm}^2$ and $v_t = 1E7 \text{ cm/s}$, yields a lifetime of 100 μs , which is ten times greater than the lifetime used in the PC-1D simulation. The free electron density shown in Figure 1 is in agreement with the PC-1D simulation, and the two simulations are in agreement with analytical theory for a two-sided step p-n junction. However, the discrepancy in the lifetimes must be resolved if

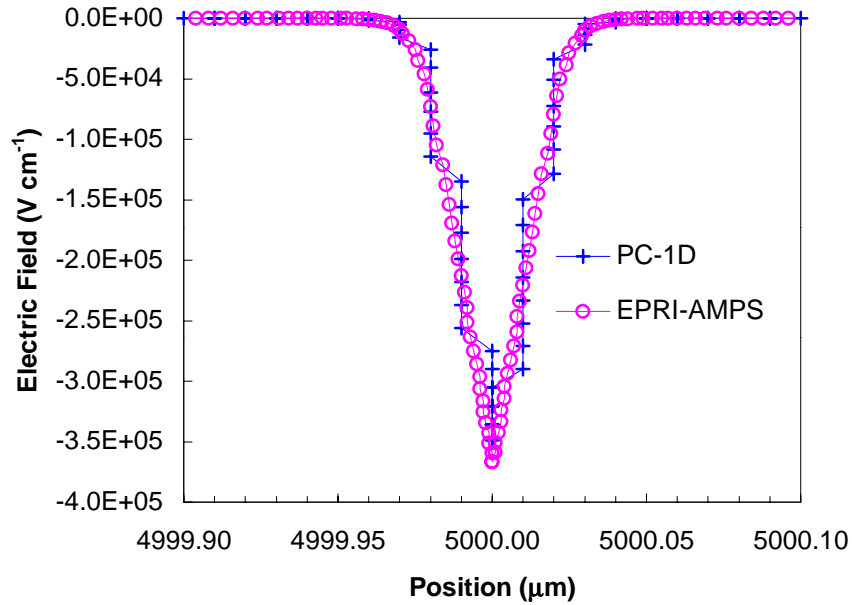


Figure 2. Simulated electric field of p-n junction near the metallurgical junction with a forward bias of 0.5 V.

one is to have confidence in applying the simulators to the analysis of devices. We will explore the discrepancy in future work.

The position dependence of the electric field was simulated with the two simulators. The results are shown in Figure 2. The electric field has the largest value at the metallurgical junction and the depletion width is about 0.05 μm for both simulations. The step like behavior in the results for the PC-1D simulation is due to rounding-off errors. The electric fields predicted by both simulators are in agreement with the analytical model.

The simulated dark J-V characteristics of the p-n junction for the EPRI-AMPS and PC-1D simulators are shown in Figure 3. Also shown is the dark J-V characteristic calculated with the analytical model:

$$J(V) = J_0 [\exp(qV/kT) - 1] \text{ where } J_0 = (kT) (\mu_p p_n / L_p + \mu_n n_p / L_n). \quad (4)$$

Substituting the values for the Boltzman constant, temperature, mobilities, minority carrier densities and diffusion lengths and into Equation (4) results in the straight line shown in Figure 3. There is good agreement between the analytical model and the simulated results in the 0.2 to 0.8 V range of forward biases. As mentioned above, the PC-1D simulator is a transient simulator, and for this reason, current densities at low voltages with depend on the device capacitance and voltage step rate. The effect of varying the step rate of the forward-bias voltage on the dark J-V characteristics is shown in Figure 4. The current charges the junction capacitance at low biases. For these simulations, the p-n junction capacitance is 0.2 $\mu\text{F}/\text{cm}^2$. When the voltage is ramped at 10 mV/s, which corresponds to 1 s/step, the current at voltages less than 200 mV is $2\text{e-}9 \text{ A}/\text{cm}^2$. Reducing the step rate to 100 s/step results in the forward-biased current decreasing by an order of magnitude. A 1000 s/step decreases the current further. The dark J-V characteristic approaches the characteristic that would be expected for the analytical model.

SINGLE-JUNCTION p-i-n SOLAR CELL MEASUREMENTS AND SIMULATIONS

Single junction p-i-n a-Si:H solar cells were deposited on bare stainless steel substrates without the use of textured back reflectors. An n-type layer about 15 nm thick was deposited on the bare stainless steel substrate followed by the deposition of a high quality a-Si:H intrinsic layer about 200 nm thick. An 8 nm thick p-type layer was then deposited on the i-type layer. All a-Si:H layers were deposited using radio-frequency plasma enhanced

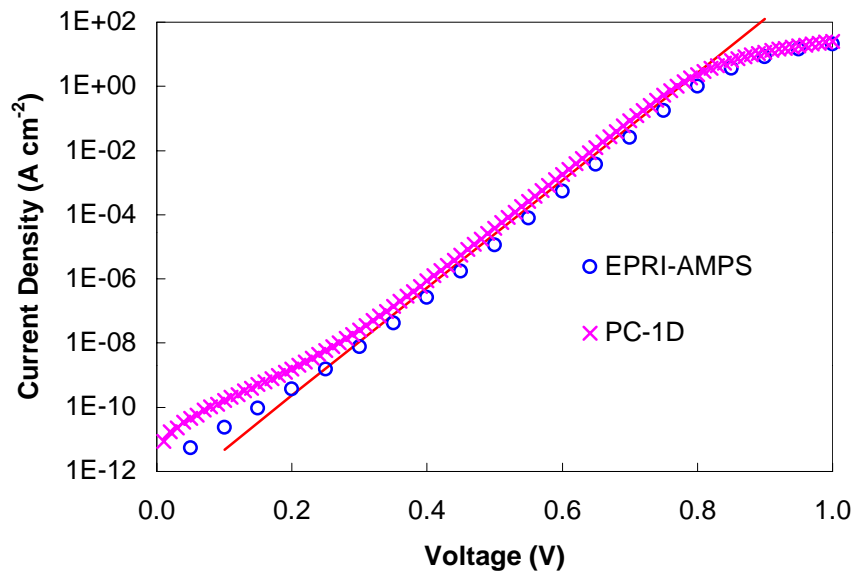


Figure 3. EPRI-AMPS and PC-1D simulated dark J-V characteristic for a two-sided-step p-n junction.

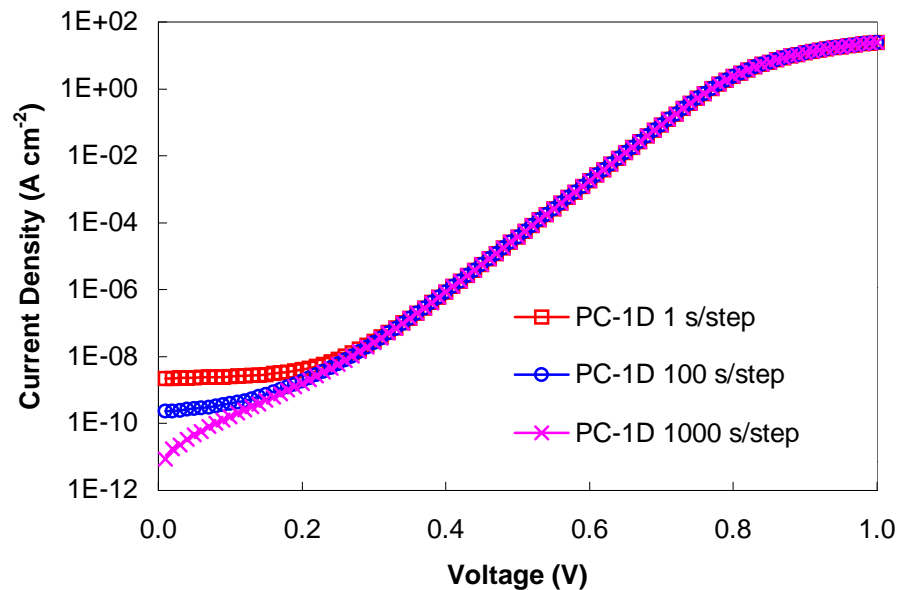


Figure 4. PC-1D simulated dark J-V characteristics for a two-sided step p-n junction with three voltage step rates.

chemical vapor deposition. Indium tin oxide, ITO, was evaporated through a mask with an area of 0.25 cm^2 . The ITO serves as the top contact and as a $\frac{1}{4}$ wavelength anti-reflective coating. Finally, Au grids were evaporated through a mask on top of the ITO. Since the cells do not employ a light scattering back reflector, the initial efficiency of the devices is about 6%. Initial dark J-V characteristics were measured after the virgin cell was annealed for two hours at 200°C in a vacuum system at about $1\text{E-}6$ Torr. A Cambridge S250 MK3 scanning electron microscope was used to irradiate the single-junction p-i-n solar cells with 40 keV electrons. The electron current was about $0.6 \mu\text{A}$ and the beam scanned over an area of about $0.55 \times 0.72 \text{ cm}^2$. Irradiation times of five hours were necessary to obtain a fluence of about $1\text{E}17 \text{ cm}^{-2}$. Following the irradiation, dark J-V characteristics were measured again. The cells were annealed a second time. A subsequent irradiation and annealing cycle was conducted. Dark J-V characteristics were measured between each irradiation and annealing step. The dark J-V characteristics were measured with a computer-interfaced Keithley Instruments model 236 source measurement unit that is programmed to source the bias voltage in 10 mV increments and measure the current at 111 separate voltages in the range of 0 to 1.10 V. The instrument and software are configured to make 320 current measurements at each source-bias voltage and calculate the average and standard deviation of the current. It took three to four minutes to measure a single J-V characteristic. The standard deviation for each of the measurements was calculated and is greater than 100 for the measurements reported in this work. This insures that the average current is representative of the device and not a transient current due to junction capacitance.

The energy deposition of the irradiating 40 keV electrons is assumed to be uniform in the cells studied in this work. While it is possible to use particle-solid interaction models to determine the spatial dependence of the electron-hole generation rate produced by the irradiation, our interest is in determining the role of the material properties on the dark J-V characteristics. Since the energy deposition is assumed to be uniform, simulated material properties were chosen to be uniform in the intrinsic layer with respect to position. This assumes that radiation induced defects do not migrate from the position where they are created.

The measured dark J-V characteristics of the p-i-n solar cell before irradiation are shown by the dots in Figure 5. The dark J-V characteristic measured after annealing at 200°C for 2 hours is labeled a11. A second J-V characteristic, a12, was measured immediately following the a11. The currents for both the a11 and the a12 measurements are linear on the semi-log graph over a range of $1\text{E-}10$ to $1\text{E-}4 \text{ A/cm}^2$. The data show that the measurement of a11 influenced the measurement of a12. Subsequent measurements of the dark J-V characteristics are similar to the a12 measurements, thereby showing saturation of the effect that produced the a12 dark J-V characteristic. Hence, the cell was annealed before each irradiation. EPRI-AMPS simulations were carried out with various material parameters in an effort to obtain a good fit between the measured simulated dark J-V characteristics. The most influential parameter that affected the dark J-V characteristics was found to be the DOS near the center of the band gap. A good fit was obtained with a DOS made up of a discrete energy level with an energy width of 0.1 eV and located at the center of the band gap. Equal numbers of acceptor and donor like states were used for the discrete energy states. The results of simulations with various densities of discrete energy states are plotted in Figure 5 as solid lines. The density of discrete energy states was increased from 0 to $1\text{E}17 \text{ cm}^{-3} \text{ eV}^{-1}$. The simulated results can be fitted with an expression of the form:

$$J(V) = J_0 [\exp(qV/nkT) - 1] \quad (5)$$

where n is the material quality factor. As the density of discrete energy states at the center of the band gap is increased, J_0 and n increase. The curve labeled 0 corresponds to a zero discrete energy state density at the center of the sub-band-gap. The recombination for a simulation with no discrete energy states is dominated by recombination from the conduction band-tail states to the valence band-tail states. Figure 5 shows that the J_0 and n terms in Equation (5) for the curve labeled 0 are significantly less than for the measured a11 data. The curve labeled $5\text{E}15$ represents a simulation with a discrete energy state density of $5\text{E}15 \text{ cm}^{-3} \text{ eV}^{-1}$ at the center of the band gap. The J_0 and n terms for this simulation are in agreement with the a11 data over 6 orders of magnitude. The curve labeled $1\text{E}16$ shows the results for a simulation with a discrete energy state density of $1\text{E}16 \text{ cm}^{-3} \text{ eV}^{-1}$ located at the center of the band gap. This simulation is in agreement with the a12 data over 6 orders of magnitude as well. The deviation in linearity between the simulated and measured dark J-V characteristics above 0.8 V is believed to be due to series resistance in the measured cells. The series resistance results from factors external to the p-i-n structure, such as contact resistance and resistance in the ITO layer. Future simulations including these factors will be carried out to obtain a better fit of the dark J-V characteristics above 0.8 V.

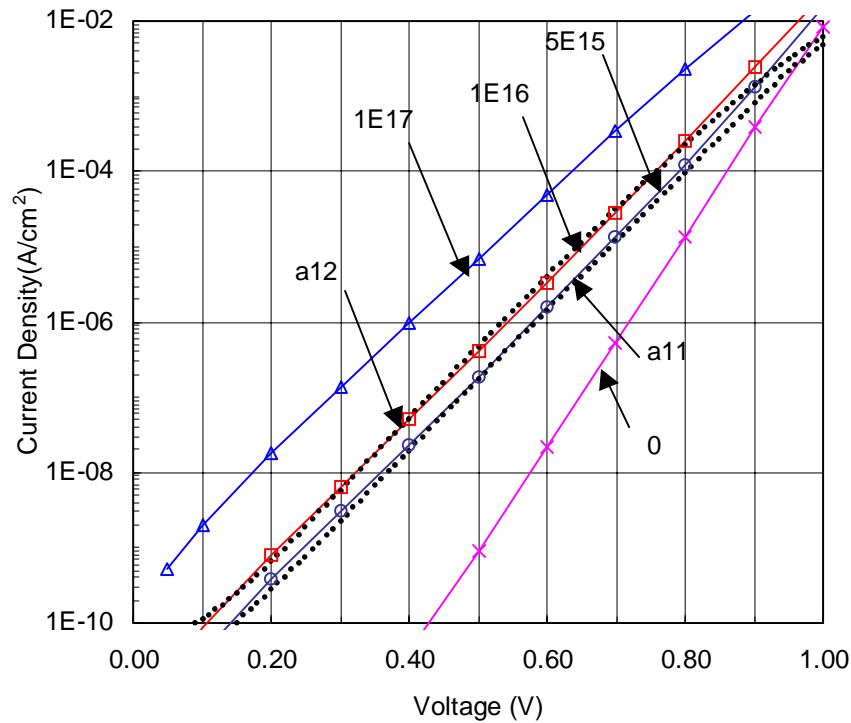


Figure 5. Measured and EPRI-AMPS simulated dark J-V characteristics for an a-Si:H p-i-n solar cell before irradiation.

Figure 5 suggests that the difference between the a11 and a12 J-V characteristics is due to an increase in the sub-band-gap energy state density from $5\text{E}15 \text{ cm}^{-3} \text{ eV}^{-1}$ to $1\text{E}16 \text{ cm}^{-3} \text{ eV}^{-1}$.

A dark J-V characteristic of a p-i-n solar cell after irradiation with 40 keV electrons to a fluence of $1\text{E}17 \text{ cm}^{-2}$ is shown in Figure 6 by the curve made up of dots and labeled r1. For comparison purposes, the measured dark J-V characteristic before irradiation is also shown by the curve made up of dots and labeled a1. Simulations were carried out with the EPRI-AMPS simulator using a discrete energy state located at the center of the band gap with densities of $7\text{E}17$ and $8\text{E}17 \text{ cm}^{-3} \text{ eV}^{-1}$. The simulated results are shown by the solid curves in Figure 6 that are labeled 7E17 and 8E17. Our previous work shows that there are three current mechanisms that contribute to the dark J-V characteristic of irradiated a-Si:H solar cells, namely, injection, shunt and CV^m mechanisms [9]. The current injection mechanism is evident in the r1 curve since the current increases exponentially with forward-bias voltage above 0.7 Volts. Below 0.7 V the shunt and CV^m mechanisms appear to contribute to the current. The r1 dark J-V characteristic has higher J_0 and n values than the a1 characteristic. The simulated results suggest that a good fit to the irradiated cell J-V characteristic above 0.7 V may be obtained with a discrete energy state density of about $7.5\text{E}17 \text{ cm}^{-3} \text{ eV}^{-1}$.

The results of the EPRI-AMPS dark J-V simulations in Figure 5 show that the cell current density for a given forward-bias voltage increases with increasing discrete energy state density up to $1\text{E}17 \text{ cm}^{-3} \text{ eV}^{-1}$. However, Figure 6 shows that increasing the discrete energy state density further to $7\text{E}17$ and $8\text{E}17 \text{ cm}^{-3} \text{ eV}^{-1}$ results in a decrease in the current density at a given voltage. Note that the measured J-V characteristic above 0.7 V shown in Figure 6 for the irradiated cell has a lower current density than that of the annealed cell for the same forward-bias voltages. Hence, in the forward-bias voltage range where current the injection mechanism dominates, the effect of irradiation on the cell is to produce a behavior in the measured J-V characteristic that is the same as increasing the discrete energy state density in the simulated dark J-V characteristics. It is plausible to assume that 40 keV electron irradiation produces defect states near the center of the band gap that serve as

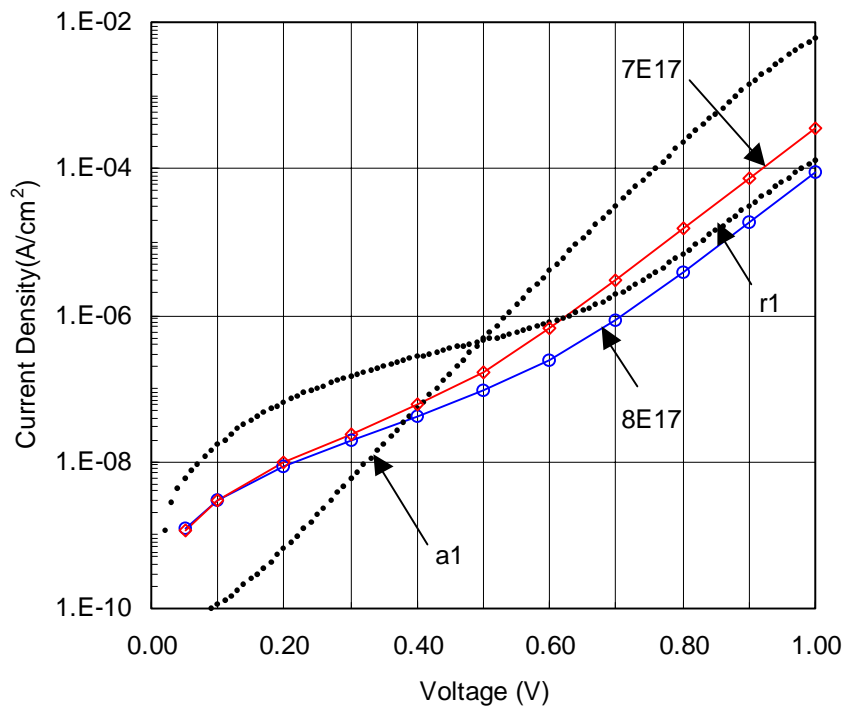


Figure 6. Measured and EPRI-AMPS simulated dark J-V characteristics for an a-Si:H p-i-n solar cell before and after irradiation with 40 keV electrons.

recombination centers. The behavior can also be explained by noting the effect of increasing the discrete energy state density, whether by simulation or irradiation, is to increase the values of J_0 and n in Equation (5). The simulated dark J-V characteristics plotted in Figure 6 show that the higher discrete energy state densities result in a non-linear current density on the log scale below 0.7 V. The same effect exists in the measured dark J-V characteristic of the irradiated cell, but it is much more pronounced; the magnitude of the current density is about an order of magnitude larger for the measured cells. In our earlier work that employed parametric fitting, we associated this effect with a shunting mechanism and a current mechanism that results in a term of the form CV^m . The EPRI-AMPS simulation studies provide an understanding of the dark J-V characteristic in the forward-bias region where the current injection mechanism dominates. Studies need to be carried out to understand the physical bases of the current mechanisms at forward biases below 0.7 V.

CONCLUSIONS

Studies have been carried out to correlate the effect of 40 keV electron irradiation on dark J-V characteristics. EPRI-AMPS and PC-1D simulators were utilized to characterize a two-sided step p-n junction before selecting a simulator for investigating a p-i-n solar cell structure. The two simulators produced dark J-V characteristics that were in agreement each other and an analytical model, but the lifetimes used in the two simulators differ by a factor of ten. The EPRI-AMPS simulator was used to simulate dark J-V characteristics of a p-i-n solar cell. In the forward-bias voltage range above 0.7 V, where the current injection mechanism dominates, the effect of irradiation on the cell is to produce a behavior in the measured J-V characteristic that is the same as increasing the discrete energy state density in the simulated dark J-V characteristics. It is plausible to assume that 40 keV electron irradiation produces defect states near the center of the band gap and that the states serve as recombination centers. The EPRI-AMPS simulation studies provide an understanding of the dark J-V characteristic when current injection dominates. Studies need to be carried out to understand the physical bases of the current mechanisms at forward biases below 0.7 V.

REFERENCES

1. Ultra-light Amorphous Silicon Alloy Photovoltaic Modules for Space Applications, J. J. Hanak, E. Chen, C. Fulton, A. Myatt and J. R. Woodyard, Space Photovoltaic Research and Technology Conference, 1986, NASA Conference Publication 2475, page 99.
2. Investigation of Current Mechanisms in a-Si:H Alloy Cells, Kenneth R. Lord II, Fazal UrRahman Syed, Michael R. Walters and James R. Woodyard, First World Conference on Photovoltaic Energy Conversion, Twenty Fourth IEEE Photovoltaic Specialists Conference-1994, page 993.
3. James R. Woodyard and Geoffry Landis, "Radiation resistance of thin-film solar cells for space photovoltaic power," Solar Cells, 31, pp. 297-329, 1991.
4. Thin Film Development Workshop Report, J. R. Woodyard, Eleventh Space Photovoltaic Research and Technology Conference-1991, NASA Conference Publication 3121, 1991, page 48-1.
5. Solid State Devices, Ben G. Streetman and Sanjay Banerjee, Prentice Hall, 2000, pages 157-185.
6. Dr. Stephen Fonash and collaborators at The Pennsylvania State University developed EPRI-AMPS; information may be obtained at <http://www.psu.edu/dept/AMPS/>.
7. Dr. Paul Basore and collaborators developed PC-1D; information may be obtained at www.pv.unsw.edu.au/pc1d/.
8. Physics and Technology of Semiconductor Devices, A. S. Grove, John Wiley and Sons, 1967, page 134.
9. Qianghua Wang, Kenneth Lord, and James R. Woodyard, "Effects of 40 keV electron irradiation on dark I-V characteristics of single-junction a-Si:H solar cells," Proceedings of the 28th Photovoltaics Specialists Conference, pp. 1057-1060.

REPORT ON PROJECT TO CHARACTERIZE MULTI-JUNCTION SOLAR CELLS IN THE STRATOSPHERE USING LOW-COST BALLOON AND COMMUNICATION TECHNOLOGIES¹

Ali Mirza, David Sant and James R. Woodyard, Wayne State University, Detroit, Michigan 48202
Richard R. Johnston, Lawrence Technological University, Southfield, Michigan 48075
William J. Brown, High Altitude Research Corporation, Huntsville, Alabama 35758

ABSTRACT

Balloon, control and communication technologies are under development in our laboratory for testing multi-junction solar cells in the stratosphere to achieve near AM0 conditions. One flight, Suntracker I, has been carried out reported earlier. We report on our efforts in preparation for a second flight, Suntracker II, that was aborted due to hardware problems. The package for Suntracker I system has been modified to include separate electronics and battery packs for the 70 centimeter and 2 meter systems. The collimator control system and motor gearboxes have been redesigned to address problems with the virtual stops and backlash. Surface mount technology on a printed circuit board was used in place of the through-hole prototype circuit in efforts to reduce weight and size, and improve reliability. A mobile base station has been constructed that includes a 35' tower with a two axis rotator and multi-element yagi antennas. Modifications in Suntracker I and the factors that lead to aborting Suntracker II are discussed.

INTRODUCTION

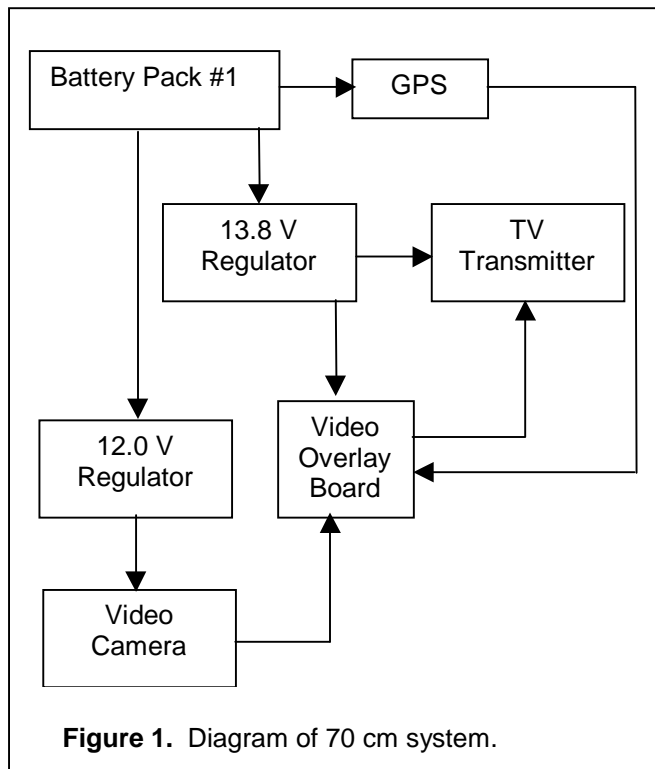
The objective of this program is to investigate and employ current balloon, control and communication technologies for testing multi-junction solar cells in the stratosphere where near AM0 conditions exist. One flight, Suntracker I, has been carried out and reported earlier [1]. We report on our efforts in preparation for a second flight, Suntracker II, that was aborted due to hardware problems. Since the Suntracker I flight our efforts have been directed at developing separate electronics and battery packs for the 70 centimeter and 2 meter systems; addressing problems with virtual stops and motor-gearbox backlash; using surface mount technology in place of a through-hole circuit; and constructing a mobile base station that includes a 35' tower with a two axis rotator and multi-element yagi antennas.

PAYLOAD DESCRIPTION

The payload includes a suntracker, GPS receivers, transmitters, batteries, and a video camera. The suntracker is designed to point a collimator and solar cell at the sun as a balloon ascends and downlink data containing the cell short-circuit current, cell temperature, electronics module temperature, video and GPS data. It employs two motors and a collimator. Each motor assembly has a motor, gearbox and encoder. The motor assemblies are used to maintain the altitude and bearing angles of the collimator between 0° and 180°. The dimensions of the collimator are 1.25"x1.25"x4.00"; the front aperture is 1.00"x1.00" and the cell area 0.79"x0.79" [1]. The dimensions of the collimator were selected to prevent light scattered from the balloon, earth, moon or clouds arriving at the solar cell. The video camera is mounted on top of the package and pointed at the suntracker to observe the operation of the suntracker as it ascends through low temperatures to the stratosphere. The payload is attached to a parachute and a latex meteorological balloon. The weight of the payload is about five pounds.

¹ This work was supported under NASA Grant NAG 3-2180.

70 CM AND 2 METER COMMUNICATION SYSTEMS



The suntracker system is designed to downlink data with two transmitters operating on the 70 cm and 2 meter bands at frequencies of 439.25 and 144.10 MHz, respectively. Cost considerations result in a design criterion for the Suntracker that emphasizes the use of commercially available devices wherever possible. The devices selected for the system operate at different voltages thereby requiring six voltage regulators. Suntracker I employed a single battery pack and linear regulators. A large fraction of the power was dissipated as heat because the device voltage requirements range between 3.7 and 13.8 V. Switching regulators were employed for Suntracker II in an effort to improve the efficiency of the regulators. Separate communication systems were designed for each frequency in order to maximize the probability that position data be available throughout the flight in the event of a system failure. Each

system has its own transmitter, GPS receiver, battery pack and supporting electronics.

The battery packs consist of four Saft LHS-14 lithium batteries. Each battery when operated at room temperature has an open-circuit voltage of 3.67 V and produces 14.7 V for a four-battery pack under no-load conditions. The terminal voltage of the battery packs under the load for each of the systems is about 13.2 V or 3.3 per cell. While the energy data sheet for the LHS-14 battery shows some energy remains down to a terminal voltage of 2.0 V, there is relatively little energy left once the terminal voltage drops below 2.9 V. Hence, voltage regulators must be employed to both boost and buck the battery output voltage for the devices used in the Suntracker.

Additionally, the power delivery systems must be designed to maintain the various voltages as the battery packs discharge from 13.2 to 11.6 V. This design requirement led us to consider switching power supplies. Since our future plans include powering the Suntracker with flexible ultra-light solar modules, it was decided to use available switching power supplies to determine their characteristics at low temperatures as well as their electromagnetic compatibility with the control systems and transmitters.

The 70 cm electronics and battery pack are shown in Figure 1. The system contains battery pack #1 that directly powers a GPS receiver and two voltage regulators; one is 12.0 V and the other 13.8 V. The 12.0 V regulator is an Astrodyne model MKCO3-12S12, a fully integrated and shielded DC/DC converter, has an efficiency of 80% and powers the video camera. The 13.8 V regulator is a National Semiconductor LM2585 based simple switcher that powers the 1.0 W TV transmitter and video overlay board. The GPS receiver output contains longitude, latitude, speed, altitude and direction data. The data are overlaid on the down-linked video camera image by the video overlay board.

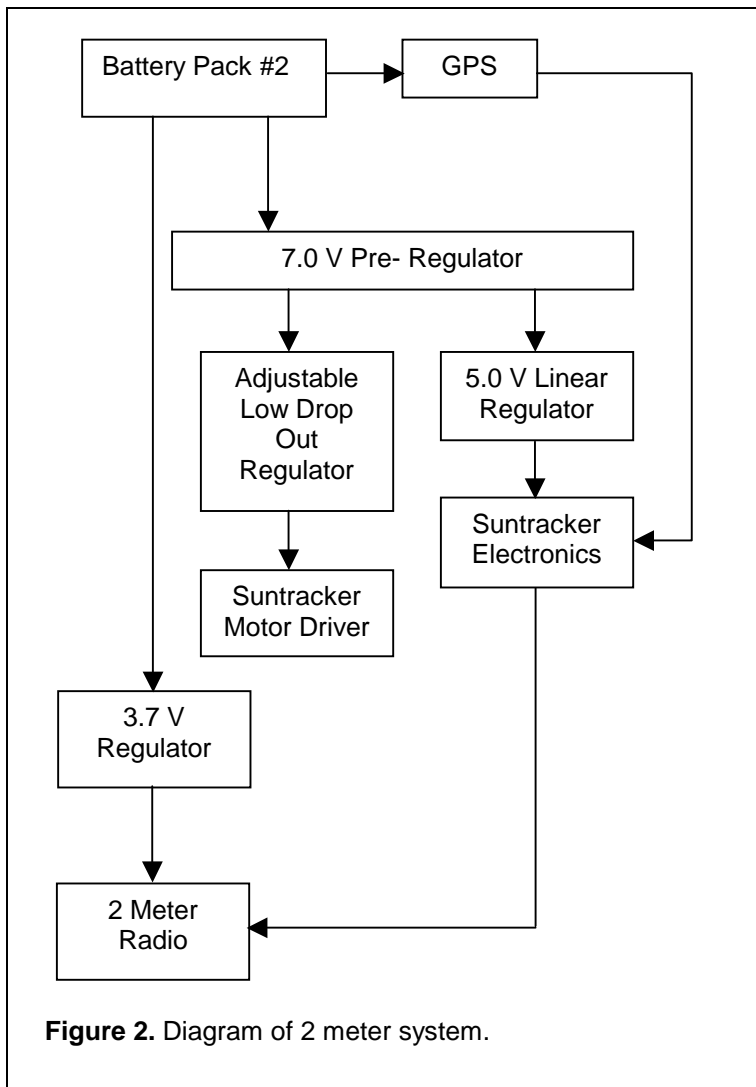


Figure 2. Diagram of 2 meter system.

The 2 meter system is shown in Figure 2. It contains battery pack #2 that directly powers a GPS receiver, and 3.7 V and 7.0 V regulators. The regulators are Power Trends model PT6101 integrated switching regulators that are programmable and rated at an efficiency of 90%. The 3.7 V regulator powers a 2 meter radio rated at 300 mW. The 7.0 V regulator serves as a pre-regulator for two other linear regulators that power the suntracker motors and electronics. The adjustable low drop-out regulator permits adjustment of the voltage to the altitude and bearing motors on the suntracker collimator; the voltage adjustment and control algorithm are used to select a slew rate for meeting the tracking requirements. The 5.0 V linear regulator provides power to the suntracker electronics that includes the MIM module, Basic Stamp 2p (BS2p) and PIC 16F84 micro-controllers, and associated electronics. Figure 2 shows the output of the GPS receiver is input to the suntracker electronics that in turn inserts

it in the encoded data stream which is output to the 2 meter transmitter.

SUNTRACKER CONTROL SYSTEM

Video downlinked during the Suntracker I flight showed that the collimator locked on the sun but was not able to track it. It was suspected that the inability of the system to track the sun during the flight was due to instability in the package because of the relatively high ascent rate of the balloon. Subsequent laboratory testing of the retrieved system suggested that backlash in the motor gearboxes and the loss of motor encoder pulses could also contribute to the inability of the system to track the sun.

Suntracker I employed MicroMo model 1016 DC motors measuring 10 mm in diameter and 16 mm in length with encoders and 256:1 gearboxes. The motor vendor was not able to provide zero backlash gearboxes in time for the scheduled Suntracker II flight. The motor assemblies were replaced with MicroMo model 1524 motors that measure 15 mm in diameter and 24 mm in length, encoders and 262:1 zero backlash gearboxes. The model 1524 motors provide higher torques at the cost of an increase in payload weight. Testing of the system showed that the BS2sx microcontroller used during Suntracker I flight was not fast enough to maintain both the virtual stops and control of the collimator. Virtual stops refer to the ability of the system to limit the collimator altitude and bearing angles to a range of 0° or 180° through the use of software. It is

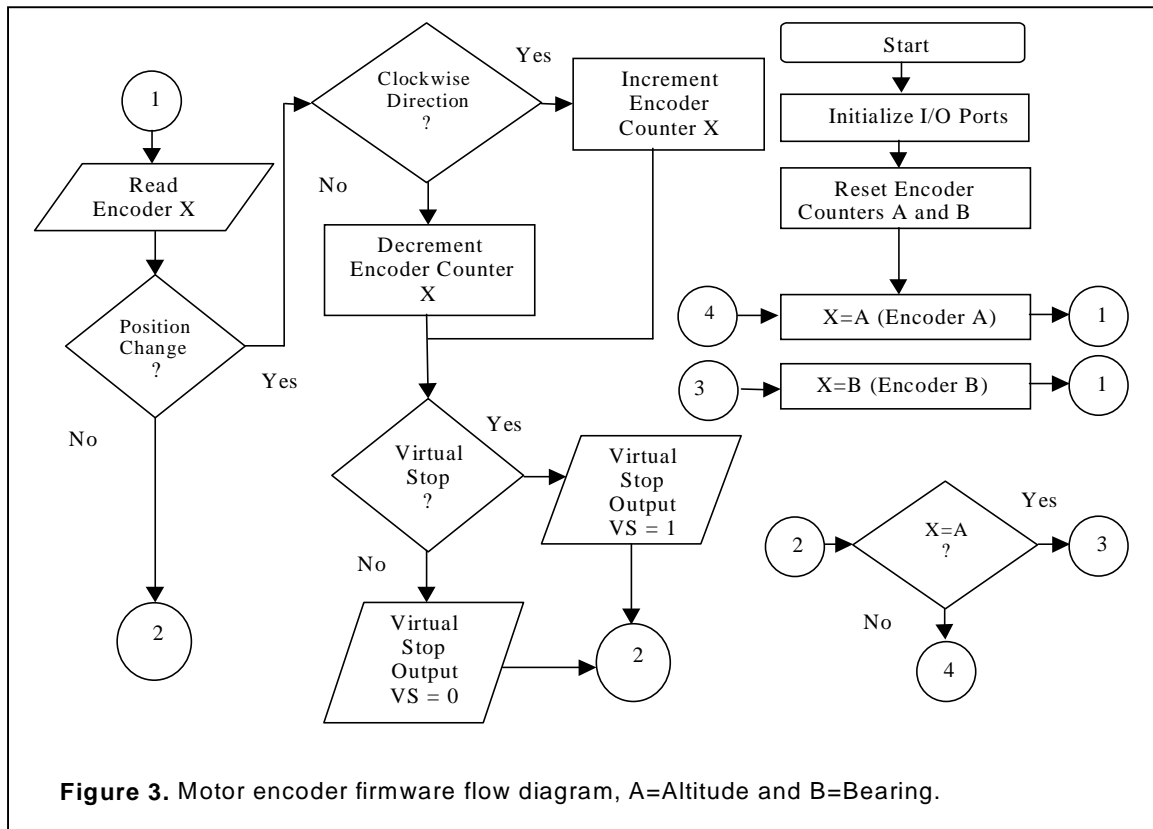
necessary to count all encoder pulses in order to maintain the virtual stops during a two-hour flight. In order to improve the counting of encoder pulses, the microcontroller was upgraded to the model BS2p. Subsequent testing showed the altitude and bearing angles still exceeded the 0° to 180° range and all the encoder pulses were not counted.

The electronics used in the Suntracker I flight were redesigned in an effort to count all the encoder pulses and effectively manage the virtual stops. A Microchip™ PIC 16F84 microcontroller was included in one of the circuits and dedicated to the task of counting encoder pulses. The PIC 16F84 microcontroller was selected because of its low support component count, small size, availability, speed, and development tools. The clock of the microcontroller utilizes an 8 MHz ceramic resonator. RAM memory in the microcontroller was used for two 16 bit encoder counters. Each encoder utilizes solid-state hall sensors with a low inertia magnetic disk to provide two output channels with 16 pulses per revolution that are in quadrature. Sixteen counts per revolution with a 262:1 gear reduction results in 2096 pulses per 180° of the collimator. The four encoder outputs are TTL compatible and connected directly to the PIC 16F84 microcontroller. The microcontroller monitors the output from the two encoders and counts all the encoder pulses. An output line connected to the BS2p microcontroller shows the status of the virtual stops.

The algorithm for the 16F84 microcontroller is shown in Figure 3. The collimator altitude and bearing angles must be set to 90°, their initial positions, before power is applied. The right side of Figure 3 shows the ports are initialized upon power up. The lines from the encoders to the 16F84 microcontroller are set as inputs. The output line from the 16F84 microcontroller to the BS2p microcontroller, VS, is set as an output. All other unused peripheral features of the 16F84 microcontroller are disabled to keep power consumption to a minimum. The two counters are initialized by setting the readings to 1048, the reading corresponding to altitude and bearing angles of 90°. The firmware in the 16F84 microcontroller first selects the altitude encoder, denoted by X=A in the flowchart. At point 1 in the algorithm polling of the encoder is carried out to determine if there has been a position change. Since quadrature encoding is utilized, both output lines of encoder A are read and compared with their previous values. If the values are the same, no position change has occurred and the firmware proceeds to check point 2 that alternately selects the second encoder, X=B, for polling. If a position change is detected then a test is preformed to determine if the encoder has rotated in the clockwise direction. The A encoder counter is incremented if a clockwise direction was detected or decremented if a counterclockwise direction was detected. The encoder counter is then checked to see if it has reached the virtual stop at 0° or 180° corresponding to counter settings of 0 or 2096, respectively. If the counter setting is less than 0° or greater than 180°, VS is set to logic 1 otherwise it is set to logic 0. The firmware proceeds to check point 2 and sets X=B and proceeds to poll encoder B. The firmware alternately polls encoders A and B and manages the virtual stops until the power is turned off. The firmware was tested using an in-circuit emulator with timing analysis features. It was determined that the firmware can operate reliably at the rated maximum motor speeds. The modified circuit was tested in the laboratory. The altitude and bearing angles operated in the 0° to 180° range and all the encoder pulses were counted for periods of time in excess of two hours, the approximate time of a flight to 100,000 feet.

CONTROLLER BOARD DESCRIPTION

The controller board used in the Suntracker I flight employed a through-hole prototype circuit. In an effort to improve reliability and as well as reduce the weight and area of the controller board for the Suntracker II flight, it was decided to use surface mount technology on a printed circuit board. The new controller board is composed of a 3" x 3.125" printed circuit board populated mostly with surface mount components. The printed circuit board area is about 11 in² smaller than the through-hole prototype circuit. It weighs approximately 1.5 oz., about 3.0 oz. lighter than the prototype board.



The cell current and temperature, and the internal package temperature, are measured with devices that are mounted on the controller board. There are devices mounted on the controller board that position the collimator and convert measurements to an AX.25 protocol for downlinking using a 2 meter transmitter [1]. The two linear power supplies discussed in the preceding section are mounted on the board. The low drop-out linear supply powers the BS2p microcontroller, A/D converter, operational amplifiers, motor driver and MIM module, all of which are mounted on the controller board. The low-drop out adjustable supply is used to vary the voltage to the motor driver in order to adjust the speed of the altitude and bearing motors. The motor driver is used to control direction and on/off states of both motors. Each motor has two control lines. By utilizing these control lines a motor can be energized in a forward or reverse direction. The driver also allows the motor leads to be connected together via an h-bridge to support dynamic braking. A built-in thermal shutdown is included in the motor driver to prevent damage to the circuit under an overload condition. Inputs to the motor driver are TTL compatible thereby simplifying the interface to the BS2p microcontroller.

Three operational amplifiers on the controller board are utilized for signal conditioning. One is used to linearize the output from a thermistor mounted on the back of the solar cell holder; the signal is used to determine the temperature of the solar cell. A second operational amplifier is used to amplify the voltage across a high precision resistor in series with the solar cell; it produces an output voltage that is proportional to the cell current. The third operational amplifier linearizes the output from a second thermistor that is used to determine the internal temperature of the suntracker package. The conditioned analog signals from the two temperature sensors and cell current are routed to the analog input lines of the MIM module. The MIM module is an ARPS compatible packet-radio telemetry unit that converts the three analog signals to 8-bit numbers via an internal A/D converter (ADC). The MIM module also has a serial port that is available at a connector mounted on the board; the port is used to receive data from a GPS receiver and configure the MIM module. Output timing of the various signals, user call sign, and message

formatting are some of the parameters that can be configured through the serial port. The MIM module packetizes the A/D data, GPS coordinates and user call sign, and sends the packets via a connector on the controller board to a 2 meter transmitter in an AX.25 protocol at 1200 baud.

The voltage from the operational amplifier that senses the solar cell current is also used as an input to the BS2p microcontroller. The analog voltage is converted to a digital form using an ADC configured in a free running mode. The ADC, once initiated, converts the output voltage from the operational amplifier to an 8-bit digital signal that is input to the BS2p microcontroller. The error rate of the ADC over the operating temperature range of 0°C to 70°C is $\pm 1/2$ bit. The BS2p microcontroller outputs logic signals to the motor driver while monitoring the VS line from the PIC 16F84 microcontroller. The algorithm used in the Suntracker I flight for programming the BS2p microcontroller has been previously described [1]. The algorithm was modified for the Suntracker II flight. The algorithm for Suntracker I employed searching and tracking modes. The tracking modes kept the motor speed constant while checking the solar cell current. The algorithm for Suntracker II decreased the motor speed as the collimator approached the position corresponding to the maximum solar cell current. The program for Suntracker II is faster and requires less of the BS2p microcontroller memory.



Figure 4. Suntracker II package.

PACKAGE, EQUIPMENT AND BASE STATION

The package for Suntracker II is shown in Figure 4. It measures about 10" in diameter and 10" high. It has a wall thickness of about one inch and weighs about five pounds including electronics, batteries, antennas etc. The package was fabricated using a two-part urethane pour foam and molds. The collimator and motors are located on top and the electronics inside the package. The video camera can be seen on the left-top side of the package. The antennas for the transmitters are not shown in Figure 4. The antenna for the 70 cm transmitter is mounted below the package and the antenna for the 2 meter transmitter is located inside the package. During flights the package is suspended 60 feet below a latex meteorological balloon that is pressurized with helium. The train from the balloon to the package includes a swivel, parachute attached to a hoop and three 0.010" diameter shrouds tied to the hoop and package. Two of the openings for attaching the shrouds can be seen on the top of the package.

One of the objectives for the Suntracker II flight was to design and build a mobile system with all the equipment needed for a flight, including

the base station, antennas, helium gas tanks, balloons and balloon inflation hardware. Figure 5 shows the system that was developed for the Suntracker II flight. The equipment for the flight was

transported with a trailer and van. A trailer was used to transport the 18'x3.3'x4" antenna box and four 8' tower sections. The trailer was equipped with a winch to raise the assembled tower, two-axis rotator and antennas. The yagi antennas measured about 17.5' in length; the 70 cm and 2 meter antennas had 25 and 12 elements, respectively. The gain of the 70 cm antenna is 16.2 and the 2 meter antenna gain is 12.6 dBd. The antennas were assembled prior to transporting them because of the task of assembling them is tedious and time consuming. The antenna box is shown in Figure 5 and is located on the left side of the trailer. The figure also shows the assembled tower supporting the rotator, antennas and cables. The antennas are about 35' above ground level. The 70 cm antenna is mounted in the horizontally polarized position while the 2 meter antenna is mounted in the vertically polarized position. The two-axis rotator enables pointing the antennas at the package during flight in order to take advantage of the directional gain of the yagi antennas. The remote-control box for the rotator and the 2 meter and 70 cm receivers are located in the van. A 12 V deep cycle marine battery is used to power the base-station equipment. The data downlinked on the 70 cm system are viewed and saved with a 9" video/VCR unit. The data downlinked on the 2 meter system are viewed and saved using a notebook computer. Mapping software is used to overlay the position of the balloon on a map to facilitate recovery of the package.

One of the design criteria for the mobile system is to minimize assembly and setup time at the launch site. Clevis pins were used in the assembly of the tower and snaps were employed for supporting the antenna and rotator remote-control cables. The antenna box can be supported on plastic horses and the top surface used for assembling the train and inflating the balloon.



RESULTS

The Suntracker II flight was scheduled for September 2, 2001 from a farm in Findlay, Ohio. Arrival time at the site was 9:00 a.m. and launch time scheduled for 1:00 p.m. Balloon tracking software was used to predict that the landing site of the balloon would be some 40 miles southwest of the launch site. While all the components of the systems were tested in the laboratory, there was not enough time to carry out the final integration and testing of the systems in the laboratory prior to the day of the launch. The base station was set up and tested at the launch site. All indications were that it performed satisfactorily. The 70 cm and 2 meter systems were integrated into the package on the day of the launch. Testing showed that the power output level of the 70 cm system was inadequate to insure reception of the video signal throughout the flight. We did not have test instrumentation on site to measure the output power, however, experienced amateur radio operators reported the output power level to be

inadequate. Testing of the 2 meter system showed that no GPS data were in the data stream. Unsuccessful attempts were made to determine the sources of the problems. After several hours of fruitless efforts the Suntracker II flight was aborted.

It took several weeks of laboratory work to determine the basis for the problems that lead to aborting the Suntracker II flight. Test equipment had to be obtained and techniques developed to measure the input power to the antennas as well as the radiated power. It was determined that the problem with the 70 cm system was intermittent and due to a faulty connector on the cable that connected the transmitter to the antenna. The connector operated satisfactorily on the laboratory bench when the cable was straight. Bending the cable, as is necessary when it is connected to the transmitter in the package, shorted the connector pin to the cable shield. The problem with the loss of the GPS data in the 2 meter data stream was traced to reversed wires on the GPS input on the MIM module. It not understood how the wires became reversed since the 2 meter system did work satisfactorily at least at one point during laboratory testing.

SUMMARY

Improvements were made in the Suntracker I system in preparation for the Suntracker II flight. A dedicated microcontroller was included in the electronics to eliminate a virtual stop problem. Zero-backlash gearboxes were installed in order to increase the probability that the suntracker will track the sun. A power distribution system was developed that has a higher efficiency and includes two separate battery packs, one for each of the frequency bands used to downlink data. A printed circuit and surface-mounted devices replaced a through-hole circuit to reduce size and weight and increase robustness. A mobile base station was developed that includes a tower with a two axis rotator and multi-element yagi antennas. One of the design criteria for the mobile system is to minimize assembly and setup time at the launch site. All the equipment was tested in the laboratory. The base station operated satisfactorily at the Suntracker II launch site. Problems developed with both the 70 cm and 2 meter systems when they were integrated into the package on the day of the launch and the Suntracker II flight was aborted.

REFERENCE

1. Investigations to Characterize Multi-Junction Solar Cells in the Stratosphere Using Low-Cost Balloon and Communication technologies, Glenroy A. Bowe, Qianghua Wang, James R. Woodyard, Richard R. Johnston and William J. Brown, Proceedings of 16th NASA Space Photovoltaic Research and Technology Conference, August 31-September 2, 1999, NASA Document NASA/CP-2001-210747, page 189.

Advance Power Technology Demonstration on Starshine 3

Phillip Jenkins¹, David Scheiman¹, David Wilt², Ryne Raffaele³, Robert Button², Mark Smith¹, Thomas Kerslake², and Thomas Miller²

¹OAI, NASA GRC 21,000 Brookpark Rd. MS 302-1 Cleveland OH 44135 PH: 216-433-2233

²NASA Glenn Research Center at Lewis Field, 21,000 Brookpark Rd. MS-302-1 Cleveland OH 44135

³Rochester Institute of Technology, NASA GRC 21,000 Brookpark Rd. MS 302-1 Cleveland OH 44135

Abstract. The Starshine 3 satellite will carry several power technology demonstrations. Since Starshine 3 is primarily a passive experiment and does not need electrical power to successfully complete its mission, the requirement for a highly reliable power system is greatly reduced. This creates an excellent opportunity to test new power technologies. Several government and commercial interests have teamed up to provide Starshine 3 with a small power system using state-of-the-art components. Starshine 3 will also fly novel integrated microelectronic power supplies (IMPS) for evaluation.

Introduction

The Kodiak Star mission is scheduled to launch on August 31, 2001. It will carry the Starshine 3 satellite to a circular orbit of 475 km inclined 67°. Starshine 3 is a 36" diameter spherical satellite covered with 1500 1"-diameter mirrors (figure 1).

The primary mission of Starshine 3 is to measure atmospheric density as a function of altitude. This is done by tracking the Starshine 3 orbital decay. Tracking is accomplished using radar, LIDAR and visual sightings against a star field.¹ Starshine 3 is essentially a passive satellite. There is no use of electrical power to assist the orbital tracking. This makes Starshine 3 an excellent platform to test new power technologies without the burden of mission success depending on the power system. We set out to design

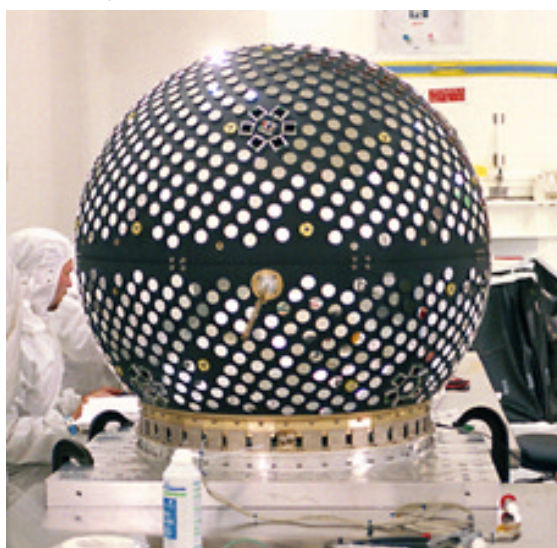


Figure 1) The Starshine 3 satellite.

a small power system that would use high performance components that are not yet flight proven and will improve future power systems. Three separate power related experiments are included on Starshine 3. They are: high efficiency solar cells and rechargeable lithium-ion batteries, integrated microelectronic power supplies, and an optical transmission test of material used for high efficiency, flexible, solar concentrator lenses. In the sections below each of these experiments will be described in detail.

Advance Solar Cells and Batteries

The solar cells used on Starshine 3 to power the electronics and transmitter are GaInP/GaAs/Ge triple-junction cells made by Emcore Corporation. The cells

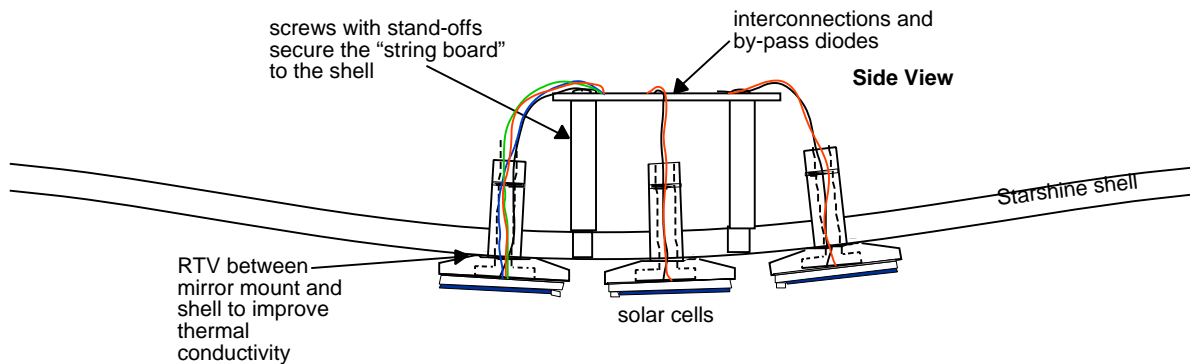


Figure 2) Sketch showing how solar cells are mounted to Starshine 3.

for Starshine 3 are 24% efficient under air mass zero (AM0). The Starshine 3 flight will mark the first time Emcore triple-junction cells have flown in space. Emcore is currently producing triple-junction cells that are 26% efficient at AM0.²

The battery used for storage of (excess) power generated by the solar cells is comprised of three Sony 18650 lithium-ion rechargeable cells. NASA has qualified these cells for one time (primary cells) use aboard the Space Shuttle, making it an excellent candidate for a rechargeable application. The main advantage of lithium-ion technology is higher energy density. Lithium-ion cells weigh approximately one-fourth what Ni-Cad cells weigh for a given Watt-hour rating. The cells of the Starshine 3 battery were stripped out of battery packs made for Canon® video cameras. The battery pack model is BP-930. The Starshine 3 battery consists of three Sony 18650 cells (nominal rating is 4.2V at 1.5 Amp-hours per cell) connected in series. The electrical power required to operate the electronics and transmitter is approximately one Watt averaged over an orbital period.

In order to ease integration of the solar cells onto the spacecraft, it was required that each cell be mounted much like one of the 1500 mirrors on the satellite. Each solar cell is mounted on a modified mirror mount that consists of a machined aluminum coupon about one inch on a side and a hollow stud on the back. The stud passes through the spacecraft shell where it is held in place with a compressive spring and clip. Wires from each solar cell pass through the stud into the spacecraft shell. Once inside the shell, the electrical leads from the solar cells are interconnected into a series string on a small circuit board. The circuit board has bypass diodes for each cell and a blocking diode on the string to prevent battery discharge through the solar cell string. Figure 2 shows a cross section of how the cells are mounted.

Since Starshine 3 is a rotating sphere and its orientation is not controlled, it was necessary to distribute the solar cells over the spacecraft in order to insure that enough power would be produced regardless of orientation. Eight small strings of solar cells are distributed across the surface of Starshine 3. Each cluster consists of a 6-cell string of 2 cm x 2 cm cells. Three strings are visible in Figure 1. A close-up of a solar cell string mounted to the body of the spacecraft is shown in Figure 3.

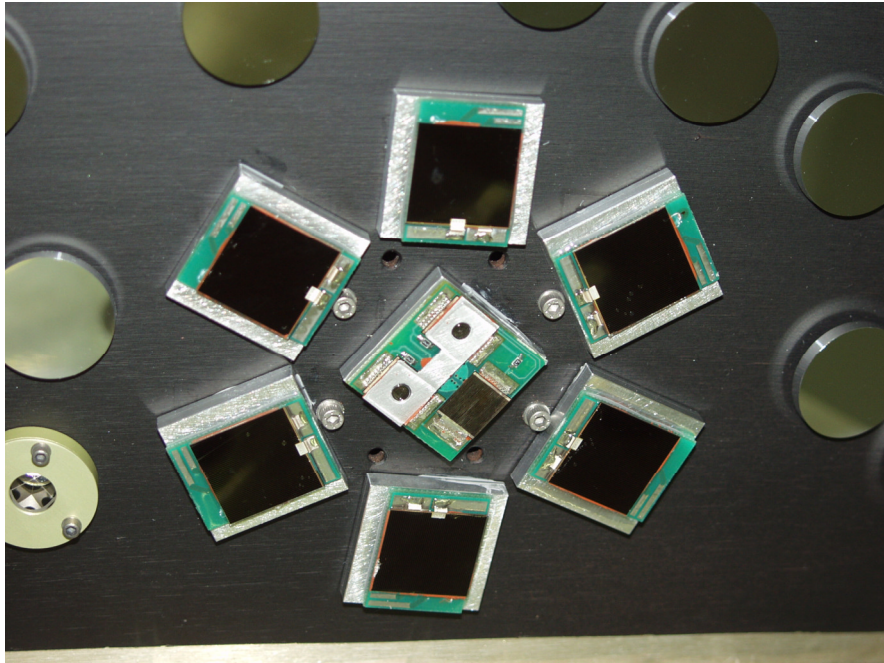


Figure 3) One of 8 solar cell strings on Starshine 3. Pictured in the center is the silicone transparency experiment.

Each string can supply 12.4 Volts at 60 mA when fully illuminated. On average, three clusters will be partially illuminated at any one time providing approximately 140 mA at 12.4 Volts to the power bus. The battery controls the operating point of the solar cell strings. Once the battery is charged to 12.4 Volts, the charge control circuitry shunts excess power into a dummy load.

The charge control schematic and the flight PMAD hardware are shown in figure 4. There is no under voltage protection of the battery. The only way to recover from a low battery voltage would be to temporarily shut down the transmitter via a ground command, allowing the battery to recharge. The voltage limits of operation are between 11 Volts and 12.4 Volts for the Starshine 3 electronics. The battery capacity is nominally 0.9 Amp-hours in this range. The anticipated discharge should not exceed 0.08 Amp-hours during an orbit. Thus the total depth of discharge compared to the nominal rating of the battery (1.5 Amp-hour) is 5.3%. The power system will be characterized by measuring the current produced by each string, the battery voltage, and the battery charge/discharge current.

Integrated Microelectronic Power Supply

The development of small micro and nano-satellites has generated a need for smaller lightweight power systems. Thin film batteries and solar cells are ideally suited to such applications. The necessity for both generation and storage of power for microelectronic applications can be achieved by combining a thin film photovoltaic array with a thin film lithium-ion battery into what is called an integrated microelectronic power supply (IMPS). These supplies can be combined with individual satellite components and are capable of providing continuous power in a variety of illumination schemes. It is a technological goal of IMPS development to have all components seamlessly integrated on a common substrate using thin film batteries and thin film solar cells. The Starshine 3 IMPS are just the first step

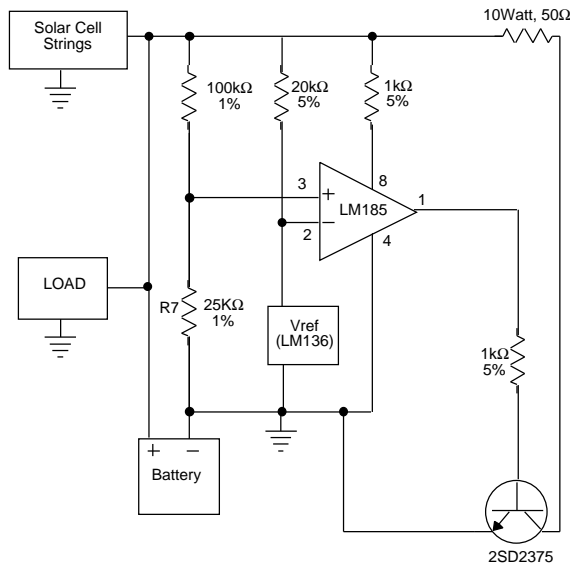


Figure 4) The schematic diagram of the electrical circuit used to control battery charging is shown on the left. On the right is the flight PMAD and battery hardware.

toward this goal and will provide valuable experience in design and operation of IMPS in a space environment.

Starshine 3 will fly five experimental integrated microelectronic power supplies pictured in figure 5.³ The experimental integrated microelectronic power supply is a stand-alone device that provides power generation, storage, and management in one compact package. The Starshine 3 IMPS consists of a solar array, a rechargeable battery, and power management electronics all fitting on one square-inch of circuit board. The IMPS are designed to deliver a constant $20 \mu\text{A}$ through a 1000Ω platinum temperature sensor. The solar array is a one square centimeter, monolithically interconnected module (MIM)⁴ of seven GaAs solar cells connected in series. The array output is nearly 7 Volts and can deliver up to 3 mA of current to the load and/or charging of the battery.

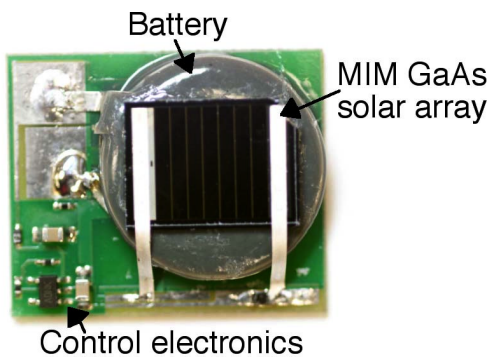


Figure 5) A Starshine 3 integrated microelectronic power supply.

Most of these electronics were necessary to avoid damage to the battery that would reduce its cycle life. Ideally, the solar array voltage and size could be matched to the battery voltage and charge current. A blocking diode could also be integrated onto the array eliminating the need for electronics.

The IMPS energy storage is a high capacity 3-Volt manganese/lithium-ion rechargeable battery. The battery is a Panasonic ML2020 with a capacity of 45 mA-hr rated for a continuous $100 \mu\text{A}$ load. The power management electronics consists of a micro-power voltage regulator and a blocking diode. The voltage regulator (MAXIM 1726EUK) keeps the battery from charging above 3 Volts. The blocking diode prevents current from flowing back through the array when it is in the dark. The load side includes two, P-type MOSFETS that shut off the load from the IMPS below 2.3 Volts. Figure 6 shows the complete IMPS and load circuitry. All of the electronic components were selected to minimize parasitic losses in the circuit and

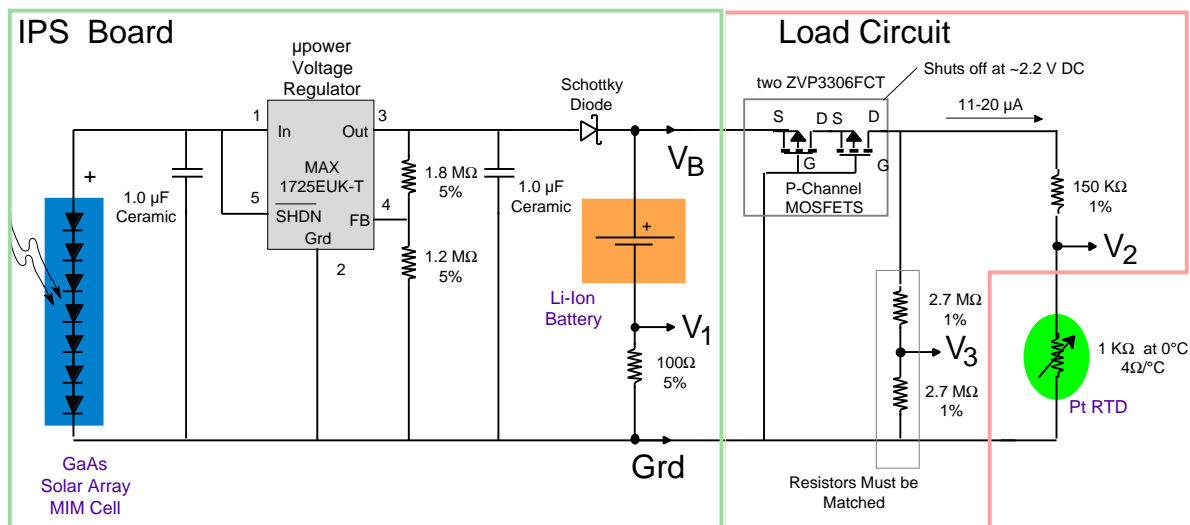


Figure 6) Circuit diagram for the IMPS circuit (left) and the load circuit (right).

Testing Concentrator Lens Materials

Concentrator solar arrays add efficiency and high radiation hardness to a power system. One such system in use is the SCARLET 2 Array⁵ on the Deep Space 1 spacecraft. However, the structure needed to support concentrator lenses (or reflectors) can offset some of the benefit of a concentrator system. One concept to reduce the mass of the concentrator assembly is to use an inflatable Fresnel lens array for solar concentration.⁶ One of the technological challenges for the inflatable array is to develop a flexible lens material that will not degrade in the harsh environment of space. The lens material of choice is a specially processed, transparent silicone rubber used for bonding cover glass to solar cells. Starshine 3 will monitor the transparency of two silicone samples as they are exposed to the space environment.

Summary

Starshine 3 has the unique opportunity to test new power technologies with little or no risk to the Starshine primary mission. Advance solar cells, batteries, silicone lens material and novel integrated micro power supplies will be demonstrated on Starshine 3.

Acknowledgements

The authors wish to thank the numerous government and commercial sponsors of this project, including the Photovoltaics Branch of the NASA Glenn Research Center at Lewis Field, the Naval Research Laboratory, the Ohio Aerospace Institute, Emcore Corporation, TRW and ITN Energy Systems. The authors also wish to thank Prof. Gilbert Moore, of Project Starshine, Dr. Aloysius F. Hepp, Mr. Henry Curtis at NASA GRC, Dr. Michael Batchelder of the South Dakota School of Mines and Dr. Don Lafevre, of Cynetics Corporation.

References

¹ Gil Moore, Bill Braun, Phillip Jenkins, Walter Holemans, and Don Lefevre, "Starshine Missions in 2001," Proceedings of the 15th Annual/USU Conference on Small Satellites, Logan UT, August 2001.

² Details of the Emcore GaInP/GaAs/Ge solar cell can be found at the web address:

http://www.emcore.com/html_documents/Photovoltaics.htm

³ R.P. Raffaele, J. Underwood, D. Scheiman, P. Jenkins, M.A. Smith, J. Maranchi and P. Kumta, D.M. Wilt, R.M. Button, A.F. Hepp, O.P. Khan, J. Harris, W.F. Maurer and C. R. Clark, "Integrated Microelectronic Power Supply," Proceedings of IECEC'01 36th Intersociety Energy Conversion Engineering Conference Savannah, Georgia, July 2001.

⁴ David M. Wilt, Naivid S. Fatemi, Phillip P. Jenkins, Richard W. Hoffman, Geoffrey A. Landis, and Raj K. Jain, "Monolithically Interconnected InGaAs TPV Module Development," Proceedings of the 25th Photovoltaics Specialists Conference, Washington D.C., May 1996.

⁵ Murphy, D.M., Allen, D.M., "SCARLET Development, Fabrication and Testing for the Deep Space 1 Spacecraft," Proceedings of the IECEC, Honolulu, HI, August 1997.

⁶ Mark J. O'Neill, Michael F. Piszczor, "Inflatable Lenses for Space Photovoltaic Concentrator Arrays," Proceedings of the 26th Photovoltaics Specialists Conference, Anaheim, CA, September 1997.

SOLAR ARRAY ARCING FAILURE MODE AND HIGH VOLTAGE ARRAY TESTING

Dale C. Ferguson
NASA Glenn Research Center
Cleveland, OH 44135

INTRODUCTION

In 1998, a new failure mode for space solar arrays was discovered (see references 1 and 2). A flowchart for this failure mode is shown below in figures 1 and 2.

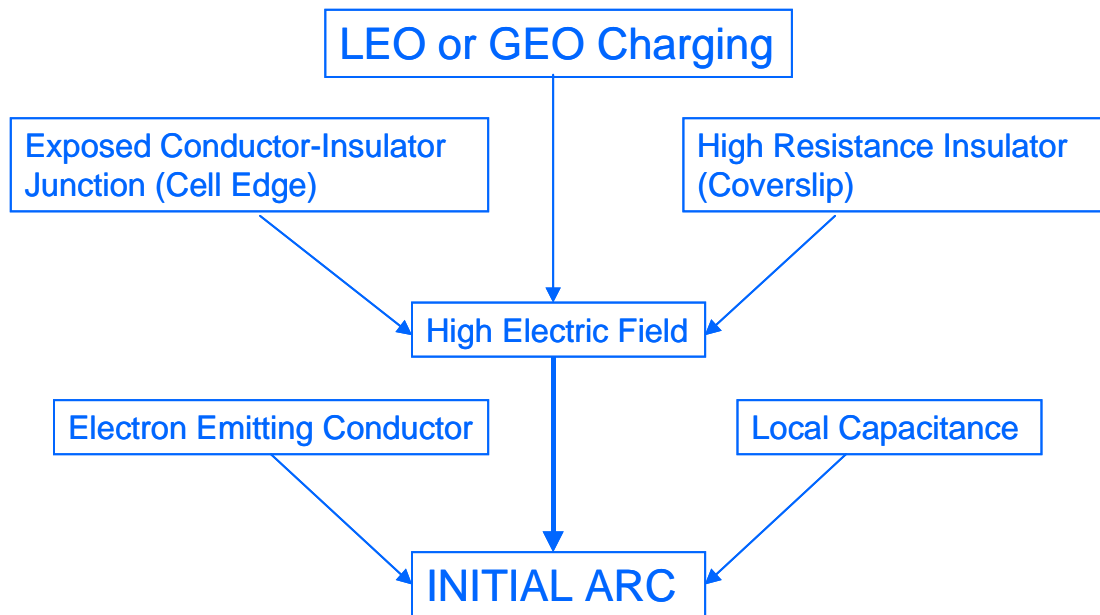


Figure 1. Flowchart for arc initiation.

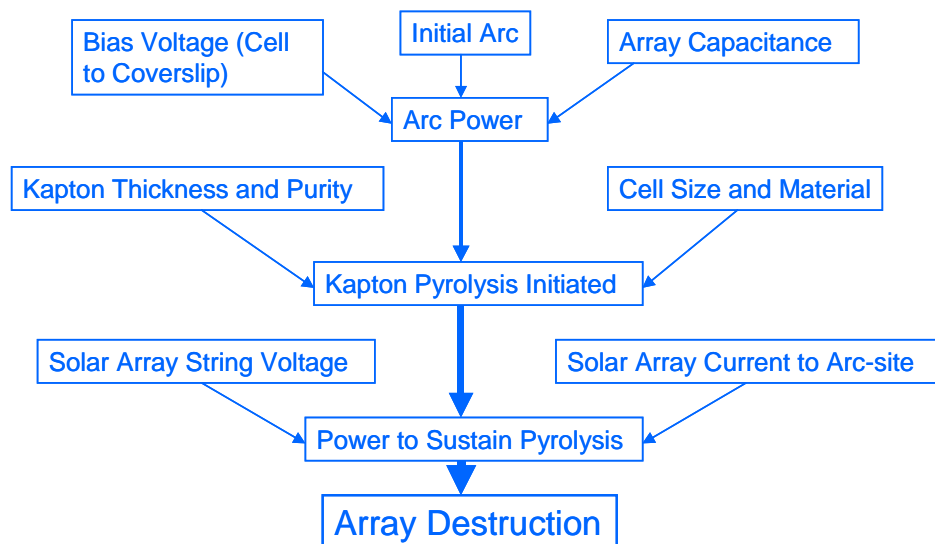


Figure 2. Flowchart for Space Array Arcing Failure Mode (Sustained Arcs)

Since the discovery of this arc failure mode, many tactics have been used to defeat it. The arc thresholds and arc mitigation strategies must be determined in vacuum-plasma tank testing on

Earth. Results from these tests must then be extrapolated to the space plasma environment. Thus, the test conditions on Earth must be adequate to reproduce the important aspects of the phenomenon in space. At Glenn Research Center, we have been testing solar arrays for their arc thresholds and sustained arcing thresholds, and in this paper, we detail the test conditions for a specific set of tests – those aimed at qualifying the Boeing Solar Tile solar arrays to operate in space at very high voltages (300 V or more).

TEST GOALS

1. Generate worst-case low Earth orbit (LEO) potentials between surfaces of solar arrays using simulated space plasma in GRC Plasma Interactions Facility.
2. Determine arc rates and/or arc thresholds for solar arrays at voltages of 300 V or more, relative to the plasma.
3. Raise potentials until sustained arcs encountered – destroy sample.

TEST CONDITIONS (GENERAL)

1. $> 10^5 \text{cm}^{-3}$ xenon plasma generated by a hollow cathode plasma source.
2. Vacuum neutral pressure $< 2 \times 10^{-5}$ Torr (collisionless).
3. Voltages and currents applied and measured with Keithley programmable electrometers.
4. Bias applied to negative end of array strings, conductive coverslide coatings floated. Substrate floated.

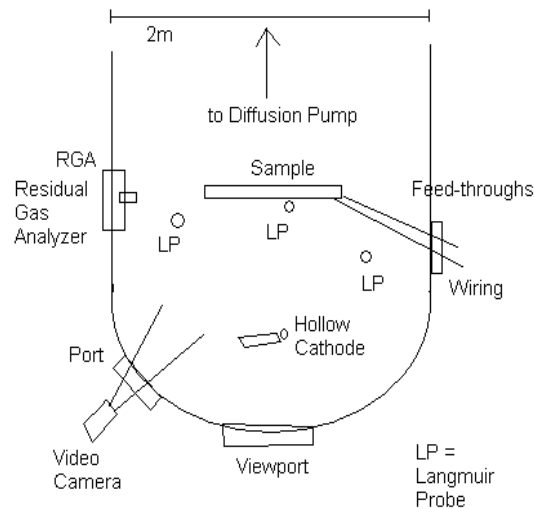


Figure 3. A Typical Test Setup

SPECIFIC TEST CONDITIONS FOR SPACE SOLAR POWER (SERT) SOLAR ARRAY TESTS

1. Plasma Source – Hollow Cathode by EPL, Inc.
2. Plasma conditions: $\text{Ne} = 10^5\text{-}10^6 / \text{cm}^3$, $\text{Te} = 0.3\text{-}1.0$ eV.
3. Neutral pressure = 10^{-6} to 10^{-5} Torr (collisionless).
4. Langmuir probe diagnostics (0.75 inch spheres), taken at beginning and end of each run.
5. RGA used to determine when plasma relatively free of contaminant gases (diffusion pump oil).
6. External Capacitance = 0.1-10 microFarad.
7. Solar Array Simulator (SAS) used to simulate rest of large array.
8. Arc limiter circuit used to prevent catastrophic arcs (with destruction of sample) – if arc current lasts > 0.5 millisecond, SAS current chopped to zero.
9. Video camera used to record entire proceedings inside tank.

10. For some arcs, high speed video triggered by arc current.
11. High speed digital oscilloscope triggered by arc voltages and/or currents.

CAVEATS (Learned the hard way)

1. Watch your neutral pressure. Too high and you get collective effects like those that invalidated the second ISS solar array collection test (ionization of neutrals within chamber).
2. Leakage currents to substrates, etc. may overload your power supply and lower your high voltages - keep your isolation large.
3. A current limiting resistor is usually used to isolate the power supply during the arcs to prevent continuous arcing – except when you are ready to destroy your sample.

RESULTS FROM THE SERT TESTS AT THE NASA GLENN RESEARCH CENTER

As detailed in another paper at this conference (ref. 3), design strategies incorporated into the Boeing Solar Tile for the Space Solar Power (SERT) Program allowed it to be tested at up to 1000 V without sustained arcs, and with the only arcs encountered being outside of the solar array proper (on the surrounding frame). We are confident that these results will apply under real space conditions, and that the design strategies for the Boeing Solar Tile may be used to arc-proof space solar arrays up to the 1000 V level.

REFERENCES

1. I. Katz, V. A. Davis, and D.B. Snyder, 1998, "Mechanism for Spacecraft Charging Initiated Destruction of Solar Arrays in GEO," at the 36th AIAA Aerospace Sciences Meeting and Exhibit, Reno, NV, Jan. 12-15, AIAA Paper # 98-1002.
2. C.F. Hoeber, E.A. Robertson, I. Katz, V.A. Davis, and D.B. Snyder, 1998, "Solar Array Augmented Electrostatic Discharge in GEO," at the 17th AIAA International Communications Satellite Systems Conference and Exhibit, Yokohama, Japan, Feb. 23-27, AIAA Paper # 98-1401.
3. B.J. Reed, D.E. Harden, D.C. Ferguson, and D.B. Snyder, 2001, "Boeing's High Voltage Solar Tile Test Results," Proceedings of the 17th Space Photovoltaic Research and Technology Conference, this volume.

CHARGING OF THE INTERNATIONAL SPACE STATION DUE TO ITS HIGH VOLTAGE SOLAR ARRAYS

Dale C. Ferguson
NASA Glenn Research Center
Cleveland, OH 44135

INTRODUCTION

The International Space Station (ISS) has the highest voltage solar arrays ever flown in Low Earth Orbit (LEO, see figure 1). The ISS power system (and structure) ground is at the negative end of the 160 V solar arrays. Due to plasma current collection balance that must be maintained in LEO, it is possible for a spacecraft to charge negative of the ambient plasma by up to its entire solar array voltage (-160 V for ISS, see reference 1).



Figure 1. ISS after mission build 7A. The 160 V solar arrays are horizontal.

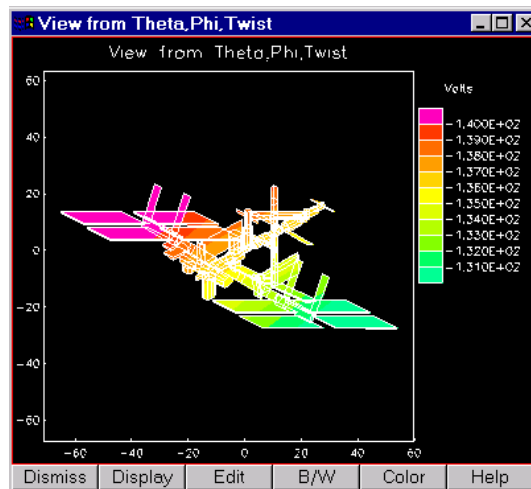


Figure 2. A model prediction of ISS “floating potentials.”

In 1990 and 1991, an Electrical Grounding Tiger Team was instituted to determine the effects on ISS of its 160 V negative ground system. The Tiger Team predicted that ISS would “float” at -140 V (see figure 2), and this would cause its anodized aluminum surfaces to undergo dielectric breakdown, ruining their thermal properties. The best estimate of the time to remove enough anodize to violate temperature constraints was determined to be two years (ref. 2). Because of this failure mechanism, in 1991, the Electrical Grounding Tiger Team recommended that the ISS potential be controlled by incorporating a Hollow Cathode Plasma Contactor to ground it to the ambient plasma (ref. 3). Plasma Contacting Units (PCUs) were baselined, constructed, and made ready to fly by ISS mission 3A, and would be activated by mission 4A, when the high voltage solar arrays would be launched and turned on (see figure 3).

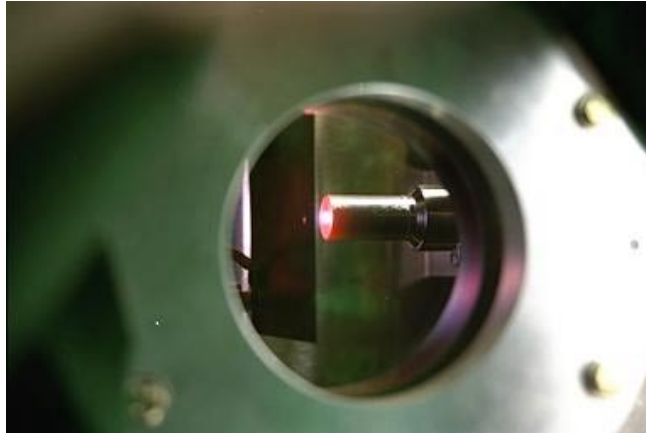


Figure 3. One of the hollow cathodes used on the ISS PCUs, undergoing ground testing in a GRC plasma chamber.

RECENT DEVELOPMENTS

In the meantime, the phenomenon of sustained arcing was discovered (by partial destruction on orbit of some SS/Loral solar arrays, see ref. 4). Sustained arcing occurs when an arc into the space plasma transitions into an arc between spacecraft surfaces that can be powered in a sustained manner by the spacecraft power system. Like the arc in a welding torch, one such sustained arc can lead to immense damage. The prospect of this new type of catastrophic arcing, combined with acceptance testing difficulties with the PCUs in early 2000, led to a re-examination of the criticality of PCU operation. After the author presented talks at the Johnson Space Center (JSC) at the invitation of the Independent Assessment Office (ref. 5), a PCU Tiger Team was set up to find answers before flight 4A in December, 2000.



Figure 4. A sustained arc on a solar array in a simulated LEO plasma.

The PCU Tiger Team results were surprising. Although sustained arcing was not verified in testing, it was found that the arc threshold voltage for materials on the Extravehicular Mobility Unit (EMU, or spacesuit) was less than -70 V (see ref. 6). A safety rule now requires that the EMU voltage be held less than -40 V from the plasma. A “sneak circuit” analysis, performed by Hamilton Standard, the EMU manufacturer, found that the astronaut would be in the path to ground of arc currents on his suit through his tether to ISS. The capacitance discharged in an arc would be >1000 μF , leading possibly to arc energies of > 10 Joules. Lethal arc currents of > 1 A were predicted in an astronaut’s body.

Suddenly, arcing on ISS became a catastrophic hazard to the astronauts, requiring two fault tolerance (3 independent controls) during EVAs (extravehicular activities, or space walks). Testing showed that both PCUs could be operated simultaneously, giving two controls. The third control would have to come from passive techniques – shunting the arrays or pointing them into their own wakes, so they couldn’t collect charging currents.

Passive potential control techniques would have to be verified on orbit, requiring measurement of the ISS floating potential. A floating potential probe (FPP) would have to be implemented on ISS before flight 4A. Amazingly, the FPP (based on plasma probes flown on STS-62, see fig. 5) was designed, constructed, qualified, integrated, and flown in only 6 months (June-November, 2000). On 4A, it was installed atop the ISS truss structure by astronauts Tanner and Noriega (fig. 7). On December 8, 2000, FPP started measuring ISS potentials and parameters of the ambient plasma.

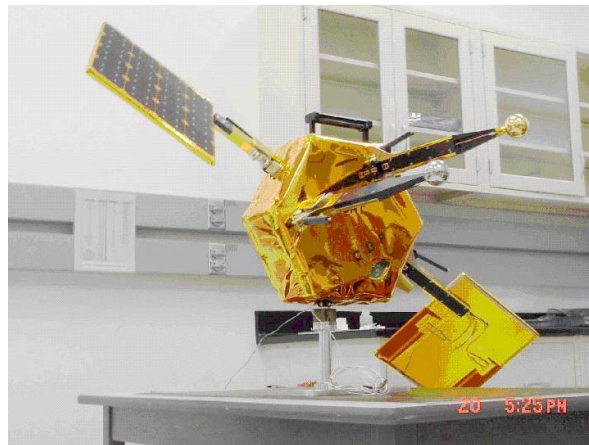


Figure 5. The FPP at Cape Canaveral, prior to launch.

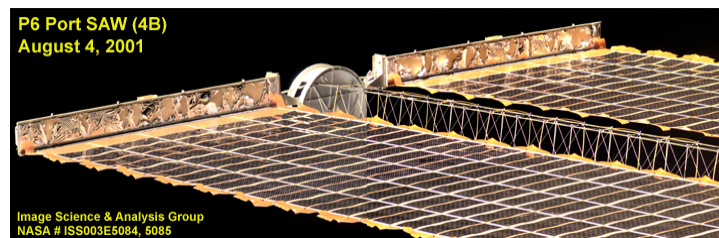


Figure 6. Wires on the Solar Array Mast collect ions.

FPP RESULTS

FPP showed that shunting and/or pointing the arrays even a little into their wakes were valid EVA shock hazard controls. FPP also showed that even with the arrays inactive, the ISS floating potential can vary by 15 volts or more during an orbit. This is due to electron collection by wires on the solar array masts (fig. 6). $v_{xB.I}$ is the amount of charging caused by the passive electron

collection. This $v_x B$ charging must be added to real solar array charging for various places on the ISS structure to find the potential with respect to the surrounding ambient plasma.

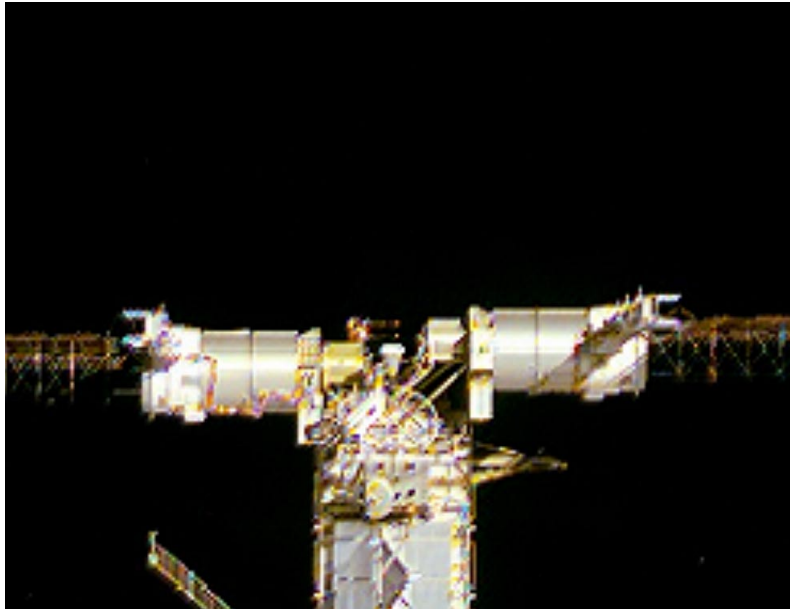


Figure 7. FPP on orbit. The two plasma diagnostic spheres are near the picture center.

FPP tests done outside EVA periods with the arrays fully unshunted and the PCUs purposely turned off showed that both solar arrays now on ISS together only charge it about -25 volts, not the -140 volts predicted (see fig. 8). Even counting a maximum of 15 volts of $v_x B$ charging, this amounts to only -40 V. Why were the predictions inadequate? The two reasons:

1. The solar arrays collect much less electron current from the plasma than expected from the previous ground and flight-test experiments.
2. The ISS structure has about 10 m^2 of extra, exposed grounded conductor in contact with the plasma, which collects ions and reduces ISS charging.

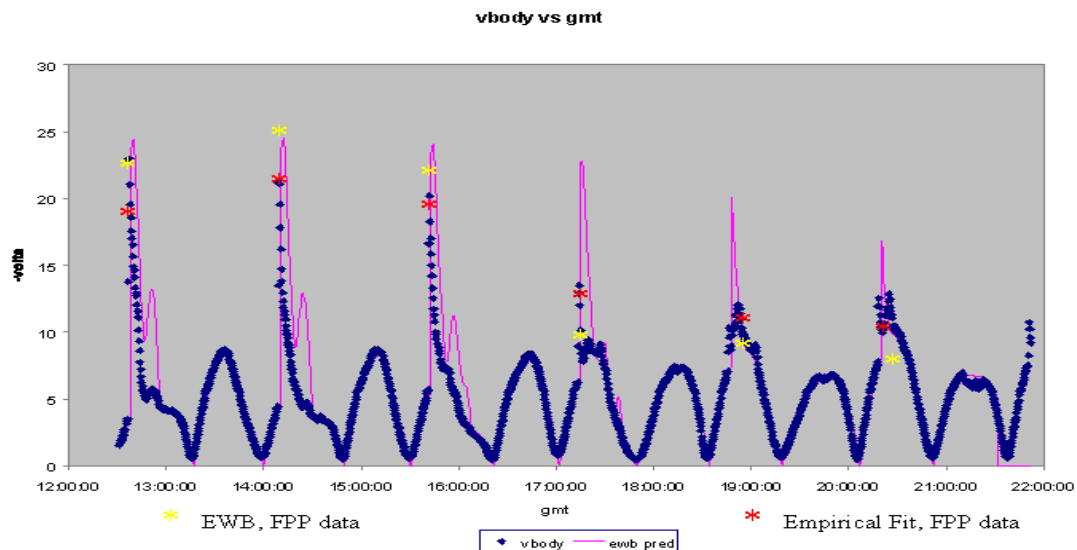


Figure 8. FPP measurements (blue) and model fits (other colors) for April 11, 2001.

ISS solar array electron collection was expected to be somewhere between the results found from the SAMPIE and PASP Plus flight experiments (1994, ref. 7). On ISS, the solar arrays collect even less current than the least amount found in those two flight tests. Although ISS is advertised to be completely covered with insulating material (thermal blankets or anodized aluminum) bare stainless steel grounded fasteners are located all over ISS structure, and these act to collect ions from the ambient plasma, minimizing negative charging.

NEW FINDINGS ABOUT PLASMA DEPENDENCES

ISS solar array electron collection and ISS charging have been found from FPP measurements to be strongly inversely related to the ambient electron temperature. An empirical ISS charging relationship (the Ferguson-Morton relation, ref. 8) has been found from FPP data to be:

$$-V = 2.69 N_e^{0.1} e^{-8T_e},$$

where N_e is the electron density (m^{-3}), and T_e is the electron temperature (eV). This surprising relation says that ISS will charge more negative when the electron density is high (a weak dependence) but the electron temperature is low (a strong dependence). Electron temperatures are lowest at dawn.

POSSIBLE FUTURE ISS CHARGING PROBLEMS

On future ISS missions (> 12A, November 2002) more solar arrays will be added, but it is unlikely that the amount of added ion collecting truss structure will be able to keep up. The new main ISS truss will maximize $v \times B$ charging. From one end of the truss to the other, $v \times B$ itself amounts to almost 40 V (the maximum the safety rule allows). Also, FPP has stopped working, and it may not be replaced by 12A. When changing arrays, or when replacing PCUs, one PCU must be inactivated. As time goes on, the ionospheric plasma temperature will decrease, as we get closer to solar minimum again. All of these circumstances make catastrophic arcing more probable.

REFERENCES

1. D.C. Ferguson and G.B. Hillard, 1997, "Lessons for Space Power System Design from the SAMPIE Flight Experiment," AIAA Paper # 97-0087.
2. D.C. Ferguson, D.B. Snyder and R. Carruth, 1990, Report of the Joint Workshop of the Space Station Freedom Plasma Interactions and Effects Working Group, the Space Station Freedom Plasma Working Group, and the Space Station Freedom EMI/EMC and Electromagnetic Effects Working Group on Evaluation of Impacts of Space Station Freedom Grounding Configurations, May 22-24, 1990. Final Report, Aug. 21, 1990.
3. D.C. Ferguson, 1991, Minutes of the Space Station Freedom Electrical Grounding Tiger Team Mtg., Rocketdyne Bldg., Cleveland, OH, Aug. 5-7, 1991. "Summary of Floating Potentials."
4. I. Katz, V. A. Davis, and D.B. Snyder, 1998, "Mechanism for Spacecraft Charging Initiated Destruction of Solar Arrays in GEO," at the 36th AIAA Aerospace Sciences Meeting and Exhibit, Reno, NV, Jan. 12-15, AIAA Paper # 98-1002.
5. D.C. Ferguson, 2000, "Orbiting in a LEO Plasma -What are the Physical Effects?," "ISS Plasma Contactor Unit," "ISS PCU – Operations Considerations," 2000, NASA JSC Independent Assessment Office, March 22.
6. M.R. Carruth et al, 2001, "ISS and Space Environment Interactions Without Operating Plasma Contactor," AIAA Paper # 2001-0401.

7. D.C. Ferguson, 1997, "Comparison of Electron Current Collection by Space Station Solar Arrays as Measured by SAMPIE and PASP Plus," in the Photovoltaic Array Space Power Plus Diagnostics (PASP Plus) Experiment Final Report, D.A. Guidice, V.A. Davis, H.B. Curtis, D.E. Hastings, F.L. Knight, D.C. Marvin, K.P. Ray, P.S. Severance, J.D. Soldi, M. Van Riet, co-authors, PL-TR-97-1013, March, 1997.

8. D.C. Ferguson and T.L. Morton, 2001, "An Empirical Model Of ISS Charging, Based On FPP And ODRC Data Of 04/11/01 Thru 04/13/01. Is Shunting One Array At Dawn Always A Good Eva Hazard Control?," a presentation to the ISS PCU Tiger Team, August 2, 2001.

Single junction InGaP/GaAs solar cells grown on Si substrates using SiGe buffer layers

S.A. Ringel,¹ J.A. Carlin,^{1*} C.L. Andre,¹ M.K. Hudait,¹ M. Gonzalez,¹ D.M. Wilt,² E.B. Clark,² P. Jenkins,² D. Scheiman,² A. Allerman,³ E.A. Fitzgerald⁴ and C.W. Leitz⁴

¹Department of Electrical Engineering
The Ohio State University
Columbus, OH 43210

²NASA Glenn Research Center
Cleveland, OH 44135

³Sandia National Laboratory
Albuquerque, NM 87185

⁴Department of Materials Science and Engineering
Massachusetts Institute of Technology
Cambridge, MA 02139

*Now with Amberwave Systems Corporation, Salem, NH 03079

Abstract

Single junction InGaP/GaAs solar cells displaying high efficiency and record high open circuit voltage values have been grown by metalorganic chemical vapor deposition on Ge/graded SiGe/Si substrates. Open circuit voltages as high as 980 mV under AM0 conditions have been verified to result from a single GaAs junction, with no evidence of Ge-related sub-cell photoresponse. Current AM0 efficiencies of close to 16% have been measured for a large number of small area cells, whose performance is limited by non-fundamental current losses due to significant surface reflection resulting from > 10% front surface metal coverage and wafer handling during the growth sequence for these prototype cells. It is shown that at the material quality currently achieved for GaAs grown on Ge/SiGe/Si substrates, namely a 10 nanosecond minority carrier lifetime that results from complete elimination of anti-phase domains and maintaining a threading dislocation density of $\sim 8 \times 10^5 \text{ cm}^{-2}$, 19-20% AM0 single junction GaAs cells are imminent. Experiments show that the high performance is not degraded for larger area cells, with identical open circuit voltages and higher short circuit current (due to reduced front metal coverage) values being demonstrated, indicating that large area scaling is possible in the near term. Comparison to a simple model indicates that the voltage output of these GaAs on Si cells follows ideal behavior expected for lattice mismatched devices, demonstrating that unaccounted for defects and issues that have plagued other methods to epitaxially integrate III-V cells with Si are resolved using SiGe buffers and proper GaAs nucleation methods. These early results already show the enormous and realistic potential of the virtual SiGe substrate approach for generating high efficiency, lightweight and strong III-V solar cells.

1. INTRODUCTION

The development of high efficiency III-V compound solar cells grown on Si substrates has received sustained interest in the photovoltaics community for more than two decades.¹⁻³ The attractiveness of III-V/Si solar cells stems from combining optimum photovoltaic materials such as InGaP, GaAs and AlGaAs with an optimum substrate material, Si. Compared to Ge, currently the dominant substrate for III-V space photovoltaics, Si possesses far superior substrate properties with respect to mass density, mechanical strength, thermal conductivity, cost, wafer size and availability. Unfortunately, the 4% mismatch in lattice constant between Si and GaAs, the latter for which is the basis material for all optimum, multijunction III-V solar cell structures, generates a high density of threading dislocations in III-V overlayers grown on Si, severely reducing GaAs material quality, carrier lifetimes, and III-V solar cell performance. Nevertheless, many groups have recognized the potential benefits of epitaxial III-V/Si solar cells, and III-V/Si integration in general, leading to investigations of many methods to control and reduce dislocation densities in this highly mismatched heterostructure. These approaches include the insertion of various III-V intermediary layers based on compositionally graded III-V buffers and strained layer superlattices, and the use of thermally-cycled annealing of intermediary layers prior to cell growth. Each has been successful in reducing threading dislocation densities in the III-V overlayers from $\sim 10^9$ - 10^{10} cm⁻² for direct GaAs on Si epitaxy, to the 10^7 cm⁻² range.³⁻⁸ While impressive, this dislocation density still limits the minority carrier lifetimes in GaAs to 1-4 ns, even after post-growth defect passivation treatments via hydrogenation.^{7,8} These values are not high enough to enable high efficiency III-V cells, and those cells that have been fabricated suffer from low open circuit voltages, typically on the order of 900 mV or lower under AM0 conditions for single junction GaAs, providing an ultimate limit on cell efficiency.

Each of the approaches highlighted above involve some form of strain management and dislocation filtering within the III-V layers and they tend to approach a similar final threading dislocation density and minority carrier lifetime for GaAs on Si after optimization. This observation has motivated the development of an alternative approach in which the surface lattice constant of the Si substrate itself is engineered prior to any III-V epitaxy by growth of compositionally-graded SiGe buffers, rather than dealing with the mismatch only within the III-V epitaxial layers. In this way, the lattice mismatch is addressed in a material system and under growth conditions that are independent from growth of the III-V solar cell region. Recently, this “virtual Ge substrate” approach has resulted in threading dislocations as low as 8×10^5 cm⁻² within relaxed GaAs overlayers,

demonstrating that the SiGe buffer approach has broken through a barrier that has limited the progress of III-V buffer approaches for GaAs on Si for more than ten years.^{9,10} The impact of this lower dislocation density value on electronic material quality is evident by yielding the highest minority carrier lifetimes reported to date for GaAs grown on Si, with values in excess of 10 ns being demonstrated in n-type GaAs.^{9,10} At this lifetime value, high efficiency III-V solar cells can be expected and the use of SiGe buffers for generating high efficiency III-V cells on Si for space photovoltaics is extremely promising.¹¹ Recently, we reported GaAs solar cells grown on Ge/SiGe/Si that displayed high efficiency and the highest open circuit voltages reported to date for GaAs cells grown on Si substrates.¹ In this paper, we extend these early results in an ongoing project to describe a quantitative picture of cell performance dependence on dislocation density, report on larger cell area development and investigate potential activity of the GaAs/Ge interface region for p on n GaAs cells on Ge/SiGe/Si substrates

2. EXPERIMENTAL DETAILS

InGaP/GaAs single junction, p on n configuration solar cells were grown by low pressure MOCVD on Ge/graded SiGe/Si wafers. The step-graded SiGe buffers were grown on (001) Si wafers offcut by 6° toward the in-plane [110] direction by ultra high vacuum chemical vapor deposition (UHVCVD) using SiH_4 and GeH_4 as source gases, at an average grading rate of 10% Ge/micron.¹² Plan-view and cross sectional transmission electron microscopy (TEM), electron beam induced current (EBIC), and etch pit density (EPD) measurements confirmed an average TDD (threading dislocation density) = $0.8 - 1.5 \times 10^6 \text{ cm}^{-2}$ present in the relaxed Ge cap layer for a large number of growth runs. EPD measurements made on GaAs overlayers grown on the Ge/SiGe/Si substrates revealed an identical TDD value as obtained for the Ge cap layers, indicating negligible dislocation nucleation by III-V growth and the formation of an ideal low mismatched GaAs/Ge interface on these substrates. That is, the graded SiGe layers were successful in forming a virtual Ge substrate on an actual Si wafer. The methodology used to eliminate additional problematic issues that are specifically related to the GaAs/Ge interface, namely antiphase domain (APD) formation and cross-diffusion leading to autodoping, can be found in earlier publications.^{10,11,13} The p on n configuration InGaP/GaAs single junction cells were grown via low pressure MOCVD at 650°C following transfer to the MOCVD growth system. The basic, non-optimized single junction cell designs reported here are shown in Figure 1. Au/Cr was used for the p-type GaAs contact in all cases. N-type contacts of Au/Sb and Al were used for cells grown on Ge

and Ge/SiGe/Si substrates, respectively. Certain cells were coated with a triple layer $\text{MgF}_2/\text{ZnS}/\text{MgF}_2$ anti-reflection coating.

3. ROLE OF DISLOCATION DENSITY ON GaAs/Ge/SiGe/Si CELL PROPERTIES

The impact of threading dislocation density on minority carrier diffusion length (L_p), and hence minority carrier lifetime (τ_p), has been well documented.^{3,14} However, the detailed, quantitative dependence of cell V_{oc} and J_{sc} on TDD is less obvious, and requires greater scrutiny to generate optimum device designs for GaAs on Si solar cells with the significant reduction in TDD that has been established using SiGe graded buffers compared to previous efforts. The average spacing between threading dislocations can be approximated by¹⁴

$$L_{TDD} = (\pi(TDD))^{1/2} \quad (1)$$

where for simplicity it is assumed that all dislocations are uniformly spaced perpendicular to the growth plane. Thus, this is a rough approximation of the actual network of 60° threading dislocations present in mismatched GaAs. To understand the implication of dislocation density, the average dislocation spacing must be compared with the minority carrier diffusion length, which for n-GaAs is given by

$$L_p = (D_p \tau_p)^{1/2} \quad (2)$$

Where, accounting for doping and TDD¹⁴

$$D_p = 7.347 \times 10^6 / (6.697 \times 10^5 + n^{1/3}) \quad (3)$$

$$1/\tau_p = 1/\tau_{po} + \pi^3 D_p (TDD)/4 \quad (4)$$

and the other terms have their usual meanings noting that the carrier mobilities at typical base doping levels are not influenced by TDD for values less than $\sim 10^8 \text{ cm}^{-2}$. Figure 2 shows the average dislocation spacing plotted as a function of TDD following equation (1), along with a plot of the expected dependence of minority carrier hole diffusion length on TDD for n-type GaAs doped at $1 \times 10^{17} \text{ cm}^{-3}$. The diffusion length dependence was calculated from equations (2) – (4). For

the latter, a value for the non-dislocation-limited lifetime (τ_{po}) for minority carrier holes of 20 ns was used, based on time-resolved photoluminescence studies on $n=1 \times 10^{17} \text{ cm}^{-3}$ GaAs grown on Ge substrate wafers at 300 K for which dislocation density was not a factor.¹¹ As seen from the figure, for TDD values greater than $\sim 2 \times 10^6 \text{ cm}^{-2}$, the diffusion length is limited by TDD spacing. That is, above this value, the average dislocation spacing is on the order of or less than one diffusion length. For TDD values lower than $1 \times 10^6 \text{ cm}^{-2}$, the average dislocation spacing becomes much larger than a diffusion length and recombination is limited by non-dislocation-related processes, which at this typical base doping value is primarily bulk Shockley-Read-Hall recombination. Note that these calculations are for one value of n-type GaAs doping. The position of the knee in the curve in figure 2, and therefore the TDD threshold required to achieve “dislocation-independent” minority carrier lifetimes and diffusion lengths, shifts to lower values as GaAs doping is reduced due to the higher lifetimes and longer diffusion lengths for lightly doped material. This must be a consideration for achieving optimum lattice-mismatched cell designs.

The effect of TDD on J_{sc} of GaAs/Si cells is largely dependent on the cell base width, which due to the large absorption coefficient of GaAs can be designed to be less than a typical GaAs minority carrier diffusion length without significantly compromising current collection due to incomplete optical absorption. Hence, the TDD limitation is somewhat relaxed by proper cell design. For instance, a TDD value of $1 \times 10^6 \text{ cm}^{-2}$ leads to an average dislocation spacing of 5.5 microns, almost twice the hole diffusion length in n-GaAs at a doping of $1 \times 10^{17} \text{ cm}^{-3}$. To absorb more than 95% of the incident AM0 light requires a total GaAs thickness of approximately 2 microns. For pn cell configurations that typically include an emitter thickness of approximately 0.5 microns, a base thickness of 2 microns is easily sufficient to avoid dislocation-limited collection. Hence, optimal base thickness can scale with TDD as long as significant optical absorption is not compromised. Indeed, this approach was verified by earlier work where high J_{sc} values for GaAs/Si cells having a base thickness of 1.3 microns were reported to be comparable with values obtained for GaAs/GaAs homoepitaxial cells, in spite of reported TDD values of $\sim 5 \times 10^6 \text{ cm}^{-2}$ that led to minority carrier lifetimes of only 1-3 ns.³ In comparison, for the GaAs/Ge/SiGe/Si system discussed here for which minority carrier lifetimes in excess of 10 ns have been demonstrated, ideal J_{sc} values should be achievable with a more conventional base thickness, allowing for more complete absorption of the solar flux. This is confirmed by figure 3, which shows a comparison of external quantum efficiency (EQE) data collected for single-junction GaAs solar cells with a 2.5 micron thick base grown on GaAs, Ge, and GeSi substrates by Molecular Beam Epitaxy. Photon collection

efficiencies are seen to be independent of substrate choice, indicating that even for a conventional base thickness in a p on n configuration, no impact of TDD on J_{sc} is observed, consistent with the low TDD values and confirming that long diffusion lengths are maintained after complete cell processing.

While creative device designs can be used to minimize the impact of TDD on J_{sc} , a flexibility that is in part due to the strong absorption coefficient for GaAs, the open circuit voltage is less forgiving and along with fill factor have proven to be the key efficiency limiting parameters for III-V cells grown on mismatched substrates. TDD will impact V_{oc} through several means. For the ideal Schockley diode solar cell model, TDD increases the D/L ratio since the diffusion coefficient, D, will not be limited by dislocation spacing whereas the diffusion length, L, is limited by dislocation spacing. High D/L values leads to increased saturation current densities (J_0) and lower V_{oc} through the expression

$$V_{oc} = (kT/q)\ln(J_{sc}/J_0) \quad (5)$$

A more likely limitation on V_{oc} is via dislocation-related recombination within the depletion region that can generate appreciable recombination current and, for higher TDD values, will generate an array of low resistance shunt paths across the junction. It is the combination of these reasons that until this work, has typically limited measured V_{oc} values for GaAs cells grown on Si to less than ~ 900 mV under AM0 conditions, far less than the typical 1 V values observed for GaAs/GaAs and GaAs/Ge single junction cells. For cells where the dominant dark current is due to depletion region recombination, the V_{oc} expression can be written as¹⁴

$$V_{oc} = (2kT/q)\ln(J_{sc}/J_{0r}) \quad (6)$$

where

$$J_{0r} = qn_i W D_p / 2L_p^2 \quad (7)$$

Figure 4 shows the theoretical dependence of V_{oc} on TDD based on these assumptions, with measured data from several groups shown along with data from our work. In all prior cases significant deviation from this model is observed. This is indicative of several possibilities. First is that V_{oc} in the earlier reports was limited by other factors not included in this simplistic model, possibly shunt currents or anti-phase domains that have been observed to dramatically reduce carrier

lifetimes and diffusion lengths. Second is the question of accurately measured TDD values. Below approximately 10^7 cm^{-2} cross sectional TEM measurements are not useful and dislocation densities must be measured by techniques with lower resolution (larger fields of view) such as etch pit density or electron beam induced current, in conjunction with plan-view TEM. With either of these methods however, it is difficult to distinguish between dislocation pileups, a common occurrence for graded buffer layers, and individual threading dislocations and counting errors can be expected. Moreover, dislocation pileups will be far more deleterious than isolated dislocations, since they can act as significant segregation sites for dopants and other impurities. A third possible explanation for the observed low V_{oc} values that was suggested by authors of the earlier studies was an increased depletion region generated by the intersection of dislocation cores with interfaces and surfaces, leading to unaccounted recombination currents.^{7,8}

In contrast to these prior reports, close agreement between this simple model and actual results have been achieved for GaAs cells on Ge/SiGe/Si substrates. Figure 5 shows light I-V AM0 data obtained for a particular set of cells having the same design, grown by MOCVD on both Ge and Ge/GeSi/Si substrates. Nearly identical cell parameters are observed for both substrates, demonstrating that the current TDD value is not limiting the device performance, consistent with the discussions above, and that ideal, low-mismatched GaAs/Ge growth has been achieved on SiGe/Si. Through several sets of cell growth and fabrication cycles, more than 100 of such high performance GaAs cells on Ge/SiGe/Si have been demonstrated, with AM0 V_{oc} values ranging from 950 mV to 1030 mV for structures having TDD values between $9 \times 10^5 \text{ cm}^{-2}$ and $2 \times 10^6 \text{ cm}^{-2}$. These V_{oc} values are the highest ever achieved for GaAs cells grown on a Si substrate by any method to date. The close match to the theoretical curve of figure 4 signifies that the performance of cells grown on SiGe virtual substrates are limited by dislocation-related recombination currents in the depletion region, with no apparent complications from other unaccounted defects or loss mechanisms. This is corroborated by dark I-V analysis that showed an increase in the diode ideality factor from ~ 1.5 to 2 for GaAs diodes grown on Ge and Ge/SiGe/Si substrates, respectively, which is probably responsible for the reduction in fill factor for the cells on Ge/SiGe/Si as compared to those on Ge in figure 5. It can be concluded that at our current TDD values, the primary limitation on cell performance is simple depletion region recombination that impacts fill factor.

4. PERFORMANCE AND ANALYSIS OF GaAs/Ge/SiGe/Si CELLS

The light I-V data of figure 5 was obtained on small area, 0.2 cm x 0.2 cm cells, which suffered from a large front contact grid coverage of >10%, and a loss of J_{sc} due to incomplete carrier collection deep within the base that is a consequence of a wafer handling step between GaAs nucleation on the Ge/SiGe/Si substrate and growth of the complete cell by MOCVD. This step is currently being eliminated from our initial process as we evolve our cell development program. The spectral response data of figure 6 clearly shows the effect of the wafer handling step. The response for cells grown on Ge and SiGe, both of which received the same handling step, are identical, whereas the cell grown on a GaAs substrate that did not require wafer handling displays improved collection at long wavelengths. Calibrated AM0 light I-V measurements indicate a J_{sc} loss of ~ 1.7 mA/cm² as a result of this process. By accounting for this non-fundamental loss, and assuming a grid coverage of 4% typical for larger area cells, single junction AM0 efficiencies of close to 20% are feasible at the V_{oc} values measured for these cells. Preliminary attempts to increase cell area are now in progress. Cells having areas of 0.6 cm x 0.6 cm (9 fold increase in area) display improved quantum efficiency due to decreased grid coverage from 10.5% to $\sim 8\%$, leading to an increase in J_{sc} from 28.5 mA/cm² to 29.7 mA/cm². Accounting for the J_{sc} loss from the wafer handling step leads to a realistically expected J_{sc} value of $\sim 31 - 32$ mA/cm², which becomes 32 - 33 mA/cm² after reducing from metal grid coverage to 4%, identical to values expected for high efficiency (> 20% AM0) homoepitaxial GaAs cells. More impressive, however, given the historical limitation on V_{oc} , is that the V_{oc} of the larger area cells are identical and may even be slightly higher than the first series of small area cells, indicating that incorporating more dislocations (but at the same dislocation density) within the active cell region do not impact performance and that scaling to large cell areas should be feasible and is currently under development.

To investigate whether the Ge cap of the virtual substrate generates a photoresponse within our measurements, since this is a well known issue for all III-V/Ge cells, a test setup was assembled to measure the open circuit photovoltage under filtered illumination that passes photons having energies less than the GaAs bandgap. A stack of conventional Si wafers or a thick (3 mm) Si wafer was inserted between the tungsten simulator lamp and the cells under test to filter out photons with wavelengths greater than 1050 nm, and intensities close to that of AM0 conditions were maintained by first comparing V_{oc} values measured under this lamp unfiltered, with calibrated AM0 tests. A light shield was assembled to block any stray light from entering and skewing the experiment. Control tests made on homoepitaxial GaAs cells indicated that no photovoltage was generated

underneath the Si long pass filter stack. Another control experiment made on a bare Ge test cell revealed photovoltages on the order of 110-150 mV, confirming the set up should detect whether a buried Ge cell has been formed as a result of our GaAs/Ge/SiGe/Si process. The cells of figure 5 were tested in this setup, revealing a measured open circuit photovoltage of 0.05 mV, equivalent to the noise floor measured for homoepitaxial GaAs cells and insignificant with respect to the AM0 V_{oc} values or 980 mV. To further verify this, and to ensure that systematic errors such as light leakage were not factors, a Ge wafer was inserted as a long pass filter for both homoepitaxial and GaAs/Ge/SiGe/Si cells since in theory none of the junctions should produce a photovoltage under the Ge window, which blocks out to ~ 1900 nm. The same noise floor result was obtained confirming that the results presented here reflect the photoresponse of a single junction GaAs cell grown on Ge/SiGe/Si substrates having a V_{oc} value of 980 mV, with no activity that can be associated with inadvertent sub-cell formation. This conclusion is consistent with our earlier findings from SIMS investigations that showed negligible interface diffusion of As, Ga and Ge after complete cell growth on Ge/SiGe/Si substrates using the growth process we have described previously.^{10,11} Recently, however, we have fabricated cells with even higher V_{oc} values, reaching up to 1030 mV and AM0 efficiencies as high as 17.1% with fill factors of 0.805 for 0.2 cm x 0.2 cm cells with the same current limitations (grid coverage) as those described here. This result is shown in figure 7, along with a control cell grown on GaAs (the difference in J_{sc} as seen is due to the wafer handling issue discussed above). While impressive, there is evidence of slight Ge junction activity for this particular growth series, which appears to be due to inadvertent p-type doping of the Ge cap under the n-type GaAs base for these runs. Detailed analysis of these cells, the solution to this problem, and a complete description of the methodology to quantify buried junction activity will be presented in a forthcoming publication.¹⁵

5. CONCLUSION

High performance GaAs single junction solar cells have been fabricated on Si substrates using graded SiGe interlayers to achieve a virtual Ge substrate for high quality InGaP/GaAs single junction cell growth using MOCVD. Record high open circuit voltages for single junction GaAs cells on Si have been achieved, with values in excess of 980 mV under AM0 conditions yielding AM0 cell efficiencies of close to 16% for more than 50 cells to date. The high voltages were confirmed to be from a single GaAs junction using filtered light I-V experiments. The breakthrough V_{oc} values are directly related to achieving low TDD values coupled with elimination of other severe

loss mechanisms associated with anti-phase domains. Conservative calculations show that the efficiencies of these first prototype cells are limited by non-fundamental issues in this first set of prototype cells, a large grid obscuration ($>10\%$) and a loss in current output due to wafer handling during the growth sequence. Calculations that account for these losses predict GaAs single junction cell efficiencies between 19-20% (AM0) are already achievable with our current state of material quality. Identical V_{oc} and improved J_{sc} values, the latter by virtue of decreased front metal grid coverage, were obtained for our first generation of larger area cells, indicating that scaling to large area cell fabrication is feasible and imminent. Unlike all prior reports on GaAs/Si cells, cell V_{oc} values for the first time match a simple theory where cell V_{oc} is limited only by depletion region recombination due to the presence of a low dislocation density, and not by other unaccounted for material defects and quality issues that have drastically lowered V_{oc} values in the past. These results also confirm that the record high minority carrier lifetimes and TDD values for GaAs grown on Ge/SiGe/Si reported in earlier publications are reflected in completed solar cells, indicating the robust nature of the GaAs/Ge/SiGe/Si heterostructure.

ACKNOWLEDGEMENTS

The authors thank Dr. Sarah Kurtz of the National Renewable Energy Laboratory for helpful discussions and encouragement concerning buried junction response measurements. This work was supported by NASA grant NCC3-899, NREL grant ACQ-1-30619-06, ARO grant 57000138 and a NASA GSRP fellowship to JAC.

REFERENCES

1. J.A. Carlin, M.K. Hudait, S.A. Ringel, D.M. Wilt, E.B. Clark, C.W. Leitz, M. Currie, T. Langdo and E.A. Fitzgerald, Proc. 28th IEEE Photovolt. Spec. Conf., 1006 (2000).
2. J.C.C. Fan, C.O. Bozler and R.W. McClelland, Proc. 15th IEEE Photovolt. Spec. Conf., 666 (1981).
3. M. Yamaguchi, J. Mater. Res. **6**, 376 (1991).
4. R.K. Ahrenkiel, M.M. Al-Jassim, B. Keyes, D. Dunlavy, K.M. Jones, S.M. Vernon and T.M. Dixon, J. Electrochem. Soc. **137**, 996 (1990).
5. R. Venkatasubramanian, M.L. Timmons, J. B. Posthill, B.M. Keyes and R.K. Ahrenkiel, J. Crystal Growth **107**, 489 (1991).
6. A. Freundlich, M. Lerouz, J.C. Grenet, A. Leycuras, G. Neu and C. Verie, Proc. 8th Euro. Comm. Photovolt. Solar Energy Conf., 1522 (1988).
7. T. Soga, M. Kawai, K. Otsuka, T. Jimbo and M. Umeno, Proc. 2nd World Conf. On Photovoltaic Solar Energy Conversion, 3733 (1998).
8. G. Wang, G.Y. Zhao, T. Soga, T. Jimbo and M. Umeno, Jpn. J. of Appl. Phys. Part 2, **37**, L1280 (1998).
9. R.M. Sieg, J.A. Carlin, J.J. Boeckl, S.A. Ringel, M.T. Currie, S.M. Ting, T.A. Langdo, G. Taraschi, E.A. Fitzgerald and B.M. Keyes, Appl. Phys. Lett. **73**, 3111 (1998).
10. J.A. Carlin, S.A. Ringel, E.A. Fitzgerald, M. Bulsara and B.M. Keyes, Appl. Phys. Lett. **76**, 1884 (2000).
11. J.A. Carlin, S.A. Ringel, E.A. Fitzgerald and M. Bulsara, Prog. Photovolt.: Res. Appl. **8**, 323 (2000).
12. M.T. Currie, S.B. Samavedam, T.A. Langdo, C.W. Leitz and E.A. Fitzgerald, Appl. Phys. Lett. **72**, 1718 (1998).
13. R.M. Sieg, S.A. Ringel, S.M. Ting E.A. Fitzgerald and R.N. Sacks, J. Electron. Mater. **27**, 900 (1998).
14. M. Yamaguchi and C. Amano, J. Appl. Phys. **58**, 3601 (1985).
15. C.L. Andre, M. Gonzalez, A. Khan, M.K. Hudait, D.M. Wilt, P. Jenkins, S.A. Ringel, submitted, 29th IEEE Photovolt. Spec. Conf. (2001).

p+ - GaAs cap (1000Å)
p - InGaP (500Å)
p - GaAs emitter (5000Å)
n - GaAs base (2 μm)
n - InGaP BSF (1000Å)
n - GaAs Buffer (1000Å)
n - Ge/GeSi/Si substrate

Figure 1. Basic pn single junction InGaP/GaAs solar cell structure grown by MOCVD on Ge and Ge/SiGe/Si substrates.

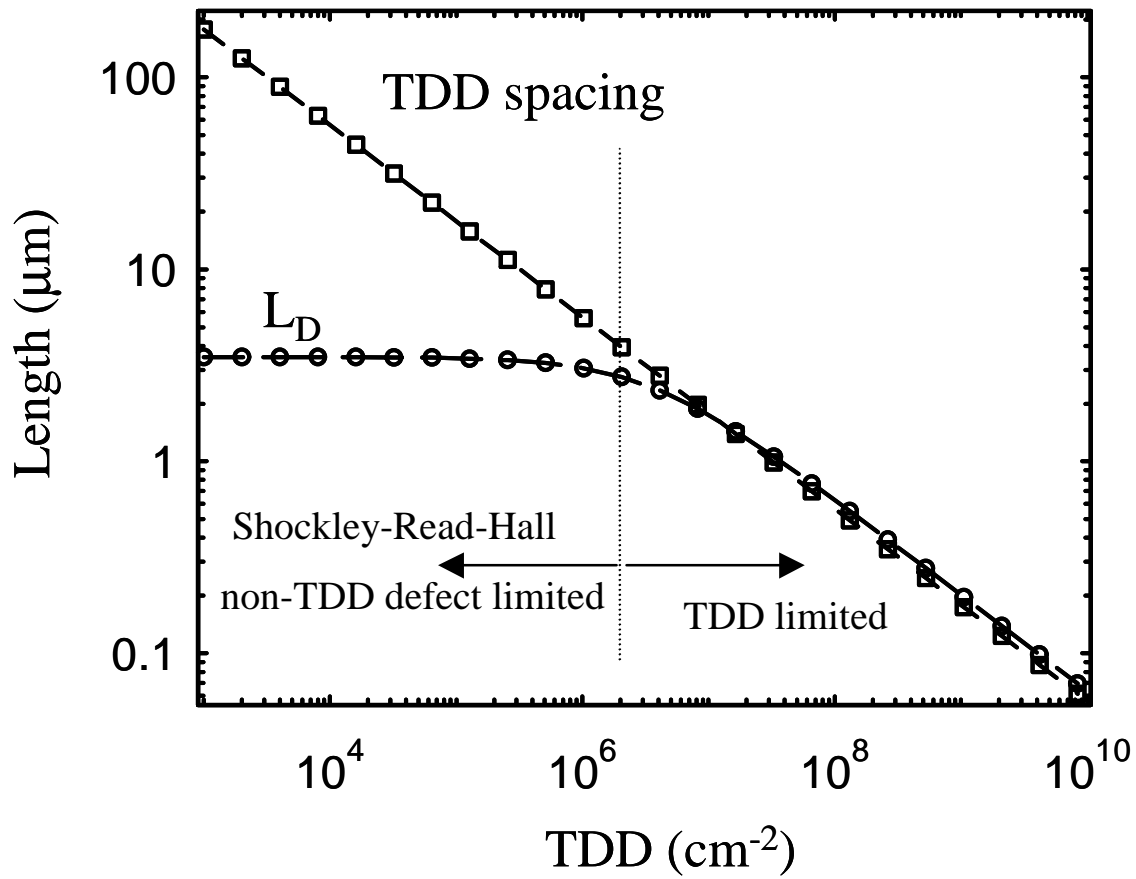


Figure 2. Calculated spacing of parallel threading dislocations as a function of threading dislocation density is shown with calculated minority carrier hole diffusion lengths based on a measured starting (non-dislocation limited) minority carrier lifetime of 20 ns for GaAs grown on Ge wafers, assuming an n-type doping of $1 \times 10^{17} \text{ cm}^{-3}$. TDD and non-TDD limited regions are shown.

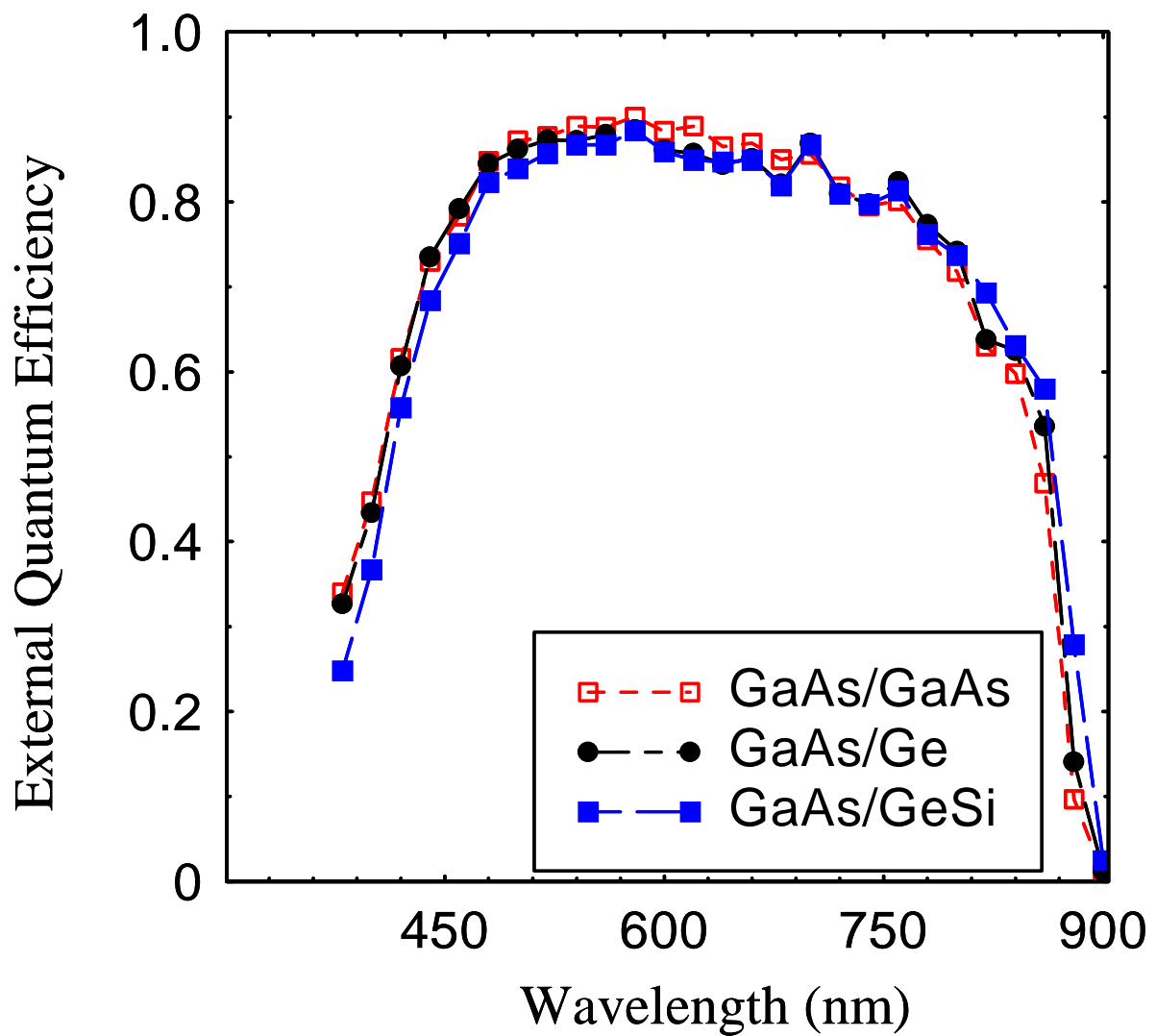


Figure 3. Spectral response measurements made on identical GaAs cell structures grown on GaAs, Ge and Ge/SiGe/Si substrates by MBE, indicating identical collection efficiency independent of substrate and lattice mismatch.

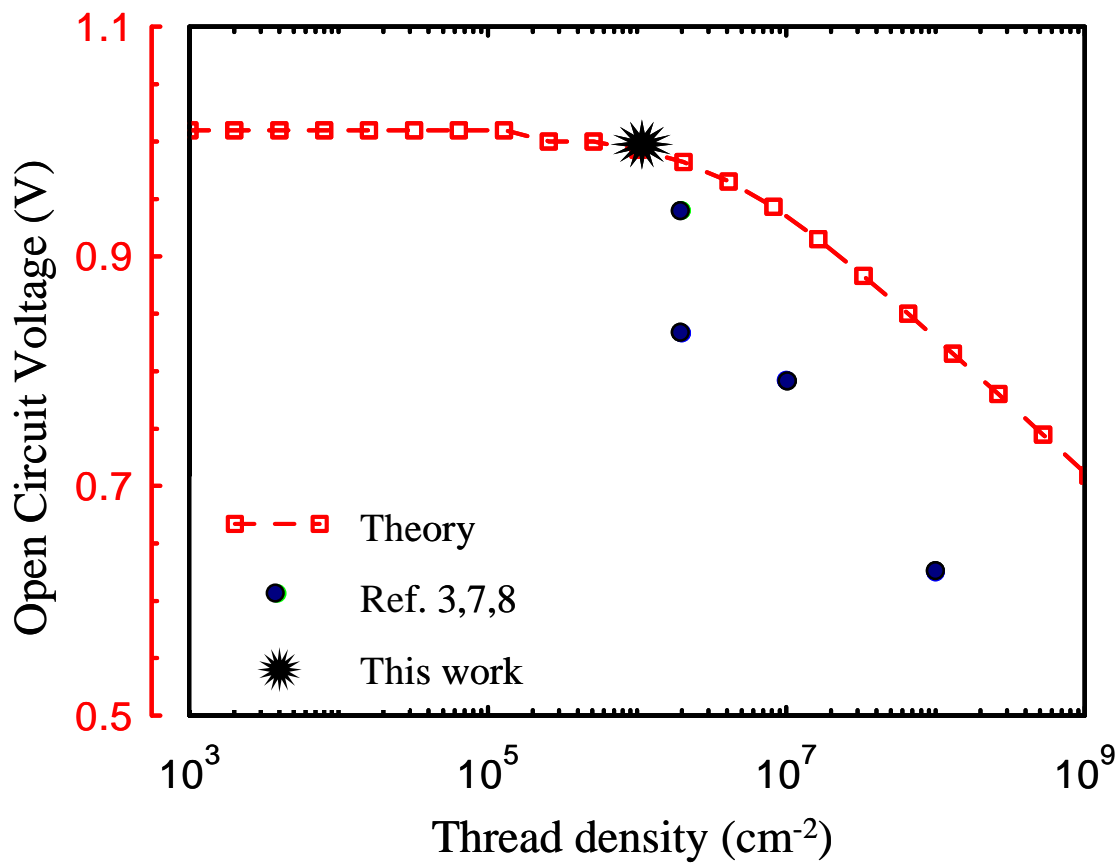


Figure 4. Plot of calculated AM0 V_{oc} values for a single GaAs junction cell as a function of threading dislocation density based on equations (6) and (7). Also shown are measured V_{oc} values from prior work (3, 7, 8) and from cells on Ge/SiGe/Si as reported here. Note the close match between theory and our data, indicating that unaccounted limitations have been resolved.

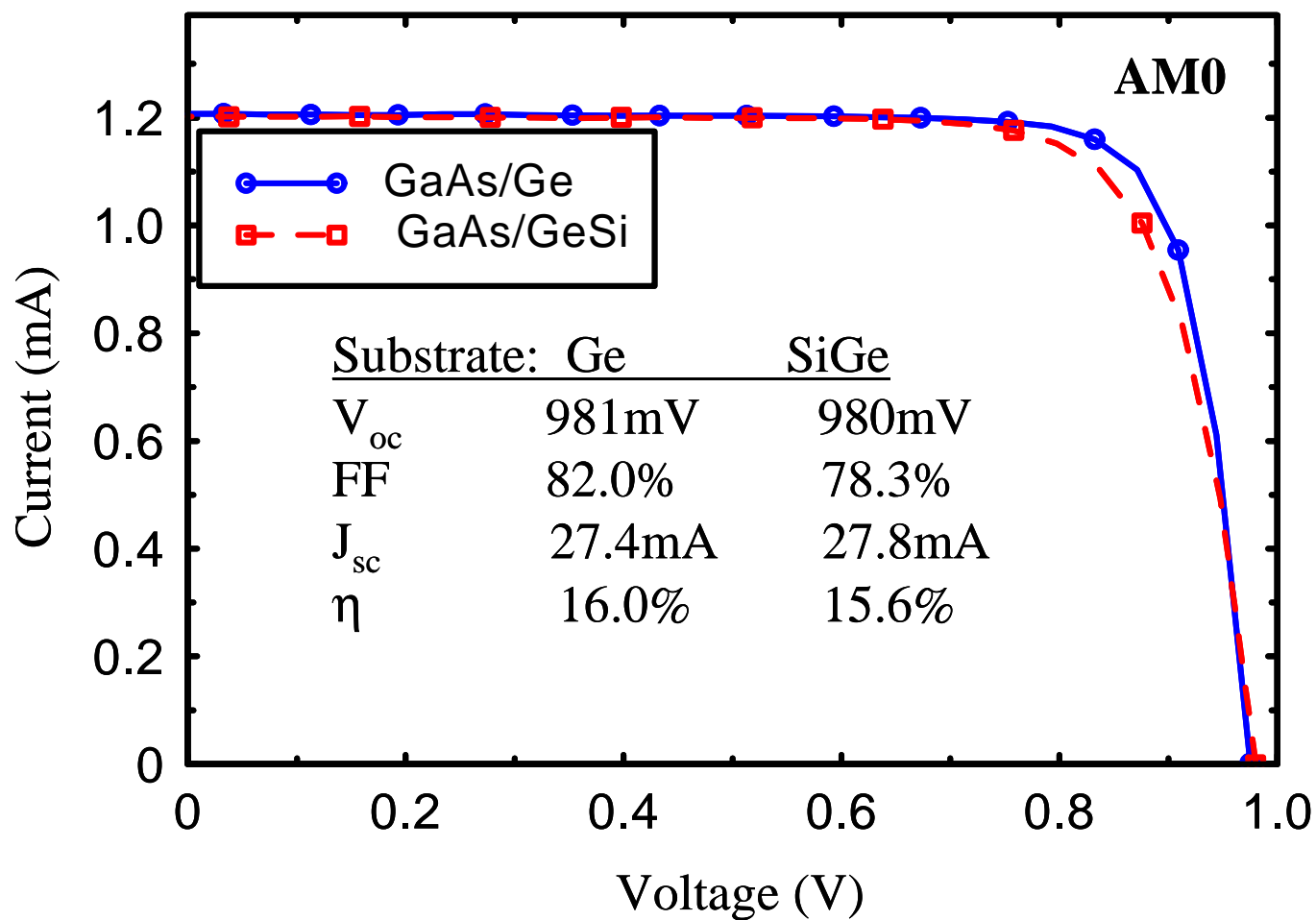


Figure 5. Calibrated AM0 light I-V response for representative 0.2 cm x 0.2 cm single junction InGaP/GaAs cell grown on Ge/SiGe/Si and Ge substrate wafers. Efficiencies are based on total area.

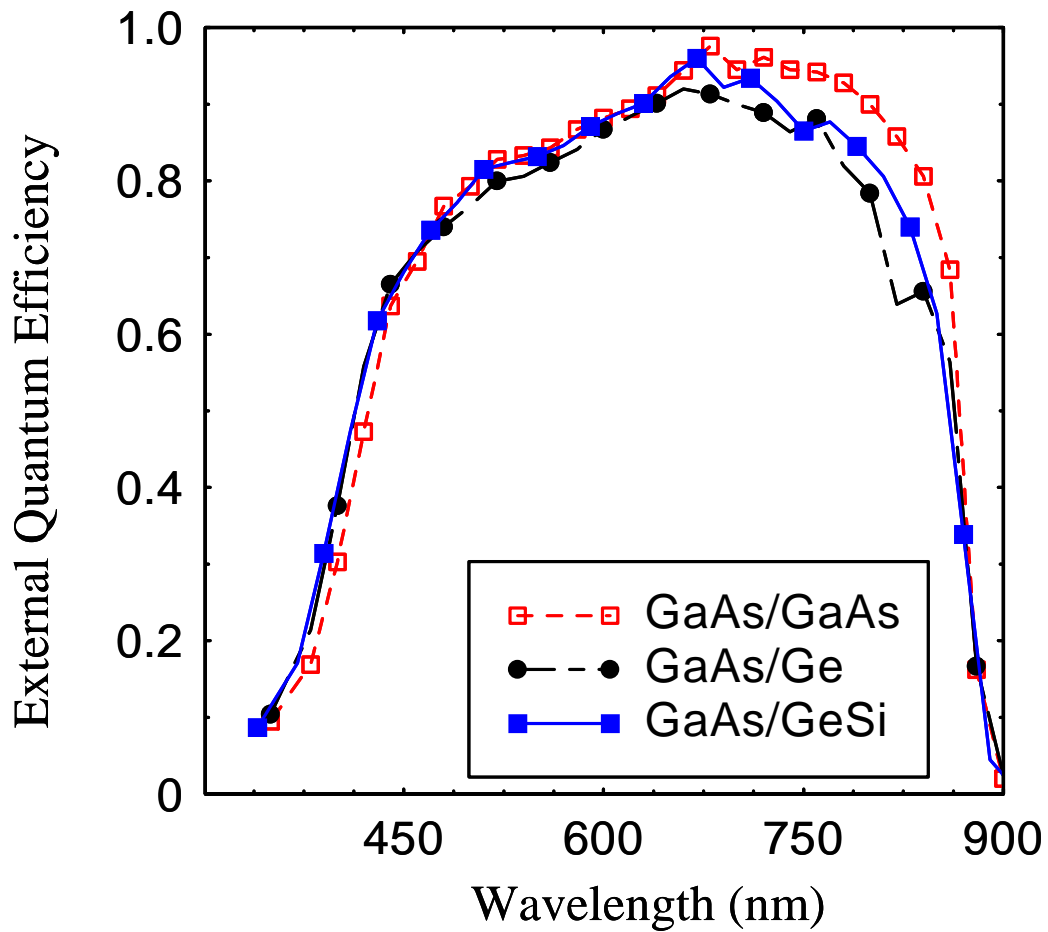


Figure 6. Spectral response results for identical InGaP/GaAs single junction cell structures grown by MOCVD on GaAs, Ge and Ge/SiGe/Si substrates. Similar collection is seen for the cells on Ge and Ge/SiGe/Si and the reduction in quantum efficiency for these cells as compared with the cell on GaAs is due to growth interruption and wafer handling in our developing growth process.

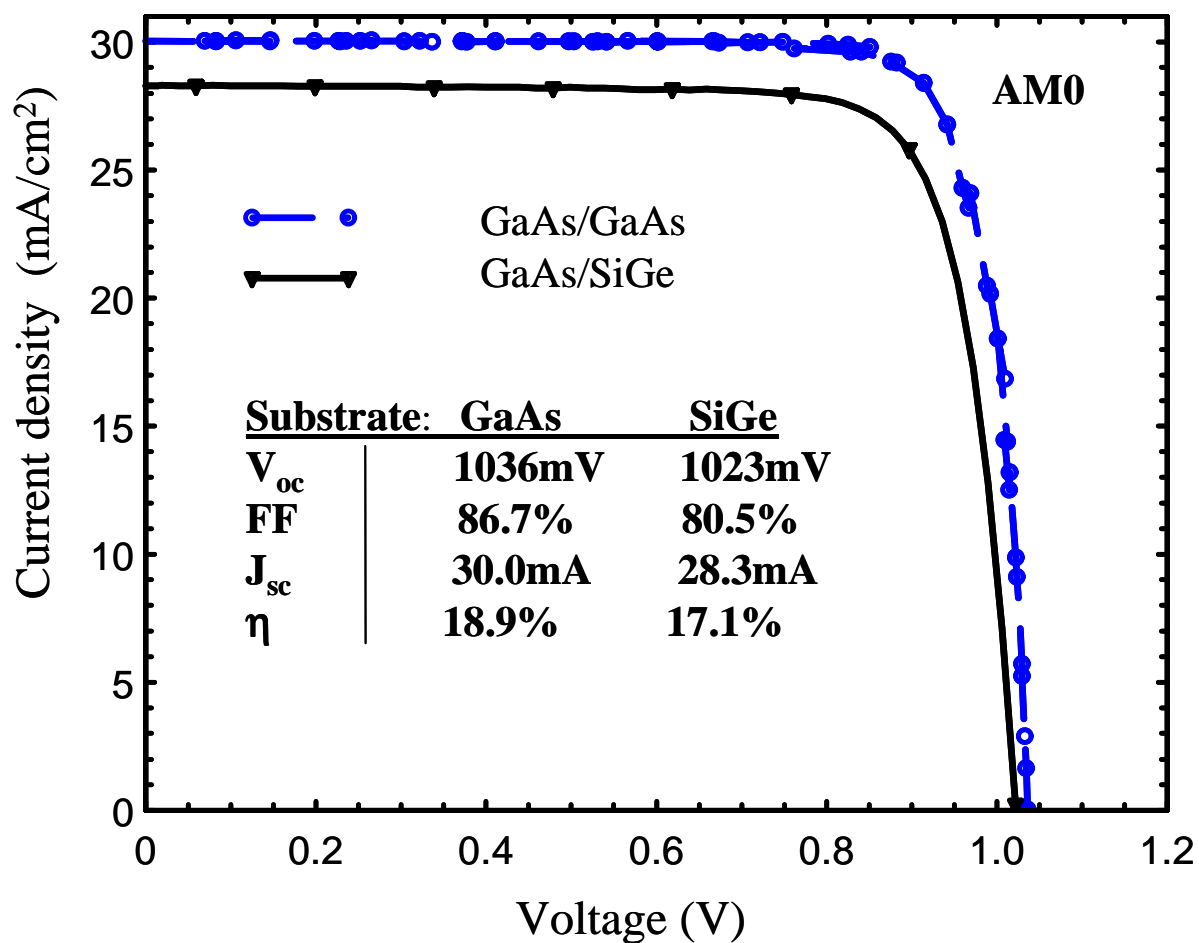


Figure 7. Calibrated AM0 light I-V response for a representative cell of a different series of InGaP/GaAs cell (0.2 cm x 0.2 cm) growths. The lower J_{sc} value is due to the wafer handling step. The high V_{oc} , now in excess of 1 V but still below that of the GaAs/GaAs control, displays evidence of a very small sub-gap photoresponse indicative of an active GaAs/Ge interface that is now under evaluation.

QUANTUM DOT SOLAR CELLS

Ryne P. Raffaele,¹ Stephanie L. Castro,² Aloysius F. Hepp,³ and Sheila G. Bailey³

1) Rochester Institute of Technology, Rochester, NY 14623

2) Ohio Aerospace Institute, Brookpark, OH 44142

3) NASA Glenn Research Center, Cleveland, OH 44135

ABSTRACT

We have been investigating the synthesis of quantum dots of CdSe, CuInS₂, and CuInSe₂ for use in an intermediate bandgap solar cell. We have prepared a variety of quantum dots using the typical organometallic synthesis routes pioneered by Bawendi, et. al., in the early 1990's. However, unlike previous work in this area we have also utilized single-source precursor molecules in the synthesis process. We will present XRD, TEM, SEM and EDS characterization of our initial attempts at fabricating these quantum dots. Investigation of the size distributions of these nanoparticles via laser light scattering and scanning electron microscopy will be presented. Theoretical estimates on appropriate quantum dot composition, size, and inter-dot spacing along with potential scenarios for solar cell fabrication will be discussed.

Introduction

The space photovoltaic community is well aware of the cost benefits to both mission and spacecraft development associated with the continued increase in solar cell efficiency. The developmental efforts in regards to both Si and GaAs based cells have resulted in nearly eliminating the efficiency differences between actual devices and theoretical estimates. Over the past decade much of the cell efficiency improvements have resulted from the move towards multi-junction devices. However, as researchers continue to push the envelope they are looking towards new approaches, such as the use of nanotechnology, in improving device efficiencies.

Theoretical results of Luque and Marti have shown that a photovoltaic device with an intermediate band of states resulting from the introduction of quantum dots can exceed the Shockley and Queisser model efficiency of not only a single junction but also a tandem cell device.¹ A quantum dot is a granule of a semiconductor material whose size is on the nanometer scale. These nanocrystallites behave essentially as a 3-dimensional potential well for electrons (i.e., the quantum mechanical "particle in a box"). By introducing a single sized dot into an ordered array within the intrinsic region of a p-i-n solar cell (see Figure 1), Luque and Marti calculated a theoretical efficiency of 63%. Quantum dots have already been used successfully to improve the performance of devices such as lasers, light emitting diodes, and photodetectors.

The idea of improving photovoltaic performance through the introduction of electronic states at or near a photovoltaic junction was proposed as far back as 1960 by Wolf.² However, Shockley and Queisser argued against this idea citing the problem of recombination losses that would make the approach impractical.³ This recombination problem has hindered other quantum mechanical approaches to improving efficiencies,

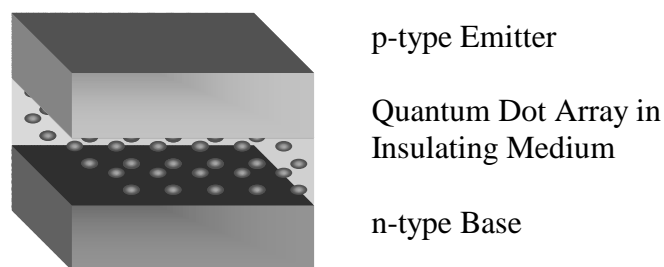


Figure 1. Intermediate Bandgap Solar Cell

such as through the use of multiple quantum well devices. Barnham and Duggan showed that a photovoltaic device incorporating multiple quantum wells theoretically could achieve efficiencies of 40%.⁴ In this model the electronic states in the potential “wells” are “quantized” and therefore have discrete energy levels. The overlap of the quantum mechanical states from well-to-well results in mini-band levels that will depend on the width of the wells. This dependence of the energy levels to well width can then be used to “tune” the device to the solar spectrum. Unfortunately, the problems associated with growing defect-free structures of this type have prohibited the anticipated efficiency improvements.

It was theoretically shown that a deep level electronic state near the junction could be used to exceed the theoretical single junction efficiency.⁵ A claim of a 35% efficient solar cell owing to the impurity photovoltaic effect was made. This claim was later retracted after the comments published by Luque, Werner, and others. However, it has been shown that the impurity photovoltaic effect can indeed improve efficiencies.⁶ This effect was demonstrated with the use of deep indium defects in a Si-based device, although the improvement was only from 0.3 to 0.6 %. It has also been shown that a quantum efficiency of greater than 1 can be achieved by the introduction of impurities, creating an inverse Auger mechanism that has a theoretical efficiency limit of 43%.⁷ In addition to the intermediate band solar cells there have been other approaches to the inclusion of quantum dots that can also aid in the improvement of device efficiency.⁸

The basic principle behind the efficiency increases offered by a quantum dot intermediate band solar cell is that the discrete states that result from the inclusion of the dots allow for absorption of sub-bandgap energies. The reason that this approach can exceed that of an ordinary dual-junction cell is that when the current is extracted it is limited by the host bandgap and not the individual photon energies. In a dual-junction solar cell the current must be “matched” between the two junctions. This means that the same amount of current must be passed through both junctions, and therefore the overall device efficiency is limited by the current generating ability of the weaker of the two junctions. In addition, if a dual-junction or other multi-junction device is grown monolithically, in which the junctions are connected in series, it is required that there be tunnel junctions grown in between the various active regions. Problems with lattice mismatch and the increased number of interfaces (and therefore interfacial defects) are impediments to this approach in photovoltaic development. Although, tremendous achievements have been made in developing multijunction solar cells, this problem will be compounded as we continue to try and increase the number of junctions. The

problems with lattice mismatch and interfacial defects are the same problems that have plagued the development in multi-quantum well structures as well.

Much like the energy dependence with multiple quantum wells, the energy states of the quantum dot are inversely proportional to their size. The ground state absorption energy of a quantum dot is determined by

$$\hbar\omega = E_g + \frac{\hbar^2}{2m_e^* r^2} \pi^2, \quad (1)$$

where E_g is the bulk semiconductor bandgap, \hbar is planck's constant, m_e^* is the electron effective mass, and r is the quantum dot radius. If quantum dots are produced in an ordered array within an insulating medium, the wavefunctions associated with the discrete electronic states of the quantum dots will overlap creating "mini-bands" within the insulating region. The lowest empty mini-band energy level should be roughly 1/3 of the bandgap energy of the semiconductor (of the n and p-type regions) above the valence band energy to maximize the device efficiency (see Figure 2). For a Si based device ($E_g = 1.12$ eV and $\chi = 4.05$ eV), an array of dots whose sizes will yield an electron affinity of ~ 4.8 eV is required to maximize the efficiency. Quantum dot candidates for Si would therefore include such materials as CuInSe₂ and CuInS₂.

If we assume dot radii in the range of 2.0 to 10 nm that is necessary for strong quantum confinement (i.e., small as compared to the exciton Bohr radius), the dots will need to be spaced at over twice their radii or at approximately 4.0 to 20.0 nm. This will provide a density of states for the intermediate band to be on the order of 10^{17} to 10^{18} cm⁻³. This range is typical for most solar cell materials and will provide the cell with a strong absorption coefficient. The width of the mini-bands under these conditions is well below the point at which stimulated emission becomes a problem.¹

To date there has been very little in the way of results on quantum dot photovoltaic devices. The photovoltaic effect has been measured for films produced with CdSe quantum dots.⁹⁻¹⁰ In addition, CdSe nanocrystalline rods have been used to make a photovoltaic device with 2% efficiencies.¹¹ There has also been some work on GaAs quantum dot solar cells.¹²⁻¹³ A theoretical efficiency improvement under 1 sun AM 1.5 conditions of 19.5 % to 25 % has been calculated with the inclusion of quantum dots.

An intermediate band solar cell requires that the quantum dots be introduced into a regular array with the individual dots separated by an insulating medium. The ability to clad semiconducting quantum dots with a wide bandgap insulator has already been demonstrated.¹⁴⁻¹⁵ In addition, several methods for arraying quantum dots have also been developed.¹⁶⁻¹⁹

At the Glenn Research Center, we have been investigating different methods of producing quantum dots that would be suitable candidates for a quantum dot photovoltaic solar cell. This is prompted not only by the fact that by improving device efficiency we can increase the specific power of space solar arrays but also by the fact that quantum dots may also have some definite thermal and radiation hardness advantages as well.²⁰

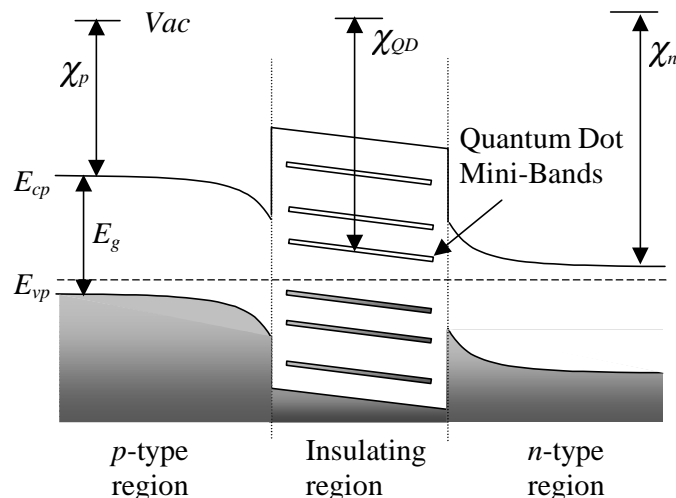


Figure 2. Idealized energy band diagram of an intermediate band solar cell.

Experimental

Traditional organometallic chemical bath synthesis was used to produce CdSe quantum dots in accordance with the method developed by Murray and Bawendi.²¹ In this method trioctylphosphine oxide (TOPO) is heated under an inert atmosphere to between 300 and 350 C. A mixture of the desired organometallic precursors are diluted in trioctylphosphine (TOP) and drawn into a syringe. The contents of the syringe are injected into the hot TOPO with vigorous stirring (see Figure 3a). The temperature of the bath will decrease due to the injection of the cooler precursor. The original temperature of the bath is referred to as the “injection temperature” and the temperature of the bath as the nucleation occurs is referred to as the “growth temperature.” The solution changes from colorless to yellow, then orange and red/brown as the quantum dots increase in size. Aliquots of the solution can be removed during the growth period to monitor the size by UV-vis spectroscopy. When the desired size is reached, the heat is removed from the flask. Upon cooling, methanol is added to remove excess reagents and solvents, yielding a powder of TOPO-capped nanocrystals.

A series of CdSe nanoparticles were prepared using various injection and growth temperatures and times (see Table I). The injection temperature is the temperature of the TOPO before the organometallic precursors are added. Once the precursors are added there is an immediate decrease in the bath temperature. The growth temperature is the temperature at which the bath is held at during the actual growth phase of the dots. A combination of all three parameters will determine the ultimate size of the dot.

In addition to the synthesis of CdSe quantum dots, a similar procedure was used to produce a series of quantum dots of CuInS₂ (see Table II). The primary difference however was in the use of a single-source precursor molecule instead of separate organometallic precursors (see Figure 3b). These are the same single-source molecules that were developed for use in the chemical vapor deposition of thin-film solar cells.²²

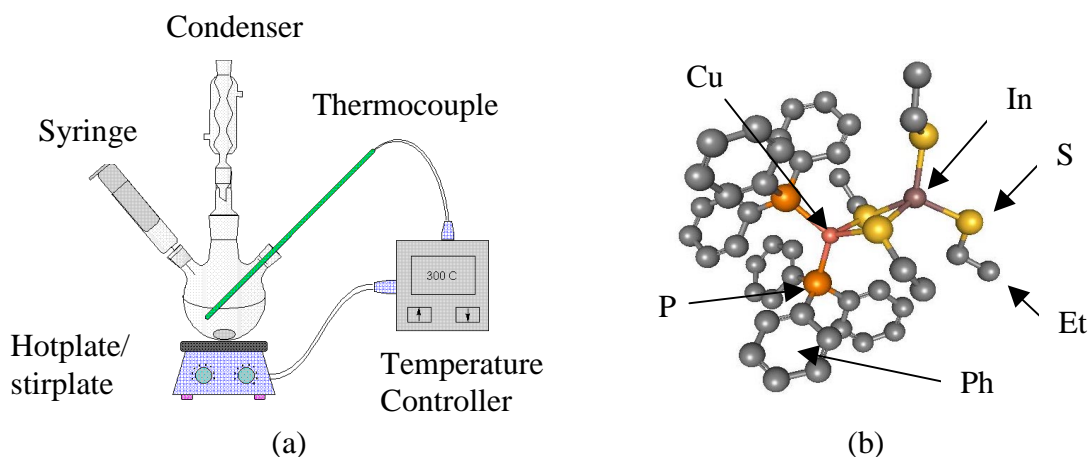


Figure 3. a) Apparatus for quantum dot chemical bath synthesis; b) Single-source CuInS₂ molecule.

Sample Emission Color	Injection Temperature (°C)	Growth Temperature (°C)	Growth Time (min.)
Green	200	125	30
Yellow	245	200	10
Orange	275	190	30
Red	300	250	60

Table I. CdSe quantum dot synthesis conditions.

CuInS ₂ Quantum Dots	Injection Temperature (°C)	Growth Temperature (°C)	Growth Time (min.)
A	160	160	360
B	300	300	3
C	237	237	15

Table II. CuInS₂ quantum dot synthesis conditions.

Size quantization in optoelectronic spectrum of the CdSe products was investigated by suspending them in hexanes and performing UV-vis spectroscopy. The CuInS₂ product was dried and characterized using powder x-ray diffractometry (XRD) and scanning electron microscopy (SEM). UV-vis spectroscopy was performed on the CuInS₂ product suspended in toluene. The particle size distribution was also determined using light scattering measurements.

Results

The CdSe product did exhibit size quantization effects such as fluorescence when illuminated by UV radiation. The change in nanoparticle size is demonstrated by a change in the fluorescent emission wavelength or apparent color (see Figure 4). The suspensions are unfortunately poly-disperse as evidenced by the lack of distinct first and second order peaks in the absorbance versus wavelength spectrum shown in Figure 5. Estimating the ground state peak in Figure 5 at approximately 624 nm yields a particle radius of 3.1 nm using Equation 1 and the bulk electron effective mass of CdSe of 0.13.²³ This is in good agreement with previous experimental studies on CdSe quantum dot size versus optical absorption.²¹



Figure 4. Photograph of luminescence change with quantum dot size indicated by change in color of the solution. The dot size increases from left to right.

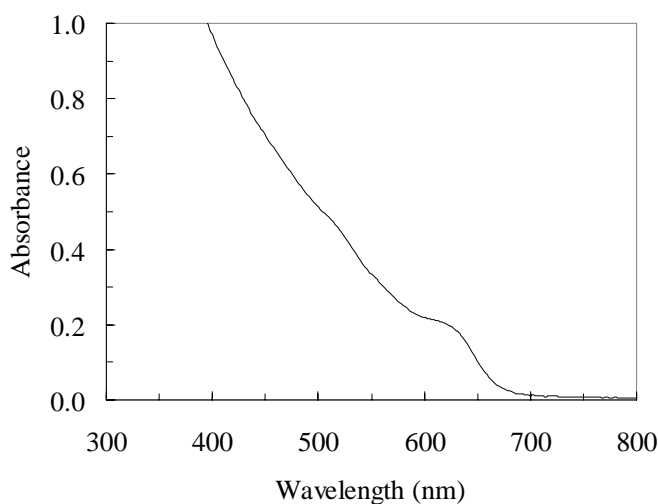


Figure 5. The absorbance versus wavelength for a CdSe nanoparticle suspension in hexanes. The small peak at 624 nm corresponds to the ground state transition and corresponds to a particle radius of 3.1 nm.

The product that resulted from the use of the Cu-In-S single source precursor molecules was found to have main Bragg peaks that are consistent with the characteristic chalcopyrite crystal structure of CuInS_2 (see Figure 6). Field emission scanning electron microscopy was used to determine that the CuInS_2 product was actually made up of agglomerates of nanoscale spheres (see Figure 7).

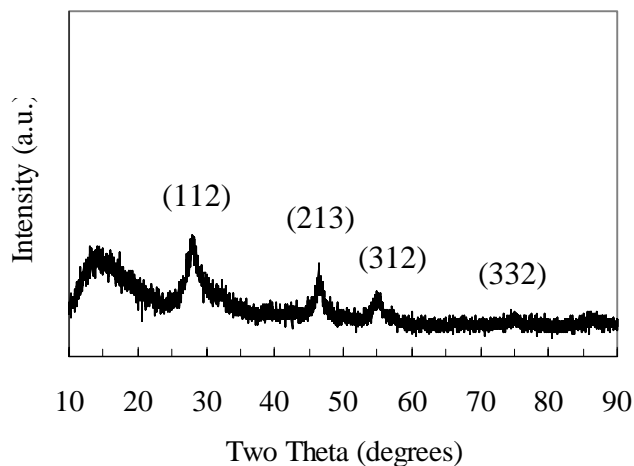


Figure 6. Powder x-ray diffraction pattern for Cu-In-S product. The plane assignments correspond to the chalcopyrite structure of CuInS_2 . (The broad peak at low angles is due to the glass substrate).

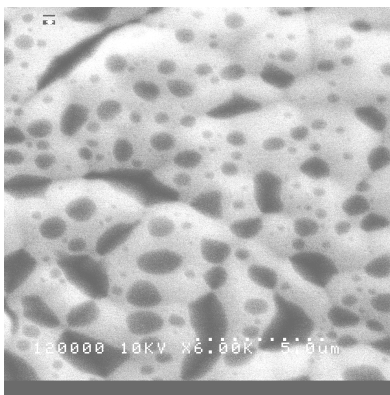


Figure 7. SEM micrograph of CuInS_2 nanoparticles agglomerated that were dispersed using methanol onto a polished silicon wafer.

The CuInS_2 product did demonstrate the expected size quantization in its optoelectronic spectrum as evidenced by absorbance changes with synthesis time. Figure 8 shows percent transmission versus wavelength for a series of CuInS_2 nanoparticles. The shift in the ground state absorption is consistent with the anticipated increase in quantum dot radius. Laser light scattering experiments showed that the samples were extremely poly-disperse with average particle radii that ranged from 13.4 nm to 30 nm.

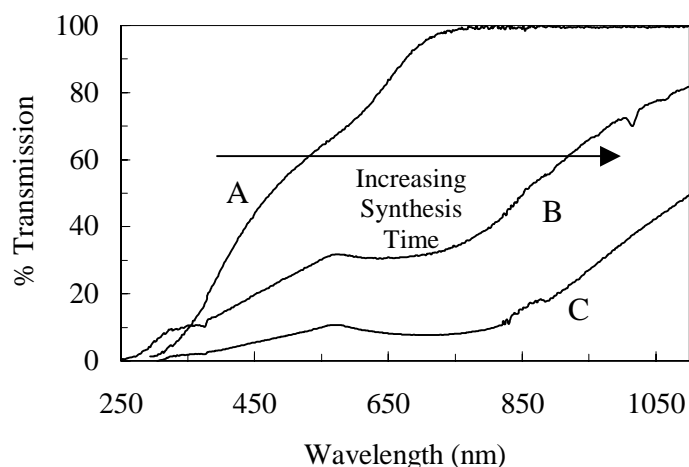


Figure 8. Percent transmission versus wavelength shows the change in apparent CuInS_2 bandgap versus synthesis time (or particle size). (Labels correspond to Table II).

Conclusions

A number of theoretical results have provided sufficient motivation to justify NASA's exploration of the development of quantum dot solar cells. There are currently several methods that exist to synthesize a variety of semiconductor quantum dots that are candidates for intermediate band solar cells. The combination of single-source precursors and traditional organometallic synthesis is a viable method for producing CIS quantum dots.

Acknowledgements

NASA Glenn Research Center Strategic Research Fund, NASA Cooperative Agreements NCC3-710, NCC3-563, Rochester Institute of Technology, Ohio Aerospace Institute, Kal Banger and Jon Cowen of Cleveland State University, and Don Henderson of Fisk University.

References

- [1] A. Luque and A. Marti, *Phys. Rev Lett.* **78**, 5014 (1997).
- [2] M. Wolf, *Proc. of IRE* **48**, 1246 (1960).
- [3] W. Shockley and H. Queisser, *J. Appl. Phys.* **32**, 510 (1961).
- [4] K. Barnham and G. Duggan, *J. Appl. Phys.* **67**, 3490 (1990).
- [5] M.J. Keevers and M.A. Green, *J. Appl Phys.* **75**, 4022 (1994).
- [6] M.J. Keevers and M.A. Green, *J. Appl. Phys.*, **78**, 8, 1994.
- [7] J. Werner, et. Al. *Phys. Rev. Lett.* **72**, 3851 (1994).
- [8] K. Barnham, et. al., *Appl. Phys. Lett.* **76**, 1197 (2000).
- [9] L. Kronik, et. al., *J. Electrochem. Soc.* **145**, 1748 (1998).
- [10] D.S. Ginger and N.C. Greenham, *J. Appl. Phys.* **87**, 1361 (2000).
- [11] W.U. Huynh, X. Peng, and A.P. Alivisatos, *Adv. Mat.* **11**, 923 (1999).

- [12] V. Aroutiounian, et. al., *J. Appl. Phys.* **89**, 2268 (2001).
- [13] D. Pan, E. Towe, and S. Kennerly, *Appl Phys. Lett.* **76**, 3301 (2000).
- [14] X. Peng, et. al., *J. Am. Chem. Soc.* **119**, 7019 (1997).
- [15] B.O. Dabbousi, *J. Phys. Chem. B* **101**, 9463 (1997).
- [16] T. Ahmadi, et. al., *Science* **272**, 1924 (1996).
- [17] X. Peng, et. al., *Nature* **404**, 59 (2000).
- [18] U. Woggan, *Optical Properties of Semiconductor Quantum Dots*, (Springer, Berlin, 1997).
- [19] D. Bimberg, et. al., *Quantum Dot Heterostructures*, (John Wiley & Sons, London, 1999).
- [20] B.G. Rax, C.I. Lee, A.H. Johnston, and C.E. Barnes, *IEEE Trans. Nucl. Sci.*, **43**, 3167 (1996).
- [21] C.B. Murray, D.J. Norris, and M.G. Bawendi, *J. Am. Chem. Soc.*, **115**, 8706 (1993).
- [22] J.D. Harris, D.G. Hehemann, J.E. Cowen, A.F. Hepp, R.P. Raffaele, J.A. Hollingsworth, 28th *IEEE Photovoltaic Specialists Conference*, September 17-22, Anchorage, Alaska (2000).
- [23]. S.M. Sze, "Physics of Semiconductor Devices," 2nd Edition (John Wiley & Sons, New York, 1981).

MISSION APPLICABILITY ASSESSMENT OF INTEGRATED POWER COMPONENTS AND SYSTEMS

R.P. Raffaele,¹ A.F. Hepp,² G.A. Landis,² and D.J. Hoffman²

1) Rochester Institute of Technology, Rochester, NY 14623

2) NASA Glenn Research Center, Cleveland, OH 44135

ABSTRACT

The need for smaller lightweight autonomous power systems has recently increased with the increasing focus on micro- and nanosatellites. Small area high-efficiency thin film batteries and solar cells are an attractive choice for such applications. The NASA Glenn Research Center, Johns Hopkins Applied Physics Laboratory, Lithium Power Technologies, MicroSat Systems, and others, have been working on the development of autonomous monolithic packages combining these elements or what are called integrated power supplies (IPS). These supplies can be combined with individual satellite components and are capable of providing continuous power even under intermittent illumination associated with a spinning or Earth orbiting satellite. This paper discusses the space mission applicability, benefits, and current development efforts associated with integrated power supply components and systems. The characteristics and several mission concepts for an IPS that combines thin-film photovoltaic power generation with thin-film lithium ion energy storage are described. Based on this preliminary assessment, it is concluded that the most likely and beneficial application of an IPS will be for small “nanosatellites” or in specialized applications serving as a decentralized or as a distributed power source or uninterruptible power supply.

INTRODUCTION

The development of small satellites has generated a need for smaller lightweight power systems.¹ These systems will most likely combine some devices for power generation and some for storage. The combination of high specific power solar cells and rechargeable thin film batteries is one attractive possibility for missions that receive intermittent solar illumination such as a small satellite in low-earth orbit (LEO). The integration of these two elements together with associated power management components is referred to as an integrated power supply (IPS).

The physical characteristics of an IPS can differ dramatically, and to a large extent will be governed by the specific application. Regardless of the configuration, every IPS will include devices for power generation, energy storage and power conditioning. Researchers at the Johns Hopkins Applied Physics Lab have designed and built an IPS that combines an array of high efficiency crystalline solar cells with high specific energy lithium batteries. In contrast, the IPS that were designed by Microsat Systems (ITN Energy Systems) combined thin film CuInGaSe₂ cells with thin film solid state rechargeable lithium batteries. Lithium Power Technologies have also developed a thin film IPS by combining a-Si thin film PV arrays with thin film polymer rechargeable lithium batteries. So far, the IPS systems created at NASA Glenn have used a variety of PV arrays.² We have tested IPS that utilized thin film CuInGaSe₂ and α -Si arrays as well as GaAs monolithically interconnected modules (MIM). The energy storage devices have

been various types of both lithium and lithium ion batteries (i.e., solid state, polymer, coin cells, thin film cells). The common feature of the devices developed at GRC thus far is that they have been designed to meet the needs of microelectronic devices in space. Most IPS systems have focused on the use of photovoltaic (PV) power generation and Li-ion battery energy storage. However, one can easily envision the use of other energy generation sources (e.g., alpha or beta voltaics, micro fuel cells, etc.) and other storage devices (e.g., super-capacitors, MEM flywheels, etc.) based upon energy needs and mission requirements.

Many of the IPS systems developed to date and those planned for the future include thin-film photovoltaic (TFPV) power generation. TFPV has been under development for some time. TFPV sample cells and panels have flown in space, but a full TFPV solar array has not yet been built. The principle benefits of TFPV arrays include very high mass specific power (W/kg), radiation tolerance and good stow-ability. The mission benefits of TFPV solar arrays have been identified, and may soon be realized once full-scale TFPV arrays are constructed and space qualified.³

In comparison to TFPV power generation, thin-film energy storage (TFES) is a relatively recent development. Very small thin-film lithium-ion batteries have been developed and tested in the lab for use in multi-chip modules (MCMs).⁴ With a typical operating range between 3.0 V and 4.2 V, the useable capacity of these initial TFES batteries is very small, ranging from 0.2 to 10 mAh/cm². However, specific energies as high as 200 Whr/kg have already been achieved with batteries that are capable of cycling 60,000 times.

Because of the similarity in the materials and processes that go into TFPV and TFES devices, it is practical to consider combination of the two. It is feasible to combine a TFPV cell on a Kapton™ substrate with a Li-ion thin-film battery sandwiched in Kapton™. With the further addition of very small power conditioning and control electronics, an Integrated Power Source (IPS) is possible.

An IPS is unique in that it combines three formerly separate functions of an electrical power system into an integrated package. Taking advantage of this feature, and it applying it locally, so to speak, results in a decentralized or distributed power bus. The use of a local IPS could allow distant portions of a satellite or space probe to be operated without a physical wire to provide power. Wiring can be 10% of the mass of a spacecraft in some cases. Removal of the physical wires would considerably simplify design. The command and control could use infrared or microwave remote control (similar to "wireless internet" control). Potential applications include:

- Actuators for deformable mirrors for large (15-25 meter) space telescopes
- Interferometric sensors
- Wireless remote actuators for spacecraft attitude control
- Gossamer spacecraft controls
- GPS attitude sensors
- Dipole array antenna element

A decentralized power bus concept applied to discrete components, leads to the notion of an IPS as an uninterruptible power source, or UPS, to increase the reliability of essential spacecraft functions. Two specific functions that could benefit from this are computer memory and spacecraft communications.

CMOS ("volatile") memory is faster than non-volatile memory and has higher density and lower mass. However, if power is not maintained on the memory, it is erased. The amount of

power required for this is extremely small, and a tiny IPS could be incorporated to make certain that even in a low-power condition, the memory remains charged.

Loss of attitude control on many satellites is a fatal error. This can occur when solar arrays lose pointing and batteries discharge. When battery voltage drops so low that the spacecraft central processing unit (CPU) and radio receiver lose power, there is no way to regain control of the satellite. An IPS could be used as a back-up power system, designed to provide enough power to run a low bit-rate omni-directional receiver and the spacecraft CPU only when the main power system failed.

IPS CHARACTERISTICS/DESCRIPTION

The physical characteristics of an IPS can differ dramatically, and to a large extent will be governed by the specific application. Regardless of the configuration, every IPS will include devices for power generation, energy storage and power conditioning. So far, TFES and IPS systems created at NASA Glenn have been developed to meet the needs of microelectronic devices in space.

The power requirements placed on an IPS will play a large role in determining the ultimate size of the device. The voltage of the PV portion of the device is determined by the nature of the p-n junction, or, in other words, the materials used. In the case of a GaAs homo-junction device this will be around 1.0 V. For thin-film a-Si or CuInSe₂ (CIS) PV, the voltage generated will be somewhat less (0.4-0.8 V).⁵ However, through the use of monolithically interconnected modules (MIM), many junctions can be put together in series to increase the voltage. Unfortunately, the available current will always be a function of the active surface area of the device. The current density presently available from a thin-film CIS cell is rather small due to its low photovoltaic conversion efficiency, although the goal of NASA Glenn's in-house TFPV program is >20% efficiency via a dual junction thin-film PV cell like the one illustrated in figure 4.

The voltage of a Li-ion battery is based on its chemistry and is primarily determined by the material used in its cathode. A vanadium pentoxide or manganese oxide battery will have an open circuit voltage of 3.0 V, whereas a nickel cobalt cell will be 4.2 V.⁶

In a way similar to PV cells, Li battery cells can be connected in series configurations to produce different voltages. However, the amount of energy that can be stored in a cell, its capacity, is determined primarily by its volume. Thus for a thin-film Li-ion battery, the capacity will be determined in the same way the current capability of the PV cell is determined - by the area of the device. The size also impacts the rate at which a battery can be charged and discharged (i.e., the smaller the battery the smaller the charging and discharging currents it can handle).

Ideally, in order to minimize the control electronics associated with an IPS, the photovoltaic array is designed such that its output voltage matches the voltage needs of the battery and its current output is sufficient to charge the battery while simultaneously providing power to the load. The precise sizing of the array and battery will also be dependent on the anticipated illumination scheme. For example, in a typical 90-minute low-earth orbit (LEO) period, the battery will have to support the electrical load for 35 minutes of eclipse. During the 55 minute insolation (daylight) period, the solar array has to provide load power while fully re-charging the battery.⁴

The matching of the solar array and batteries for these small power systems is essential as the parasitic power loss in a conventional charge controller normally used in a larger power system actually exceeds the output of a small IPS. Once the PV and battery are matched, the only

additional components required are a blocking diode to prevent the battery from discharging through the PV array during eclipse.

The Li-ion batteries play a large role in determining the temperature regime in which these systems are suitable. Li-ion cells will deliver a sizeable fraction (i.e. 80%) of their capacity at temperatures as low as -20°C .⁷ Below such a temperature they do not perform well. However, they do not exhibit permanent damage if they are cycled between larger temperatures regimes (i.e., plus or minus 80°C).⁸ The high temperature performance is much less of an issue with thin-film Li-ion batteries as they have been shown to operate well at temperatures up to 60°C .⁹ Thermal control issues associated with IPS applications are discussed later.

POTENTIAL BENEFITS

As one might anticipate, the primary benefit resulting from the combination of two extremely light weight devices providing distinct functions is a less complex, reduced volume, light weight system providing an integrated function. A thin-film IPS could serve as the main power system on a spacecraft or satellite. Scaling up the manufacturing methods should allow an IPS to deliver the highest specific power and energy for the lowest cost. Reducing power system mass, which is typically 20% to 30% spacecraft dry mass, will help reduce launch mass, perhaps enough to enable a mission concept previously too heavy to fly, or allow the use of a smaller, cheaper launch vehicle. Incorporating energy storage with power generation reduces volume formerly required by traditionally separately located chemical batteries, freeing up valuable space for other systems or an increased payload.

The main benefit of using an IPS as a distributed power system is a reduction in spacecraft complexity, especially with respect to power distribution wiring, simplifying spacecraft integration. In this instance, numerous IPSs are used to provide continuous power to loads, either spacecraft bus components or payload instruments, *in situ*, wherever the component is located. Of course this does require components to be located such that they have view of the sun for at least some portion of the orbit. The use of IPSs as power sources for MCM sensors that may be placed wherever they are needed in a “postage stamp” fashion could have tremendous benefit in future nanosatellite design.

STARSHINE 3

The first in-space demonstration of an IPS, although with a GaAs monolithically integrated module (MIM) solar cell and a Li-ion thick “coin” battery, should occur on launch of the Starshine-3 satellite in late summer 2001.¹⁰

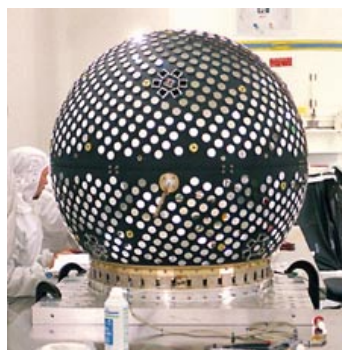


Figure 1. Starshine 3.

The Starshine 3 satellite is 1.0 m in diameter and has a mass of 88 kg. Its surface is covered with 1500 student polished mirrors, 31 laser retroreflectors, 48 - 2 cm x 2 cm triple junction solar cells manufactured by Emcore, and our 5 integrated power supplies. It is scheduled for launch on a Lockheed Martin Athena I rocket from Kodiak Alaska on September 29, 2001. It will be deployed by a Lightband system at a 67 ° inclination with a fixed rotational velocity of 5 ° per second in a low earth orbit (LEO) with a period of 92 minutes. The data will be downloaded using a transmitter operating at a frequency of 145.825 MHz.^{11, 12}

The IPS we have developed combines a 7 junction - 1 cm² monolithically interconnected GaAs module (MIM) (see Figures 2 and 3) with a lithium ion battery. Ideally, the output of the high-voltage small area MIM would be designed to match the open circuit voltage of the lithium ion battery.² The MIM we used in this case has more than enough voltage and current to both charge a Li ion battery with a CoO₂-based cathode (e.g., $V_{oc} = 4.2$ V)⁶ and power an equivalent load.

The load for this demonstration is a small temperature sensor. These sensors are strategically placed about the spacecraft to monitor the temperatures of the critical components (e.g., batteries, solar cells, electronic boards), both inside and outside of the satellite.

Three prototype IPS were developed. The first incorporated a commercial Panasonic ML2020 rechargeable manganese dioxide Li ion battery (see Figure 2a).⁷ This 3.0 V “coin cell” had a diameter of 2.0 cm, thickness of 2.0 mm, mass of 2.2 g, and a nominal capacity of 45.0 mAh.

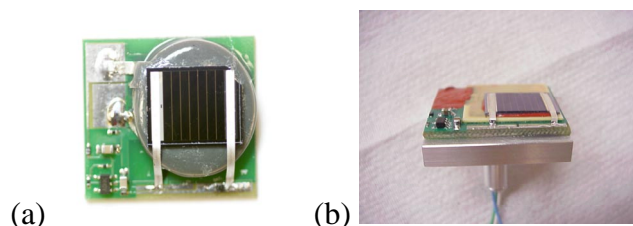


Figure 2. a) Starshine 3 IPS prototype with Panasonic battery; b) IPS with Litestar battery on mounting stub.

The second was a solid state thin film Litestar battery developed by Infinite Power Solutions (see Figure 2b).¹³ This 4.2 V had a $\text{LiNi}_x\text{Co}_{1-x}\text{O}_2$ cathode, a LiPON electrolyte, and Li metal anode. It had an active area of 2.69 cm², capacity of 800 μAh , and approximate mass of 1.23 g, including its substrate, contacts and sealants. The third battery was a 4 cm² and 1.38 g thin film polymer battery developed at the NASA Glenn Research Center. The electrolyte for this 4.2 V battery consisted of lithium (bis) trifluoromethane-sulfonimide, ethylene and propylene carbonate, and the polymer polyacrylonitrile (PAN). The cathode was this same polymer impregnated with $\text{LiNi}_{0.8}\text{Co}_{0.2}\text{O}_2$. The anode was also the same polymer impregnated with graphite.

The IV photoresponse of the MIM was measured at the Glenn Research Center using a simulated air mass zero (AM0) spectrum. The array had a short circuit current of 3.16 mA, an open circuit voltage of 6.93 V, an 80% fill factor, and an efficiency of 12.18 % (see Figure 3).

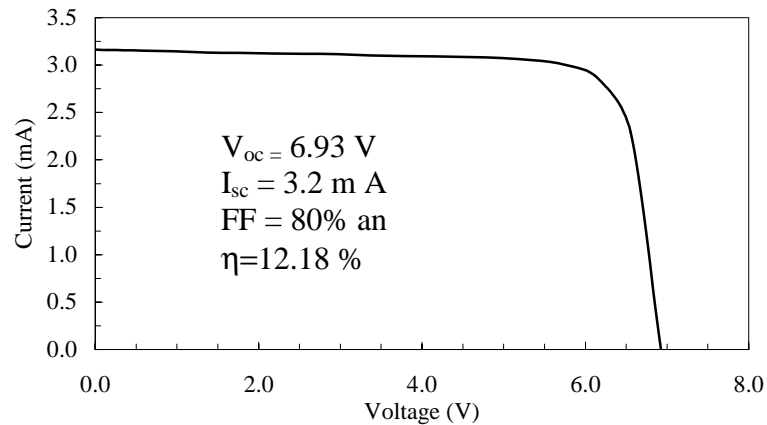


Figure 3. AM0 photoresponse of the GaAs MIM.

The capacity of the various batteries used in the IPS were measured. A typical charge/discharge curve for the Glenn polymer battery is shown in Figure 4. The coin cell has the largest capacity but is also the largest and most massive. Conversely the Litestar has less capacity but is substantially lighter and thinner. It has the highest specific power at 200 Wh/kg.

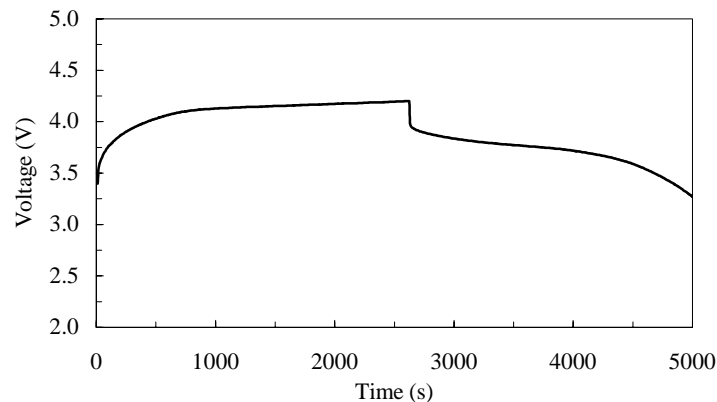


Figure 4. Charge/discharge behavior of 4.2 V lithium polymer battery with a 100 μ A discharge rate.

The prototype IPS were cycled under a simulated AM0 illumination scheme designed to mimic the on-orbit conditions. The IPS will experience a cyclic charging due to the fixed 5° per second rotation which will result in 24 s of charge followed by 48 s of discharge for each 72 s rotation. In addition, this cycling will occur for 56 minutes and be followed by 36 minutes of eclipse or continuous discharging due to the 92 minute LEO.⁶ The IPS was tested under a illumination scheme based on the above times using a simulated AM0 source. Examining a single LEO orbit shows the charge discharge behavior due to the rotation of the satellite (see Figure 5).

In addition to the variation in illumination the IPS will also see a thermal variation associated with the LEO orbit. It is anticipated that the IPS will go from 44.0 °C while in the sun to – 1.0 °C when in eclipse. Figure 6 shows the voltage on a prototype IPS with a Litestar battery during

a simulated LEO orbit with an even more rigorous thermal cycles than anticipated (e.g., plus-or-minus 40 °C).

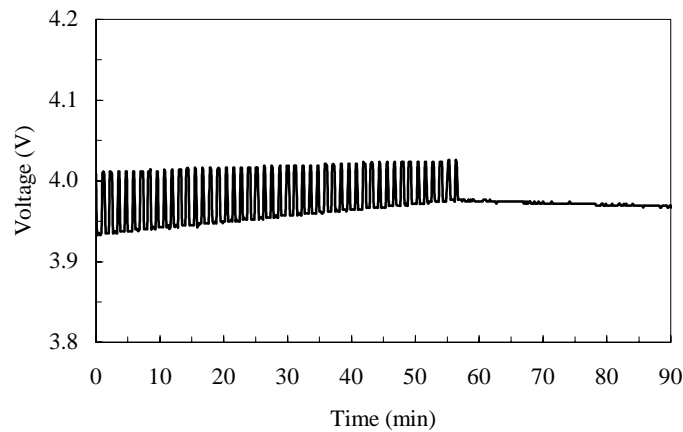


Figure 5. IPS (with Litestar battery) voltage under simulated illumination consistent with a single Starshine 3 orbit (i.e., 5°/sec rotation and 92 min LEO orbit).

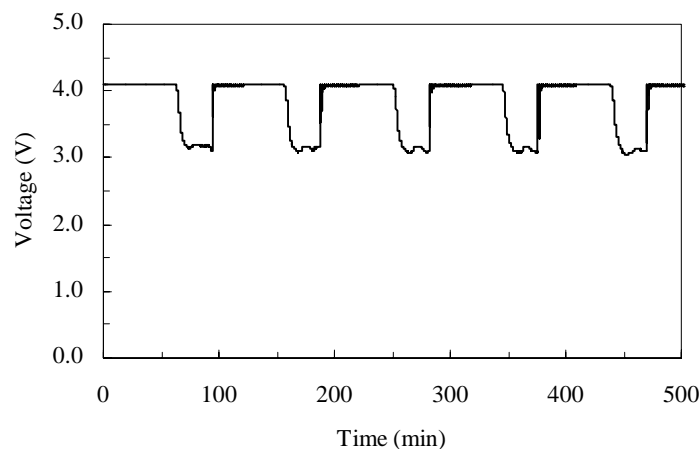


Figure 6. IPS (with Litestar battery) voltage under simulated illumination consistent with a Starshine orbit and thermal fluctuation (i.e., 5°/sec rotation, 92 min LEO orbit, and -40 to 40 °C temperature variations).

CONCLUSION

An IPS that combines three traditionally separate power system functions into a single, integrated device is ideal for future small satellites. IPSs should enjoy near-term applicability in specialized instances where they can serve as de-centralized or distributed power sources or un-interruptible power supplies for discrete components. In addition, with future improvement in both thin-film power generation and energy storage they should also find application as a main power system for upcoming missions using constellations of very small spacecraft, or nanosatellites.

ACKNOWLEDGMENTS

The authors would like to acknowledge the work performed under NASA Cooperative Agreements NCC3-710 and NCC3-563 with the Rochester Institute of Technology. The authors would also like to thank the Gil Moore and the entire Starshine 3 team, especially our colleagues at the NASA Glenn Research Center.

REFERENCES

1. P.V. Panetta, H. Culver, J. Gagosian, M. Johnson, J. Kellogg, D. Mangus, T. Michalek, V. Sank, and S. Tompkins, "NASA-GSFC NanoSatellite Technology Development", SSC98-VI-5, 12th AIAA/USU Conference on Small Satellites, Logan, UT, August 1998.
2. R.P. Raffaele, J. Underwood, J.D. Harris, J. Cowen, D. Scheiman, and A.F. Hepp, 28th IEEE Photovolt. Spec. Conference, Anchorage, AK, September 2000.
3. D.J. Hoffman, T.W. Kerslake, A.F. Hepp, M.K. Jacobs, D. Ponnusamy, AIAA-2000-2919, 35th IECEC, Vol.1, pp. 670-680, July 2000 (also NASA/TM-2000-210342).
4. Raffaele, R.P., Harris, J.D., Hehemann, D., Scheiman, D., Rybicki, G., Hepp, A.F., "A Facile Route to Thin Film Solid State Lithium Microelectronic Batteries", preprint of *J. of Power Sources* **89**, 52 (2000).
5. M.A. Green, K. Emery, D.L. King, S. Igari, W. Warta, *Prog. In Photovolt.* **10**, 1 (2002).
6. R. Koksang, J. Barker, H. Shi, M.Y. Saidi, *Solid State Ionics* **84**, 1 (1996).
7. Lithium Handbook, Panasonic, September 2000.
8. R.P. Raffaele, J.D. Harris, D. Hehemann, D. Scheiman, G. Rybicki, A.F. Hepp, AIAA-2000-2808, 35th IECEC, Vol.1, pp. 58-62, July 2000.
9. K. Takada, S. Kondo, *Ionics* **4**, 42 (1998).
10. <http://www.azinet.com/starshine/>
11. G. Moore, W. Braun, P. Jenkins, W. Holemans, and D. Lefevre, Proceedings of the 15th Annual/USU Conference on Small Satellites, Logan UT, August 2001.
12. P. Jenkins, D. Scheiman, D. Wilt, R. Raffaele R. Button, M. Smith, T. Kerslake, and T. Miller, Proceedings of the 15th Annual Small Satellite Conference, AIAA/Utah State University, August 13-16, 2001.
13. C. Clark, J. Summers, J. Armstrong, AIAA-2000-2922, 35th IECEC, Vol.1, pp. 692-698, July 2000.

A Summary of The 2000-2001 NASA Glenn Lear Jet AM0 Solar Cell Calibration Program

David Scheiman
OAI, Brookpark, Ohio 44142

David Brinker, David Snyder, Cosmo Baraona
NASA GRC, Cleveland, Ohio, 44135

Phillip Jenkins
OAI, Brookpark, Ohio 44142

William J. Rieke (NASA) , Kurt S. Blankenship (NASA), and Ellen M. Tom (FAA)
Cleveland, Ohio 44135

Calibration of solar cells for space is extremely important for satellite power system design. Accurate prediction of solar cell performance is critical to solar array sizing, often required to be within 1%. The NASA Glenn Research Center solar cell calibration airplane facility has been in operation since 1963 with 531 flights to date. The calibration includes real data to Air Mass (AM) 0.2 and uses the Langley plot method plus an ozone correction factor to extrapolate to AM0. Comparison of the AM0 calibration data indicates that there is good correlation with Balloon and Shuttle flown solar cells. This paper will present a history of the airplane calibration procedure, flying considerations, and a brief summary of the previous flying season with some measurement results. This past flying season had a record 35 flights. It will also discuss efforts to more clearly define the ozone correction factor.

HISTORY

The design and sizing of space solar arrays requires precise calculations. Too large an array and the satellite will run hot having to reject the excess energy and have increased launch costs, too small and the satellite will not fulfill its mission draining the batteries and shortening life expectancy. The need for AM0 calibrated solar cells is obvious. One method of calibration is the Langley plot method. This method was developed in the early 1900's when a relationship was found between the solar intensity and the thickness of the atmosphere the sunlight must pass through (Air Mass). Plotting the logarithm of solar cell short circuit current, proportional to solar intensity, as a function of air mass permits extrapolation to an unmeasured air mass and AM0 (ref. 1). Early ground based measurements were done throughout the day as the sun moved across the sky, passing through more atmosphere in the early and late hours and minimizing at solar noon. This method was later used with an airplane, changing altitude to vary the air mass.

The first solar cell calibration airplane flight took place on June 13th, 1963. The airplane was a modified B57B airforce jet, flying 120 flights between 1963 and 1967 (Figure 1). The test cells were placed at the end of an exposed 4:1 collimating tube mounted in the fuselage, this tube was designed to allow 2° change in pointing. Next to the collimating tube was a cavity radiometer to measure the solar intensity. The pilot keeps the tube pointed at the sun during measurements using a sun sight in the cockpit aligned to the tube. Because of the technology limitations, the plane would fly level at several altitudes while measuring the amplified voltage from a 1 ohm shunt resistor using a strip chart recorder. On the ground, the data was plotted manually to determine the intercept points. Data was taken at different altitudes reaching an air mass of 0.25 or 50000 feet along 40°N latitude.

Early data analysis pointed out two important anomalies. First, the AM0 extrapolation was slightly low compared to radiometer data, this was found to be due to ozone absorption of sunlight in the upper atmosphere. Second,

a change in the data linearity was seen when the plane flew below the tropopause, this was because of Mie scattering from particles and absorption by moisture; primarily in the blue end of the spectrum (ref. 2). As a result, a 1% correction was applied to the data to account for ozone absorption and all flight data below the tropopause was not used.



Figure 1: B57B and Collimating Tube, Radiometer and Electronics

The second plane used for calibration was an F106 (Figure 2). This plane was also modified as above and flew 85 flights between 1975 and 1981. This plane flew in the south at $\sim 30^\circ\text{N}$ with a higher sun angle and was able to reach AM 0.17 at the same altitude of 50,000 feet. The calibration technique was similar to that used above.



Figure 2: F106 and Collimating Tube with Radiometer

The third and current plane used is a Lear 25A jet. It is still used today and has flown 324 flights since 1984. The plane can fly to $\sim 50,000$ feet and gets above AM0.2 at 45°N latitude. The flying technique and electronics have progressed to a point where the plane now flies a continuous descent while taking data rather than remaining level over a range of altitudes. A window of the plane was removed to provide sun access for the collimating tube. An operator is no longer required to fly, everything can be controlled from the cockpit.

The Lear test setup has a 5:1 collimating tube illuminating a 4.1 inch diameter temperature controlled plate. The tube angle can be adjusted between 19° and 51° for the sun angle. The electronics are computer controlled and provide an active bias on the test cell to measure short circuit current. In addition to short circuit current, open circuit voltage and full IV curves (>25 points) can also be measured. During descent up to 6 cells, a pressure transducer, thermopile, temperature sensor, and "take data" signal are all measured. The solar cells are measured using kelvin probes (power leads + sense leads) assuring accurate measurements at the cell. The

cells are held at a constant temperature $\pm 1^\circ \text{C}$, this can be set by the computer allowing for temperature dependence. Occasionally, an absolute cavity radiometer with a 5° FOV is flown to measure solar intensity. The new test plate also contains access for a fiber optic connection. This fiber provides input for spectroradiometer which can measure the solar spectrum from 250-2500 nm with 6 nm resolution, a second spectrometer is now available which measures the spectrum from 200-800 nm with 1 nm resolution. Both of these spectrometers will be used to check for any spectral anomalies and provide information on the ozone absorption.



Figure 3: Lear 25A (2nd window on right removed)

The test electronics consist of a Keithley 2420 Sourcemeter connected to the plate by a Keithley 7001 Scanner, both controlled by a Grid 386X computer through an IEEE488 interface. The test plate holds up to 6 solar cells with 2 front contacts for each cell and 2 back contacts common to all 6 cells (the plate). A temperature sensor in the plate is used to regulate two 40W heaters.



Figure 4: Collimating Tube and Cell Test Plate

Error analysis on this calibration method shows that the accuracy is with $\pm 1\%$ (ref. 3). This accuracy has been shown to be comparable with other calibration techniques from around the world (ref. 4).

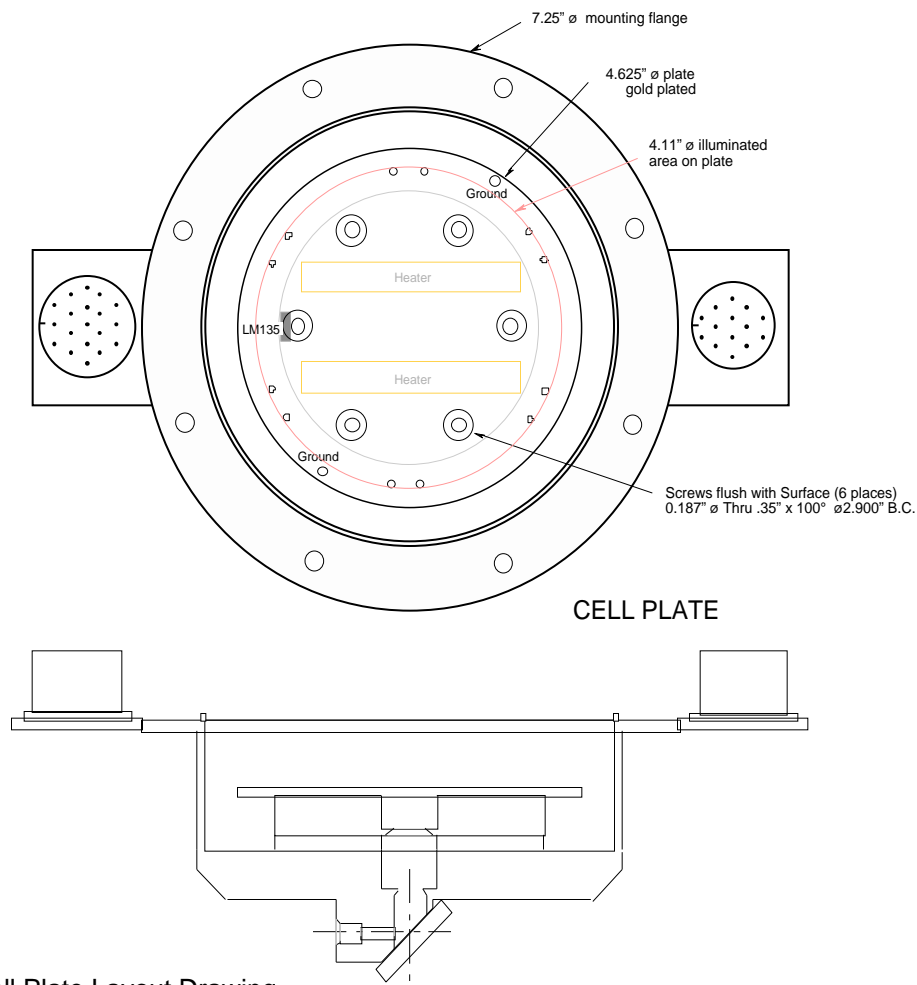


Figure 5: Cell Plate Layout Drawing

LANGLEY PLOT METHOD

Solar cells can be calibrated using the Langley Plot Method. This method was developed by Samuel P. Langley in the early 1900's. It involves plotting the Log of short circuit current (I_{sc}) vs. Air Mass, where air mass is the amount of atmosphere sunlight must pass through to reach a test cell. A linear fit through the data points predicts an AM0 intercept by extrapolation. Traditional Langley plots were done on the ground at high elevations and the air mass varied as the sun moved across the sky throughout the day, air mass being the lowest at solar noon. Clouds and moisture in the atmosphere often skew the results of this method and it required constant spectral correction. The airplane method uses altitude to vary air mass with all the measurements at or near solar noon. Therefore the airplane method can achieve much lower air mass and cleaner air than the ground-based methods applying a small ozone correction to the data with approximately a 3% difference between the measured data and the extrapolated AM0 value.

Air Mass is calculated as shown using the measured pressure p , where $p_o = 14.6944$ psi, and the Sun Declination angle θ . The measurements are also adjusted for earth sun distance r by multiplying by $1/r^2$. Both θ and r can be found in an astronomical almanac. All calibrations are made at 25°C.

$$\text{Air Mass} = \frac{p}{p_o} \sec(\theta) \quad \text{Earth to Sun } I_{SC} \text{ Correction : } I_{SC} = \frac{I_{SC \text{ measured}}}{r^2}$$

An example of the Langley Plot method is shown in Figure 6, notice that the intercept calculation does not vary by much even with noise. The two lines above and below the center one indicate different linear extrapolations with

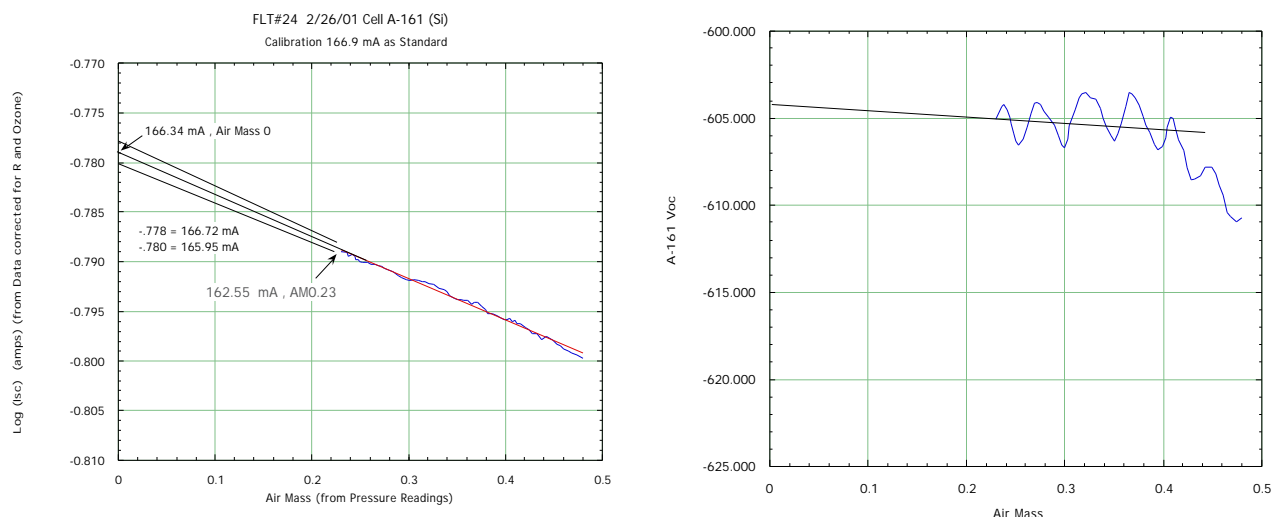


Figure 6: Langley Plot of Cell Data I_{SC} and V_{OC} .

intercepts as shown varying by less than .2%. The second plot also shows that this method can be applied to open circuit voltage (V_{OC}), there is more scatter in the voltage measurement due to its temperature sensitivity, the drop at the end of the curve is due to a drop in temperature.

FLIGHT DATA

The 2000-2001 flying season was a record 35 flights. The data in Table I is a partial summary of the season results, some of the solar cells have been calibrated previous years. There were a total of 51 different cells flown, the data is only a partial list for proprietary reasons, future season summaries will publish more results as permission is granted. Only short circuit currents (I_{SC}) is presented and includes a 1% correction for ozone, open circuit voltage (V_{OC}) was measured but the data is only preliminary. The cells with "A" in the name represent NASA GRC standards. The design of the plate allows for testing of "bare" cells which have front and back contacts, the front contact is made using a spring loaded clip. Some of the cells with higher standard deviations may have had poor connections and/or equipment problems during the flight. The data represents a variety of cell types ranging from Si to the triple junction InGaP/GaAs/Ge.

The flying seasons extend between late October and March which are the limitations of the adjustments to the collimating tube. The collimating tube is set based on the sun angle which changes approximately .3° per day. This season is also the time of year when the tropopause drops low enough for the plane to fly above it and get data during a 10000 foot descent. Data on the tropopause can be obtained from weather balloons on the morning before a flight which is used to determine if a flight will be made that day.

OZONE CORRECTION

The airplane is capable of flying to altitudes close to 50,000 feet. In the airplane calibration technique, the data was found to be inaccurate for two reasons, one being moisture and scatter in the atmosphere and the second

being ozone absorption. Moisture in the atmosphere could be virtually eliminated by staying above the tropopause, the tropopause is lower (<40,000 feet) during colder months of the year. Ozone exists at much higher altitudes and therefore a correction was applied to the AM0 extrapolation. Ozone typically absorbs light from 200-800 nm (ref. 5, ref. 6), and varies across this band (see figure 7). The ozone correction was found to be 1% based on early calculations using ozone absorption coefficients plus the amount of ozone, both applied to the spectral response of Si and GaAs solar cells.

Table I : 2000-2001 Flying Season Calibration Data (all include a 1% ozone correction)

Cal Value	Flight Count	Average	Std Dev	Cell	Area (cm)	Cell Type
	5	176.43	3.88	"Wb13R"	4	Si
166.9	18	165.62	0.83	"A-161"	4	Si
151.2	7	149.61	0.81	"SSF-2"	4	Si
109.8	6	106.28	1.19	"A-133"	4	GaAs
22.5	5	25.71	0.26	"160-2"	0.5	InGaAs
134.8	6	129.21	1.41	"A-181"	4	InP
	7	61.48	0.95	"134-5-6"	4	InGaP
	7	63.61	0.26	"133-5-4"	4	Dual Junction
122.9	1	119.22		"A-188"	4	GaAs
	5	71.81	0.31	"132-5-2"	4	GaSa w/InGaP window
115.3	2	110.91	0.75	"A-168"	4	GaAs
77.8	5	74.91	0.44	"A-186"	1.77	Si
257.6	1	251.98		"A-190"	8	GaAs
162.9	1	164.18		"A-177"	4	Si
113.4	1	107.49		"A-166"	4	GaAs
150.7	3	148.53	0.37	"A-104"	4	Si
	2	61.15	0.15	"TS 2-29"	4	Triple Junction
	2	62.44	0.90	"SL 5-5-6"	4	Triple Junction
	5	128.05	0.96	"ISO-1"	4	GaAs
	2	112.80	0.20	"ISO-2"	4	GaAs
	4	167.99	0.66	"ISO-6"	4	Si
	2	178.32	0.22	"ISO-5"	4	Si
	3	153.24	0.34	"ISO-3"	4	Si
	2	119.38	0.01	"ISO-4"	4	GaAs

This ozone correction worked well for many years but as different cell types enter the market, This correction factor will be changed to reflect cell types. Solar cells with higher bandgaps are more sensitive in the ozone absorption bands and will require a greater correction. Today, the amount of ozone in the atmosphere is measured continually and therefore a more precise ozone quantity can be applied. This ozone correction factor will be discussed in greater detail in the future. Preliminary results of this correction factor applied to previously flown cells show that the range of error for the airplane calibration method will decrease.

Ozone Absorption Coefficients (OAC), Figure 7 illustrates the OAC in the UV, VIS, and NIR portions of the spectrum. These coefficients must be applied to the amount of ozone to determine the loss in cell performance. The amount of ozone in the atmosphere is measured both by the TOMS satellite and surface measurements in Dobson units. 1 Dobson Unit (DU) is defined to be 0.01 mm thickness at stp (0°C 1 atm).

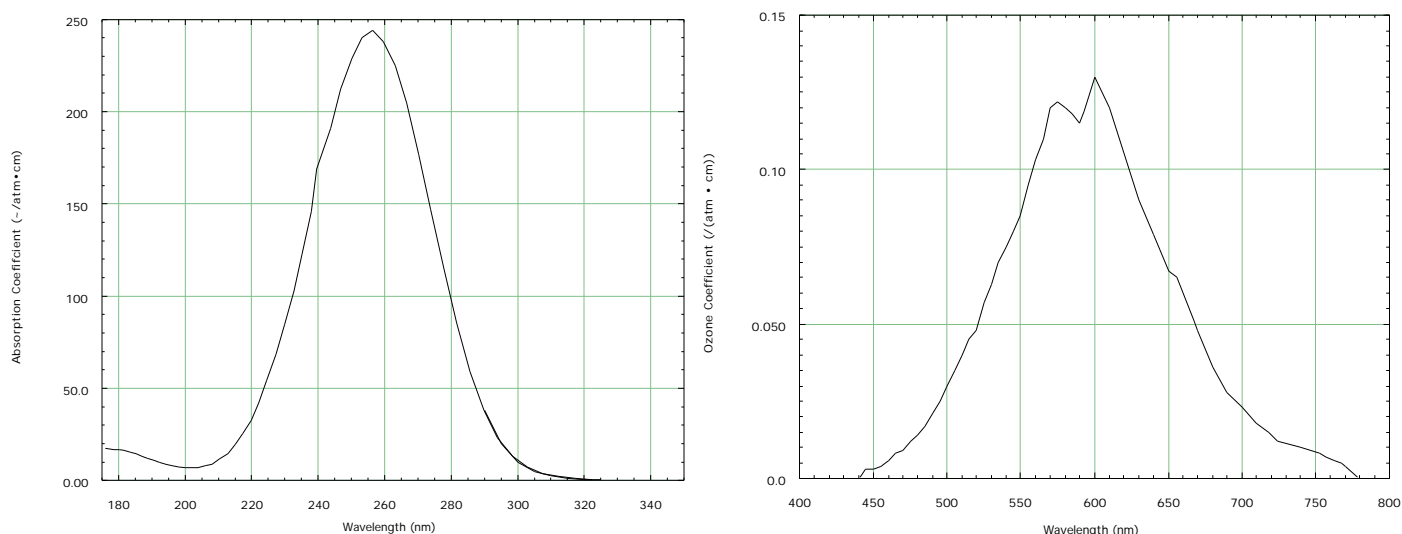


Figure 7: Ozone Absorption Coefficients

CONCLUSION

The NASA Glenn Lear Jet AM0 Solar Cell Calibration Program has been running for 16 years with hundreds of flights and over a 35 year history. Error analysis of the calibration resulted in an accuracy of $\pm 1\%$ and an international intercomparison of calibration techniques shows good agreement. With the improvements to the electronics and the application of a new improved ozone correction factor the accuracy of the calibration will improve. The facility is available for calibrations at a very reasonable cost.

REFERENCES

- 1) H. Brandhorst Jr., E. Boyer, "Calibration of Solar Cells Using High-Altitude Aircraft", NASA TN D-2508, 1965.
- 2) H. Brandhorst Jr. "Anomalies in Solar Cell Langley Plots Associated with the Tropopause", Applied Optics, Vol. 7, No. 4, April 1968.
- 3) P. Jenkins, D. Brinker, D. Scheiman, "Uncertainty Analysis of High Altitude Aircraft Air Mass Zero Solar Cell Calibration", Proceedings of the PVSC 26, Sept. '97, p. 857-860.
- 4) S. Matsuda, D. Hood, T. Gomez and Yang, "Results from the First International Round Robin Calibration and Measurement of Space Solar Cells" Proceeding from PVSC 26, 1997, p. 1043
- 5) E. Vigroux, "Contribution to the Experimental Study of the Absorption of Ozone", Annales de Phys., vol. 8, Sept.-Oct. 1953, pp. 709-762.
- 6) A. M. Bass and R. J. Paur, "The ultraviolet cross-section of ozone: I. The measurements", in "Atmospheric Ozone, Proc. Quadrennial Ozone Symposium", Eds. C. S. Zerefos and A. Ghazi, Reidel publ., 606-610, 1985.

Space and Terrestrial Photovoltaics – Synergy and Diversity

Sheila Bailey,^a Ryne Raffaele,^b and Keith Emery^c

a) NASA Glenn Research Center at Lewis Field, Cleveland, OH 44135

b) Rochester Institute of Technology, Rochester, NY 14623

c) National Renewable Energy Lab, Golden, CO 80401

ABSTRACT

A historical view of the research and development in photovoltaics from the perspective of both the terrestrial and the space communities is presented from the early days through the '70s and '80s and the '90s and beyond. The synergy of both communities in the beginning and once again in the present and hopefully future are highlighted, with examples of the important features in each program. The space community which was impressed by the light-weight and reliability of photovoltaics drove much of the early development. Even up to today, nearly every satellites and other scientific space probe that has been launched has included some solar power. However, since the cost of these power systems were only a small fraction of the satellite and launch cost, the use of much of this technology for the terrestrial marketplace was not feasible. It was clear that the focus of the terrestrial community would be best served by reducing costs. This would include addressing a variety of manufacturing issues and raising the rate of production. Success in these programs and a resulting globalization of effort resulted in major strides in the reduction of PV module costs and increased production. Although, the space community derived benefit from some of these advancements, its focus was on pushing the envelope with regard to cell efficiency. The gap between theoretical efficiencies and experimental efficiencies for silicon, gallium arsenide and indium phosphide became almost non-existent. Recent work by both communities have focused on the development thin film cells of amorphous silicon, CuInSe₂ and CdTe. These cells hold the promise of lower costs for the terrestrial community as well as possible flexible substrates, better radiation resistance, and higher specific power for the space community. It is predicted that future trends in both communities will be directed toward advances through the application of nanotechnology. A picture is emerging in which the space and terrestrial solar cell communities shall once again share many common goals and, in fact, companies may manufacture both space and terrestrial solar cells in III-V materials and thin film materials. Basic photovoltaics research including these current trends in nanotechnology provides a valuable service for both worlds in that fundamental understanding of cell processes is still vitally important, particularly with new materials or new cell structures. It is entirely possible that one day we might have one solar array design that will meet the criteria for success in both space and on the Earth or perhaps the Moon or Mars.

INTRODUCTION

In 1839 Becquerel observed that a photovoltage resulted from the action of light on an electrode in an electrolytic solution. In the 1870s it was discovered that the solid material selenium demonstrated the same effect and by the early 1900s selenium photovoltaic cells were widely used in photographic exposure meters. By 1914 these cells were still less than 1% efficient. In 1954, Chapin reported a solar

conversion efficiency of 6% for a silicon single-crystal cell marking the beginning of modern day photovoltaics. At approximately the same time the first thin film solar cells of CdS/CuS₂ were being developed by the US Air Force Laboratory in Dayton, Ohio. These cells had an efficiency of ~1.5%. In 1955 the first III-V cells (GaAs, InP) were made and by 1956 GaAs had a reported efficiency of 6%. By 1958, small area Silicon solar cells had reached an efficiency of 14% under terrestrial sunlight. The big push to develop solar power, however, came from its obvious space application. On March 17, 1958 the world's first solar powered satellite was launched, Vanguard 1. It carried two separate radio transmitters to transmit scientific and engineering data concerning, among other things, performance and lifetime of the 48 p/n silicon solar cells on its exterior. The battery powered transmitter operated for 20 days; the solar cell powered transmitter operated until 1964, at which time it is believed that the transmitter circuitry failed. Setting a record at the time for satellite longevity, Vanguard 1 proved the merit of space solar cell power. The solar cells were fabricated by Hoffman Electronics for the U.S. Army Signal Research and Development Laboratory at Fort Monmouth. In 1961 many of the staff from the silicon cell program at Fort Monmouth transferred to NASA Lewis Research Center (now Glenn Research Center) in Cleveland, Ohio. From that time to the present, the Photovoltaic Branch at Glenn has served as the research and development base for NASA's solar power needs. Impressed by the light-weight and reliability of photovoltaics, almost all communication and military satellites and scientific space probes have been solar powered.

The Early Years

As the first photovoltaic devices were being created there were corresponding theoretical predictions emerging citing ~20% as the potential efficiency of Si and 26% of an optimum bandgap material (1.5eV) under terrestrial illumination. In addition the concept of a tandem cell was proposed to enhance the overall efficiency. An optimized three-cell stack was soon to follow with a theoretical optimum efficiency of 37%. Research was focused on understanding and mitigating the factors that limited cell efficiency (e.g., minority carrier lifetime, surface recombination velocity, series resistance, reflection of incident light, and non-ideal diode behavior). However, it was pointed out that solar cells were too expensive to compete with fossil fuels for electricity, citing that a 10% efficient Si cell would cost \$357 per peak watt.

The launch of the USSR Sputnik in 1957 provided the missing application for solar cells and therefore, funding, for continued photovoltaic research. Early satellites needed only a few watts to several hundred watts. The power source must be available, reliable and ideally have a high specific power (W/kg) since early launch costs were ~ \$10K/kg or more. The cost of the power system for these satellites was not of paramount importance since it was a small fraction of the satellite and launch cost. The size of the array was important for many early satellites due to the body-mounted array design, therefore limiting total power. Thus there were multiple reasons to focus on higher efficiency solar cells. Explorer I launched in 1958 discovered the van Allen radiation belts, adding a new concern for space solar cells that was not present in the terrestrial environment (i.e., electron and proton irradiation damage). Radiation damage studies at the Naval Research Laboratories in the '60s provided guidance to the spacecraft designers with regard to cell degradation. The launch of Telstar in 1962 created new markets for space photovoltaics (i.e., terrestrial communications). Telstar's beginning of life (BOL) power was 14 W but high radiation caused by a nuclear weapon test reduced the power output.

There was a great deal of both theoretical and experimental research in the '60s. The early CdS/CuS₂ solar cells were found to degrade over time. CdTe cells were developed reaching efficiencies of ~ 7.5%. However, the higher efficiency and stability of the silicon solar cells assured their preeminence in satellite power for the next 3 decades. Research on thin film cells, because of their higher specific power and projected lower costs, was also funded at lower levels by the space

community. Aside from the cell response to a radiation environment, the goals of both the terrestrial and space community were the same.

The ‘70s and ‘80s

As the ‘70s began, solar cells were still too expensive at around \$300/W for widespread terrestrial use. Nuclear power plants were being built for large power utilities. It was clear that the focus of the terrestrial community would be best served by reducing costs. This would include addressing a variety of manufacturing issues and raising the rate of production. Figure 1 shows PV module production and cost as a function of time from 1980 to 1999 (data courtesy of National Center for Photovoltaics Research).

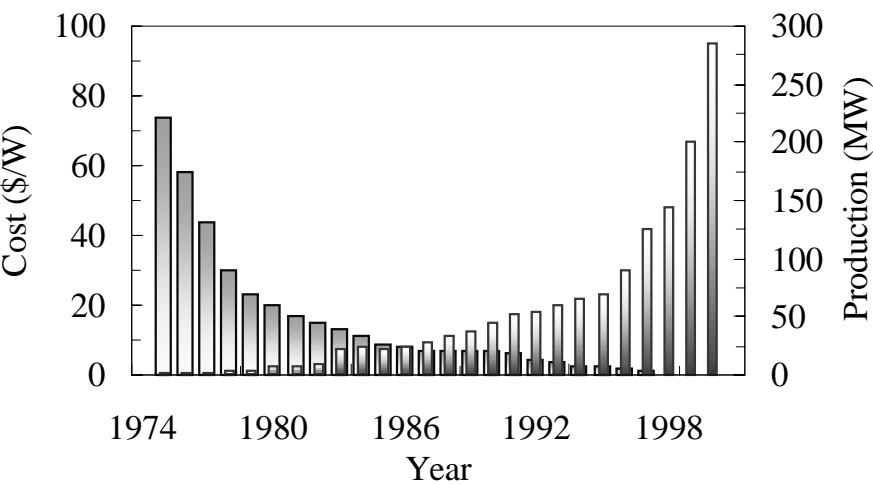


Figure 1. Photovoltaic cell cost and photovoltaics shipments per year from 1975 to 2000. (The wider bar shaded at the top are for cost and the narrow bars shaded at the bottom represent production).

The OPEC oil embargo of 1973 also provided impetus to the photovoltaic community. The US Solar Energy Research Institute in Golden Colorado was established. The DOE Photovoltaic Budget by fiscal year is shown below in Figure 2.

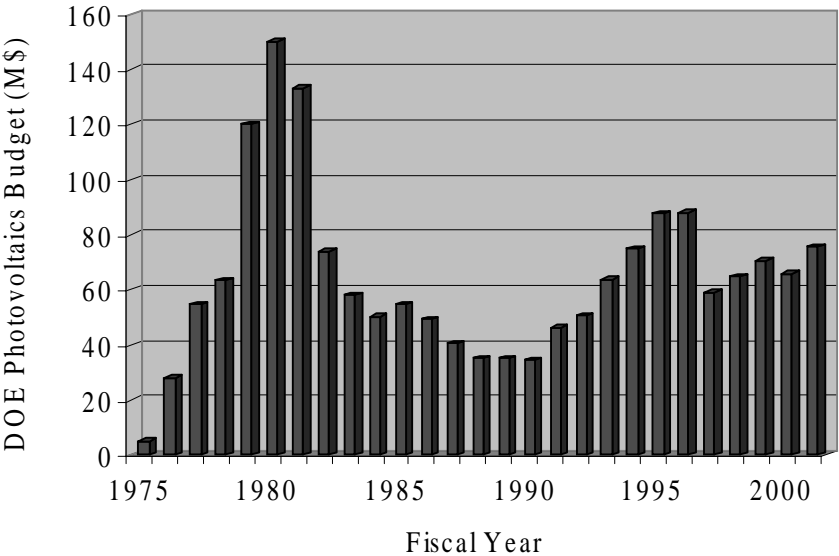


Figure 2. US Department of Energy Budget by Fiscal Year.

In the '80s other countries developed national programs in Photovoltaics. The increased funding in both photovoltaic research and in private industry yielded a substantial reduction in PV module costs from \$300/W in 1980 US dollars to \$5/W in 1990 US dollars and production increased by a factor of 4. The gap between theoretical efficiencies and experimental efficiencies for silicon, gallium arsenide and indium phosphide became almost non-existent (see Figure 3). New thin film cells of amorphous silicon, CuInSe₂ and CdTe renewed the enthusiasm for the promise of lower costs for the terrestrial community and the potential for increasing the thin film efficiency and making them on flexible substrates excited the space community.

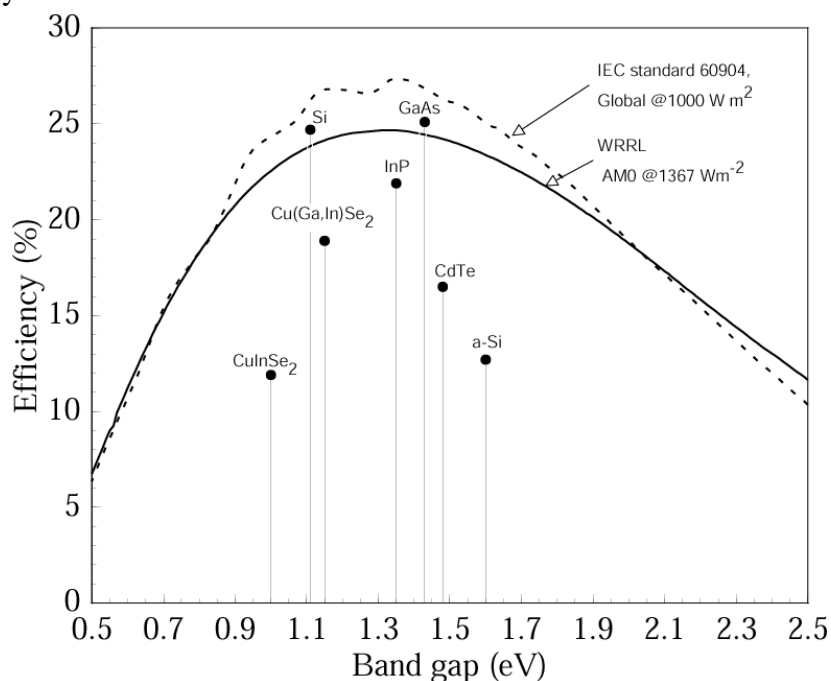


Figure 3. Theoretical efficiency for a single-junction cell with 100% external quantum efficiency as a function of energy gap at one-sun and 25 °C using the model described in reference 11. The standard global¹² and AM0¹³ reference spectra are used. Independently confirmed efficiencies at one-sun, 25 °C global for several state-of-the-art single-junction solar cells are also shown for comparison purposes.^{14, 15}

During these two decades silicon provided the power for space, culminating in the design of the solar arrays for Space Station, which became an International Space Station (ISS) in 1988, see Figure 4.

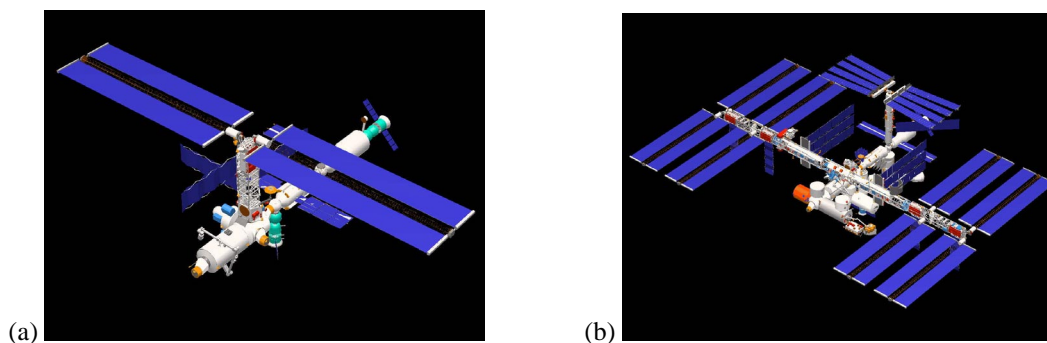


Figure 4. (a) Current status of ISS and (b) Planned Configuration of ISS by 2004.

The International Space Station will have the largest photovoltaic power system ever present in space. It will be powered by 262,400 (8cm x 8cm) silicon solar cells with an average efficiency of 14.2% on 8 US solar arrays (each ~ 34 m x 12 m). This will generate about 110 kW of average power, which after battery charging, life support, and distribution, will supply 46 kW of continuous power for research experiments. The Russians also supply an additional 20kW of power to ISS.

Research in the 80's however focused more on the III-V solar cells and multi-junction cells which had higher efficiencies and were more tolerant of the radiation environment. Satellites grew in both size and power requirements and structures were designed to deploy large solar arrays during this decade. However, the mass and fuel penalty for attitude control still dictated a move to more efficient cells. Costs for satellite power system remained at about a US\$1000/W.

The '90s and beyond

In the terrestrial world, cost is still the driver in photovoltaic development, but more options seem imminent in the thin film systems. The smaller material costs and higher production potential for thin film arrays may drive PV modules below current costs with US\$1/W as a goal. This necessitates the development of a 20% thin film cell. The problem is more complicated for space applications since these cells must be developed on a low cost, light-weight flexible substrate with at least 15% air mass zero (AM0) efficiencies to be cost-effective for satellite power systems. The space world has transitioned to commercially available III-V cells with 24-26% AMO of GaInP/GaAs/Ge. Tables I and II below list the current status of cell efficiencies for AM1.5 and AM0.

Cells	Efficiency(%) AM 1.5 global	Efficiency(%) AM 0	Area (cm ²)	Description
c-Si	24.7		4.0	UNSW PERL ¹⁶
c-Si	22.3	21.1	21.45	Sunpower ¹⁶
Poly-Si	19.8		1.09	UNSW/Eurosolare ¹⁶
Poly-Si	18.6	17.1*	1.0	Georgia Tech/HEM ¹⁶
c-Si(thin film transfer)	15.3		1.015	U. Stuttgart (24μm thick) ¹⁶
c-Si film	16.6	14.8*	.98	Astropower ¹⁶
GaAs	25.1	22.1*	3.91	Kopin ¹⁶
GaAs	23.8	20.7	4.0	ASE Heilbronn ¹⁷
InP	21.9	19.3*	4.02	Spire ¹⁶
GaInP (1.88ev)	14.7	13.5	1.0	ISE ¹⁷
GaInP/GaAs/Ge	31.0	29.3	.25	Spectrolab ¹⁸
GaInP/GaAs/Ge	25.0	21.7*	4.0	ASEC ¹⁷
Cu(Ga,In)Se	18.8	16.4*	1.04	NREL, on glass ¹⁶
CdTe	16.4	14.7*	1.131	NREL, on glass ¹⁶
a-Si/a-Si/a-SiGe**	13.5	12.0	.27	USSC ¹⁶
Photo-electrochemical	10.6	9.8*	.25	EPFL,nanocrystalline dye ¹⁶

The efficiency and Jsc for global reference conditions (25°C, 1000 W/m², IEC 60904-3, ASTM E892 global) were taken from the references and translated to AM0 using the new ASTM E490-2000 reference spectrum. The calculated efficiency assumes that the fill factor does not change for the increased photocurrent. Quantum efficiencies corresponding to the table entries were used in the calculations.

** unstabilized

Table I. AM1.5 and AM1.0 Efficiencies for Small Area Cells

Module	Efficiency (%) Global AM1.5	Area (cm ²)	Description
c-Si	22.7	778	UNSW?Gochermann ¹⁶
multi-c-Si	15.3	1017	Sandia/HEM ¹⁶
CIGSS	12.1	3651	Siemens Solar ¹⁶
CdTe	10.7	4874	BP Solarex ¹⁶
a-Si/a-Si/a-SiGe	10.4	905	USSC ¹⁶
photochemical	4.7	141.4	nanocrystalline dye sub module ¹⁶

Note: that an approximate conversion from global AM1.5 to AM0 depends on cell type and ranges from 0.87 for GaAs and CIGS to 0.945 for crystalline Si and GaInP/GaAs/Ge. The assumed intensities are 1000 W/m² AM1.5 and 1367 W/m² AM0 at 25 °C for both.

Table II. AM1.5 Efficiencies for Modules.

Research in the III-V multi-junction solar cells has been focused on fabricating either lattice-mismatched materials with optimum stacking bandgaps or new lattice matched materials with optimum bandgaps. In the near term this will yield a 30% commercially available space cell and in the far term possibly a 40% cell. Cost reduction would be achieved if these cells could be grown on a silicon rather than a germanium substrate since the substrate is ~65% of the cell cost. The advent of this new competitor in 1998 and other factors combined to reduce space cells costs by ~ 40% of their 1997 cost. A few possible cell structures for future III-V devices are illustrated in Figure 5.

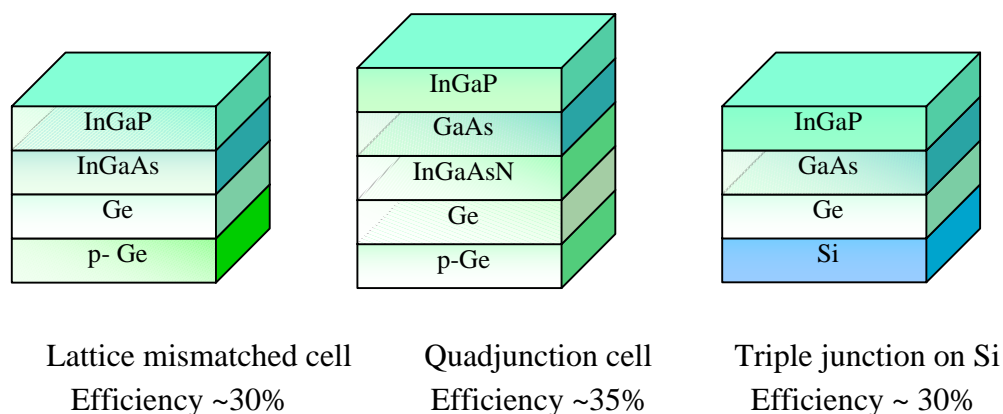


Figure 5. Proposed structures for III-V tandem cell development

The problem areas with projected III-V cell development include the material growth difficulty of the InGaAsN 1.05 eV bandgap material, minimizing defect growth in lattice mismatched material, and current limiting in the Ge subcell.¹⁹ Other approaches using GaAs substates (higher cost and efficiency), mechanical stacking, or 3 and 4-terminal monolithic designs are also being pursued. Longer-term projects in the area of multi-junction III-V cells would include the potential of growing these cells on a low cost ceramic substrate and the possibility of efficiency enhancement by nano-structures. With a recurring interest in terrestrial concentrators, once again the space community and terrestrial community may also have common goals for high efficiency III-V cells.

A recent USAF driven initiative has renewed interest in thin film array development for space. The program addresses the concern of higher efficient cells on flexible substrates and also the development of light-weight array structures. An example of a large structure for solar electric propulsion is shown below in Figure 6.



Figure 6. Proposed Mars solar electric propulsion vehicle

Spacecraft systems studies which consider the system level implications of increased array area indicate that thin film cells of less than 15 to 20 % efficient would not be cost effective except for certain applications which might involve a high radiation environment, or a stowage volume problem in the launch configuration, or perhaps a unique spacecraft configuration. This is due to a variety of possible cost considerations including array development, spacecraft attitude control,

Current terrestrial thin film programs will benefit the space community as manufacturing techniques are improved bringing the small area cell efficiencies in Table I closer to the large area modules in Table II. The Space community requires that thin film cells must be produced on a lightweight substrate due to the mass penalties imposed in launching. The best thin film cells to date have required processing temperatures in excess of 600°C, which prohibit the use of current polyimide substrates. Research has focused on both finding high temperature tolerant substrates and on reducing the processing temperature of the thin film cells. A low cost flexible substrate would also benefit the terrestrial community by replacing the expensive and fragile heavy glass structures.

Clearly, the ability to increase thin film cell efficiencies would impact both the terrestrial and space cell communities. Semiconductor quantum dots are currently a subject of great interest by both communities. This is mainly due to their size-dependent electronic structures, in particular the increased band gap and therefore tunable optoelectronic properties. A quantum dot is a granule of a semiconductor material whose size is on the nanometer scale. These nanocrystallites behave essentially as a 3-dimensional potential well for electrons (i.e., the quantum mechanical “particle in a box”). To date these nanoparticles have been primarily limited to sensors, lasers, LEDs, and other optoelectronic devices. However the unique properties of the size dependent increase in oscillator strength due to the strong confinement exhibited in quantum dots and the blue shift in the band gap energy of quantum dots are properties that can be exploited for developing photovoltaic devices that offer advantages over conventional photovoltaics. The increased oscillator strength of the quantum dots will produce an increase in the number of photons absorbed and consequently, the number of photogenerated carriers. On the other hand, the blue shift in the band gap energy allows for engineering an ensemble of quantum dots in a size range that will capture most of the radiation from the terrestrial and space solar energy spectrum (see Figure 7a).

There have been several proposed methods to improve solar cell efficiency through the introduction of quantum dots. One of the main methods is to produce an ordered array of quantum dots within the intrinsic region of a p-i-n solar cell (see Figure 7b). The overlap of the discrete wavefunctions associated with the electronic states of the individual dots will produce narrow electronic energy bands or “mini-bands.” By adjusting the dot size and spacing, a device can be manufactured such that these mini-bands will lie energetically between the valence and conduction bands of the host semiconductor, or in other words within their bandgap. The quantum dots in an intermediate bandgap solar cell can be thought of as an array of semiconductors that are individually size-tuned for optimal absorption at a desired region

of the solar energy emission spectrum. This is in contrast with a bulk material where photons are absorbed at the band gap and energies above the band gap where the photogeneration of carriers is less efficient. In addition, bulk materials used in solar energy cells suffer from reflective losses at energies about the band gap, whereas for individual quantum dots reflective losses are minimized. It is also predicted that quantum dot solar cells may have other attractive features for space utilization (i.e., high radiation tolerance and small temperature coefficients). To a first approximation the energy levels of quantum dot structures are temperature independent. In fact thermal energy assists in populating those levels. This implies a lower temperature coefficient than a normal pn-junction solar cell. Unfortunately, it is difficult to estimate the potential temperature range due to the temperature dependence of other cell components.

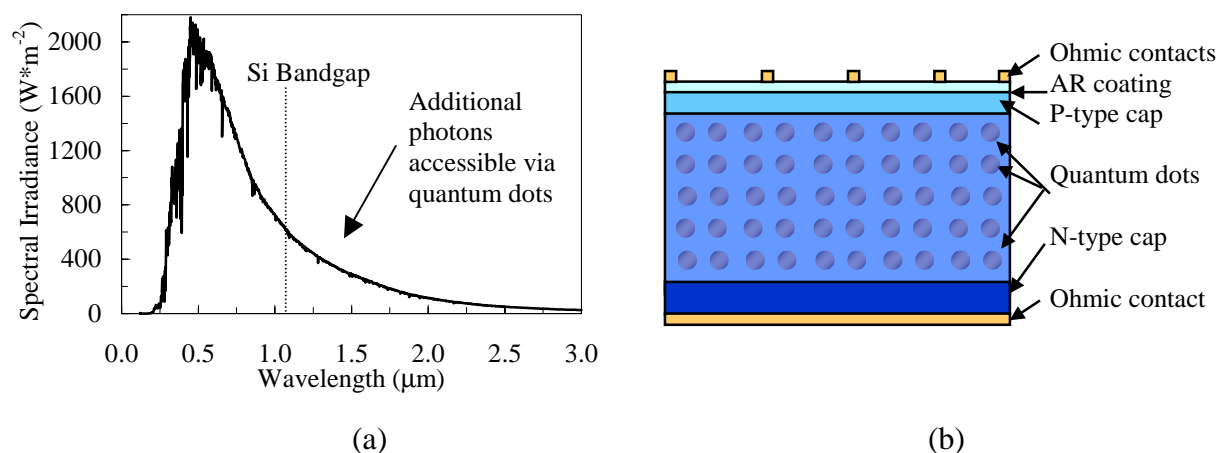


Figure 7. a) Air mass zero spectrum (ASTM E-490) and (b) proposed quantum dot solar cell structure.

Including graded quantum dots in a solar cell offers the opportunity to engineer the band gap energy of a solar cell over a wide range, thereby maximizing the capability of the emitted photons of the sun's spectrum to photogenerate carriers. Theoretical studies predict a potential efficiency of 63.2 %, for a single size quantum dot, which is approximately a factor of 2 better than any state-of-the-art (SOA) device available today.²⁰ For the most general case, a system with an infinite number of sizes of quantum dots has the same theoretical efficiency as an infinite number of bandgaps or 86.5%.²⁰ Furthermore, the use of quantum dot technology is also applicable to thin-film devices offering a potential 4-fold increase in power-to-weight ratio over SOA thin film cells.

Conclusions

A picture of the future is emerging in which the space and terrestrial solar cell communities shall once again share many common goals and, in fact, companies may manufacture both space and terrestrial solar cells in III-V materials and even thin film materials. The research community provides a valuable service for both worlds in that fundamental understanding of cell processes is still vitally important, particularly with new materials or new cell structures. It is entirely possible that one day we might have one solar array design that will meet the criteria for success in both space and on the ground on Earth or perhaps the Moon or even Mars.

References

- [1] Becquerel E. (1839), *On electron effects under the influence of solar radiation*, Comptes Rendues 9, 561.
- [2] Chapin D.M., Fuller C.S., Pearson, G.L. (1954), *A new silicon photocell for converting solar radiation into electrical power*. J. Appl Phys. 25, 676.
- [3] Reynolds D.C., Leies G., Antes L., Marburger R.E. (1954), *Photovoltaic effect in cadmium sulfide*, Phys. Rev. 96, 533.
- [4] Jenny D.A., Loverski J.J., Rappaport P. (1956), *Photovoltaic effect in GaAs p-m-junctions and solar energy conversion*, Phys. Rev. 101, 1208.
- [5] Easton R.L., Votaw M.J. (1959), *Vanguard I IGY Satellite (1958 Beta)*, Rev. of Scientific Instruments, 30, 2, pp. 70-75.
- [6] Loeferski J.J. (1956), *Theoretical considerations governing the choice of the optimum semiconductor for the photovoltaic solar energy conversion*, J. Appl. Phys. 27, 777.
- [7] Jackson E.D. (1955), *Areas for improvement of the semiconductor solar energy converter*. Trans. Of the Conf. On the Use of Solar energy, Tucson, Arizona, 5, 122.
- [8] Cherry W. (1955), *Military considerations for a photovoltaic solar energy converter*, Trans. of the Conf. On the Use of Solar energy, Tucson, Arizona, 5, 127.
- [9] Statler R.L., Curtin D.J. (1973), *Silicon solar cell degradation in the space environment*, Proc. International Conf. On the Sun in the Service of Mankind, p. 361.
- [10] *The Telstar Experiment* (1963), Bell Syst. Tech. J. 42.
- [11] M.W. Wanlass, K.A. Emery, T.A. Gessert, G.S. Horner, C.R. Osterwald, and T.J. Coutts, "Practical Considerations in Tandem Cell Modeling," Proc. SERI 9th Photovoltaics Advanced Research and Development meeting, May 24-26, 1989, Solar Cells, vol. 27, pp. 191-204, 1989.
- [12] M.A. Green and K. Emery, D.L. King, S. Igari, and W. Warta "Solar Cell Efficiency Tables (version 19)," Progress in Photovoltaics Research and Applications, vol. 10, pp. 55-61, 2002.
- [13] W. E. Devaney, R. A. Mickelsen, and W. S. Chen, "Recent improvements in CuInSe₂/ZnCdS thin film solar cell efficiency," presented at Eighteenth IEEE Photovoltaic Specialists Conference, Las Vegas, NV, p. 1733, 1985
- [14] Standard IEC 60904-3, Measurement Principles for Terrestrial PV Solar Devices with Reference Spectral Irradiance Data, International Electrotechnical Commission, Geneva, Switzerland.
- [15] Wehrli C, Extraterrestrial Solar Spectrum, Physikalish-Meterologisches Observatorium and World Radiation Center, Tech. Report 615, Davos-Dorf, Switzerland, July 1985
- [16] M.A. Green and K. Emery, D.L. King, S. Igari, and W. Warta "Solar Cell Efficiency Tables (version 18)," Progress in Photovoltaics Research and Applications, vol. 9, pp. 287-293, 2001.
- [17] K. Bücher, S. Kunzelmann, "The Fraunhofer ISE PV Charts: Assesment of PV Device Performance," Proc. 2nd World Conference and Exhibition on Photovoltaic Solar Energy Conversion, Vienna Austria July 6-10, 1998, Joint Research Center report EUR 18656, pp. 2329-2333.
- [18] M.A. Green, K. Emery, K. Bücher, D.L. King, and S. Igari "Solar Cell Efficiency Tables (version 11)," Progress in Photovoltaics: Research and Applications, vol. 6, pp. 35-42, 1998.
- [19] R.R. King, M. Haddad, T. Isshiki, P. Colter, J. Ermer, H. Yoon, D.E. Joslin, and N.H. Karam, "Metamorphic GaInP/GaInAs/Ge Solar Cells," 28th IEEE Photovolt. Specialist Conference, Anchorage, AK, 2000.
- [20] A. Luque and A. Marti, *Phys. Rev. Lett.* **78**, 5014 (1997).

Weinberg Award Winner

Henry B. Curtis

17th Space Photovoltaic Research and Technology Conference at the Ohio Aerospace Institute

1961 to 1975 Instrument & Computing Division

Henry's duties in the Instrument & Computing Division included total hemispherical emittance and normal solar absorptance measurements; design and characterization of solar simulators; optical measurements of materials; and a variety of instrument systems.

1975 to Present Photovoltaic and Space Environments Branch

Henry was transferred to the PV Branch in 1975 to work in the terrestrial PV program. His duties included calibration and distribution of reference cells; measurement of all the Block I and Block II terrestrial modules; purchase and setup of the two flash simulators; and writing of standards for terrestrial PV measurements. The last item involved coordination with JPL, Sandia, SERI, Lincoln Labs; and several terrestrial cell vendors.

As the terrestrial program waned in 1980, Henry moved to space PV. He started research contracts with Varian, ASEC, Hughes, and others involving multi-junction and concentrator solar cells for space use. His in-house research centered on radiation damage of multi-junction and concentrator cells, modeling of multi-junction cell performance, optical characterization of optical reflectors on silicon cells, and flight programs.

Much effort was spent on the PASP Plus flight experiment. Pre-launch measurements of all the modules, many review meetings, an end-to-end test of the entire experiment at Boeing, launch preparations, launch and flight support, and a great deal of data analysis. This involved close coordination with Hanscom AFB, other Lewis flight hardware groups, space data people at Onizuka AFB, and Orbital Science, the actual spacecraft builder.

In 1983, Henry was chosen by Lockheed to be part of a two-man government advisory team for the GaAs solar cell program that Lockheed was doing with ASEC. He has also spent considerable time on government review teams for SUPER, a program for survivable space power; Skipper, a BMDO program to look at interactions between the upper atmosphere and re-entering space objects; and the recent Scarlet programs on concentrator arrays.

Currently, Henry is acting as a TPA manager, is serving on a JPL committee to write a PV “roadmap” for research for Code-S, and is planning to start modeling for the in-house III-V program.

Henry is also author and co-author on about 90 papers and conference publications. He has given a tutorial at the PVSC and has been involved several times with the program committee of the PVSC; and has also taken a turn as SPRAT chairman!



REPORT DOCUMENTATION PAGE			Form Approved OMB No. 0704-0188	
Public reporting burden for this collection of information is estimated to average 1 hour per response, including the time for reviewing instructions, searching existing data sources, gathering and maintaining the data needed, and completing and reviewing the collection of information. Send comments regarding this burden estimate or any other aspect of this collection of information, including suggestions for reducing this burden, to Washington Headquarters Services, Directorate for Information Operations and Reports, 1215 Jefferson Davis Highway, Suite 1204, Arlington, VA 22202-4302, and to the Office of Management and Budget, Paperwork Reduction Project (0704-0188), Washington, DC 20503.				
1. AGENCY USE ONLY (Leave blank)		2. REPORT DATE October 2002		3. REPORT TYPE AND DATES COVERED Conference Publication
4. TITLE AND SUBTITLE 17th Space Photovoltaic Research and Technology Conference			5. FUNDING NUMBERS WU-344-96-5B-00	
6. AUTHOR(S) Phillip Jenkins, compiler				
7. PERFORMING ORGANIZATION NAME(S) AND ADDRESS(ES) National Aeronautics and Space Administration John H. Glenn Research Center at Lewis Field Cleveland, Ohio 44135-3191			8. PERFORMING ORGANIZATION REPORT NUMBER E-13525	
9. SPONSORING/MONITORING AGENCY NAME(S) AND ADDRESS(ES) National Aeronautics and Space Administration Washington, DC 20546-0001			10. SPONSORING/MONITORING AGENCY REPORT NUMBER NASA CP-2002-211831	
11. SUPPLEMENTARY NOTES Proceedings of a conference held at Ohio Aerospace Institute and sponsored by NASA Glenn Research Center, Brook Park, Ohio, September 11-13, 2001. Responsible person, Eric Clark, organization code 5410, 216-433-2233.				
12a. DISTRIBUTION/AVAILABILITY STATEMENT Unclassified - Unlimited Subject Category: 20 Available electronically at http://gltrs.grc.nasa.gov This publication is available from the NASA Center for AeroSpace Information, 301-621-0390.			12b. DISTRIBUTION CODE	
13. ABSTRACT (Maximum 200 words) The 17th Space Photovoltaic Research and Technology (SPRAT XVII) Conference was held September 11-13, 2001, at the Ohio Aerospace Institute (OAI) in Cleveland, Ohio. The SPRAT conference, hosted by the Photovoltaic and Space Environments Branch of the NASA Glenn Research Center, brought together representatives of the space photovoltaic community from around the world to share the latest advances in space solar technology. This year's conference continued to build on many of the trends shown in SPRAT XVI; the use of new high-efficiency cells for commercial use and the development of novel array concepts such as Boeing's Solar Tile concept. In addition, new information was presented on space environmental interactions with solar arrays.				
14. SUBJECT TERMS Solar cell; Photovoltaics power; Radiation damage; Space environmental effects			15. NUMBER OF PAGES 223	
			16. PRICE CODE	
17. SECURITY CLASSIFICATION OF REPORT Unclassified	18. SECURITY CLASSIFICATION OF THIS PAGE Unclassified	19. SECURITY CLASSIFICATION OF ABSTRACT Unclassified	20. LIMITATION OF ABSTRACT	